Chemical, Isotopic, and Temporal Variations during Crustal Differentiation: Insights from the Dariv Igneous Complex, Western Mongolia

by

Claire Elizabeth Bucholz

B.S. Geology and Geophysics
Yale University, 2009

Submitted in partial fulfillment of the requirements for the degree of

DOCTOR OF PHILOSOPHY
in Geochemistry
at the
MASSACHUSETTS INSTITUTE OF TECHNOLOGY
and the
WOODS HOLE OCEANOGRAPHIC INSTITUTION

February 2016

Signature redacted

Author.....
Joint Program in Marine Geology and Geophysics
Massachusetts Institute of Technology
and Woods Hole Oceanographic Institution
September 3, 2015

Signature redacted

Certified by .....
Oliver Jagoutz
Associate Professor of Geology
MIT

Signature redacted

Accepted by: .....
Timothy L. Grove
Professor of Geology, MIT
Chair, Joint Committee for Marine Geology and Geophysics

Chemical, Isotopic, and Temporal Variations during Crustal Differentiation: Insights from the Dariv Igneous Complex, Western Mongolia

by Claire Elizabeth Bucholz

Submitted to the Joint Program in Oceanography/Applied Ocean Science and Engineering
Massachusetts Institute of Technology and
Woods Hole Oceanographic Institution
on September 3, 2015,
in partial fulfillment of the requirements for the degree of
Doctor of Philosophy

Abstract

Fractional crystallization of mantle-derived basaltic melts is a critical process in producing a compositionally stratified continental crust characterized by a silicic upper crust and a mafic lower crust. This thesis explores outstanding questions associated with fractional crystallization through detailed field, petrological, and geochemical studies of the Dariv Igneous Complex in Western Mongolia. The Dariv Igneous Complex records the crystallization of a high-K primitive arc melt at shallow crustal levels, preserving both biotite-bearing ultramafic and mafic cumulates, as well as liquid-like evolved plutonics, such as (quartz-)monzonites. Chapter 2 presents comprehensive field and petrographic descriptions of the complex and establishes the petrogenetic groundwork to understand the conditions under which it formed. Results of this study indicate that the observed lithologies formed through the fractional crystallization of a high-K hydrous basalt, typical of alkali-rich basalts found in subduction zone settings, at 0.2-0.5 GPa and elevated oxygen fugacities. Chapter 3 presents a quantitatively modeled liquid line of descent (LLD) for the complex based on whole rock geochemical analyses, which is able to explain the trends observed in the monzonitic plutonic series observed in continental arcs. The oxygen isotope trajectory of fractionally crystallizing melts is rigorously constrained through modeling and mineral analyses in Chapter 4. This study indicates that large (1 to 1.8‰) increases in $\delta^{18}O$ as a melt evolves from basaltic to granitic in composition due to the fractionation of low $\delta^{18}O$ minerals. As such, the majority of $\delta^{18}O$ values of upper crustal silicic plutonics can be explained through fractional crystallization of primitive arc basalts alone without needing to invoke assimilation of high $\delta^{18}O$ crustal material. Finally, Chapter 5 explores the timescales associated with fractional crystallization through high precision U-Pb geochronology of zircon from the Dariv Igneous Complex. Evolution from a basaltic melt to a silica-rich monzonitic melt in the Dariv Igneous Complex occurred in <300 ka. If rates of fractional crystallization are primarily a function of cooling, this study provides an end-member constraint for fractional crystallization of a basaltic melt at relatively cool, shallow crustal levels. Together, these studies advance our understanding of the compositional, isotopic, and temporal variations associated with the formation of the continental crust.

Thesis Supervisor: Oliver Jagoutz
Title: Associate Professor of Geology, MIT

Acknowledgements

The past five years of my work on this thesis are founded on mentoring, support, and inspiration from numerous people. First and foremost, I would like to thank my advisor Oliver Jagoutz. Oli encouraged me to approach my scientific pursuits with an open and creative mind, letting one question lead to another equally or more stimulating and interesting one. As an advisor, he patiently explained concepts whether in the field or in the lab, challenged me to develop, broaden, and strengthen my ideas, and supported me in pursuing all opportunities that came my way. As a friend, he helped me find a balance between my work and home life, supported me in major life transitions, and pushed me to climb higher and harder. Oli, it's been a tremendous privilege to work with you and I look forward to many years of continuing friendship and collaboration.

I'd also like to thank my committee. Glenn, thanks for the being an incredible mentor and collaborator. You've given me an appreciation for recreating geologic situations in the lab and digging deeply into the fundamentals of how the world works. Mark, thanks for helping me with the math and teaching me how to translate geologic concepts into quantitative models. Tim, it was always a pleasure to stop by the 12th floor to chat about potential experiments or what you had under the probe or microscope. Thanks for always taking the time to talk. Sam, you've been supportive of me through the entire thesis, encouraging me to pursue projects in your lab and think beyond the status quo.

Beyond my committee, several people have been particularly integral to the success of this thesis. Max Schmidt supported me during a number of analytical sessions at ETH in Zürich, generously hosted me in his lovely home in Switzerland, joined me in Mongolia to help with fieldwork, and endlessly challenged ideas that I proposed. Zhengrong Wang let me spend many days upon days on the basement oxygen isotope fluorination line at Yale University and helped hone concepts pertaining to the oxygen isotope analyses in this thesis. Francis Macdonald, thanks for patiently explaining sedimentary concepts in the field for me, pushing me to think about my rocks in larger tectonic frameworks, and for all the interactions with your group at Harvard. I've learned a ton from you and look forward to future collaborations. Mike Eddy, thanks for doing all those analyses for me and having long discussions linking petrology and U-Pb geochronology. Neel Chatterjee, you helped me through many electron microprobe sessions, ensuring that I got only the highest quality data. Jill VanTongeren, thanks for sharing your endless knowledge of the Bushveld Complex and advice for navigating the academic world as a young scientist. Patricia Walsh made sure that all logistics, from fieldwork and conference travels to samples shipments ran smoothly. Oyungerel Sambuu and Uyanga Bold were instrumental in making sure that my fieldwork in Mongolia was successful and smooth.

The support from many fellow graduate students, postdocs, and undergraduates needs to be mentioned. You made life at MIT seem normal and fun! Elena Steponaitis, Ben Klein, Katie Pesce, Ben Mandler, Alexandra Andrews, Stephanie Brown, Max Collinet, Annie Bauer, Roger Fu, Ben Black, Erin Shea, Mike Krawcznyski, Christy Till, Nick Van Buer, Mauricio Ibanez-Mejia, Ben Thompson, and Adam Bockelie.

Helping to support me in and simultaneously balance my work life, my family was an amazing ballast through this time. My parents have encouraged me in my geologic pursuits since I was a little girl and declared that I wanted to be a "rock scientist". Thanks, Mom and Dad, for giving me the opportunities and reinforcement to achieve whatever I wanted. I can't think of a more incredible gift. My sisters, Emily and Hana, thanks for grounding me in reality when work got to be a bit much and being the closest of friends. Nadine and Ira Baumgarten, thanks for providing a relaxing place to stay on weekends when Devin and I were commuting across the northeast and for helping out in the last chaotic months of this PhD. Your constant love and support made this thesis possible.

Now coming to the last two. Owen, thanks for redefining my priorities in life and sitting patiently in my lap as I put this thesis together. You've brought so much happiness into this world with you, beautiful boy. Lastly, Devin. I can't imagine the world without you. You are my lodestone. Thanks for believing in me always, lifting me up during my lows, and building a vision for the future with me. Here's to the next chapter in our lives.

Table of Contents

List of Figures

List of Tables

Introduction

Earth is unique from other planets in the solar system in its bimodal topography characterized by a low-standing, thin basaltic oceanic crust and a high-standing, silicic continental crust (CC). Although the formation of the oceanic crust through decompression melting of the mantle at mid-ocean spreading centers is well understood, some aspects of the origin of the CC remain enigmatic. Based on trace element similarities between arc volcanics and the bulk continental crust, it is generally accepted that the majority of the continental crust was formed at subduction zones (e.g., Rudnick, 1995). There, hydrous mantle melting produces primitive, basaltic melts, which then rise to form the precursors of the continental crust. In order to produce an andesitic composition characteristic of the CC, these basalts must differentiate, either through fractional crystallization or through solidification followed by partial melting. These processes result in the production of low silica cumulates or residues, respectively, and high silica melts. This differentiation leads to a stratified crust, characterized by a silica-rich (granitic) upper crust and a mafic to ultramafic lower crust, which may ultimately delaminate to produce a bulk CC that is andesitic in composition. Field (Greene 2006; Jagoutz 2010) and experimental studies (Müntener et al. 2001; Grove et al. 2003; Alonso-Perez et al. 2009; Blatter et al. 2013; Nandedkar et al. 2014) have corroborated the importance of fractional crystallization in producing this stratified crust, however many questions remain concerning the compositional and isotopic variations, as well as, timescales associated with fractional crystallization in the arc crust.

For example, primitive melts generated in the mantle wedge at subduction zones display a wide variation in major element compositions and water contents, which will control the stabilities of different mineral phases as these melts crystallize in the crust. Different crystallizing mineralogies may lead to distinctly different liquid lines of descent (LLDs) or melt compositional trends during crystallization, which may explain the diversity in upper crustal silicic rocks observed. Differentiation trends for calc-alkaline, tholeiitic, and high Mg-andesites have been explored both experimentally and through field-studies, but the evolution of primitive alkali-rich basalts has received little attention. Further, although major and trace element trends of crystallizing melts have been studied in detail, the effect of fractional crystallization on the stable isotope trajectories has not been thoroughly investigated. Elevated oxygen isotope values are often used to identify degrees of assimilation of supra-crustal material, however oxygen isotope values of melts may also increase during fractional crystallization of low $^{18}O/^{16}O$ minerals. Quantifying the effects of fractional crystallization versus assimilation on the oxygen isotope composition of melts in the crust is critical to understand the degree of juvenile input versus crustal recycling occurring during CC formation. In addition, the timescales over which fractional crystallization occurs remain poorly constrained, but are essential in order to understand the rates at which magmas evolve, the factors controlling these rates, and the thermal budget associated with crustal differentiation.

In order to investigate these outstanding questions, this thesis focuses on the Dariv Igneous Complex in Western Mongolia where a unique exposure of plutonic rocks ranging from ultramafic cumulates through to evolved granitoids records the fractional crystallization of an arc-related primitive high-K melt. The Dariv Igneous Complex lies at the heart of the Central Asian Orogenic Belt, a massive subduction accretion complex, which is responsible for a large proportion of crustal growth in that last 1.0 Ga (Sengör et al. 1993). Four field seasons, two of which I participated on, were spent documenting this igneous complex in detail to constrain field relationships, map, and sample key lithologies. Following fieldwork, petrographic investigation, whole rock and mineral major and trace element geochemistry, oxygen isotopic analyses, and U-Pb zircon geochronology were all undertaken to explore questions surrounding fractional crystallization of primitive basaltic melts.

I first lay the groundwork for understanding the Dariv Igneous Complex with detailed field and petrographic descriptions, as well as mineral chemistry (**Chapter 2**). The lithological variation observed in the complex can be ascribed to a fractionation sequence dominated by clinopyroxene and biotite with characteristic lithologies, such as phlogopite wehrlites, clinopyroxenites, and monzogabbros. Major and trace element mineral chemistry allows for the characterization of the pressure, temperature, oxygen fugacity, and p_{H2O} conditions during crystallization. Our findings indicate that the complex was formed during the fractional crystallization of a high-K primitive basaltic melt at shallow (<0.5 GPa) pressures and elevated oxygen fugacities. Calculated parental melt trace element compositions are suggestive of an alkaline primitive melt originating from a subduction-imprinted mantle. Comparison to a global compilation of primitive arc melts demonstrates that Dariv primitive melts are similar in composition to high-K primitive melts found in some continental arcs. Thus, the high-K fractionation sequence exposed in the Dariv Igneous Complex may be a previously unrecognized important fractionation sequence resulting in alkali-rich upper crustal granitoids in continental arc settings.

Perhaps the best constrained arc-related crystallization sequence and associated LLD is the calc-alkaline trend (Miyashiro 1974), which is defined by high-pressure crystallization dominated by olivine, clinopyroxene, amphibole, oxides, and Ca-rich plagioclase from water-rich melts. Primitive calc-alkaline melts are characterized by moderate K_2O contents (<1.5 wt.%), yet K_2O of some primitive arc melts, however, may be much higher (up to 4-5 wt.%), begging the question whether high-K melts follow a distinct crystallization sequence and LLD. In order to constrain the geochemical evolution of a crystallizing high-K primitive melt, I present whole rock geochemistry from the Dariv Igneous Complex and develop a quantitative fractionation model (**Chapter 3**). The modeled LLD reproduces the geochemical trends observed in the 'liquid'-like plutonics from the Dariv Igneous Complex, which follow the monzonitic series (monzodiorites, monzonites, and quartz monzonites) characterized by elevated total alkali contents at a given SiO_2 content. Although volumetrically less significant than calc-alkaline batholiths, the monzonitic series are widely present in arcs. This chapter documents their formation through fractional crystallization of high-K primitive arc basalts. Comparison of the modeled LLD and

whole rock geochemistry of the Dariv Igneous Complex to the more common calc-alkaline trend indicates that biotite and K-feldspar fractionation in the high-K arc series results in the moderation of K_2O/Na_2O values and LILE concentrations with increasing SiO_2 as compared to the more common calc-alkaline series characterized by amphibole and plagioclase crystallization and strong increases in K_2O/Na_2O values. In addition, I explore the effect of melt major element composition and water content on the stability of the hydrous phases biotite and amphibole in crystallizing arc melts in this chapter.

Although fractional crystallization is an important process to produce a silicic continental crust, assimilation of previously existing crustal material can also result in increases in melt SiO_2. Elevated oxygen isotope values in igneous rocks are often used to identify assimilation of material that once resided near the surface of the earth (Taylor and Sheppard 1986; Harmon and Hoefs 1995). Crystallization of low $\delta^{18}O$ phases, such as olivine, oxides, pyroxenes, amphibole, and biotite, typical of hydrous arc crystallization sequences, however, should also result in an increase in $\delta^{18}O$ of a crystallizing melt. In **Chapter 4** I constrain the changes in melt $\delta^{18}O$ due to closed-system fractional crystallization. First, I develop a mass balance modeling method that incorporates variable temperatures of crystallization, melt compositions, and crystallizing mineralogy. Second, for comparison with our model, I measured $\delta^{18}O$ values of mineral separates from two end member crystallization sequences: the high-K, hydrous sequence from the Dariv Igneous Complex, as well as, a relatively dry, tholeiitic sequence from the Upper and Upper Main Zones (UUMZ) of the Bushveld Complex (South Africa). Results from this study indicate that increases in melt $\delta^{18}O$ of 1.0 to 1.8‰ can be attributed to closed-system crystallization alone from ~50 to 70 wt.% SiO_2 for modeled LLDs. Hydrous, alkaline or calc-alkaline melts undergo larger increases in $\delta^{18}O$ during early stages of crystallization due to their lower magmatic temperatures, greater initial increases in SiO_2 content, and high temperature stability of low $\delta^{18}O$ phases. Conversely, relatively dry, tholeiitic melts only experience significant enrichment in $\delta^{18}O$ at melt fractions less than ~0.2. As primitive basalts produced at subduction zones have values from ~5.7-8.0‰, whole rock $\delta^{18}O$ values of ~7-9.8‰ in granites can be explained through fractional crystallization of mantle-derived melts alone without invoking intracrustal assimilation of high $\delta^{18}O$ material. This range of values is sufficient to explain the majority of upper crustal silicic plutonic rocks, with only S-type granites, which form through partial melting of pelitic sediments, exceeding 10‰.

Lastly, I address the timescales associated with fractional crystallization (**Chapter 5**). In general, this is a difficult problem as locations with clear evidence for fractional crystallization, as well as, the accessory phases required for radiometric dating are rare. The Dariv Igneous Complex presents an excellent opportunity to tackle this question due to the early saturation of zircon in the parental melt to the complex. Indistinguishable crystallization ages from Th-corrected $^{206}Pb/^{238}U$ dates of zircons from 5 samples across the sequence indicate that fractionation from a basalt to high silica (>65 wt.% SiO_2) melt occurred in ≤300 ka between 502-503 Ma. If crystallization rates in crustal intrusions are primarily a function of cooling, rates of fractionation will be strongly dependent on the size and depth of the

magmatic system, as well as, the dynamics of magma chamber replenishment. Therefore, the Dariv Igneous Complex, which crystallized at relatively shallow, cool levels in the crust, represents an end-member constraint for timescales associated with fractional crystallization of a basaltic melt. Fractional crystallization of mantle-derived basalts in the lower crust may occur on more protracted timescales due to greater ambient temperatures at depth and repeated influx of hot basalts.

In summary, although fractional crystallization of primitive basaltic melts is an important process in the generation of the silicic, high standing continental crust, numerous outstanding questions remain regarding this process. The Dariv Igneous Complex, which is the focus of this thesis, allows for the investigation of the fractional crystallization of an end-member primitive, high-K basaltic melt to constrain the compositional and oxygen isotopic variation in arc LLDs, as well as, the timescales associated with fractional crystallization. **Chapter 2** lays the field, petrographic, and petrogenetic groundwork to understand the origin of the complex. **Chapter 3** constrains the LLD associated with the crystallization of high-K primitive basaltic melts. **Chapter 4** presents both natural data and modeling results to explore the oxygen isotopic trajectories of fractionally crystallizing basaltic melts. **Chapter 5** describes the results of high precision U-Pb geochronology to constrain the timescales associated with fractional crystallization. Together, these chapters advance our understanding of a process fundamental to the production of the continental crust from a multi-perspective view.

The chapters in this dissertation are intended to be four separate manuscripts, which are published (**Chapter 2** & **3**) under review (**Chapter 4**), and in preparation (**Chapter 5**). The corresponding publication references are listed below in the order of the chapters presented here.

Bucholz, C. E., Jagoutz, O, Schmidt, M. W., & Sambuu, O. 2014a. Phlogopite- and Clinopyroxene-dominated Fractional Crystallization of an Alkaline Primitive Melt: Petrology and Mineral Chemistry of the Dariv Igneous Complex, Western Mongolia. *Contributions to Mineralogy & Petrology* 167:994.

Bucholz, C. E., Jagoutz, O, Schmidt, M. W., & Sambuu, O. 2014b. Fractional Crystallization of High-K Arc Magmas: Biotite- vs. Amphibole-dominated Fractionation Series in the Dariv Igneous Complex, Western Mongolia. *Contributions to Mineralogy & Petrology* 168:1072.

Bucholz, C. E., Jagoutz, O., Vantongeren, J. A., and Wang, Z. (submitted to *Geochimica et Cosmochimica Acta*). The Oxygen Isotope Trajectory of Crystallizing Melts.

Bucholz, C. E., Eddy, M. P., Jagoutz, O, and Bowring, S. A. (in preparation for *Geology*). Constraining the Timescales of Magmatic Differentiation with U-Pb Zircon Geochronology.

References

Alonso-Perez R, Muntener O, Ulmer P (2009) Igneous garnet and amphibole fractionation in the roots of island arcs: experimental constraints on andesitic liquids. Contributions to Mineralogy and Petrology. doi: 10.1007/s00410-008-0351-8

Blatter DL, Sisson TW, Hankins WB (2013) Crystallization of oxidized, moderately hydrous arc basalt at

mid- to lower-crustal pressures: implications for andesite genesis. Contrib Mineral Petrol 166:861–886. doi: 10.1007/s00410-013-0920-3

Greene AR (2006) A Detailed Geochemical Study of Island Arc Crust: the Talkeetna Arc Section, South-Central Alaska. Journal of Petrology 47:1051–1093. doi: 10.1093/petrology/egl002

Grove TL, Elkins-Tanton LT, Parman SW, et al (2003) Fractional crystallization and mantle-melting controls on calc-alkaline differentiation trends. Contrib Mineral Petrol 145:515–533. doi: 10.1007/s00410-003-0448-z

Harmon RS, Hoefs J (1995) Oxygen isotope heterogeneity of the mantle deduced from global 18O systematics of basalts from different geotectonic settings. Contrib Mineral Petrol

Jagoutz OE (2010) Construction of the granitoid crust of an island arc. Part II: a quantitative petrogenetic model. Contrib Mineral Petrol 160:359–381. doi: 10.1007/s00410-009-0482-6

Miyashiro A (1974) Volcanic rock series in island arcs and active continental margins. American Journal of Science 274:321–355. doi: 10.2475/ajs.274.4.321

Müntener O, Kelemen PB, Grove TL (2001) The role of H2O during crystallization of primitive arc magmas under uppermost mantle conditions and genesis of igneous pyroxenites: an experimental study. Contrib Mineral Petrol 141:643–658. doi: 10.1007/s004100100266

Nandedkar RH, Ulmer P, Müntener O (2014) Fractional crystallization of primitive, hydrous arc magmas: an experimental study at 0.7 GPa. Contrib Mineral Petrol 167:1015. doi: 10.1007/s00410-014-1015-5

Rudnick, R.L., 1995. Making continental crust. Nature 378, 571–578.

Sengör A, Natal'In BA, Burtman VS (1993) Evolution of the Altaid tectonic collage and Palaeozoic crustal growth in Eurasia. Nature 364:299–307. doi: 10.1038/364299a0

Taylor HP, Sheppard SMF (1986) Igneous rocks; I, Processes of isotopic fractionation and isotope systematics. Reviews in Mineralogy and Geochemistry 16:227–271.

Villiger S, Ulmer P, Müntener O, Thompson AB (2004) The Liquid Line of Descent of Anhydrous, Mantle-Derived, Tholeiitic Liquids by Fractional and Equilibrium Crystallization - an Experimental Study at 1.0 GPa. Journal of Petrology 45:2369–2388. doi: 10.1093/petrology/egh042

CHAPTER 2:
Field Relationships, Petrology, and Mineral Chemistry of the Dariv Igneous Complex, Western Mongolia

Abstract

We present field relationships, petrography, and mineral major and trace element data for the Neoproterozoic Dariv Igneous Complex of the Altaids of Western Mongolia. This unique complex of high-K plutonic rocks is composed of well-exposed, km-scale igneous intrusions of wehrlites, phlogopite wehrlites, apatite-bearing phlogopite clinopyroxenites, monzogabbros, monzodiorites, and clinopyroxene-bearing monzonites, all of which are intruded by late stage lamprophyric and aplitic dikes. The biotite-dominated igneous complex intrudes depleted harzburgitic serpentinite. The observed lithological variability and petrographic observations suggest that the plutonic rocks can be ascribed to a fractionation sequence defined by olivine + clinopyroxene ± Fe-Ti oxides → biotite + apatite → K-feldspar + plagioclase → amphibole + quartz. Notably, biotite is the dominant hydrous mafic mineral. Petrogenesis of the observed lithologies through a common fractionation sequence is supported by a gradual decrease in the Mg# (molar $Mg/(Fe_{total} + Mg) \times 100$) of mafic minerals. Crystallization conditions are derived from experimental phase petrology and mineral chemistry. The most primitive ultramafic cumulates crystallized at ≤ 0.5 GPa and 1210-1100°C and oxygen fugacity (f_{O_2}) of +2-3 ΔFMQ (log-units above the fayalite-quartz-magnetite buffer). Trace element modeling using clinopyroxene and apatite REE compositions indicates that the dominant mechanism of differentiation was fractional crystallization. The trace element composition of a parental melt was calculated from primitive clinopyroxene compositions and compares favorably with the compositions of syn-magmatic lamprophyres that cross-cut the fractionation sequence. The parental melt composition is highly enriched in Th, U, large ion lithophile elements (LILE), and light rare earth elements (LREE) and has a pronounced negative Nb-Ta depletion, suggestive of an alkaline primitive melt originating from a subduction-imprinted mantle. Comparison to a global compilation of primitive arc melts demonstrates that Dariv primitive melts are similar in composition to high-K primitive melts found in some continental arcs. Thus, the high-K fractionation sequence exposed in the Dariv Igneous Complex may be a previously unrecognized important fractionation sequence resulting in alkali-rich upper crustal granitoids in continental arc settings.

2.1 Introduction

Trace element similarities between subduction zone igneous rocks, bulk arc, and bulk crust estimates (e.g., enrichment in light REE, depletion in Nb and Ti, and enrichment of Pb) suggest that subduction-related magmatism is the main contributor to the present-day continental crust (CC) (e.g., Jagoutz and Schmidt 2012; Rudnick and Fountain 1995). Studying the generation and subsequent modification of arc primitive melts is therefore essential to understand the formation of the continental crust. After extraction from the mantle, primitive arc-related melts can either erupt at the surface or, more commonly, crystallize at depth, giving rise to ultramafic and mafic cumulates and residual melts. The phases that crystallize from the melts and their order of appearance depends on external parameters such as P, T, and f_{O_2}, but also strongly on the composition of the primitive melt. Primitive arc magmas fall into three broad compositional categories: 1) high-Mg andesites, 2) tholeiitic/calc-alkaline basalts, and 3) basalts with alkaline affinity (Tatsumi et al. 2008). Crystallization of tholeiitic/calc-alkaline magmas and high-Mg andesites at arc crustal conditions have been studied experimentally (e.g., Alonso-Perez et al. 2009; Grove et al. 2003; Sisson and Grove 1993) and in the field (e.g., Greene et al. 2006; Jagoutz et al. 2011; Jagoutz 2010), yet the fractionation of primitive alkali-rich basalts remains poorly defined. In part, the reason for the paucity of studies on alkaline basalt differentiation in arcs is the lack of field exposure and the limited, fragmentary evidence from cumulate xenoliths. Currently, the primary evidence of alkali-basalt fractionation arises from phlogopite-bearing ultramafic xenoliths in alkali-basalts and lamprophyres, which indicate that the fractionation sequence involves the crystallization of olivine + clinopyroxene + phlogopite ± apatite (Buhlmann et al. 2000; Dawson and Smith 1992; Downes et al. 2004; Giannetti 1982; Giannetti and Luhr 1990; Righter and Rosas-Elguera 2001). Experimental phase-equilibria of hydrous alkali-rich magmas corroborate the limited evidence from high-K ultramafic xenoliths (Barton and Hamilton 1978; Barton and Hamilton 1979; Edgar et al. 1980; Elkins-Tanton and Grove 2003; Esperança and Holloway 1987; Melzer and Foley 2000; Righter and Carmichael 1996), yet, until now, an exposed, continuous plutonic sequence documenting such a fractionation sequence has not been described.

Here we present results from a newly discovered alkaline fractionation sequence in the Dariv Range of Western Mongolia. The Dariv Igneous Complex consists of a ~10 km thick sequence of high-K lithologies ranging from phlogopite-bearing ultramafic cumulates situated in a harzburgitic mantle to feldspar-bearing monzogabbros, monzodiorites, and quartz-monzonites. As such, this series represents an unparalleled opportunity to constrain the crystallization conditions of a primitive, high-K, arc-related basalt. We describe field observations, petrology, and mineral chemistry (major and trace element) of this unique plutonic sequence with the aim of constraining the pressure, temperature, H_2O content, and f_{O_2} during the crystallization of the alkali-rich parental melt. We present a detailed map of the northern plutonic sequence of the Dariv range, which is based on a total of 10 weeks of field work distributed over four field seasons (for a map documenting the areas visited see Appendix A) and then was completed based on satellite images. Field mapping and satellite images analysis has been done iteratively such that

any uncertainties on the satellite images have been verified in the field. We also calculate the trace element composition of a primitive, parental melt composition to the high-K igneous complex that compares favorably with late stage syn-magmatic mafic dikes that cross-cut the alkaline complex. We then compare the primitive melt composition to a global compilation of primitive arc melts and model the incompatible element composition of the primitive melt in terms of a partial melt of the mantle and a component derived from a subducted slab.

2.2 Geological Setting and Previous Work

The Dariv Range is located in southwestern Mongolia and is part of the Mongolian Altaids (Fig. 2-1a). The Mongolian Altaids are part of the Central Asian Orogenic Belt (CAOB), a massive subduction complex that extends from the Urals to the Pacific Ocean and from the Siberian and Baltic cratons to the North China and Tarim cratons. The CAOB is comprised of island arcs, ophiolites, accretionary wedges, and continental fragments that were accreted to the margin of Siberia beginning at *c.* 1.0 Ga and continuing until *c.* 250 Ma, when the Paleo-Asian ocean closed along the Solonker suture (Buslov et al. 2001; Khain et al. 2003; Sengör et al. 1993; Sengör et al. 1994). The CAOB contributed ~5.3 million km^2 of land area to Asia, strongly augmenting the temporal crustal growth curve during the Neoproterozoic and Paleozoic (Sengör et al. 1993). The Dariv Range exposes the contact between what we refer to as the Altai Allochthon, which is locally composed of high-grade Proterozoic metamorphic rocks (amphibolite- to granulite-facies meta-igneous and metasedimentary lithologies), and the Lake Terrane (an Ediacaran-Early Paleozoic island arc system) (Fig. 2-1b) (Badarch et al. 2002). The Lake Terrane is part of an extensive island-arc terrane composed of ophiolites and arc-related plutonic and volcanic rocks, which preserves fragments of the Palaeoasian ocean floor and associated island arc systems (Khain et al. 2003). In Dariv, the Lake Terrane is composed of six primary units: (1) a mantle section (serpentinized harzburgite and dunite), which is intruded by (2) an alkaline series ranging from phlogopite-rich mafic and ultramafic cumulates to alkaline granitoids, that together are the focus of this study. In addition, (3) an ophiolite sequence (gabbro, dike complex, and lavas) intrudes and lies structurally above the mantle section to the northwest (Figs. 2-1c, 2-2). The northern and western parts of the range are comprised of the (4) Lake Zone volcanics and volcaniclastics, poorly studied weakly metamorphosed igneous and sedimentary rocks (agglomerates, conglomerates, volcanics, and volcaniclastic rocks). Lastly, (5) a series of hornblendites, hornblende-gabbros and –diorites and (6) large red (alkali-)granites that intrude (1), (2), and (5) are also present. The few previous studies of the area have not recognized the hydrous cumulate sequences, but have rather considered them part of the larger Dariv Ophiolite (also referred to as 'Bayannur' or 'Bayannor') ophiolite (Dijkstra et al. 2006; Khain et al. 2003; Kozakov et al. 2002).

The relatively complete igneous section of the ophiolite sequence (following the Penrose prototype) (Conference Participants 1972) suggests an origin at an oceanic spreading ridge. In addition, its location within the Lake Terrane implies that it formed in an oceanic environment. Dijkstra et al., (2006), however, identified geochemical characteristics that include Nb-Ta depletions and enrichment in

LILE and suggested that this ophiolite formed in an arc environment and not a mid-ocean spreading center (Dijkstra et al. 2006). Calculated melt compositions in equilibrium with clinopyroxene from the ophiolitic gabbronorites have trace element signatures similar to that of boninites and island-arc tholeiites (Dijkstra et al. 2006). The ophiolite has thus been postulated to have formed in a fore-arc environment (Dijkstra et al. 2006; Khain et al. 2003). The polarity of subduction and the overall structure of the Dariv Range, however, are debated and not well constrained. Dijkstra et al. (2006) interpret the area as a stack of steeply south-dipping thrust sheets, with the ophiolite being tectonically overlain by meta-sedimentary and meta-igneous rocks, and argue for a south-dipping subduction zone. In contrast, Khain et al. (2003) conclude that the ophiolite was thrust over the Dariv metamorphic complex in a subduction zone dipping to the north (Khain et al. 2003). This latter model is in agreement with the classical model of Sengör et al. (1993; 1994) of a long-lived north-facing subduction zone. The polarity of subduction, however, is still an open question that requires a more rigorous investigation of field relationships, structural data, and geochronology.

2.3 Field Relationships

Several prominent west-northwest to east-southeast and northwest-southeast fault zones post date and cross cut the igneous and metamorphic sequences (Figs. 2-1c, 2-2). Our field mapping indicates that the units of the metamorphic sequence dip steeply (~80°) to the south, but they are juxtaposed with the northern igneous sequence along high angle dextral faults rather than thrust faults. Their original thrusting relationship to the metamorphic sequence in the north, if any, is thus obscured. The field relationships of the ophiolite, the alkaline fractionation sequence, and the mantle section are described in greater detail below. Except for the ophiolite sequence, these lithologies are very fresh and do not display evidence of pervasive hydrous alteration as would be expected if the intrusion experienced the same regional fluid flux that lead to the complete serpentinization of the harzburgitic mantle. Consequently, it appears that the granitoids and the cumulates post-date and are not responsible for the serpentinization.

2.3.1 Alkaline Fractionation Sequence

A ~3.5 km thick biotite-bearing, ultramafic cumulate sequence is found within the harzburgite/dunite. The contact between the serpentinite and the cumulate sequence is marked by numerous fingers filled with cumulate minerals that cut into the serpentinite (Fig. 2-c, 2-4a). A broadly systematic lithological variation is observed from northwest to southeast in present-day reference frame (Fig. 2-2c). In the northwest primitive wehrlites characterized by bright green Cr-diopside, olivine, and minor phlogopite grade into clinopyroxenites, phlogopitites, and phlogopite monzogabbros towards the southeast. A detailed profile across part of the cumulate sequence was studied and sampled to document the mineralogical and geochemical changes associated with the systematic lithological variation that could represent progressive fractionation (Fig. 2-4). Lithological layering in the cumulate sequence in this detailed profile dips shallowly to the east-northeast. Late stage 10-100 cm wide K-feldspar-rich aplite

dikes and mafic lamprophyre dikes with biotite phenocrysts cross cut the cumulate sequence (Figs. 2-3b,d & 2-4). Diffuse margins between the aplite dikes and the monzonites indicate a comagmatic origin (Fig. 2-3b), whereas the margins of mafic dikes are more sharply defined. Xenoliths of biotite cumulates and enclaves of mafic dikes are common in the monzonites (Fig. 2-3c,d). Volumetrically minor intrusions and veins of amphibole+clinopyroxene±biotite±feldspar bearing cumulates are also observed within the biotite-dominated cumulate sequence. In addition, the serpentinite is intruded by small (10-100 m in diameter) vertically oriented stocks of evolved granitoids and two large ~8 by 5 km wide intrusions of red (alkali-)granite (Fig. 2-2). The stocks are dominated by red (alkali-)granites and quartz monzonites, although other minor lithologies such as hornblende-bearing gabbros are also present. When observable, granitoid contacts with the serpentinite are defined by a fine-grained margin 10-20 cm thick.

2.3.2 Ophiolite and Mantle Sequence

The ophiolite and mantle sequence combined are comprised from top to bottom of a dike complex, gabbro, and serpentinized harzburgite and dunite, all overprinted by the same greenschist hydration/serpentinization event. The dikes are 1-2 m thick, fine-grained, and range in composition from basaltic andesites to rhyolites, with more felsic compositions becoming more common to the northwest. Plagioclase and augite phenocrysts are present in the basaltic andesite dikes, whereas porphyritic plagioclase and hornblende are occasionally present in the more evolved dikes. The dikes have variable orientations, striking southwest to northwest and dipping between 45 and 80°. The contact of the dike complex and the gabbro is transitional, with single dikes occasionally intruding the gabbro. The exposed gabbro sequence is 2-3 km thick and has limited modal mineral variations, consisting dominantly of 55% clinopyroxene + 45% plagioclase with a variable grain size of 0.1 to 1 cm. The gabbro intrudes the harzburgite and dunite along a steep (~210°/65°) igneous contact (Fig. 2-2b). The harzburgite and dunite are highly serpentinized, but the serpentinization was static as original textures are preserved. In thin section the harzburgites display a mesh texture of serpentine + brucite enclosing bastite pseudomorphs after orthopyroxene. The dunite generally occurs in decimeter- to meter-scale discordant veins in sharp contact with the harzburgite. The veins are vertically oriented and strike north-northwest. Chromium spinel is present in both the dunite and harzburgite.

2.4 Petrography

As the focus of this study, the rocks comprising the biotite-rich alkaline fractionation sequence and associated (alkali-)granites are described in detail below. The rocks are generally very fresh, but occasionally clinopyroxene exhibits alteration to actinolitic amphibole. This is more pronounced in the monzodiorites and (qtz-)monzonites. None of the samples exhibit field or microstructural evidence of deformation. The modal mineralogy of representative samples is given in Table 1. Mineral percentages given in the following text are volume percentages.

2.4.1 Wehrlites and Phlogopite Wehrlites

The wehrlites are fine- to medium-grained (0.5-2 mm). The most primitive (i.e., highest mineral and whole rock Mg#) phlogopite wehrlites consist of bright green clinopyroxene (~65%) and olivine (~25-30%) with intercumulus phlogopite (~2-10%) and occasional accessory titano-magnetite. Olivine occurs as subhedral to anhedral crystals that are poikilitically enclosed within phlogopite. In some samples, olivine shows highly irregular margins and is surrounded by phlogopite (Fig. 2-5a). Titanomagnetite (50-100 μm) grows along grain boundaries and within the rims of clinopyroxene. The modal percentage of biotite is variable in the wehrlites and gradually increases (to ~45%), while that of olivine and pyroxene decrease (to <10% and to ~45% respectively), resulting in a pronounced orthocumulate texture of olivine and clinopyroxene poiklitically enclosed within phlogopite (Fig. 2-5b). In one sample (MO-11-9) orthopyroxene occurs as sub- to euhedral crystals 0.5-1 mm in diameter as an orthocumulate phase with clinopyroxene or sometimes poikilitically enclosed by biotite.

2.4.2 Phlogopite clinopyroxenites and phlogopitites

The phlogopite wehrlites grade into phlogopite clinopyroxenites that are comprised of clinopyroxene (70-80%), phlogopite (20-30%), and apatite with accessory hemo-ilmenite, titanite, and zircon. In the phlogopite clinopyroxenites, brown-reddish phlogopite grows interstitially to the clinopyroxene and occasionally completely encloses clinopyroxene (Fig. 2-5c,d). Titanite crystallizes in the rims of the phlogopites. In the one sampled phlogopitite (MO-11-10), phlogopite is the dominant phase (75%) and apatite becomes an important constituent (~4-5%). Phlogopite occurs both as an intercumulus phase and as elongate light brown euhedral laths up to 1-2 mm in length with subhedral clinopyroxene and stout prismatic apatites. Apatites are poikilitically enclosed by both euhedral and intercumulus biotite (Fig. 2-5d).

2.4.3 Monzogabbros

Monzogabbros consist of alkali-feldspar and plagioclase (together 28-50%), phlogopite (13-25%), and clinopyroxene (31-55%) with accessory subhedral titanite, apatite, zircon, and hemo-ilmenite (Fig. 2-5e). Phlogopite grows both interstitially and in large laths (1-2 cm in length), occasionally poikilitically encloses titanite and apatite. Oligoclase to andesine (An ~20-40) and alkali-feldspar occur together in patchy intergrowths. Apatite occurs as stubby, subhedral 1-2 mm long crystals. Typically secondary green actinolite partially replaces ~20% of both clinopyroxene and biotite.

2.4.4 Clinopyroxene-Bearing Monzodiorites and Quartz-Monzonites

The monzodiorites and quartz-monzonites are composed of large alkali-feldspar megacrysts with albite, quartz, biotite, amphibole, and clinopyroxene as major constituents and with accessory apatite, titanite, zircon, and hemo-ilmenite (Fig. 2-5f,g). In the quartz-monzonites, alkali-feldspars are large (1-2 cm in length) euhedral laths around which the other minerals grow. Quartz displays interlobate grain boundaries. Biotite occurs as stubby laths, 1-4 mm in length. Secondary green actinolite extensively

replaces clinopyroxene. Clinopyroxene contains both biotite and numerous apatite inclusions (5-100 μm diameter). Apatite is often also enclosed in biotite.

2.4.5 Lamprophyres

The late stage lamprophyre dikes that cross-cut the alkaline fractionation sequence are comprised of biotite, plagioclase, and clinopyroxene with accessory apatite, zircon, and hematite. Biotite (30%) occurs in 100-200 μm long blocky laths often enclosing zircon and hematite. Subhedral, rounded 20-100 μm clinopyroxene crystals (25%) are surrounded by plagioclase (45%). Plagioclase crystals display irregular margins and appear to have crystallized after biotite. Zircon is an abundant accessory phase occurring as 20-150 μm long prismatic crystals within both plagioclase and biotite.

2.4.6 (Alkali-)Granites

The red (alkali-)granites consist of coarse-grained (>2 cm), strongly porphyritic K-feldspar phenocrysts (50%) surrounded by smaller crystals of quartz (30%), alkali-feldspar, plagioclase (15%), and biotite and amphibole (5%) with accessory zircon and titanite (Fig. 2-5h). The K-feldspar phenocrysts occasionally exhibit Carlsbad twinning with perthitic exsolution. Smaller K-feldspar grains often have tartan twinning. Quartz displays undulose extinction and has lobate grain boundaries.

2.5 Analytical Methods

The major element chemistry of minerals from 21 samples across the biotite-dominated fractionation sequence were determined by electron microprobe analysis (EMPA) using a JEOL JXA-8200 Superprobe at both the Massachusetts Institute of Technology and at ETH Zurich. An acceleration voltage of 15 kV, a beam current of 20 nA, and a beam diameter of 1-10 μm were used. Measuring times were 40 s for all elements. Background counting time was half of the peak counting time. The CITZAF correction procedure of Armstrong (1995), including the atomic number correction, the absorption coefficients, and fluorescence correction therein, were used to reduce the data and obtain quantitative analyses. Detection limits are typically in the range of 0.02 to 0.05 wt %. Exceptions to this are detection limits for FeO and MnO of ~0.06 wt % and for F 0.09 wt %. Trace element chemistry of the minerals was determined using LA-ICP-MS at ETH Zurich. Samples were loaded along with the NIST610 glass standard in an ablation cell and the ablated material was transported to the ICP-MS by a He carrier gas. The ablation system consists of a 193 nm ArF Excimer laser (Lambda Physik) with a homogenized beam profile connected to an Elan6100 DRC quadrupole ICP-MS. The background was measured for ~40s prior to each analysis and the laser signal was integrated over 40-50 s. A 40 μm spot size was used and rims and cores of minerals were analyzed when possible. The analytical set-up was tuned for optimum performance across the entire mass range and daily optimization of the analytical conditions were performed to ensure a ThO production rate of below 0.2% (i.e. Th/ThO intensity ratio <0.002) and a Th/U sensitivity ratio of 1 measured on the NIST610 glass standard. Two analyses on the NIST610 standard at the beginning and at the end of each set bracketed up to 20 analyses of unknowns. The NIST610 standard

was used as an external standard to calibrate analyte sensitivities and to correct for a linear drift during a set of analyses. Data reduction of LA-ICP-MS analyses followed the procedures described in Longerich et al., (1996). CaO was used for clinopyroxene, Al_2O_3 for phlogopite, and MgO for olivine as the internal standard element to correct for matrix effects and calculate trace element concentrations.

Four whole rock major and trace element compositions of mafic dikes are included in the presented data set. Fresh pieces with no indication of weathering or veining were cut from samples to ensure uncontaminated and representative chemical analyses. Samples were powdered in an agate mill, which was cleaned with silica sand in between samples. The powders were then oven-dried overnight at 105°C. Loss on ignition was determined from mass loss after heating in a 1050°C oven. Glass discs were prepared using lithium tetraborate as a flux during the fusion process. Major elements were measured using a wave-length dispersive X-ray fluorescence (XRF) spectrometer at ETH. Trace elements of the fusion discs were determined by laser ablation inductively coupled plasma mass spectrometer (LA-ICPMS) at ETH described above. In addition, a lithium tetraborate blank was measured at the beginning of each session and its spectrum subtracted from the unknown spectra. The XRF glass discs were broken and analyses were performed directly on freshly broken surfaces. Analytical procedures and data reduction are the same as described above for the mineral trace element analyses, except that a 90 μm beam size was used. A minimum of 3 shots per disc in unique locations were done to examine homogeneity of the analyzed pellet. CaO was used as the internal standard element to correct for matrix effects and calculate trace element concentrations. CaO was used as the internal standard element to correct for matrix effects and calculate trace element concentrations.

2.6 Mineral Chemistry

The average mineral major and trace element chemistry for individual samples of the biotite-dominated cumulate sequence are provided in Appendix B. The chemical characteristics of the primary fractionating minerals are described below.

2.6.1 Olivine

None of the serpentinite samples investigated preserved olivine such that all olivine can be ascribed to the magmatic suites. Olivine occurs as an early cumulate phase in the most primitive wehrlites and phlogopite wehrlites. Wehrlite olivines have an Mg# of 87-85 whereas the most primitive phlogopite wehrlite has olivines Mg# = 82-80. Compositional gaps observed in the Mg# are likely an artifact of sampling. The transition from phlogopite wehrlites to olivine-free phlogopite clinopyroxenites is associated with a constant decrease in the modal percentage and Mg# of olivine (down to Mg# = 65). Although variable, the NiO content of olivine generally decreases from 0.15-0.21 wt.% in the wehrlites to 0.07 to 0.15 wt.% in the phlogopite wehrlites (Fig. 2-6a). MnO contents of olivine increase with decreasing Mg# from 0.18-0.2 in the wehrlites to 0.40 to 0.55 in the most evolved phlogopite wehrlites (Fig. 2-6b). Both the NiO and MnO contents for a given Mg# of olivine are lower than typical average mantle olivine values (Sato 1977), indicating that the olivine is magmatic in origin and that the primitive

melts may have already precipitated olivine-dominated cumulates (dunites). CaO contents are generally close to the detection limit of the electron microprobe.

2.6.2 Clinopyroxene

Orthopyroxene is absent from the fractionation sequence except in one sample (MO-11-9). The ortho- and clinopyroxene in this sample, however, are severely out of Fe-Mg equilibrium with a $K_D \approx 0.6$ (as compared to the empirically determined equilibrium value of 1.09 ± 0.14) (Putirka 2008). The Fe-Mg equilibrium suggests instead that the orthopyroxene was originally olivine, which later through peritectic reaction with melt formed enstatite. Therefore, clinopyroxene appears to be the only fractionating pyroxene and remains a fractionating phase into the most evolved quartz-monzonites. Clinopyroxene's persistence as a crystallizing phase allows for its geochemical characterization across the entire fractionation sequence. The most magnesian clinopyroxenes in wehrlites have Mg#'s of 89-91. The Mg# of clinopyroxenes in phlogopite-bearing ultramafic cumulates vary between 80-88. Monzogabbro, monzodiorite, and monzonite clinopyroxene Mg# values vary between ~60-75. Cr_2O_3 contents decrease from values of 0.38-0.65 wt.% in the primitive wehrlites to <0.10 wt.% in the plagioclase-bearing lithologies. TiO_2 increases with decreasing Mg# before Fe-Ti oxides become a dominant crystallizing phase, and then dramatically declines (Fig. 2-6c). The Al_2O_3 content of clinopyroxene generally increases with decreasing Mg# in the cumulates lacking plagioclase and decreases once feldspar becomes a co-fractionating phase. This trend has been previously observed in pyroxenes from the Aleutian arc volcanic rocks (Kay and Kay 1985), from lower crustal cumulates (DeBari et al. 1987; Jagoutz et al. 2007), and in experimental studies on pyroxenites (Müntener et al. 2001). Some sub-solidus Tschermakitic exchange ($(Fe,Mg)_2Si_{-1}Al_{-1}$) during cooling of clinopyroxene in the ultramafic cumulates is indicated by a decrease in clinopyroxene Al_2O_3 contents with increasing Mg# within individual samples (Fig. 2-6d).

The trace element characteristics of clinopyroxene (Fig. 2-7a) were determined for five phlogopite wehrlites (MO-10-323, MO-10-392, MO-10-394, MO-11-8, MO-11-9), one phlogopite clinopyroxenite (MO-10-325), one phlogopitite (MO-11-10), one monzogabbro (MO-11-12), three monzodiorites (MO-11-13, MO-11-14, MO-11-21) and one monzonite (MO-11-26). In general, the overall concentration of incompatible elements (except for Sr and Eu) in clinopyroxene increases by ~10x with progressive fractionation (Fig. 2-7a). Concentrations in a single grain are generally homogeneous, but some samples show variations between core and rim concentrations with rims having slightly higher incompatible trace element concentrations. All clinopyroxenes are characterized by depletion in heavy rare earth elements (HREEs) relative to light rare earth elements (LREEs). This depletion becomes less pronounced with increasing fractionation ($(Ce/Yb)_N$ is ~5.8-9.0 in primitive phlogopite wehrlites and clinopyroxenites and ~2.9-4.3 in the monzogabbros, monzodiorites, and monzonites). Nb, Pb, Zr, and Hf are depleted in all clinopyroxenes across the entire fractionation sequence. Analyzed clinopyroxenes are also depleted in Sr except those from the most primitive analyzed wehrlite (MO-10-394). Eu is depleted with respect to neighboring REE in the monzogabbros, monzodiorites, and monzonites. This depletion

becomes more pronounced with progressive fractionation. V concentrations in the clinopyroxenes increase from ~74 ppm in the most primitive phlogopite wehrlites to >360 ppm in the more evolved phlogopite clinopyroxenites. V concentrations in clinopyroxene from the plagioclase-bearing lithologies vary between 128-233 ppm.

2.6.3 Biotite

The most primitive phlogopite wehrlites have biotites with Mg#'s of 85-88, whereas Mg#'s of biotite in the more evolved wehrlites decrease to ~70. The clinopyroxenites, phlogopitite, monzogabbros, monzodiorites, and monzonites have biotite Mg#'s of 67-73, 70-71, 57-62, 46-60, and 43-49, respectively. Biotites in the analyzed lamprophyre dike have Mg#'s of 59-65. The Al_2O_3 contents of the biotite in the ultramafic cumulates (13.8-16.3 wt.%) and lamprophyre (13.9-16.8 wt.%) are generally higher than that in the mafic and more evolved lithologies (12.6-14.4 wt.%) (Fig. 2-6e). TiO_2 contents are high and vary between 2.2-5.3 wt.% in the ultramafic cumulates and 3.4-4.6 wt.% in the feldspar-bearing lithologies. The Na_2O contents of biotite are variable within each sample, but generally decrease with decreasing Mg# from ~1.0 wt.% at Mg# ~85 to <0.1 wt.% at Mg# 45-50. Biotites in the feldspar bearing lithologies have uniformly low Na_2O (0.05-0.15 wt.%) (Fig. 2-6f). MnO increases with decreasing Mg# from 0-0.15 in the ultramafic cumulates to 0.12-0.33 in the monzogabbros through monzonites. Cl contents are below the detection limit (d.l.) in the ultramafic lithologies, but also vary between 0.07-0.12 wt.% in the feldspar-bearing lithologies. F contents are variable (<d.l. to 0.7 wt.%) and do not display any correlation with biotite Mg#.

Trace element analyses for biotite (Fig. 2-7b) were done on four phlogopite wehrlites (MO-10-323, MO-10-392, MO-10-394, MO-11-8), one phlogopite clinopyroxenite (MO-10-325), one phlogopitite (MO-11-10), one monzogabbro (MO-11-12), three monzodiorites (MO-11-13, MO-11-14, MO-11-21) and one monzonite (MO-11-26). Biotite concentrates alkali elements. In particular, Cs, Rb, and Ba concentrations are 10^2-10^3 times primitive mantle values (Fig. 2-7b). Ba is especially concentrated in the phlogopites from the more primitive cumulates (e.g., 5798 ppm in one biotite from MO-10-392). Similarly, Sr is enriched in the biotites of the ultramafic cumulates. The Sr-enrichment is not present in the monzogabbros and monzodiorites, indicating that in these lithologies, Sr fractionates into feldspars. An enrichment of Pb, Zr, Hf, and notably Nb is present in biotites of all lithologies. Nb concentrations generally increase with progressive fractionation from 4.6-9.1 ppm in the phlogopite wehrlites (though one phlogopite wehrlite (MO-10-394) has an average Nb concentration of 39.8 ppm Nb in biotite) to 32.3-78.4 ppm in the more evolved lithologies. The high concentrations on TiO_2, Nb, Zr, and Hf are all in accordance with the compatibility of high field strength element (HFSE) in biotite. V is also highly compatible in biotite with concentrations varying between ~200-800 ppm.

2.6.4 Fe-Ti Oxides

Fe-Ti oxides first appear as minor fractionating phases in the phlogopite wehrlites, occurring as 50-200 μm subequant grains in between olivine, clinopyroxene, and phlogopite. The composition is

dominated by magnetite-ülvospinel solid solution (Fig. 2-8a). Occasionally, oxides are enclosed by olivine, which exhibit minor chromitite substitution. Magnetite-ülvospinel$_{solid\text{-}solution}$ oxides persist as crystallizing phases into the phlogopite clinopyroxenites where they occur mainly enclosed by clinopyroxene. Oxides in the phlogopitite, more evolved monzogabbros and monzodiorites, and lamprophyre are predominantly members of the hematite-ilmenite solid solution, though some magnetite is also present (Fig. 2-8a).

2.6.5 Feldspars

Alkali-feldspar and plagioclase first crystallize in the biotite monzogabbro in patchy intergrowths. In the more evolved lithologies, plagioclase grows in smaller crystals around megacrysts of alkali-feldspar. Anorthite (An) contents of plagioclase are uniformly low, with plagioclases in monzogabbros and monzodiorites varying from An_{16} to An_{44} and those in monzonites to quartz monzonites between An_{13} and An_{30} (Fig. 2-8b). An contents in the rims of plagioclase are 1-2 mol.% lower than the cores. The alkali-feldspar generally has compositions of ~$Or_{0.9}Ab_{0.1}$. Only plagioclase (An_{29} to An_{44}) is present in the analyzed lamprophyre.

Trace element concentrations of both plagioclase and alkali-feldspar were determined for one monzogabbro (MO-11-12), three monzodiorites (MO-11-13, MO-11-14, MO-11-21), and one monzonite (MO-11-26). Trace element patterns of plagioclases and alkali-feldspar are generally similar, with the exception that alkali-feldspars are more enriched in LILEs and plagioclase is enriched in light to middle REEs (Fig. 2-7c). The LILEs are variably enriched in the K-feldspar with Ba generally displaying the most pronounced enrichment (380-1011 times primitive mantle). HREEs are significantly depleted (0.01-1 times primitive mantle) and Pb, Sr, and Eu are enriched with respect to LREE.

2.6.6 Apatite

Trace elements for apatite in one phlogopitite (MO-11-10), one monzogabbro (MO-11-12), three monzodiorites (MO-11-13, MO-11-14, MO-11-21), and one monzonite (MO-11-26) were analyzed. The apatites are LREE enriched (Ce_N/Yb_N = 28.4-60.4) (Fig. 2-7d). Apatites are generally depleted in Eu, Sr, Pb, Zr, and Hf. Prior and concurrent crystallization of titanite ($CaTiSiO_5$), which is observed in both the ultramafic and more evolved lithologies of the fractionation sequence, could sequester Eu and Sr, depleting crystallizing apatite in these elements. Other notable depletions include Nb, Rb, & Ba, indicating both the inability of apatite to incorporate large amounts of these elements (except for Ba, which can be accommodated in alforsite, a Ba-end member phosphate), but also the affinity of biotite for these three elements and K-feldspar for Rb & Ba (Pan and Fleet 2002).

2.6.7 Amphibole

Amphibole is found as both a primary magmatic phase and as secondary metamorphic overgrowth on clinopyroxene. Metamorphic amphibole is actinolitic and will not be discussed further. In the biotite-dominated fractionation sequence amphibole appears in the crystallization sequence only in the

more evolved feldspar-bearing lithologies (i.e., monzodiorites and monzonites). The composition of these amphiboles is dominantly magnesiohornblende. Mg#'s of the amphiboles vary from 56-67 in the monzodiorites to 48-56 in the monzonites. Trace elements analyses were done on three monzodiorites from the biotite-dominated fractionation sequence (MO-11-13, MO-11-14, MO-11-21). Primitive mantle-normalized trace element patterns of amphibole in the monzodiorites are characterized by enrichment in LREE over HREE ($(La/Yb)_N$ = 2.7-4.5). In addition, they display depletions in Sr, Pb, and Eu.

2.7 Discussion

2.7.1 Fractionation Sequence

There are several lines of field and petrographic evidence that indicate that the observed biotite-bearing lithologies could comprise a common plutonic cumulate sequence resulting from a single liquid line of descent. First, the contacts between the different plutonic rocks are gradational, with a general transition from more primitive to more evolved compositions from approximately northwest to southeast. Second, the poikilitic and orthocumulate textures observed in the phlogopite wehrlites and clinopyroxenites strongly suggest a cumulate origin (Fig. 2-5b,c,d). We therefore interpret the observed lithological variability to a primary fractionation sequence where the onset of crystallization of each phase is defined by the sequence olivine + clinopyroxene → Fe-Ti oxides → phlogopite + apatite → k-feldspar + plagioclase + amphibole → quartz. Notably, phlogopite is the dominant hydrous mafic mineral. In terms of lithology, this progression is manifested as wehrlites, to phlogopite wehrlites, to apatite-bearing phlogopite clinopyroxenites, to monzogabbros, to monzodiorites, and finally, to (quartz-)monzonites. Conspicuously, there are two large (km-scale) and many minor intrusions of red (alkali-)granites in close spatial proximity to the alkaline fractionation sequence. Field evidence is inconclusive to whether these intrusions are related to the fractionation sequence (primarily due to the fact that the contacts between the large red (alkali-)granite intrusions and the cumulate sequence are not readily exposed). Unpublished U-Pb zircon ages, however, indicate that these (alkali-)granites are significantly younger than the alkaline complex and are neither cogenetic nor contemporaneous with the biotite-dominated lithologies. We described them above for complete characterization of the observed plutonic igneous lithologies.

2.7.2 Magmatic Biotite

There are multiple textural lines of evidence indicating that biotite is a primary magmatic phase. Most importantly, there is a gradual decrease in biotite Mg# from the ultramafic lithologies to the more evolved lithologies. Continuity in composition (increases or decreases with Mg#) is also observed for minor and trace element, (e.g., Na_2O, Cl, MnO, Ni, Cr). Further, in several samples, biotite is the dominant phase and reaches up to 1-2 cm, suggesting that it was a primary crystallizing phase. Its texture indicates that it is either an intercumulus or orthocumulate phase (subhedral to euhedral shape). In addition, no pervasive alteration of the cumulate sequence by a high or low temperature fluid is observed. Both clinopyroxene and biotite enclose small euhedral apatite prisms, indicating that they both continued

to crystallize after apatite. Lastly, biotite is found in the widely documented melting reaction of olivine with a potassic melt with decreasing temperature (Barton and Hamilton 1979; Modreski and Boettcher 1972; Yoder and Kushiro 1969):

forsterite + melt = phlogopite + melt

indicating a peritectic reaction that is most likely responsible for the exhaustion of olivine in the ultramafic cumulates with progressive fractionation.

2.7.3 Experimental Studies Relevant to the Dariv Fractionation Sequence

The majority of experimental crystallization studies performed on hydrous, high-K, mafic to ultramafic starting materials (leucitite, biotite mafurite, ugandite, madupite, basanite, lamprophyre, Di-Fo-Ks-Qz synthetic materials etc.) have found olivine + clinopyroxene + phlogopite ± spinel at multiple saturation (Edgar et al. 1980; Elkins-Tanton and Grove 2003; Esperança and Holloway 1987; Melzer and Foley 2000; Righter and Carmichael 1996). Only two studies obtained conditions conducive to orthopyroxene saturation and both required CO_2 to stabilize it (Edgar et al. 1980; Sato 1997). Apatite and sanidine have also been found as lower temperature, late crystallizing phases (Barton and Hamilton 1978; Barton and Hamilton 1979; Melzer and Foley 2000; Righter and Carmichael 1996). The phase relations determined by the experimental studies are generally consistent with the order of crystallization we have deduced for the biotite-dominated fractionation series of the Dariv Igneous Complex. The most important constraint that these experiments provide for the crystallization conditions of the Dariv biotite fractionation sequence is the temperature of the liquidus as it is broadly invariant (1100-1200°C) over a large range of pressures. Therefore, initial crystallization temperatures for the ultramafic cumulates were likely between 1100-1200°C. The liquidus mineralogy, however, can vary. In particular, the stability of olivine as a crystallizing phase in K-rich mafic melts is dependent on the reaction olivine + liquid → phlogopite + liquid (Yoder & Eugster, 1954; Yoder and Kushiro, 1969). High f_{O_2}, P, H_2O, and K_2O contents will drive this reaction to the right (Esperança and Holloway 1987). This reaction is responsible for the shrinkage of the stability field of olivine in K-rich melts with increasing pressure and the decrease in olivine modal abundance with the appearance of phlogopite (Barton and Hamilton 1978; Barton and Hamilton 1979; Esperança and Holloway 1987; Righter and Carmichael 1996). As we observed a significant interval of olivine fractionation in Dariv (olivine Mg# 87 to 67), this suggests that pressures were not excessively high. The fact that no leucite was observed, however, suggests that pressures were not below ~0.2 GPa. Therefore, these experimental studies indicate that the Dariv ultramafic lithologies crystallized from magmas at temperatures of 1100-1200°C at pressures of >0.2 GPa. In the following section, we place more specific constraints on crystallization conditions using thermobarometers and oxygen barometers.

2.7.4 Crystallization Conditions

Pressure and Temperature

Thermometry based on major element clinopyroxene compositions (Putirka, 2008, eq. 32d) indicates that the phlogopite-bearing ultramafic and mafic rocks crystallized progressively over a temperature range of ~1210-1100°C (Table 13). This range of crystallization temperatures is in good agreement with experimental phase relations on high-K basaltic liquids (see discussion above). Pressure conditions of formation were approximated using the experimental Ba biotite-liquid equilibria of Righter & Carmichael, (1996). Ba concentrations of the melt in equilibrium with the most primitive analyzed phlogopite wehrlite, MO-10-394, were calculated using clinopyroxene Ba concentrations and the clinopyroxene-basalt partition coefficient of Hart & Dunn, (1993). Calculated Ba melt concentrations were slightly higher than that of mafic dikes with primitive compositions. Ultimately, a range of calculated Ba melt concentrations (1000-1500 ppm) for the primitive melt and the average Ba concentration (2220 ppm) in biotites from MO-10-394 were used in the calculations. Using the average clinopyroxene-thermometry temperature estimate for sample MO-10-394 (1206°C), the range of calculated pressure is 0.6 to 0.8±0.4 GPa.

For the more evolved rocks of the sequence, hornblende geochemistry was used to estimate temperature and pressure conditions of crystallization. The Al content in hornblende has been shown to increase with pressure, provided that quartz, K-feldspar, plagioclase, biotite, hornblende, titanite, and Fe-Ti oxides are also present as mineral phases in a rock (Hammarstrom and Zen 1986; Hollister et al. 1987; Schmidt 1992). Using the experimental calibrations of Schmidt, (1992) we calculated pressures of ~0.2-0.3 GPa using the Al-content of magnesio-hornblendes in the evolved rocks of the fractionation sequence. Temperature estimates using plagioclase-hornblende thermometry (Holland and Blundy 1994) yield temperature ranges of 642-726°C, which is close to the wet solidus of magmas which finally crystallize two feldspar+quartz assemblages. Slightly lower temperature estimates (538-672°C) were obtained from two-feldspar thermometry (Putirka 2008, Eq. 27a), indicating subsolidus re-equilibration of some feldspars.

The monzodiorites and monzonites are in a continuous, undeformed fractionation sequence with the ultramafic cumulates and spatial distances between the evolved and ultramafic cumulates (<1-5 km) allow for a pressure difference of 0.1-0.2 GPa. As there is significant uncertainty in estimated crystallization pressures of the ultramafic cumulates (e.g., the calibration of the Ba biotite-liquid exchange equilibrium has an error of 0.4 GPa and the liquid composition is calculated from cpx/melt Ba partition coefficients), crystallization pressures of 0.2-0.3 GPa for the evolved magmatic rocks and 0.3-0.5 GPa for the ultramafic cumulates is consistent with geobarometric constraints and field observations. Collaborative but indirect evidence for intrusion depths stems from the coexistence of brucite+serpentine in the serpentinites. As this mineral assemblage is limited to 360-390 °C (at 0.3-0.5 GPa) (Trommsdorff and Connolly 1996), its presence in the serpentinites indicates depths of <12-13 km (<0.34-0.38 GPa) assuming a typical continental geotherm of 30 °C/km. As arc geotherms are generally higher, this would provide a maximum depth limit.

Water Content of Melt

The water content of a melt strongly controls both the types of mineral that it will crystallize and their order of crystallization. The hydrous minerals found in the alkaline fractionation sequence of Dariv, predominantly biotite, but also amphibole, require some water to crystallize. Although biotite can crystallize at fairly low H_2O-contents (e.g., <0.5 wt.% H_2O in a granodiorite with 67.51 wt.% SiO_2), amphibole requires a minimum of 4 wt.% H_2O at 0.2 GPa and 2.5 wt.% H_2O at 0.8 GPa in the same magma (Naney 1983). The biotite-dominated fractionation sequence of Dariv suite does not display evidence for amphibole fractionation until relatively late (i.e., in the monzodiorites). This is consistent with the generally incompatible behavior of water in magmas which results in an increase in H_2O content with differentiation. Further, an increase in water contents with progressive crystallization is supported by the widespread resorption and alteration of clinopyroxene to actinolitic hornblende in the monzonites and quartz monzonites. If we assume that at the onset of monzodiorite crystallization the melt achieved the minimum amount of water required to crystallize hornblende at 0.2-0.3 GPa (3.8 - 4.0 wt.% H_2O), we can back-calculate the amount of water in the primitive melt parental to the cumulate sequence. If the primitive melt crystallized 40-50 wt.% (by mass) of biotite-bearing ultramafic and mafic cumulates which contain on average ~20 wt.% biotite (with 3-4 wt.% structurally bound H_2O), and therefore ~0.6-0.8 wt.% H_2O in the bulk cumulate, the primitive melt would need to contain ~2.2-2.6 wt.% H_2O in order to saturate in amphibole when reaching the fractionation stage of the monzodiorites. Lower or higher H_2O-contents in the primitive melt should lead to a later or earlier onset of amphibole crystallization, respectively. At 0.3-0.5 GPa, H_2O-saturated basaltic melts contain ~6-8 wt.% in aqueous fluid. Therefore, the primitive melts of the biotite-dominated fractionation sequence were certainly hydrous, but not H_2O-saturated.

Oxygen Fugacity

The oxygen fugacity during crystallization of the biotite-dominated fractionation sequence can be estimated using various experimentally determined oxygen-barometers. Calculations using the olivine-orthopyroxene-spinel oxygen barometer of Ballhaus et al., 1991 yield f_{O_2} estimates of +1.8 to +3.2 ΔFMQ for the phlogopite wehrlites. As orthopyroxene is not present in the ultramafic lithologies of Dariv, we accounted for the effect of the shift in the activity of silica (a_{SiO_2}) relative to orthopyroxene saturation on the f_{O_2} estimates using the formulations of O'Neill and Wall (1987) to calculate the a_{SiO_2} of olivine-orthopyroxene equilibria and the estimates of a_{SiO_2} for typical melt compositions (Ghiorso & Carmichael, 1988). This correction resulted in a shift of -0.6 log units. In addition, vanadium (V) partitioning between melt and clinopyroxene can also be used to estimate f_{O_2} (Canil 2002; Canil and Fedortchouk 2000). The crystal structure of clinopyroxene preferentially incorporates V^{3+} over V^{4+} and V^{5+}, therefore, $D_V^{cpx/melt}$ decreases with increasing f_{O_2}. Using V concentrations from analyses of primitive basaltic dikes (see

"Composition of the Primitive, Parental Melt" section below) and measured V values in clinopyroxene from the most primitive analyzed wehrlite (MO-10-394), we calculated $D_V^{cpx/melt}$. Then, implementing experimentally determined relationships between $D_V^{cpx/melt}$ and f_{O_2} (Canil and Fedortchouk 2000), we obtained estimates of +1.2 to +1.7 ΔFMQ. Both the olivine-spinel and the V-in-cpx oxygen barometers suggest that the Dariv ultramafic cumulates crystallized at elevated f_{O_2}'s. Other, subduction-related mafic alkaline magmas (phlogopite- and hornblende-bearing lamprophyres, shoshonites etc.) have also been observed to have particularly elevated f_{O_2}'s (+3 to +6 FMQ) compared to those of tholeiitic and calc-alkaline magmas (0 to +2 FMQ) (Carmichael 1991; Luhr and Carmichael 1981; Rowe et al. 2009; Vigouroux et al. 2008; Wallace and Carmichael 1989).

2.7.5 In-situ Trace Element Modeling of Fractionation Mechanisms

The gradual change in mineral modes across the fractionation sequence (i.e., from wehrlites to phlogopite- and apatite-rich clinopyroxenites to feldspar-bearing monzogabbros), indicating the accumulation of a progressively different fractionating mineral assemblage, and the steady decrease in Mg# of olivine, clinopyroxene, and biotite indicate that fractional crystallization was the dominant crystallization process in the formation of the ultramafic and mafic lithologies. To quantitatively assess the degree of differentiation (F) and the amount of interstitial liquid (L) trapped between cumulus minerals, we modeled the mineral trace element data following the method described by Hermann et al., (2001) based on the equations of Langmuir, (1989). In this model, we calculated mineral REE patterns starting from an average primitive melt composition (constrained from whole rock analyses of late-stage, co-genetic mafic dikes as discussed below). F and L are varied until a best fit to the measured REE data is obtained. This allows for assessment of both the degree of differentiation of a sample, of the amount of residual liquid in a cumulate, and whether some rocks represent true crystallized liquid compositions. For each observed and measured cumulate lithology, a best fit can be calculated with corresponding F and L values.

For the most ultramafic cumulates we modeled the mineral compositions of three phlogopite wehrlites (MO-10-392 (Mg# = 78.1), MO-10-323 (Mg# = 77.1), and MO-11-8 (Mg# = 76.3)) to capture the range of wehrlite fractionation. We also selected these samples because the constituent minerals do not show any zoning with respect to REEs, indicating that any trapped interstitial liquid present completely equilibrated with the cumulus phases. Clinopyroxenes from the most primitive analyzed wehrlite (MO-10-394) display some zoning, with the rims being 1.4-2.4 times enriched in REE as compared to the cores. For this reason, this sample was not modeled. From the measured clinopyroxene-mineral K_D values, other mineral-melt partition coefficients were calculated and the model results were varied to obtain a best fit to the average clinopyroxene composition.

As REEs are more compatible and diffuse more rapidly in apatite than clinopyroxene at a given temperature (Cherniak 2000; Hart and Dunn 1993; Van Orman et al. 2001; Watson and Green 1981), the

REE concentrations in apatite were used in the modeling for apatite-bearing lithologies. We selected one clinopyroxene-bearing phlogopitite (MO-11-10), one monzogabbro (MO-11-13) and one monzodiorite (MO-11-14) to model. Due to the more "evolved" nature of the feldspar-bearing lithologies the primitive melt composition used to model the phlogopite wehrlites is inappropriate as a starting composition. Therefore, we used a model liquid composition that is in equilibrium with the mean composition of clinopyroxenes from the most evolved apatite-free wehrlite (MO-11-8). From the measured apatite-mineral K_D values, other mineral-melt partition coefficients were calculated and the model results were varied to obtain a best fit to the average apatite composition.

Results of Mineral Trace Element Modeling

The *in situ* crystallization model reproduces the mineral trace element patterns of the phlogopite wehrlites when fractional crystallization is the dominant mechanism. The average clinopyroxene REE pattern of MO-10-392 is best fit when F = 63.5% and L = 0.5% (Fig. 2-9a), MO-10-323 when F = 67.3% and L = 0.6%, and MO-11-8 when F = 72% and L = 0.5%. The increase in the calculated degree of fractionation across the wehrlites is consistent with the decrease in the mineral Mg#'s. The model results support the aforementioned evidence that the wehrlites are dominated by fractionated phases with insignificant amount of small interstitial liquid. Further, the mineral trace element patterns of the apatite-bearing phlogopite clinopyroxenite and the feldspar-bearing lithologies are also reproduced by a fractional crystallization model. Beginning with the new parental melt concentration at the onset of apatite crystallization (i.e. the melt composition at F = 72% for the original primitive melt), the average apatite REE concentrations of the phlogopitite (MO-11-10) are best produced when F = 29% and L = 0% (Fig. 2-9b), the monzogabbro (MO-11-13) when F = 44.5% and L = 0.5% (Fig. 2-9c), and the monzodiorite (MO-11-14) when F = 82.5% and L = 0.

2.7.6 Comparison to Phlogopite-Bearing Ultramafic Xenoliths

Xenoliths of lithologic similarity to the biotite-bearing cumulates of the Dariv Igneous Complex (i.e. phlogopite-bearing wehrlites and clinopyroxenites) have been found in high-K magmas from numerous localities (e.g. Eifel, Germany; Uganda; the Italian Volcanic Province; Sweet Grass Volcanics, Alberta & Montana; the Western Mexican Volcanic Belt) (Aoki and Kushiro 1968; Beccaluva et al. 2002; Buhlmann et al. 2000; Dawson and Smith 1992; Downes et al. 2004; Giannetti 1982; Giannetti and Luhr 1990; Righter and Rosas-Elguera 2001). In general, the xenoliths have been divided into two groups, 1) fragments of supra-subduction zone metasomatized mantle and 2) cumulates of high-K magmas. The first group is identified by their typical deformation texture of mantle derived spinel peridotites, including porphyroclastic and coarse granular textures (e.g., Downes et al., 2004). Studies examining the mantle xenoliths have suggested that the high-K host magmas are produced through partial melting of metasomatized mantle and that the xenoliths are entrained fragments of this source region, (Ertan and Leeman 1996; Shaw and Eyzaguirre 2000). These studies propose that the phlogopite clinopyroxenites

are created as veins or disseminated alteration by subsolidus metasomatism of a lherzolitic mantle by subduction zone fluids or melts rich in K, Ba, Rb, Sr, Ce, and water (Conticelli and Peccerillo 1992; Elkins-Tanton and Grove 2003; Wyllie and Sekine 1982). Other xenoliths have been interpreted as the products of crystal fractionation of high-K magmas similar to the alkali-basalts in which they are found (Aoki and Kushiro 1968; Buhlmann et al. 2000; Downes et al. 2004; Righter and Rosas-Elguera 2001). This is supported by cumulate textures and a mineral chemistry similar to the phenocrysts in their host minettes. In addition, calculated REE patterns of melts in equilibrium with the clinopyroxenes in the xenoliths are very similar to those of the minettes (e.g., Downes et al. 2004) and both the xenoliths and the high-K lavas tend to have low ε_{Nd} and radiogenic Sr signatures ($\varepsilon_{Nd} \cong -10$, $^{87}Sr/^{86}Sr = 0.706\text{-}0.710$) (Buhlmann et al. 2000; Farmer et al. 2002; Wannamaker et al. 2000). The Dariv ultramafic rocks are texturally and geochemically similar to this latter group of xenoliths. In most proposed scenarios, a previously enriched, mica-bearing mantle wedge above a subduction zone (represented by xenolith group 1) is remelted at a later time due to decompression melting or a heating event to produce the melts parental to the cumulates (xenoliths of group 2) (e.g., Downes et al. 2004; Righter and Rosas-Elguera 2001). Indeed, the occurrence of both groups of xenoliths (i.e. those representative of a metasomatized mantle wedge and those cumulative in origin) in the same lava flows or volcanic province suggests a closely linked origin. To assess whether the petrogenetic process described above is applicable to the Dariv Igneous Complex, we constrain the nature of the parental melts and the implication this has for their mantle source region in the following section.

2.7.7 Composition of the Primitive, Parental Melt

Primitive, syn-plutonic mafic dikes that cross cut the cumulate sequence (e.g., Fig. 2-4) have the appropriate composition to be parental to the cumulates. Several lines of evidence suggest that these dikes are late-stage, syn-plutonic dikes representative of a parental melt composition to the cumulates they intrude. First, the dikes have phenocryst and groundmass mineralogy similar to cumulates, namely biotite, clinopyroxene, and Fe-Ti oxides, secondly rounded enclaves, mineralogically identical to the mafic dikes are common in the monzodiorites and monzonites, and lastly the dike enclaves contain xenocrysts of minerals (quartz & k-feldspar) from the evolved granitoids (Fig. 2-3c). The first observation indicates that the dikes could have the appropriate composition to be parental to the cumulates. The latter two observations demonstrate that the mafic dikes were emplaced while the intrusions that lead to the cumulate sequence were still at relatively high temperatures, allowing for some mobilization of the mafic dikes and mingling with the evolved magma.

From whole rock geochemical analyses of dikes, primitive melt compositions were identified by the following chemical criteria: Mg# 65-75, Cr ~500-900 ppm, and Ni ~150-450 ppm. Four samples that met these constraints were identified. Accordingly, the range of their compositions might be representative of a primary primitive melt composition. This range in compositions corresponds to a near-primary, shoshonitic (Na_2O = 1.83-2.66 wt.%, K_2O = 1.42-2.82 wt.%) basalt to basaltic-andesite (49.8-

53.3 wt.% SiO_2) (Table 14). We used the clinopyroxene compositions of the most primitive analyzed phlogopite wehrlites (MO-10-394, MO-10-325, and MO-10-323) and known K_d's to estimate trace element concentrations in the parental melt. The calculated compositions are in good agreement with the trace elements of the primitive mafic dikes, supporting the hypothesis that the dikes are indeed representative of a parental melt composition to the fractionation sequence (Fig. 2-10a).

Comparison to Primitive Arc Melts

Both the calculated primitive melt compositions and those of the primitive dikes are highly enriched in Th, U, Ba, Rb, K, and LREE and have pronounced negative Nb-Ta depletion, geochemical hallmarks of subduction-zone related primitive magmas (Fig. 2-10a). Accordingly, a key question in this study is whether the Dariv primitive melt compositions are similar to primitive melt compositions generated at subduction zones and whether the fractionation sequence observed in Dariv may be common in other arcs. Using a global compilation of primitive melt compositions occurring in arcs from the GEOROC database (using the criteria Mg# = 0.65-0.79, Ni = 150-500, Cr = 250-1200), we compared the Dariv primitive melt compositions to those found in arcs. Arc lavas are dominated by tholeiitic and calc-alkaline compositions (Fig. 2-11a), but primitive andesites and alkaline basaltic primitive magmas also occur. Subduction zones generating primitive melts similar to that observed in Dariv, with higher K_2O and K_2O+Na_2O contents at similar SiO_2 contents than calc-alkaline and tholeiitic arc basalts at similar SiO_2 contents, are predominately continental arcs (e.g., Tonga/Kermadec, the Mexican Volcanic Belt, Honshu, Italy, the Andes, New Zealand, and Sunda/Banda) (Fig. 2-11). In addition, Dariv primitive melts are characterized by strong enrichments in LILE, LREE, Th, U, Pb, and Sr comparable to primitive continental calc-alkaline, high-K, and shoshonitic arc melts, significantly more enriched than primitive melts from calc-alkaline and tholeiitic oceanic arcs (Fig. 2-10b). In terms of other major element compositions, the Dariv primitive melt compositions are well within the range of observed values for primitive arc melt. Thus, the Dariv primitive melts appear to be most similar in composition to those found in continental arcs, suggesting that recycling of continental material plays an important role in their generation, most likely through subduction of weathered clastic sediments and the transfer of their geochemical signature into the mantle wedge. Although assimilation of crustal material during ascent through the overlying crust could help to produce the observed enrichments in incompatible elements, significant assimilation would dilute the primitive character of the melts, therefore we do not consider assimilation a significant process in the generation of the Dariv parental melts.

Compositions of high-K starting materials in experiments where olivine + phlogopite + clinopyroxene were found as crystallizing or residual phases are shown in Figure 15 for comparison. Although many of the starting materials have higher K_2O, K_2O+Na_2O, and K_2O/Na_2O ratios than commonly observed in primitive arc basalts, several have compositions similar to that of the Dariv primitive melts. In particular, Sisson et al. (2005) found phlogopite + amphibole + plagioclase + apatite +

titanomagnetite (+ minor olivine) to be in equilibrium with 18-29% melt of a starting material with the composition of a shoshonitic high-alumina basalt (AD19-93: K_2O = 2.32; Na_2O = 3.76). This composition (S05 in Figure 11) has similar alkali contents as the Dariv primitive basalts, suggesting that high-K calc-alkaline to shoshonitic primitive arc melts are capable of producing the evolved lithologies observed in Dariv through fractionation of SiO_2-poor, biotite-rich cumulates.

2.7.8 Modeling of the Subduction-Derived Component in the Primitive Melt Composition

Following our conclusion that the Dariv primitive melts are similar to high-K primitive melts found in continental arcs, we constrained the trace element characteristics of a slab-derived component contributing to the Dariv primitive melts. We followed the method of Grove et al., (2002) in which it is assumed that elements are contributed to a primitive melt either from melting of mantle peridotite or from a subduction-related H_2O-rich component. The trace element concentration of the subduction component can be calculated from the following expression:

$$C_{PM} = C_{mantle}\left(1 - \frac{X_{H_2O}}{\alpha}\right) + \left(\frac{X_{H_2O}}{\alpha}\right) * C_{slab}$$

where C_{PM}, C_{mantle}, and C_{slab} are the concentrations of the element of interest in the primitive melt, the melt that would result from melting an unmetasomatized mantle peridotite, and in the slab-derived component, respectively. X_{H_2O} is the weight fraction of water in the primitive melt and a proxy for the amount of slab component contribution. α is a correction factor to account for the major element contribution of the slab-derived component. Grove et al., (2002) found that a correction of factor of ~0.6 was appropriate, therefore we used that value in our calculations.

In order to implement these calculations C_{mantle} and X_{H_2O} must be constrained. For C_{mantle} we implement a non-modal batch melting model (e.g., Shaw, 1970) to constrain the degree of partial melting of the mantle source. We start with a harzburgite depleted source composition (Grove et al. 2002) and incrementally melted the mantle to best reproduce the HREE element characteristics of the primitive melt composition. A best fit is obtained when 10% of partial melting occurs in the spinel field. X_{H_2O} was approximated using the estimated water concentrations for the Dariv primitive melts (~2.5 wt.% H_2O). However, we calculated slab-derived components using a range of water concentrations (2.5-10 wt.%) in the primitive melt to investigate the range of potential slab component compositions.

Results

The trace element composition of the slab-derived component is strongly enriched in LILE and LREE, and slightly enriched in HREE (Fig. 2-12a). The slab component accounts for 90-100% of the highly incompatible elements (Rb, Ba, Th, U, K, Nb, La, Ce, Pb, and Sr), 64-90% of the less incompatible elements (Nd, Zr, Hf, Sm, Eu, Gd), and 5-45% of the HREE (Fig. 2-12b). Compared to

estimates of slab-derived component from Mt. Shasta in the Cascades (Grove et al. 2002), the Marianas Islands (Stolper and Newman 1994), and the Kohistan paleo-arc (Jagoutz et al. 2007), our calculated slab-component is comparable in absolute concentrations when X_{H_2O} is high (10 wt.%). Pre-eruptive water contents of 10 wt.% in primitive magmas are extremely high and likely represent the upper limit of H_2O contents deduced for basaltic arc magmas with <6 wt.% H_2O being a more common range for arc-related magmas (Grove et al. 2012). Further, our estimates for the Dariv primitive melts (2-3 wt.% H_2O) are not compatible with such high water concentrations. This suggests that either the incompatible elements in the Dariv primitive melts reflect a particularly enriched subduction component or that an alternative model, where water and incompatible elements transfer to the primitive melt are decoupled in a two-stage process, must be considered. In the first scenario, high incompatible element concentrations in the slab component could be due to a particularly large contribution from subducted sediments. A particularly thick section of subducted sediment and/or high slab-top temperatures (during incipient subduction or tearing of the subducting slab) facilitating the transfer of subducted sediment into the mantle wedge could explain the strong enrichment in LILE, Th, U, K, and LREE observed in the Dariv subduction component.

In the second scenario, contribution of an incompatible element enriched component to the primitive melt would occur in two stages. First, a water- and incompatible-rich component could migrate from the slab progressively enriching a cold mantle wedge through the precipitation of phlogopite, amphibole, and potentially other hydrous phases. During this initial process H_2O would be partly lost, whereas most of the incompatible elements would be retained in the crystallized phases. In a second step the mantle is reheated resulting in the melting of the previously precipitated hydrous phases and the production of a incompatible-element enriched, primitive melt with relatively low water contents. For the alkaline complex observed in the Dariv Range, we cannot yet discern between these two scenarios. Nevertheless, the close spatial occurrence of metasomatic and cumulative biotite-bearing ultramafic xenoliths from other localities with high-K magmas would seem to support the second scenario. In addition, high-K volcanics with biotite phenocrysts from other localities have been inferred to have formed through second-stage melting of a subduction-metasomatized mantle. For example, high-K basalts with subduction trace element patterns in the Sierra Nevada erupted in the Pliocene, well after Mesozoic-Cenozoic subduction ceased, and therefore must have been derived from melting of previously metasomatized mantle (Farmer et al. 2002; Van Kooten 1980). In addition, biotite-phenocrystic high-K basalts, lamprohyres, and basanites from the Western Mexican Volcanic Belt have very low B/Be ratios (indicating little direct input from slab-derived fluids into their source region), but elevated Ba/Ce and other common measures of subduction zone trace element enrichment (Hochstaedter et al. 1996). This suggests that their genesis involved a multi-stage process whereby the high-K lavas were generated through later-stage melt of a metasomatized mantle selectively enriched in Ba (e.g., through precipitation of minerals such as biotite) (Foley 1992), instead of having formed through direct fluxing of subduction zone fluids. In both scenarios, a secondary remobilization event whether through lithospheric

delamination and upwelling of hot asthenosphere (Ducea and Saleeby 1998; Farmer et al. 2002) or decompression (Hochstaedter et al. 1996) is required for their generation.

2.8 Conclusion

The km-scale exposure of phlogopite- and clinopyroxene-dominated ultramafic lithologies of the Dariv igneous complex in Western Mongolia are remarkable in that they have hereto only been described as xenoliths in alkaline basalts. The range of high-K igneous rocks from phlogopite wehrlites to quartz monzonites of the Dariv Range provide an unparalleled opportunity to study the fractionation of a high-K arc-related primitive basalt. Detailed fieldwork and geochemistry suggests that the observed lithologies comprise a common fractionation sequence derived from a moderately hydrous, incompatible element-enriched primitive arc melt. Petrography and mineral chemistry indicate that fractional crystallization was the dominant mechanism in the formation of the observed lithologies. The ultramafic rocks crystallized at 0.3-0.5 GPa and 1200-1100°C. Estimates of water content and f_{O_2} of crystallization and an estimated parental melt composition indicate that the Dariv Igneous Complex formed due to the fractionation of a primitive high-K basalt with 2-3 wt.% H_2O under conditions that were fairly oxidizing from the onset of crystallization ($\geq$FMQ+2). Comparison to a global dataset of primitive arc melts indicates that the primitive melts similar in composition to the Dariv primitive melts are common in continental arc settings. Modeling of the Dariv primitive melt in terms of a partial melt of a depleted mantle wedge and a slab-derived component indicates that the incompatible-element rich character of the Dariv primitive melt was likely due to either a particularly enriched subduction component or progressive enrichment of a cold supra-subduction zone mantle that was re-melted at a later time.

References

Allan J, Carmichael I (1984) Lamprophyric lavas in the Colima graben, SW Mexico. Contributions to Mineralogy and Petrology 88(3):203-216

Alonso-Perez R, Müntener O, Ulmer P (2009) Igneous garnet and amphibole fractionation in the roots of island arcs: experimental constraints on H2O undersaturated andesitic liquids. Contributions to Mineralogy and Petrology 157:541-558

Aoki Ki, Kushiro I (1968) Some clinopyroxenes from ultramafic inclusions in Dreiser Weiher, Eifel. Contributions to Mineralogy and Petrology 18(4):326-337

Armstrong JT (1995) Citzaf-a package of correction programs for the quantitative Electron Microbeam X-Ray-Analysis of thick polished materials, thin-films, and particles. Microbeam Analysis 4(3):177-200

Badarch G, Dickson Cunningham W, Windley BF (2002) A new terrane subdivision for Mongolia: implications for the Phanerozoic crustal growth of Central Asia. Journal of Asian Earth Sciences 21(1):87-110

Ballhaus C, Berry R, Green D (1991) High pressure experimental calibration of the olivine-orthopyroxene-spinel oxygen geobarometer: implications for the oxidation state of the upper mantle. Contributions to Mineralogy and Petrology 107(1):27-40

Barton M, Hamilton D (1978) Water-saturated melting relations to 5 kilobars of three Leucite Hills lavas. Contributions to Mineralogy and Petrology 66(1):41-49

Barton M, Hamilton DL (1979) The melting relationships of a madupite from the Leucite Hills, Wyoming, to 30 Kb. Contributions to Mineralogy and Petrology 69(2):133-142

Beccaluva L, Coltorti M, Di Girolamo P, Melluso L, Milani L, Morra V, Siena F (2002) Petrogenesis and evolution of Mt. Vulture alkaline volcanism (Southern Italy). Mineralogy and Petrology 74(2):277-297

Buhlmann AL, Cavell P, Burwash RA, Creaser RA, Luth RW (2000) Minette bodies and cognate mica-clinopyroxenite xenoliths from the Milk River area, southern Alberta: records of a complex history of the northernmost part of the Archean Wyoming craton. Canadian Journal of Earth Sciences 37(11):1629-1650

Buslov MM, Saphonova IY, Watanabe T, Obut OT, Fujiwara Y, Iwata K, Semakov NN, Sugai Y, Smirnova LV, Kazansky AY (2001) Evolution of the Paleo-Asian Ocean (Altai-Sayan Region, Central Asia) and collisions of possible Gondwana-derived terranes with the southern marginal part of the Siberian continent. Geoscience Journal 5(3):203-224

Canil D (2002) Vanadium in peridotites, mantle redox and tectonic environments: Archean to present. Earth and Planetary Science Letters 195(1):75-90

Canil D, Fedortchouk Y (2000) Clinopyroxene-liquid partitioning for vanadium and the oxygen fugacity during formation of cratonic and oceanic mantle lithosphere. Journal of geophysical research 105:26

Carmichael IS (1991) The redox states of basic and silicic magmas: a reflection of their source regions? Contributions to Mineralogy and Petrology 106(2):129-141

Cherniak D (2000) Rare earth element diffusion in apatite. Geochimica et Cosmochimica Acta 64(22):3871-3885

Conference Participants (1972) Penrose field conference on ophiolites. Geotimes 17:24-25

Conticelli S, Peccerillo A (1992) Petrology and geochemistry of potassic and ultrapotassic volcanism in central Italy: petrogenesis and inferences on the evolution of the mantle sources. Lithos 28(3,Äì6):221-240

Dawson JB, Smith JV (1992) Olivine-mica pyroxenite xenoliths from northern Tanzania: metasomatic products of upper-mantle peridotite. Journal of Volcanology and Geothermal Research 50:131-142

DeBari S, Kay SM, Kay RW (1987) Ultramafic xenoliths from Adagdak Volcano, Adak, Aleutian Islands, Alaska; deformed igneous cumulates from the Moho of an island arc. Journal of Geology 95(3):329-341

Dijkstra AH, Brouwer FM, Cunningham WD, Buchan C, Badarch G, Mason PRD (2006) Late Neoproterozoic proto-arc ocean crust in the Dariv Range, Western Mongolia: a supra-subduction zone end-member ophiolite. Journal of the Geological Society, London 163:363-373

Downes H, MacDonald R, Upton BGJ, Cox KG, Bodinier J-L, Mason PRD, James D, Hill PG, Hearn BC (2004) Ultramafic Xenoliths from the Bearpaw Mountains, Montana, USA: Evidence for Multiple Metasomatic Events in the Lithospheric Mantle beneath the Wyoming Craton. Journal of Petrology 45(8):1631-1662

Ducea M, Saleeby J (1998) A case for delamination of the deep batholithic crust beneath the Sierra Nevada, California. International Geology Review 40(1):78-93

Edgar AD, Condliffe E, Barnett RL, Shirran RJ (1980) An Experimental Study of an Olivine Ugandite Magma and Mechanisms for the Formation of its K-Enriched Derivatives. Journal of Petrology 21(3):475-497

Elkins-Tanton LT, Grove TL (2003) Evidence for deep melting of hydrous metasomatized mantle: Pliocene high-potassium magmas from the Sierra Nevadas. J Geophys Res 108(B7):2350

Ertan IE, Leeman WP (1996) Metasomatism of Cascades subarc mantle: Evidence from a rare phlogopite orthopyroxenite xenolith. Geology 24(5):451-454

Esperança S, Holloway JR (1987) On the origin of some mica-lamprophyres: experimental evidence from a mafic minette. Contributions to Mineralogy and Petrology 95(2):207-216

Farmer GL, Glazner AF, Manley CR (2002) Did lithospheric delamination trigger late Cenozoic potassic volcanism in the southern Sierra Nevada, California? Geological Society of America Bulletin 114(6):754-768

Foley S (1992) Vein-plus-wall-rock melting mechanisms in the lithosphere and the origin of potassic alkaline magmas. Lithos 28(3):435-453

Giannetti B (1982) Cumulate inclusions from K-rich magmas, Roccamonfina volcano, Italy. Earth and Planetary Science Letters 57(2):313-335

Giannetti B, Luhr JF (1990) Phlogopite-clinopyroxenite nodules from high-K magmas, Roccamonfina Volcano, Italy: evidence for a low-pressure metasomatic origin. Earth and Planetary Science Letters 101:404-424

Greene AR, DeBari SM, Kelemen PB, Blusztajn J, Clift PD (2006) A Detailed Geochemical Study of Island Arc Crust: the Talkeetna Arc Section, South-Central Alaska. Journal of Petrology 47(6):1051-1093

Grove TL, Elkins-Tanton LT, Parman SW, Chatterjee N, Müntener O, Gaetani GA (2003) Fractional crystallization and mantle-melting controls on calc-alkaline differentiation trends. Contributions to Mineralogy and Petrology 145:515-533

Grove TL, Parman SW, Bowring SA, Price RC, Baker MB (2002) The role of an H2O-rich fluid component in the generation of primitive basaltic andesites and andesites from the Mt. Shasta region, N. California. . Contributions to Mineralogy and Petrology 142(4):375-396

Grove TL, Till CB, Krawczynski MJ (2012) The role of H2O in subduction zone magmatism. Annual Review of Earth and Planetary Sciences 40:413-439

Hammarstrom JM, Zen E-a (1986) Aluminium in hornblende: an empirical igneous geobarometer. American Mineralogist 71:1297-1313

Hart SR, Dunn T (1993) Experimental cpx/melt partitioning of 24 trace elements. Contributions to Mineralogy and Petrology 113(1):1-8

Hermann J, Müntener O, Günther D (2001) Differentiation of Mafic Magma in a Continental Crust-to-Mantle Transition Zone. Journal of Petrology 42(1):189-206

Hochstaedter AG, Ryan JG, Luhr JF, Hasenaka T (1996) On B/Be ratios in the Mexican volcanic belt. Geochimica et Cosmochimica Acta 60(4):613-628

Holland T, Blundy J (1994) Non-ideal interactions in calcic amphiboles and their bearing on amphibole-plagioclase thermometry. Contributions to Mineralogy and Petrology 116(4):433-447

Hollister LS, Grissom GC, Peters EK, Stowell HH, Sisson VB (1987) Confirmation of the empirical correlation of Al in hornblende with pressure of solidification of calc-alklaline plutons. American Mineralogist 72:231-239

Jagoutz O, Müntener O, Schmidt MW, Burg J-P (2011) The roles of flux- and decompression melting and their respective fractionation lines for continental crust formation: Evidence from the Kohistan arc. Earth and Planetary Science Letters

Jagoutz O, Müntener O, Ulmer P, Pettke T, Burg J-P, Dawood H, Hussain S (2007) Petrology and Mineral Chemistry of Lower Crustal Intrusions: the Chilas Complex, Kohistan (NW Pakistan). Journal of Petrology 48(10):1895-1953

Jagoutz O, Schmidt M (2012) The formation and bulk composition of modern juvenile continental crust: The Kohistan arc. Chemical Geology 298-99:79-96

Jagoutz OE (2010) Construction of the granitoid crust of an island arc. Part II: a quantitative petrogenetic model. Contributions to Mineralogy and Petrology 160:359-381

Kay SM, Kay RW (1985) Role of crystal cumulates and the oceanic crust in the formation of the lower crust of the Aleutian arc. Geology 13(7):461-464

Khain EV, Bibikova EV, Salnikova EB, Kröner A, Gibsher AS, Didenko AN, Degtyarev KE, Fedotova AA (2003) The Palaeo-Asian ocean in the Neoproterozoic and early Palaeozoic: new geochronological data and palaeotectonic reconstructions. Precambrian Research 122:329-358

Kozakov IK, Salnikova EB, Khain EV, Kovach VP, Berezhnaya NG, Yakoleva SZ, Plotkina YV (2002) Early Caledonian Crystalline Rocks of the Lake Zone in Mongolia: Formation History and Tectonic Settings as Deduced from U-Pb and Sm-Nd Datings. Geotectonics 36(2):156-166

Krawczynski MJ (2011) Experimental studies of melting and crystallization processes in planetary interiors. Massachusetts Institute of Technology

Langmuir CH (1989) Geochemical consequences of in situ crystallization. Nature 340(6230):199-205

Luhr JF, Allan JF, Carmichael IS, Nelson SA, Hasenaka T (1989) Primitive calc-alkaline and alkaline rock types from the Western Mexican Volcanic Belt. Journal of Geophysical Research: Solid Earth 94(B4):4515-4530

Luhr JF, Carmichael IS (1981) The Colima volcanic complex, Mexico: Part II. Late-quaternary cinder cones. Contributions to Mineralogy and Petrology 76(2):127-147

Maria AH, Luhr JF (2008) Lamprophyres, basanites, and basalts of the western Mexican volcanic belt: volatile contents and a vein,Äiwallrock melting relationship. Journal of Petrology 49(12):2123-2156

Melzer S, Foley SF (2000) Phase relations and fractionation sequences in potassic magma series modelled in the system CaMgSi2O6-KAlSiO4-Mg2SiO4-SiO2-F2O, at 1 bar to 18 kbar. Contributions to Mineralogy and Petrology 138(2):186-197

Modreski PJ, Boettcher AL (1972) The stability of phlogopite + enstatite at high pressures; a model for micas in the interior of the Earth. American Journal of Science 272(9):852-869

Müntener O, Kelemen P, Grove T (2001) The role of H2O during crystallization of primitive arc magmas under uppermost mantle conditions and genesis of igneous pyroxenites: an experimental study. Contributions to Mineralogy and Petrology 141(6):643-658

Naney M (1983) Phase equilibria of rock-forming ferromagnesian silicates in granitic systems. American Journal of Science 283(10):993-1033

Ownby SE, Lange RA, Hall CM (2008) The eruptive history of the Mascota volcanic field, western Mexico: age and volume constraints on the origin of andesite among a diverse suite of lamprophyric and calc-alkaline lavas. Journal of Volcanology and Geothermal Research 177(4):1077-1091

Pan Y, Fleet ME (2002) Compositions of the Apatite-Group Minerals: Substitution Mechanisms and Controlling Factors. Reviews in Mineralogy and Geochemistry 48(1):13-49

Putirka KD (2008) Thermometers and Barometers for Volcanic Systems. Reviews in Mineralogy and Geochemistry 69(1):61-120

Righter K, Carmichael ISE (1996) Phase equilibria of phlogopite lamprophyres from western Mexico: biotite-liquid equilibria and P-T; estimates for biotite-bearing igneous rocks. Contributions to Mineralogy and Petrology 123(1):1-21

Righter K, Rosas-Elguera J (2001) Alkaline Lavas in the Volcanic Front of the Western Mexican Volcanic Belt: Geology and Petrology of the Ayutla and Tapalpa Volcanic Fields. Journal of Petrology 42(12):2333-2361

Rowe MC, Kent AJR, Nielsen RL (2009) Subduction Influence on Oxygen Fugacity and Trace and Volatile Elements in Basalts Across the Cascade Volcanic Arc. Journal of Petrology 50(1):61-91

Rudnick RL, Fountain DM (1995) Nature and composition of the continental crust: A lower crustal perspective. Rev Geophys 33(3):267-309

Sato H (1977) Nickel content of basaltic magmas: identification of primary magmas and a measure of the degree of olivine fractionation. Lithos 10(2):113-120

Sato K (1997) Melting experiments on a synthetic olivine lamproite composition up to 8 GPa: Implication to its petrogenesis. J Geophys Res 102(B7):14751-14764

Schmidt MW (1992) Amphibole composition in tonalite as a function of pressure: an experimental calibration of the Al-in-hornblende barometer. Contributions to Mineralogy and Petrology 110:304-310

Sengör AMC, Natalín BA, Burtman VS (1993) Evolution of the Altaid tectonic collage and Palaeozoic crustal growth in Eurasia. Nature 364:299-307

Sengör AMC, Natalín BA, Burtman VS (1994) Tectonic evolution of Altaides. Russian Geology and Geophysics 35:33-47

Shaw CSJ, Eyzaguirre J (2000) Origin of megacrysts in the mafic alkaline lavas of the West Eifel volcanic field, Germany. Lithos 50(1,Äì3):75-95

Sisson TW, Grove TL (1993) Experimental investigations of the role of H2O in calc-alkaline differentiation and subduction zone magmatism. Contributions to Mineralogy and Petrology 113:143-166

Sisson TW, Ratajeski K, Hankins WB, Glazner AF (2005) Voluminous granitic magmas from common basaltic sources. Contributions to Mineralogy and Petrology 148:635-661

Stolper E, Newman S (1994) The role of water in the petrogenesis of Mariana trough magmas. Earth and Planetary Science Letters 121(3):293-325

Tatsumi Y, Shukuno H, Tani K, Takahashi N, Kodaira S, Kogiso T (2008) Structure and growth of the Izu-Bonin-Mariana arc crust: 2. Role of crust-mantle transformation and the transparent Moho in arc crust evolution. J Geophys Res 113(B2):B02203

Trommsdorff V, Connolly JA (1996) The ultramafic contact aureole about the Bregaglia (Bergell) tonalite: Isograds and a thermal model. Schweiz Mineral Petrogr Mitt 76(3):537-547

Van Kooten GK (1980) Mineralogy, petrology, and geochemistry of an ultrapotassic basaltic suite, central Sierra Nevada, California, USA. Journal of Petrology 21(4):651-684

Van Orman JA, Grove TL, Shimizu N (2001) Rare earth element diffusion in diopside: influence of temperature, pressure, and ionic radius, and an elastic model for diffusion in silicates. Contributions to Mineralogy and Petrology 141(6):687-703

Vigouroux N, Wallace PJ, Kent AJ (2008) Volatiles in high-K magmas from the western Trans-Mexican Volcanic Belt: evidence for fluid fluxing and extreme enrichment of the mantle wedge by subduction processes. Journal of Petrology 49(9):1589-1618

Villemant B (1988) Trace element evolution in the Phlegrean Fields (Central Italy): fractional crystallization and selective enrichment. Contributions to Mineralogy and Petrology 98(2):169-183

Villemant B, Jaffrezic H, Joron J-L, Treuil M (1981) Distribution coefficients of major and trace elements; fractional crystallization in the alkali basalt series of Chaîne des Puys (Massif Central, France). Geochimica et Cosmochimica Acta 45(11):1997-2016

Wallace P, Carmichael ISE (1989) Minette lavas and associated leucitites from the western front of the Mexican Volcanic Belt: petrology, chemistry, and origin. Contributions to Mineralogy and Petrology 103(4):470-492

Wannamaker PE, Hulen JB, Heizler MT (2000) Early Miocene lamproite from the Colorado Plateau tectonic province, Southeastern Utah, USA. Journal of Volcanology and Geothermal Research 96(3,4):175-190

Watson EB, Green TH (1981) Apatite/liquid partition coefficients for the rare earth elements and strontium. Earth and Planetary Science Letters 56:405-421

Wyllie PJ, Sekine T (1982) The formation of mantle phlogopite in subduction zone hybridization. Contributions to Mineralogy and Petrology 79(4):375-380

Yoder HS, Kushiro I (1969) Melting of a Hydrous Phase: Phlogopite. American Journal of Science 267-A:558-582

2.9 Figures and Captions

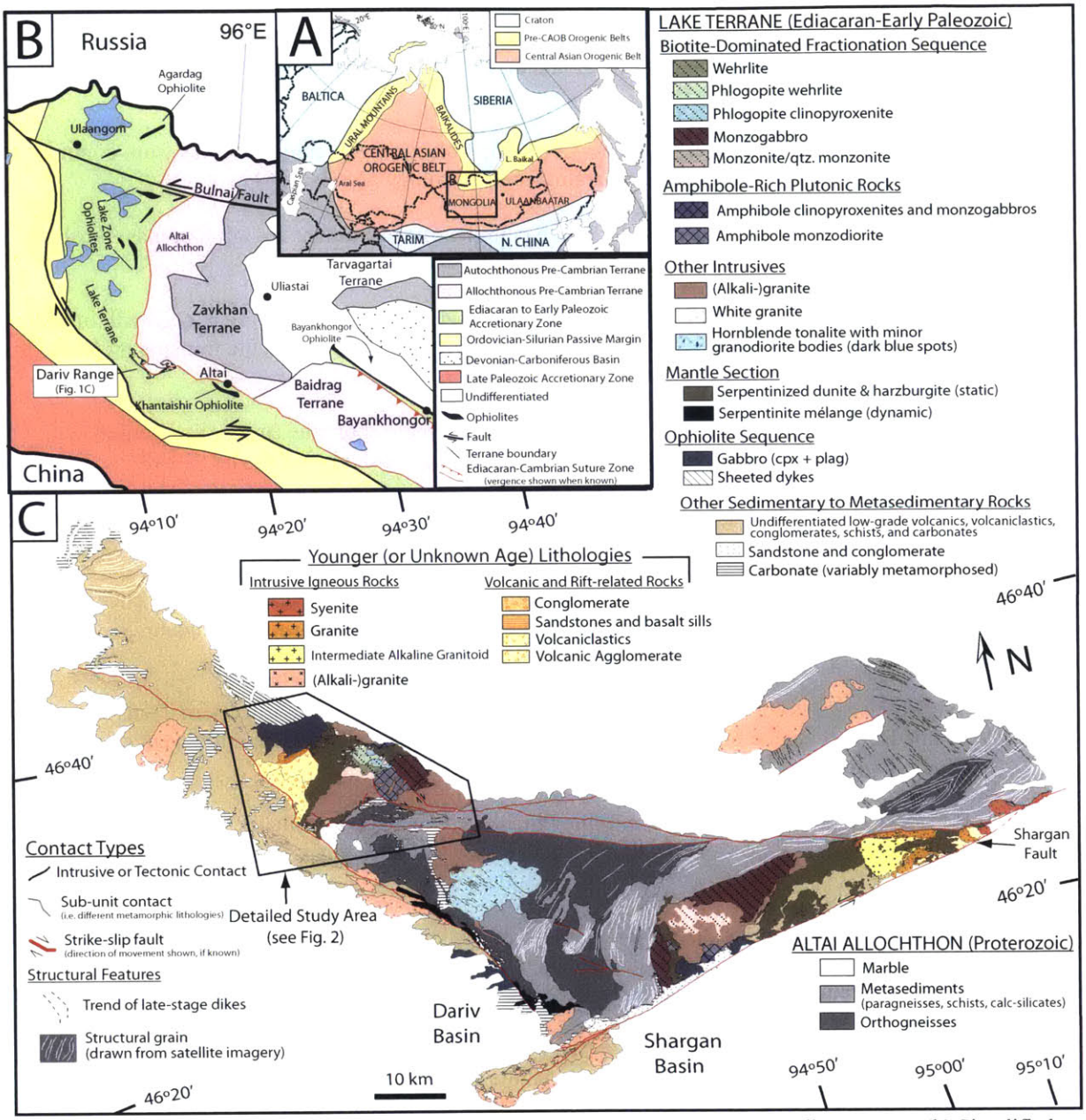

Fig. 2-1 (a) Simplified map of the Central Asian Orogenic Belt (CAOB) and surrounding cratons. (b) Simplified terrane map of Mongolia. Notably, Mongolia consists of Pre-Cambrian autochthonous terranes surrounded by accreted allochthonous terranes, ophiolites, and island arc-related units to the South and West. The Dariv Range is located at the boundary of the Pre-Cambrian Altai Allochthon and the Lake Terrane. (c) Geological map of the Dariv Range based on field mapping, interpretation of Landsat images, and previously constructed maps of the area (Dijkstra *et al.*, 2006; Khain *et al.*, 2003). Our field mapping predominantly focused on the alkaline igneous sequences (both in the northwest and southeast parts of the Range) and the ophiolite sequence. See Appendix A for a map of the areas that were visited in the field.

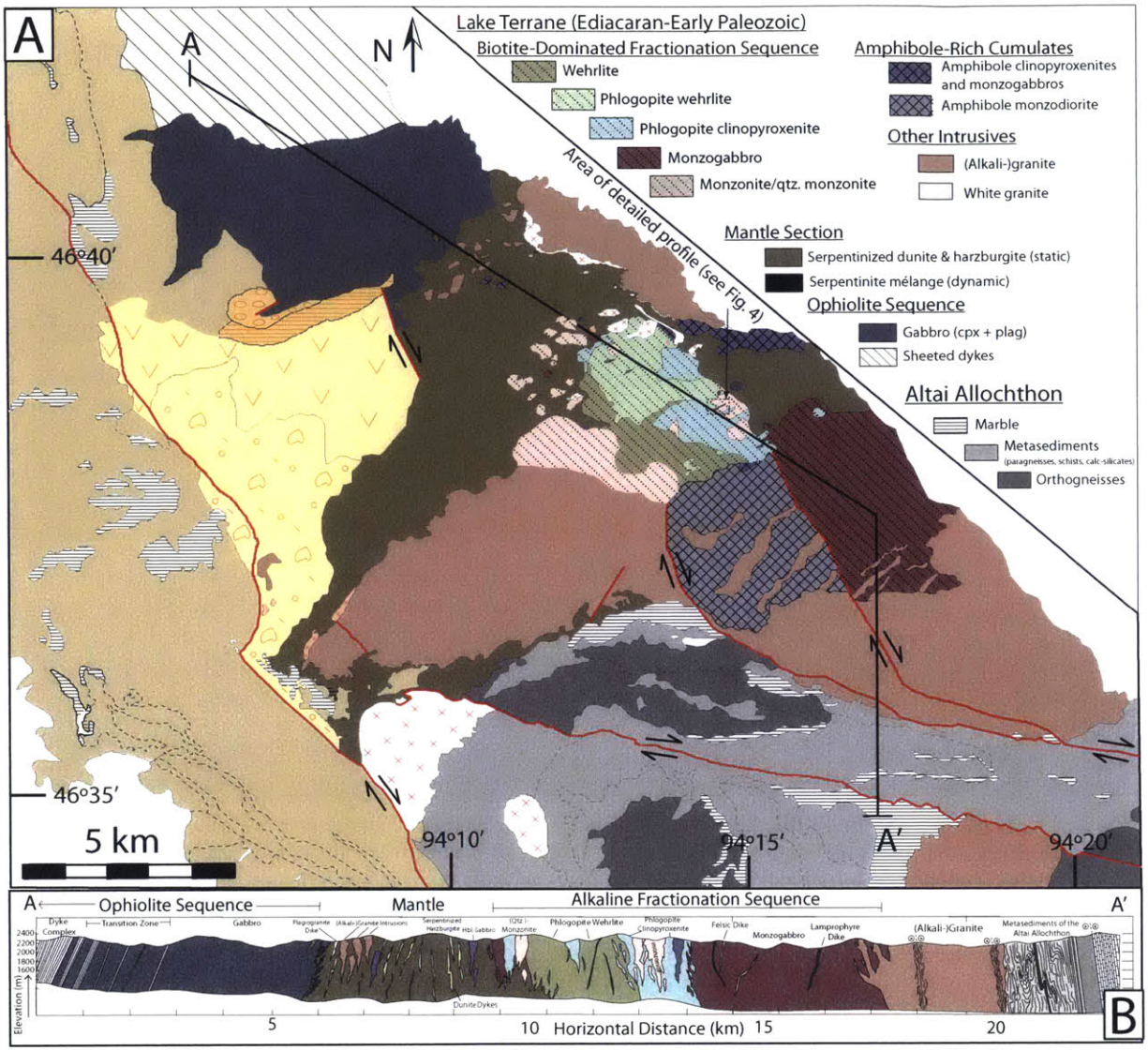

Fig. 2-2 (a) Geological map of detailed study area (see Fig. 2-1c for location) showing relationships between the Lake Terrane (the ophiolite sequence, the mantle section, the alkaline fractionation sequence, low grade metasediments), and the metamorphic Altai Allochthon. For legend with all lithologic units in the Dariv Range, see Fig. 2-1c. (b) Cross-section through Dariv Range showing the overall structure and relationship between various units. Profile location is indicated in Fig. 2-2a. Note that most contacts in this profile are of intrusive nature. The only two major faults are within the red (alkali-)granites.

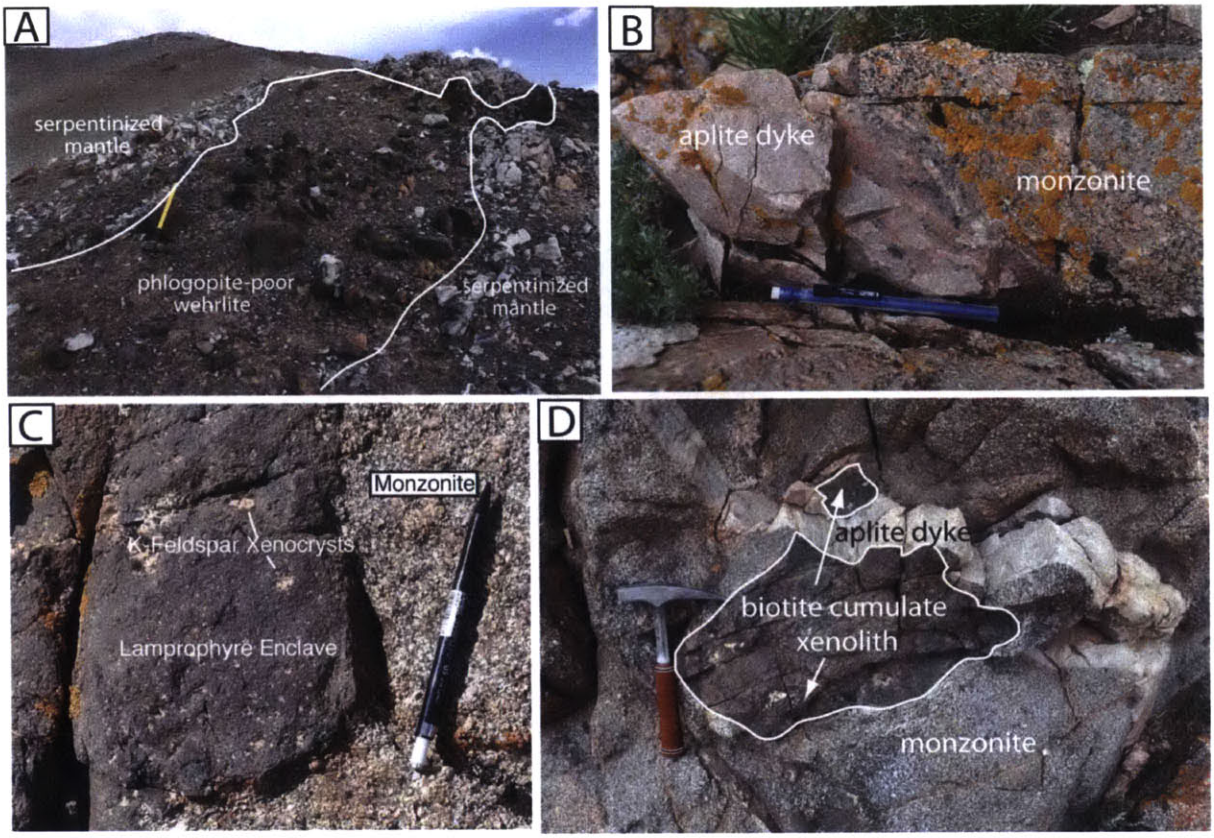

Fig. 2-3 Field photographs indicating field relationships. a) Intrusion of phlogopite-poor wehrlite in serpentinized mantle (sledgehammer is approximately 0.9 m long). b) Diffuse contact between monzonite and late stage aplite dike indicating comagmatic formation. Pencil is 15 cm long. c) Mafic dike inclusion (lamprophyre enclave) with K-feldspar xenocrysts in monzonite. Pencil is 13.5 cm long. d) Rounded biotite cumulate xenolith included in the monzonite, both of which are cross-cut by a late stage aplite dike. Rock hammer is 33 cm long.

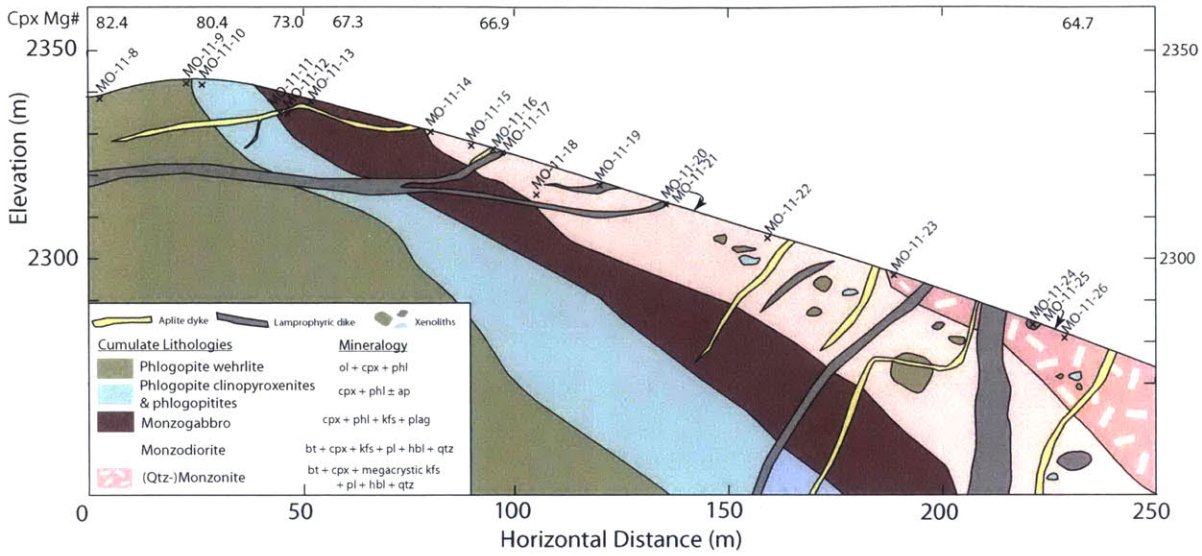

Fig. 2-4 Detailed cross-section across alkaline fractionation sequence. Clinopyroxene Mg#'s corresponding to distance along profile are given at top of figure. Lithologies become more evolved from left to right, starting with phlogopite wehrlites and grading into clinopyroxene-bearing monzonites. Contacts are drawn as sharp lines for clarity, but boundaries between lithologies are gradational. Profile location is indicated in Fig. 2-2a. Mineral abbreviations: ol – olivine, cpx – clinopyroxene, phl – phlogopite, ap – apatite, bt – biotite, ksp – K-feldspar, pl – plagioclase, hbl – hornblende, qtz – quartz.

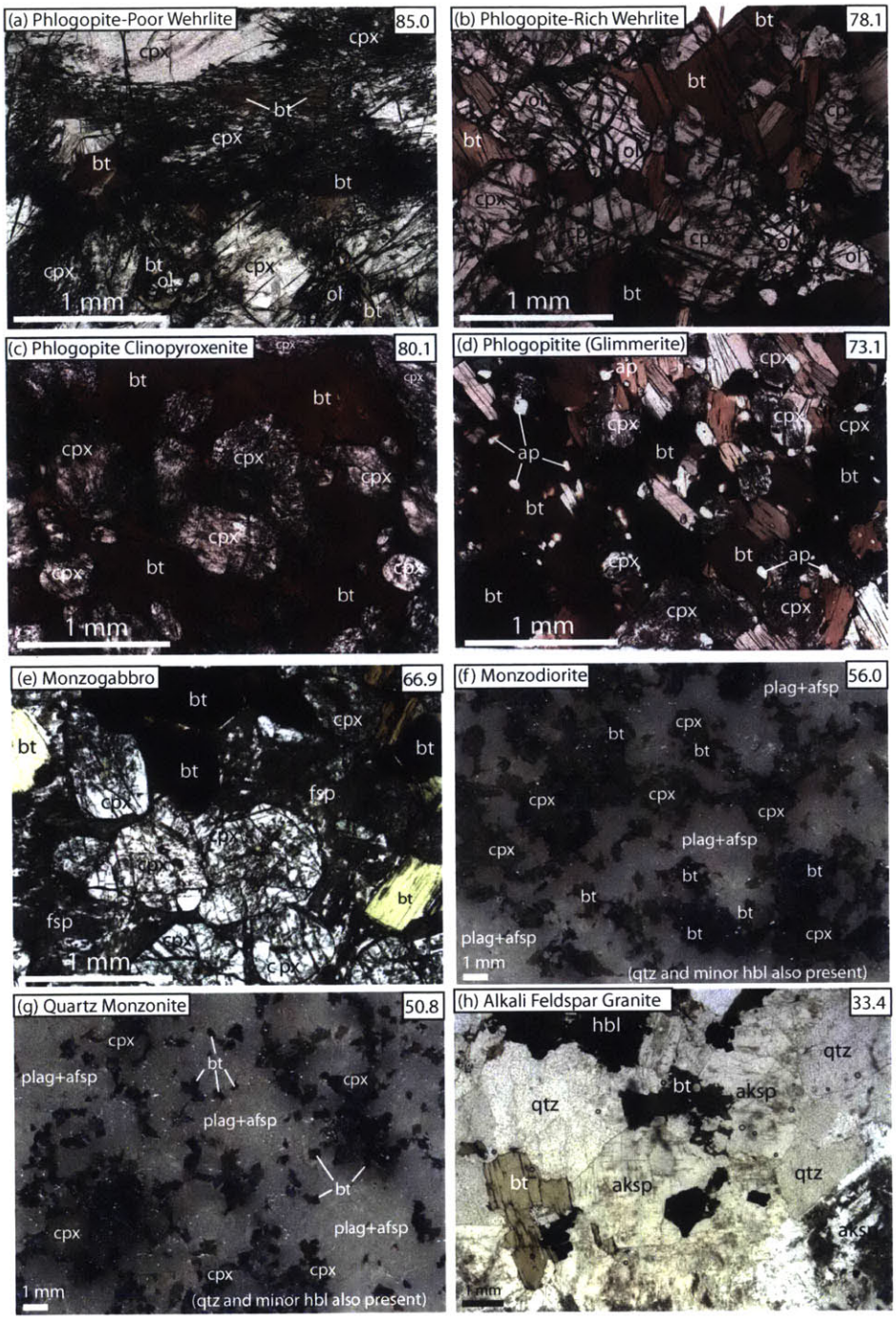

Fig. 2-5 Representative photomicrographs illustrating the studied fractionation sequence. Whole rock Mg# (unpublished data) are plotted in the upper right corners of the images. a, b, d, e, & h were taken in plane-polarized light, c was taken in cross polarized, and f & g are scanned thin section images. All thin sections except h (the alkali-feldspar granite) are 100 μm thick. Mineral abbreviations are as in Fig. 2-4. a) Phlogopite wehrlite (MO-10-394) with minor phlogopite. Olivine shows irregular margins surrounded by phlogopite, reflecting reaction and consumption of primary olivine to form phlogopite. b) Phlogopite-rich wehrlite (MO-10-392) with increased modal percent of biotite. c) Phlogopite clinopyoxenite (MO-10-325) with interstitial biotite poikilitically enclosing subhedral clinopyroxenes. d) Clinopyroxene phlogopitite (glimmerite) (MO-11-10) with abundant and large apatite crystals. e) Biotite monzogabbro (MO-11-12) with biotite, clinopyroxene, and feldspar. f) Quartz-bearing monzodiorite (MO-11-14). g) Quartz monzonite (MO-11-26), notably clinopyroxene is still a fractionating phase. h) Red (alkali-)granite (MO-9-239).

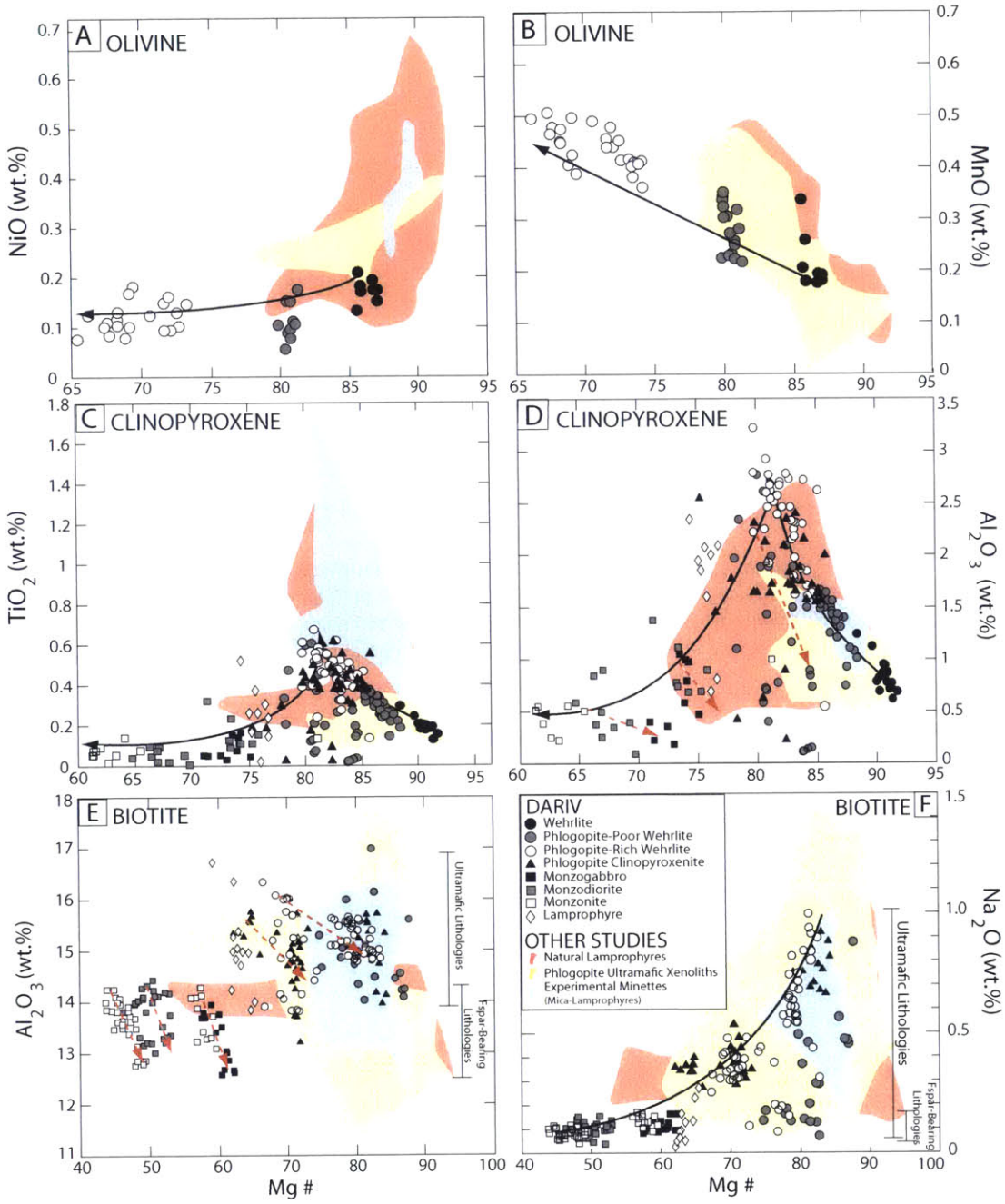

Fig. 2-6 Summary of individual analyses of olivine, clinopyroxene, and biotite major element compositions versus Mg#. Averages for samples are reported in Appendix B. Fields from other studies are based on data from lamprophyres (Allan and Carmichael, 1984; Carmichael *et al.*, 1996; Wallace & Carmichael, 1989; Carlier *et al.*, 1997; Luhr & Carmichael, 1981; Buhlmann *et al.*, 2000, Righter & Rosas-Elguera, 2001; Prelevic *et al.*, 2004; Maria & Luhr, 2008; van Bergen *et al.*, 1983), phlogopite-bearing dunite and wehrlite xenoliths (Downes *et al.*, 2004; Buhlmann *et al.*, 2000; Gianetti & Luhr, 1990; Aoki & Kushiro, 1968; Cid *et al.*, 2003) and experimentally crystallized minettes (Esperanca & Holloway, (1987); Righter & Carmichael, (1996)). Solid black lines with arrow represents the average igneous trend determined from core compositions. In (d) and (e) the trend for metamorphic Tschermak exchange $(Fe,Mg)_2Si_{-1}Al_{-1}$ during cooling is shown by dashed red arrows. (a) Olivine NiO. (b) Olivine MnO. (c) Clinopyroxene TiO_2. There is no systematic variation between cores and rims, rather TiO_2 concentrations appear to be related to local equilibration with Fe-Ti oxide. (d) Clinopyroxene Al_2O_3. (e) Biotite Al_2O_3. b) Biotite Na_2O.

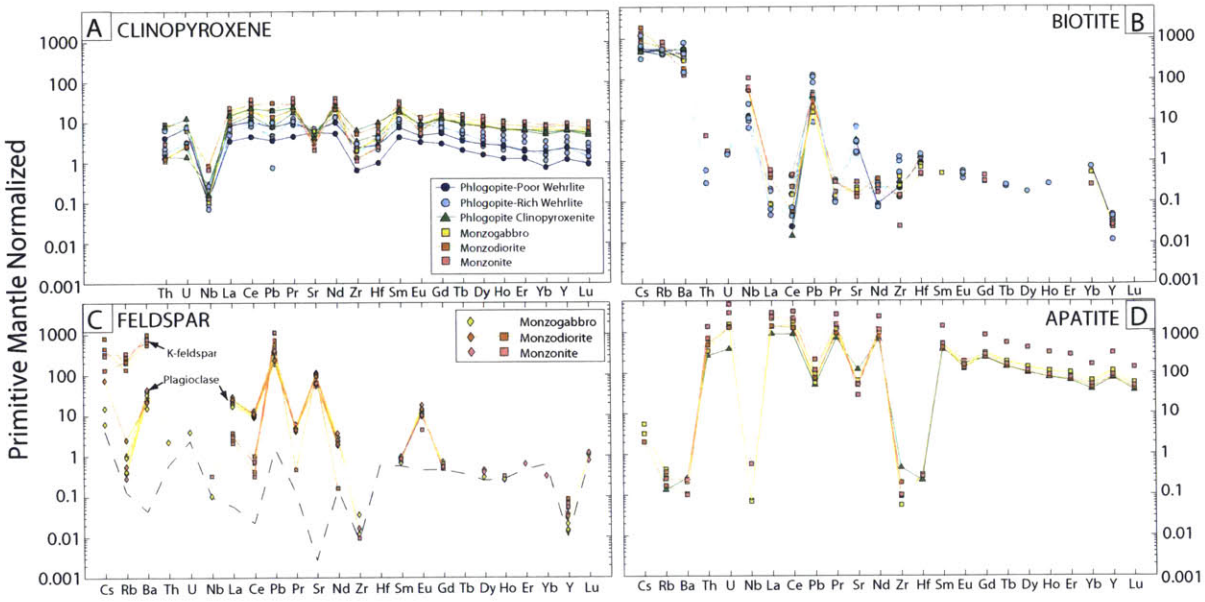

Fig. 2-7 Average mineral trace element compositions normalized to primitive mantle (Sun & McDonough, 1989). 2σ inter-mineral variance of single samples are reported in Appendix B. a) Clinopyroxene cores. Legend given in (a) applies to b and d, as well. b) Biotite. c) Feldspar from monzogabbros, monzodiorites, and monzonites. K-feldspar data is shown in squares, plagioclase in diamonds. The lower dashed line indicated the LA-ICP-MS detection limit. d) Apatite.

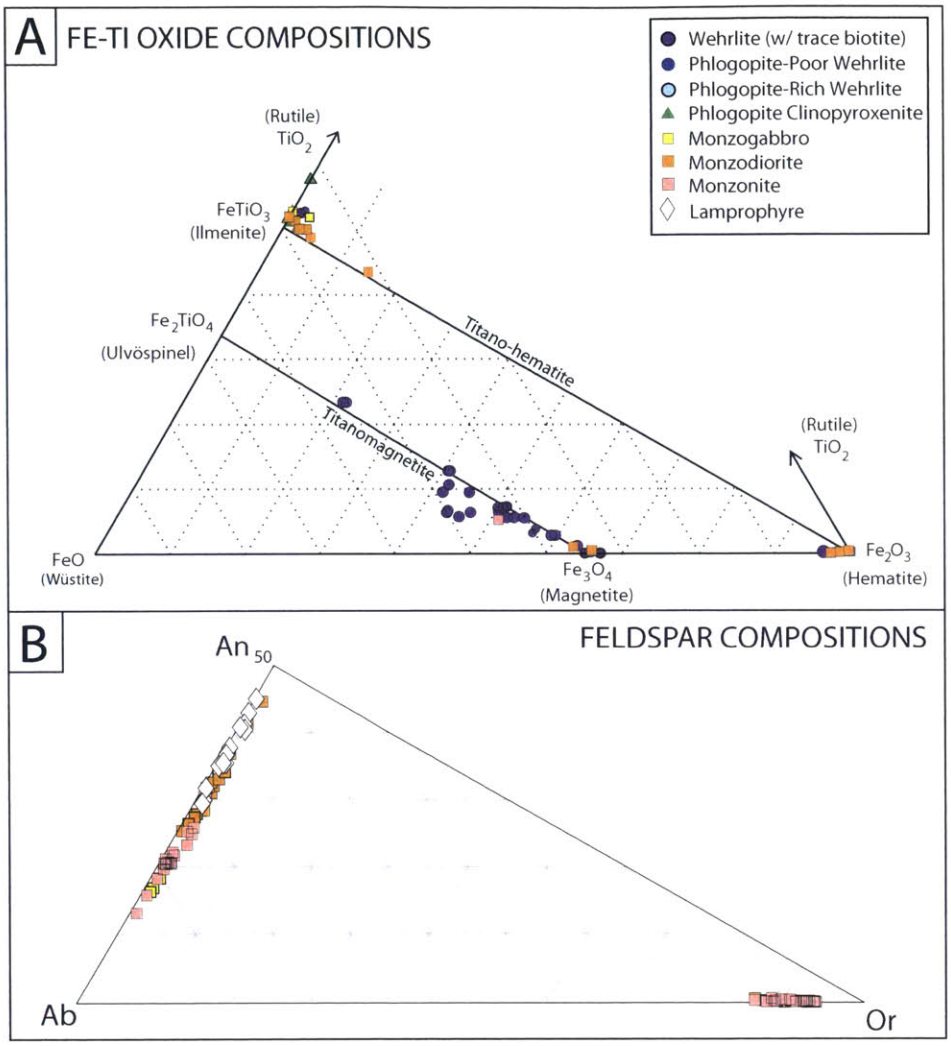

Fig. 2-8 (a) Individual analyses of Fe-Ti oxides on the FeO-TiO_2-Fe_2O_3 ternary. (b) Individual analyses of plagioclase and alkali-feldspar on an An-Ab-Or ternary diagram. Average feldspar compositions are reported in Appendix B.

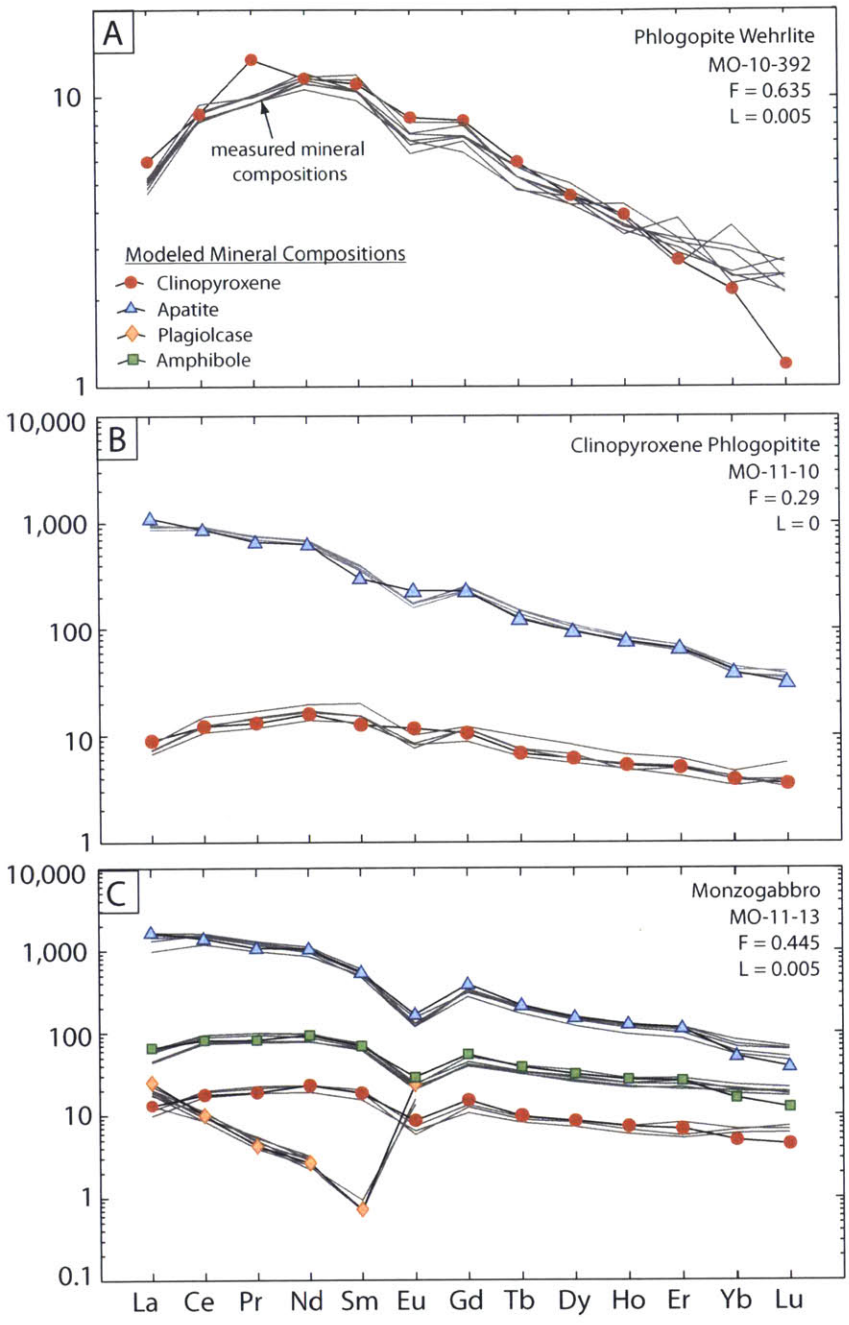

Fig. 2-9 Primitive mantle normalized (Sun & McDonough, 1989) results from in-situ crystallization modeling following the approach of Hermann et al., (2001). Partition coefficients for clinopyroxene-melt were predominantly from Foley et al., (1996), however for several elements partition coefficients were taken from different studies (Nb, Pb, & Hf from Hart & Dunn, 1993; Th, U from Villemant et al., 1981) Apatite-melt partition coefficients are from Watson & Green (1981). Modeling results suggest that fractional crystallization was the dominant mechanism and that essentially no interstitial liquid re-equilibrated with the clinopyroxene or apatite. Black filled symbols are the modeled mineral compositions and gray lines are actual mineral analyses. Results from the modeling of three samples are shown. a) Sample MO-10-392. Trace elements in clinopyroxene can be best explained 63% differentiation of a primitive alkaline melt. b) Sample MO-11-10 modeled with 29% differentiation of a melt in equilibrium with the most evolved phlogopite wehrlite with no modal apatite (i.e. the composition of the melt immediately before the onset of apatite fractionation.) c) A monzogabbro (MO-11-13) modeled with 44.5% differentiation, again starting from a more evolved melt composition as described in b.

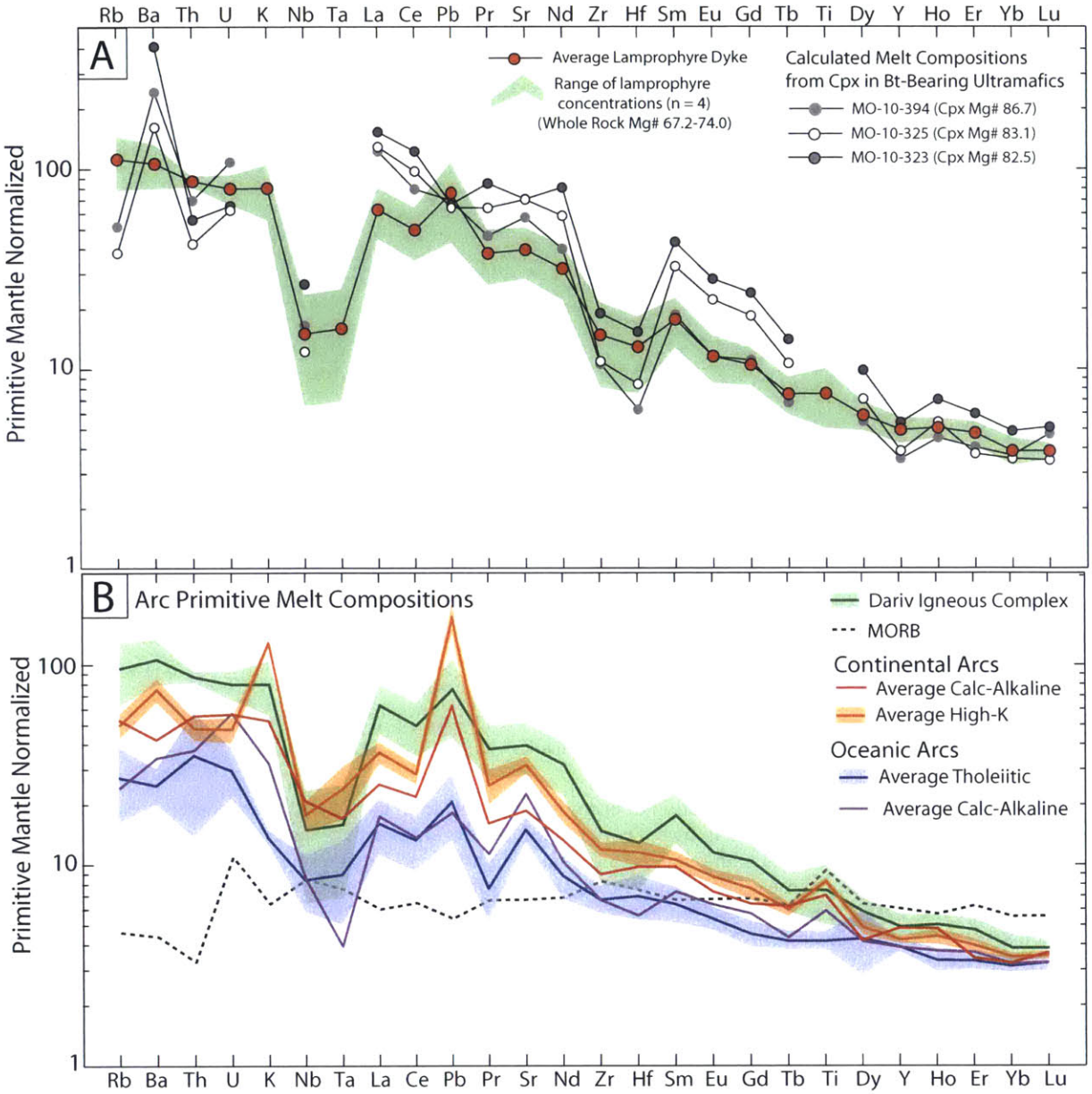

Fig. 2-10 Trace element composition of the estimated Dariv primitive melt. a) Average trace element concentration of melts calculated in equilibrium with clinopyroxenes from the three most primitive cumulate samples (Mg# of the clinopyroxene is given in parentheses), compared to the trace element composition of the four most primitive lamprophyre dikes (Table 3). (See Fig. 2-9 for a compilation of partition coefficients used) . b) Spider diagram for average compositions of MORB, primitive arc melts, and the primitive melt compositions from Dariv normalized to primitive mantle (Sun & McDonough, 1989). Average compositions of various continental and oceanic arcs are from the compilation described in text. Melts were characterized as low-K, calc-alkaline, high-K, or shoshonitic based on their K_2O contents using the classification of Pecerillo & Taylor (1976). Average MORB composition is from Kelemen et al., (2003). Solid line for each group indicates average. Shaded areas given for the Dariv primitive melts indicates the total range of analyzed compositions. Shaded areas for the average high-K continental arc and average tholeiitc oceanic arc show the $2\sigma_{SE}$ on averages. Other $2\sigma_{SE}$ ranges are omitted for clarity.

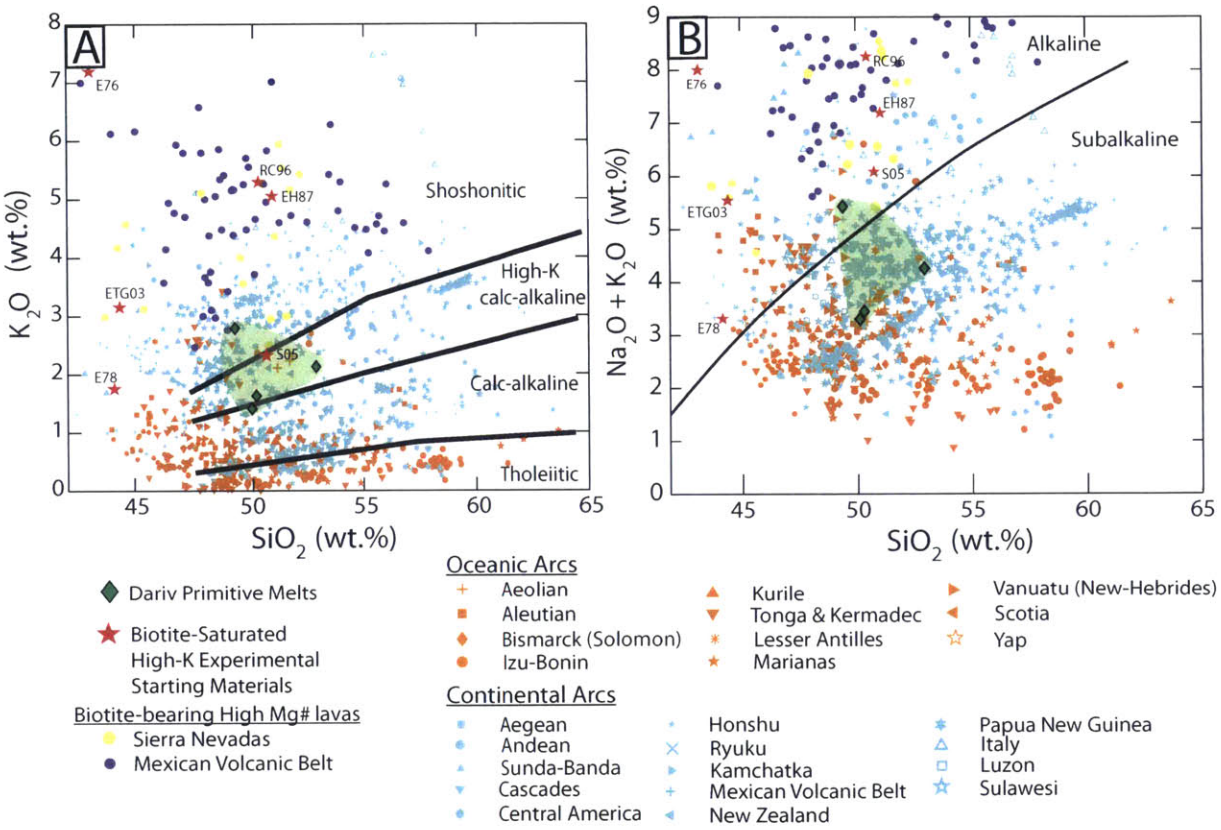

Fig. 2-11 Major element data for compilation of primitive arc melts from the GEOROC database. Oceanic arcs are denoted in orange and continental arcs in blue. Dariv primitive melts are shown as dark green diamonds and their compositional range is represented with light green shading. High-K experimental starting materials where biotite was found as a crystallizing phase are indicated by red stars and the following labels. (**E76:** Edgar et al., 1976; **E78**: Edgar et al., 1978; **EH87**: Esperanca and Holloway, 1987; **RC96**: Righter & Carmichael, 1996; **ETG03**: Elkins-Tanton & Grove, 2003; **S05**: Sisson et al., 2005) (a) K_2O v. SiO_2 with boundaries following (Peccerillo & Taylor, 1976), (b) TAS diagram (Irvine & Baragar, 1976). Biotite-bearing high Mg# (>60) lavas are from the Sierra Nevadas (yellow circles) (Van Kooten, 1980) and the Western Mexican Volcanic Belt (purple circles) (Allan & Carmichael (1984), Luhr & Carmichael (1981), Luhr et al. (1989), Wallace & Carmichael (1989), Carmichael et al. (1996), Righter & Carmichael (2001); Maria et al., (2008); Maria & Luhr (2008), Ownby et al. (2008), Vigouroux et al. (2008)).

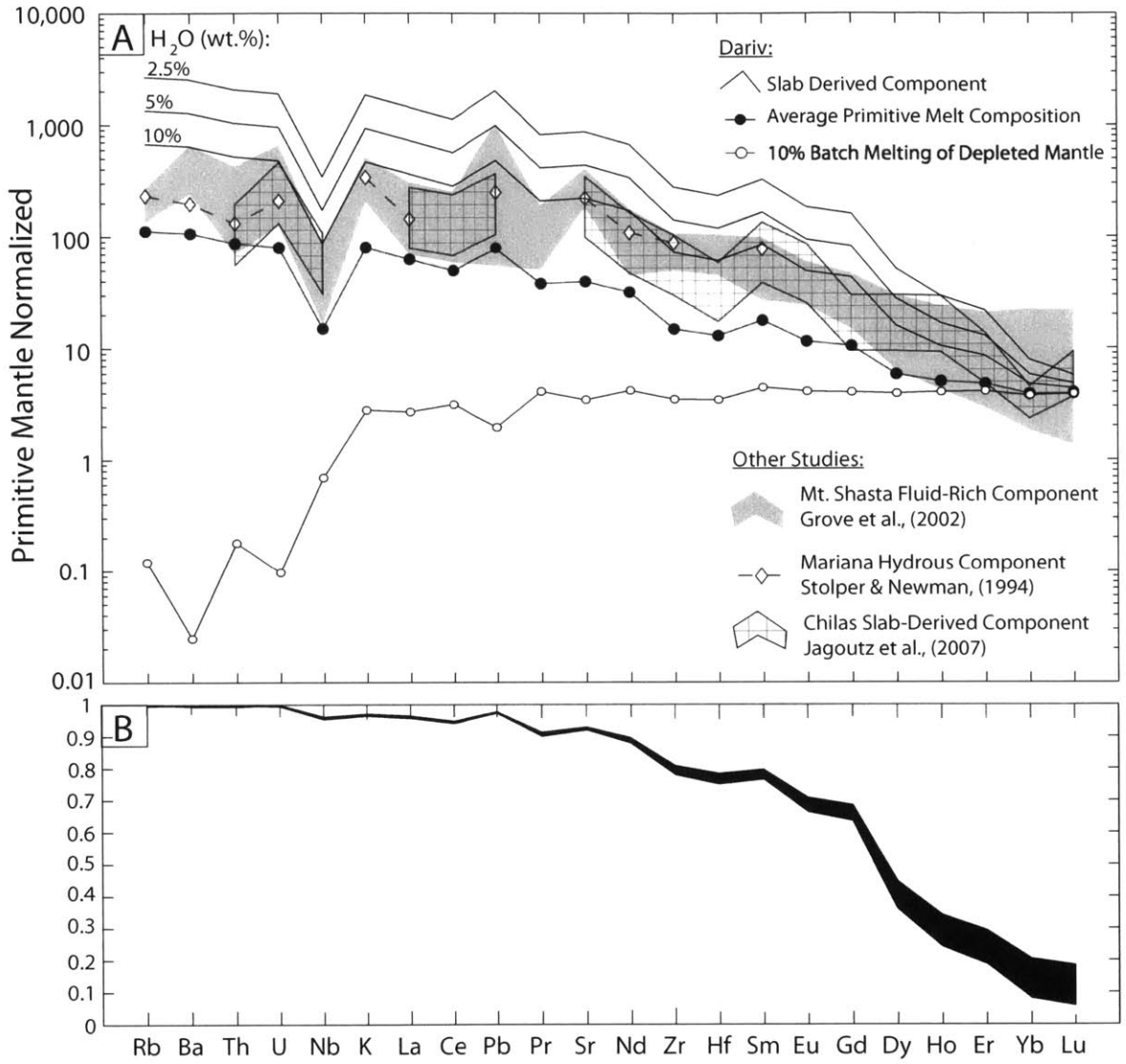

Fig. 2-12 Results from slab-component modeling. a) Primitive mantle normalized trace element diagram comparing the average Dariv parental melt composition (from whole rock analyses of syn-magmatic primitive mafic dikes), the calculated Dariv slab-derived component, the result of ~10% batch melting from a depleted source, and estimated slab-derived components from other arcs and paleo-arcs. Calculations of the slab-derived component are shown for 2.5, 5, and 10% X_{H_2O}. See text for further discussion. b) Fractional contribution of slab-derived component to the total primitive melt budget of individual trace elements.

2.10 Tables

Table 2-1: Summary of Analyzed Samples with GPS Locations and Modal Proportions of Minerals[1]

Sample #	Rock Type	GPS Location		Modal Proportion (%)						
		Longitude (E)	Latitude (N)	ol	cpx	bt	pl/ksp	amph	qtz	Accessory
MO-10-396	Phlog. Wehrlite	94°13'14"	46°38'59.1"	30	70	<2	-	-	-	
MO-10-394	Phlog. Wehrlite	94°13'50.8"	46°39'19.2	20	75	5	-	-	-	
MO-10-322	Phlog. Wehrlite	94°12'6"	46°40'17.9"	20	50	30	-	-	-	
MO-9-248	Phlog. Wehrlite	94°15'17.6"	46°38'57.7"	15	60	25	-	-	-	Ap
MO-10-385	Phlog. Wehrlite	94°14'30"	46°39'22.4"	15	70	15	-	-	-	
MO-10-392	Phlog. Wehrlite	94°14'18.9"	46°39'19.6"	15	45	40	-	-	-	
MO-10-323	Phlog. Wehrlite	94°12'6"	46°40'17.9"	10	45	45	-	-	-	
MO-11-8	Phlog. Wehrlite	94°14'25.2"	46°39'10.2"	10	85	5	-	-	-	Cr-Spl, Mag, Usp
MO-10-325	Phlog. Cpxenite	94°12'6"	46°40'17.9"	-	70	30	-	-	-	Spn
MO-10-324	Phlog. Cpxenite	94°12'6"	46°40'17.9"	-	70	20	5/0	-	-	Spn, Ap, Zrn
MO-11-9	Phlog. Wehrlite	94°14'25.7"	46°39'10.8"	-	80	20	-	-	-	Ap, Mag, Usp
MO-11-10	Phlogopitite	94°14'25.9	46°39'10.8"	-	20	75	-	-	-	Ap (5%), Mag, Usp
MO-11-12	Monzogabbro	94°14'26.7"	46°39'10.7"	-	35	30	30	-	-	Ap, Zrn, Spn
MO-11-13	Monzogabbro	94°14'26.9"	46°39'11"	-	25	30	45	-	-	Ap, Zrn, Spn
MO-11-14	Monzodiorite	94°14'28.1"	46°39'11.2"	-	10	15	25/30	10	10	Ap, Hem, Ilm
MO-11-15	Monzodiorite	94°14'28.7"	46°39'11.2"	-	~5	15	30/30	15	10	Ap
MO-11-21	Monzonite	94°14'30.7"	46°39'12.1"	-	~5	15	30/20	15	15	Ap
MO-11-23	Monzonite	94°14'32.9"	46°39'12.4"	-	~5	10	40/20	10	15	Ap
MO-11-26	Qtz. Monzonite	94°14'34.6"	46°39.13.1"	-	~5	10	40/20	5	20	Spn
MO-10-386	Qtz. Monzonite	94°14'27"	46°39'18.9"	-	~5	15	40/20	10	15	Ap, Spn, Zrn
MO-11-19	Lamprophyre	94°14'29.8"	46°39'11.7"	-	25	30	45	-	-	Ap, Zrn, Hem

[1] Modal compositions have been approximated by a combination of thin section observation and image analysis.

Table 2-2: Temperature, pressure and oxygen fugacity calculated using different thermobarometers & oxygen barometers.

	TEMPERATURE (°C)			**PRESSURE (GPa)**	**fO_2 (ΔFMQ)**	
	Clinopyroxene-Only Thermometer	*Amphibole-Plagioclase Thermometer*	*Two Feldspar Thermometry*	*Al-in-hornblende barometer*	*Olivine-Spinel Oxygen Barometer*	*V in Cpx*
Reference: **SAMPLE**	Putirka (2008) eq. 32d[a]	Holland & Blundy (1994)[b]	Putirka (2008), Eq. 27b[c]	Schmidt (1992)	Ballhaus et al. (1991)	Canil & Fedortchouk (2000)
MO-10-396	1206 ± 2 (n = 16)	-	-	-	-	-
MO-10-394	1195 ± 4 (n = 4)	-	-	-	3.90 ± 0.02 (n=11)	1.97 ± 0.37 (n = 4)
MO-10-385	1122 ± 27 (n = 2)	-	-	-	3.11 ± 0.01 (n = 9)	-
MO-10-392	1157 ± 16 (n = 8)	-	-	-	-	-
MO-10-323	1162 ± 4 (n = 10)	-	-	-	2.91 ± 0.16 (n = 7)	-
MO-11-8	1135 ± 24 (n = 3)	-	-	-	2.84± 0.21 (n = 7)	-
MO-11-9	1184 ± 5 (n = 6)	-	-	-	2.60	-
MO-10-325	1091 ± 37 (n = 10)	-	-	-	-	-
MO-10-324	1137 ± 20 (n = 8)	-	-	-	-	-
MO-11-10	1158 ± 12 (n = 4)	-	-	-	-	-
MO-11-12	1110 ± 23 (n = 5)	-	510-558	-	-	-
MO-11-13	1122 ± 12 (n = 3)	-	535-612	-	-	-
MO-11-14	-	693	546-648	0.152 ± 0.08 (n = 3)	-	-
MO-11-15	-	726	514-583	0.208 ± 0.05 (n = 5)	-	-
MO-11-21	-	702	528-548	0.199 ± 0.10 (n = 4)	-	-
MO-11-23	-	642	474-564	0.244 ± 0.05 (n = 3)	-	-
MO-11-26	-	682	474-533	0.154 ± 0.02 (n = 2)	-	-
MO-10-386	-	703	451-576	0.336 ±0.02 (n = 8)	-	-

Errors are give as $2\sigma_{SE}$ variation on averages of individual analyses.
[a] Calculated at 0.5 GPa for ultramafics and 0.3 GPa for feldspar bearing lithologies.
[b] Calculated at pressure of Al-in-hornblende of Schmidt (1992)
[c] Calcualted at 0.3 GPa. Given ranges are the maximum calculated using various combinations of $1\sigma_{SD}$ variations of average plagioclase and alkali-feldspar compositions.

Table 2-3: Primitive Dike Compositions[a]

Sample #	MO-11-19	MO-9-228	MO-9-230	MO-9-263	Average	$2\sigma_{SD}$
SiO_2	48.69	52.92	50.29	50.10	50.50	3.53
TiO_2	1.25	0.79	0.61	1.23	0.97	0.64
Al_2O_3	14.09	13.96	14.17	12.68	13.73	1.40
FeO	8.34	6.83	7.48	8.38	7.76	1.49
MnO	0.17	0.18	0.19	0.18	0.18	0.02
MgO	9.60	10.51	11.92	12.01	11.01	2.33
CaO	9.45	9.39	10.63	10.48	9.99	1.32
Na_2O	2.60	2.13	1.82	1.89	2.11	0.70
K_2O	2.76	2.13	1.63	1.41	1.98	1.19
P_2O_5	0.66	0.26	0.25	0.53	0.43	0.40
SrO	-	0.08	0.09	0.10	0.09	0.02
BaO	-	0.06	0.08	0.07	0.07	0.02
L.O.I.	1.49	-	-	-	-	-
Total	99.10	99.24	99.17	99.07	99.14	0.16
Mg#	67.24	73.28	73.96	71.87	71.59	6.05
Sc	22.8	23.9	29.3	25.6	25.4	5.7
V	197	132	188	152	167	60
Cr	520	643	642	643	612	122
Co	32.0	31.8	37.8	42.1	35.9	9.9
Ni	144	166	171	277	189	120
Cu	16.9	3.18	13.7	39.9	18.4	30.9
Zn	66.9	57.5	64.1	62.1	62.6	7.9
Rb	75.6	76.5	61.8	30.6	61.1	42.9
Sr	1181	614	772	785	838	483
Y	26.1	19.6	19.6	24.8	22.5	6.8
Zr	264	125	89.9	188	167	153
Nb	16.3	8.32	3.25	15.2	10.8	12.2
Sn	2.14	2.52	9.42	9.59	5.92	8.28
Cs	1.39	1.76	2.34	0.749	1.56	1.34
Ba	1007	561	729	684	745	377
La	59.0	29.8	38.3	45.8	43.2	24.8
Ce	124	62.0	77.0	90.7	88.4	53
Pr	14.8	7.14	9.06	11.1	10.5	6.5
Nd	59.9	28.3	38.9	45.6	43.2	26.5
Sm	10.5	5.25	7.18	8.59	7.89	4.5
Eu	2.64	1.40	1.76	1.98	1.94	1.04
Gd	7.74	4.68	5.68	6.93	6.26	2.70
Tb	1.03	0.63	0.72	0.86	0.81	0.35
Dy	5.11	3.59	3.84	4.77	4.33	1.46
Ho	0.928	0.739	0.761	0.902	0.833	0.192
Er	2.22	2.19	2.03	2.74	2.30	0.62
Tm	0.298	0.237	0.312	0.330	0.294	0.081
Yb	2.01	1.52	1.87	2.26	1.91	0.62
Lu	0.312	0.256	0.274	0.307	0.287	0.054
Hf	6.04	3.27	2.13	4.55	4.00	3.36
Ta	0.988	0.529	0.185	0.928	0.658	0.750
Pb	7.86	4.86	2.39	6.52	5.41	4.71
Th	7.48	7.44	7.93	6.75	7.40	0.97
U	1.89	1.82	1.75	1.26	1.68	0.57

[a]Major elements oxides are given wt.%. Trace elements are given in ppm.

CHAPTER 3:
Fractional Crystallization of High-K Arc Magmas

Abstract

Many studies have documented hydrous fractionation of calc-alkaline basalts producing tonalitic, granodioritic, and granitic melts, but the origin of more alkaline arc-sequences dominated by high-K monzonitic suites has not been thoroughly investigated. This chapter presents results from a combined field, petrologic, and whole rock geochemical study of a paleo-arc alkaline fractionation sequence from the Dariv Range of the Mongolian Altaids. The Dariv Igneous Complex of Western Mongolia is composed of a complete, moderately hydrous, alkaline fractionation sequence ranging from phlogopite-bearing ultramafic and mafic cumulates to quartz-monzonites to late-stage felsic (63-75 wt.% SiO_2) dikes. A volumetrically subordinate more hydrous, amphibole-dominated fractionation sequence is also present and comprises amphibole(±phlogopite) clinopyroxenites, gabbros, and diorites. We present 167 whole rock analyses for the biotite- and amphibole-dominated series. First, we constrain the liquid line of descent (LLD) of a primitive, alkaline arc melt characterized by biotite as the dominant hydrous phase through a fractionation model that incorporates the stepwise subtraction of cumulates of a fixed composition. The modeled LLD reproduces the geochemical trends observed in the 'liquid'-like intrusives of the biotite series (quartz monzonites and felsic dikes) and follows the water-undersaturated albite-orthoclase cotectic (at 0.2-0.5 GPa). Second, as distinct biotite- and amphibole-dominated fractionation series are observed, we investigate the controls on high temperature biotite versus amphibole crystallization from hydrous arc melts. Analysis of a compilation of hydrous experimental starting materials and high-Mg basalts saturated in biotite and/or amphibole suggests that the degree of K-enrichment controls whether biotite will crystallize as an early high-T phase, whereas the degree of water saturation is the dominant control of amphibole crystallization. Therefore, if a melt has the appropriate major element composition for early biotite and amphibole crystallization, as is true of the high-Mg basalts from the Dariv Igneous Complex, the relative proximity of these two phases to the liquidus depends on the H_2O-concentration in the melt. Third, we compare the modeled LLD and whole rock geochemistry of the Dariv Igneous Complex to the more common calc-alkaline trend. Biotite and K-feldspar fractionation in the alkaline arc series results in the moderation of K_2O/Na_2O values and LILE concentrations with increasing SiO_2 as compared to the more common calc-alkaline series characterized by amphibole and plagioclase crystallization and strong increases in K_2O/Na_2O values. Lastly, we suggest that common calc-alkaline parental melts involve addition of a moderate pressure, sodic, fluid-dominated slab component while more alkaline primitive melts characterized by early biotite saturation involve the addition of a high pressure potassic sediment melt.

3.1 Introduction

Based on trace element similarities, it is well established that subduction-related magmatism is essential for the production of continental crust (CC). Understanding how primitive arc basalts evolve and form continental crust of an andesitic bulk composition, with granitic rocks dominating the upper CC, has been the focus of much research (Jagoutz and Schmidt 2012; 2013; Jagoutz 2010; Lee et al. 2007; Müntener and Ulmer 2006; Sisson et al. 2005). In general, two end member models have been proposed to produce silica-rich derivative liquids: (1) partial melting in the lower continental crust and (2) hydrous fractionation of Si-poor cumulates. Differentiating between these two end-member processes by only studying granites (or the residual/derivative liquids) is difficult as large degrees of fractional crystallization or small amounts of partial melting of basalt produce liquids of similar compositions. Indeed, Tuttle and Bowen (1958) lamented, "Field studies of granites deal with the end products of processes long since completed, and the most detailed mapping and study of these products may fail to give convincing evidence concerning the exact nature of the processes responsible for the relations." Since Tuttle and Bowen's early experimental work on granite genesis, however, several key field localities have been identified where relationships between cumulates/restites and derivative liquids have been observed. For primitive calc-alkaline magmas the importance of hydrous fractionation has been documented through careful study and analysis of preserved lower crustal paleo-arc sections of Kohistan (Pakistan) and Talkeetna (Alaska) (DeBari and Greene 2011; Greene et al. 2006; Jagoutz et al. 2011; Jagoutz 2010). In addition, experimental work on primitive basaltic melts have supported the evidence from the field (Grove et al. 2003; Müntener et al. 2001; Sisson and Grove 1993), indicating that in order to produce tonalites, granodiorites, and granites from primitive calc-alkaline basalts, cumulates dominated by SiO_2-poor minerals such as amphibole, garnet, oxides, or An-rich plagioclase must fractionate from the melt.

Although volumetrically less significant than calc-alkaline batholiths, the monzonitic series (monzodiorites, monzonites, and quartz monzonites) characterized by elevated total alkali contents at a given SiO_2 content, are widely present in arcs (e.g., Miller 1977; Miller 1978; Rapela and Pankhurst 1996; Sylvester et al. 1978). Due to their high Na_2O+K_2O and LILE contents, they may constitute significant contributors to the incompatible element budget of the continental crust. Nevertheless, the origin of this monzonitic series has only been investigated in the field to a limited extent. Several field studies on high-K granitoids have suggested that biotite- and clinopyroxene-dominated fractionation from high-K primitive melts is capable of producing these derivative granitic liquids (Fowler and Henney 1996; Fowler et al. 2001; Lobach-Zhuchenko et al. 2008). However, these studies lack exposure of high-K ultramafic and mafic cumulates in significant enough quantities to substantiate the volumes required by their fractionation models. The only other field evidence for biotite+clinopyroxene fractionation from high-K primitive melts comes from the fragmentary evidence provided by phlogopite-bearing ultramafic cumulate xenoliths in high-K volcanics (Buhlmann et al. 2000; Downes et al. 2004; Giannetti and Luhr 1990).

Here, we present whole rock geochemical data for the recently discovered Dariv Igneous Complex (~50 km^2) in Western Mongolia, which is comprised of two distinct alkaline fractionation sequences. The first is a complete, moderately hydrous alkaline fractionation sequence ranging from phlogopite-rich ultramafic (wehrlites and clinopyroxenites) and biotite-rich mafic (monzogabbros and monzodiorites) cumulates through quartz-monzonites. The second, more incomplete sequence is comprised of isolated patches of amphibole(±phlogopite)-clinopyroxenites and stocks to km-sized intrusions of amphibole-bearing monzogabbros and (quartz-)monzonites. Through LLD modeling we show that evolved quartz-monzonites and felsic dikes associated with the biotite-dominated sequence can be produced through fractionation of the observed biotite-dominated cumulates from a primitive alkali-rich basalt. In light of the two fractionation sequences observed in Dariv (i.e., with early biotite versus amphibole saturation, respectively), we discuss the potential controls on high temperature amphibole and biotite crystallization in alkaline magmas with a particular emphasis on bulk magma chemistry and water content and highlight the effects of amphibole versus biotite crystallization on the fractionated melt chemistry. We then discuss the different subduction components influencing the mantle wedge and contributing to arc-related calc-alkaline versus high-K parental melts. The whole rock geochemistry and the modeled LLD are discussed in terms of the phase relationships in the quartz-K-feldspar-albite ternary and geochemical trends are compared to the more commonly studied calc-alkaline series.

3.2 Field Relationships and Petrography

Field relationships observed over four summers of fieldwork are described in detail in Chapter 2, to which the reader is referred to for the field geology, including field photographs. We briefly present the salient features of the alkaline igneous complex of the northwestern part of the Dariv Range (Fig. 3-1b).

A ~3.5 km wide ultramafic cumulate sequence is located within the central southern part of a 15 x 10 km serpentinized harzburgite/dunite body. The ultramafic cumulates are dominated by biotite-bearing lithologies, however there are minor volumes of amphibole(±biotite)-bearing ultramafic cumulates, which are described in more detail below. The contact between the serpentinite and the cumulate sequence is marked by numerous small intrusions that cut into the serpentinite and are composed of cumulate minerals. A broadly systematic lithological variation is observed from northwest to southeast (Fig. 3-1c). Primitive wehrlites characterized by bright green Cr-diopside with minor phlogopite grade into biotite-dominated wehrlites and phlogopite-rich clinopyroxenites and biotite monzogabbros. Monzodiorite to quartz monzonite bodies are also present, sometime occurring as individual stocks cross-cutting other cumulate lithologies and other times gradually transitioning into the monzogabbros. Late stage 10-100 cm wide K-feldspar-rich felsic dikes and biotite-bearing basaltic dikes cross cut the cumulate sequence. Diffuse margins between the felsic dikes and monzonites indicate a comagmatic origin, whereas the margins of mafic dikes are sharply defined. Xenoliths of biotite cumulates and basaltic dikes are common in the monzonites. The serpentinite and both alkaline sequences are intruded by small (10-100 m in

diameter) vertically oriented stocks and several large (up to 8 x 5 km wide) intrusions of alkali-feldspar-porphyric granite (Fig. 3-1b,c). Unpublished U-Pb zircon ages indicate that these (alkali-)granites are significantly younger than the alkaline complex and are neither cogenetic nor contemporaneous with the biotite-dominated lithologies. For this reason, we do not discuss them further.

The plutonic rocks with biotite as the dominant mafic, hydrous mineral comprise a common cumulate sequence resulting from a single LLD (Chapter 2) and can be ascribed to a fractionation sequence defined by olivine + clinopyroxene ± Fe-Ti oxides → biotite + apatite → K-feldspar + plagioclase → amphibole + quartz. These rocks are generally very fresh and only clinopyroxene exhibits occasional alteration to actinolitic amphibole, particularly in the evolved rocks. None of the samples exhibit field or microstructural evidence of deformation.

The second sequence of alkaline cumulates, with amphibole as the primary hydrous mineral, is comprised of amphibole±biotite clinopyroxenites, hornblendites, amphibole-monzogabbros, -monzodiorites, and -monzonites which intrude both the biotite-dominated sequence and the serpentinite. The ultramafic cumulates occur as isolated outcrops or as centimeter- to meter-scale intrusions in the serpentinite each with variable modal abundances of constituent minerals. The feldspar-bearing lithologies are generally found as isolated stocks to km-scale intrusions intruding both the serpentinite and the biotite-dominated cumulate sequence (Fig. 3-1b,c). Monzodiorites and monzonites with amphiboles aligned due to magmatic flow are the predominant lithologies. These bodies are cross-cut by K-feldspar- and plagioclase-porphyric diorites to monzonites and numerous dikes, including felsic pegmatites, aplites, K-feldspar-plagioclase-quartz-porphyric felsic dikes, and basalts, which are mostly oriented E-W or NW-SE. Although cross-cutting relationships between the different dikes are complex in the field, it seems that the felsic and pegmatitic dikes are the oldest dikes as they are cross cut by the basaltic and K-feldspar porphyric dikes. Although the amphibole-dominated sequence is not continuous in the field, a general mineralogical progression can be observed from the ultramafic lithologies to the more-evolved, feldspar-dominated ones. For this sequence, we infer a mineral crystallization order of clinopyroxene + apatite → amphibole + biotite → plagioclase + K-feldspar → quartz.

3.2.1 Petrography of the Biotite-Dominated Fractionation Sequence

Wehrlites and Phlogopite Wehrlites

The wehrlites are fine- to medium-grained (0.5-2 mm). The most primitive ($Mg\#^{bulk}$=85-91) phlogopite wehrlites consist of bright green clinopyroxene (~65%, all percentages in the text are modal) and olivine (25-30%) with intercumulus phlogopite[1] (2-10%) and occasional accessory titano-magnetite (Fig. 3-2a). Olivine occurs as subhedral to anhedral crystals that are commonly poikilitically enclosed within phlogopite. In some samples, olivine shows highly irregular margins surrounded by phlogopite. The modal percentage of phlogopite is variable in the wehrlites and gradually increases to a maximum of

[1] Throughout the text, we use 'phlogopite' when describing biotite in ultramafic lithologies and 'biotite' when describing biotite in feldspar-bearing lithologies.

45%, while that of olivine and pyroxene decrease (to <10% and to 45% respectively), resulting in a pronounced orthocumulate texture of olivine and clinopyroxene poikilitically enclosed within phlogopite (Fig. 3-2b).

Phlogopite clinopyroxenites and phlogopitite

The phlogopite clinopyroxenites are comprised of phlogopite, clinopyroxene, and apatite with accessory hemo-ilmenite, titanite, and zircon (Fig. 3-2c). In the clinopyroxenites, brown-reddish phlogopite grows interstitially between the clinopyroxene and occasionally encloses clinopyroxene. In one sample (MO-11-10), phlogopite is the dominant phase (~75%) and apatite becomes an important constituent (4-5%). Phlogopite occurs both as an intercumulus phase and as elongate light brown euhedral laths up to 1-2 mm in length with subhedral clinopyroxene and stout prismatic apatites. Apatites are poikilitically enclosed by both euhedral and intercumulus biotite.

Biotite Monzogabbros

Monzogabbros consist of alkali feldspar and plagioclase (together 28-50%), biotite (13-25%), and clinopyroxene (31-55%) with accessory subhedral sphene, apatite, zircon, and hemo-ilmenite (Fig. 3-2d). Biotite grows both interstitially and in large laths (1-2 cm in length), and may poikilitically enclose sphene and apatite. Oligoclase to andesine (An ~20-40) and K-feldspar occur together in subsolvus intergrowth. Apatite occurs as stubby, subhedral 1-2 mm long crystals.

Clinopyroxene Monzodiorites to Quartz-Monzonites

The monzodiorites, monzonites, and quartz-monzonites are composed of large K-feldspar megacrysts (1-2 cm in length) surrounded by smaller grains of K-feldspar and andesine (together 50-60%), quartz (10-20%), biotite (10-15%), amphibole (5-15%), and clinopyroxene (≤5%) with accessory apatite, sphene, zircon, and hemo-ilmenite. Biotite occurs as stubby laths, 1-4 mm in length. Clinopyroxene contains both biotite and numerous apatite inclusions (5-100 μm diameter). Apatite is also enclosed in biotite.

3.2.2 Amphibole-Dominated Fractionation Sequence Petrography

Amphibole Clinopyroxenites and Hornblendites

Amphibole-bearing clinopyroxenites are comprised of subhedral, 1-2 mm interlocking pargasitic amphibole (~40-50%), 100-300 μm subhedral clinopyroxene (~40-50%), 20-100 μm elongated to stubby apatites (up to 5%), and minor magnetite (Fig. 3-2e-g). In some samples, minor andesine (An_{45}-An_{35}) and K-feldspar occur as interstitial anhedral grains. When present, phlogopite is a minor phase (<5 modal %), occurring as laths either enclosed in amphibole or interstitially. Apatite is generally poikilitically enclosed by amphibole. In some coarse-grained facies amphibole comprises up to 80% of modal mineralogy and reaches 3 cm in length, with more common dimensions of 1-2 cm.

Amphibole Monzogabbros

Monzogabbros generally display hypidomorphic equigranular textures with subhedral mm to cm-scale amphibole (~35-60%) surrounded by patchy intergrowths of K-feldspar and andesine (40-60%) and clinopyroxene (in part retrograded to actinolite) (<20%) (Fig. 3-2h). Biotite is often present, but limited to <10%. Accessory minerals include sphene, Fe-Ti oxides, and apatite. Apatite can be up to 1 mm in length and often occurs as inclusions within amphibole. Twinning within plagioclase is common.

Amphibole-rich Granitoids

Felsic intrusives of this series range from amphibole-bearing monzodiorites to quartz-monzonites. These intermediate to evolved lithologies are generally equigranular (though some more porphyric facies are present), and fine- to medium- grained. The rocks are generally undeformed, but locally display magmatic flow textures with distinct foliated appearance. Both plagioclase and K-feldspar occur as mm to cm scale phenocrysts and as smaller grains interlocking with quartz, amphibole, and biotite in the groundmass. Plagioclase often displays both Carlsbad and polysynthetic twinning. Accessory minerals include zircon, apatite, Fe-Ti oxides, and sphene.

3.2.3 Late-Stage Amphibole and Biotite-Bearing Basaltic to Andesitic Dike Petrography

Late stage basaltic to andesitic dikes that cross-cut the plutonic rocks of the alkaline fractionation series can be broadly grouped into three categories: 1) biotite-bearing, 2) amphibole-bearing, and 3) biotite- and amphibole-bearing. Group 1 dikes are comprised of phlogopite, plagioclase, and clinopyroxene with accessory apatite, zircon, and hematite. Phlogopite (50%) occurs in 100-200 μm long blocky laths often enclosing zircon and hematite. Subhedral, rounded 20-100 μm clinopyroxene crystals (5%) are surrounded by oligoclase-andesine (An_{28}-An_{44}) (45%). Plagioclase crystals display irregular margins and appear to have crystallized in between phlogopite. Zircon is an abundant accessory phase occurring as 20-150 μm long prismatic crystals within both plagioclase and phlogopite. Group 2 amphibole-bearing dikes contain primarily amphibole (50-60%) and plagioclase (40-50%) in the groundmass with accessory Fe-Ti oxides and apatite. Groundmass amphibole is pale green, subhedral, and up to 300 μm in its longest dimension. Groundmass plagioclase has irregular margins, generally growing around amphibole. Up to 20 μm long euhedral, elongate apatite is poikilitically enclosed in plagioclase. In some dikes, amphibole and plagioclase occur as ~0.5-1 cm phenocrysts. Group 3 dikes are similar to Group 2 dikes in mineralogy and texture, however, biotite also occurs as a groundmass phase (10-15%) generally along the rims of amphibole.

3.3 Analytical Methods

168 whole rock major and trace element compositions are included in the presented data set. Most samples are from the northwestern part of the Dariv Range, though 14 are from the southeastern part of the range where a few similar alkali-rich lithologies are observed. Fresh pieces with no optical indication

of weathering or veining were cut from samples to ensure uncontaminated and representative chemical analyses. Samples were powdered in an agate mill, which was cleaned with silica sand in between samples. The powders were then dried overnight at 105°C. Loss on ignition was determined from mass loss after heating to 1050°C for most samples and to 950°C for samples with high silica contents. Glass discs were prepared using a lithium tetraborate flux. Major elements were measured using a wave-length dispersive X-ray fluorescence (XRF) spectrometer at ETH in Zürich. Trace elements of the fusion discs were determined by laser ablation inductively coupled plasma mass spectrometer (LA-ICPMS) at ETH. The XRF glass discs were broken and analyses were performed on freshly broken surfaces. Samples were loaded along with the NIST610 glass standard and a lithium tetraborate blank in an ablation cell and the ablated material was transported to the ICP-MS by a He carrier gas. The ablation system consists of a 193 nm ArF Excimer laser (Lambda Physik) with a homogenized beam profile connected to an Elan6100 DRC quadrupole ICP-MS. The background was measured for ~40 s prior to each analysis and the laser signal was integrated over 40-50 s. Using a 90 μm laser spot size, a minimum of 3 shots per disc were done to ensure homogeneity of the analyzed pellet. The analytical set-up was tuned for optimum performance across the entire mass range and daily optimization of the analytical conditions were performed to ensure a ThO production rate of below 0.2% (i.e. Th/ThO intensity ration <0.002). and a Th/U sensitivity ratio of 1 measured on the NIST610 glass standard. Two analyses on the NIST610 standard at the beginning and end of each set bracketed up to 20 analyses of unknowns. The blank was measured at the beginning of each session and its spectrum subtracted from the unknown spectra. The NIST610 standard was used as an external standard to calibrate analyte sensitivities and to correct for linear drift during analyses. Data reduction of LA-ICP-MS analyses followed the procedures described in Longerich et al. (1996). CaO was used as the internal standard element to correct for matrix effects and calculate trace element concentrations.

3.4 Whole Rock Geochemistry

3.4.1 Major Element Chemistry

GPS locations and whole rock major and trace element chemistry of the analyzed samples are provided in Appendix C. Based on total major element chemistry and modal mineralogy, both the biotite- and amphibole-dominated series follow a calc-alkaline trend. The feldspar-bearing rocks belong to the sub-alkalic trend of monzogabbros, monzodiorites, and (quartz-) monzonites (Fig. 3-3c) (Lameyre and Bowden 1982). Following the classification of Frost et al. (2001), the monzodiorites, monzonites, and quartz-monzonites are meta-aluminous, magnesian, and belong predominately to the alkali-calcic trend using the modified alkali-lime index (MALI: $Na_2O + K_2O - CaO$). The late-stage felsic dikes are metaluminous to slightly peraluminous ($0.95 < Al/(Ca-1.67P+Na+K) < 1.1$) and predominantly magnesian.

Biotite-Dominated Sequence

With progressing fractionation, the Mg# (molar $Mg/(Mg+Fe^T)$ x 100) decreases from the most primitive ultramafic cumulates to the evolved (quartz-)monzonites (Fig. 3-3a). The major element chemistry of the ultramafic cumulates mainly depends on the mode of olivine, clinopyroxene and biotite. The phlogopite -free wehrlites contain 47-52 wt.% SiO_2, 1.0-1.5 wt.% Al_2O_3 and almost no K_2O, while the phlogopite clinopyroxenites have 43-52 wt.% SiO_2, 3.1-10.7 wt.% Al_2O_3 and up to 4.4 wt% K_2O (Fig. 3- 3b,d). SiO_2 increases with the increasing abundance of feldspar in the monzogabbros and more evolved rocks to ~63 wt.% in the monzonites and to 70-75 wt.% in the late-stage granitic dikes. CaO decreases constantly with decreasing Mg#, due to the decrease in modal abundance of clinopyroxene and the decrease in anorthite content in plagioclase with progressive fractionation. Al_2O_3 contents peak at ~19 wt.% in the monzodiorites and quartz-monzonites due to the abundance of feldspar (Fig. 3-3b). The felsic dikes are consistently lower in Al_2O_3 than the most evolved monzonites (14-16 wt.%). Na_2O contents remain low in the ultramafic cumulates (<0.3 wt.%) and do not increase much until alkali-feldspar becomes a fractionating phase. Total alkalis reach 8 wt.% in the quartz monzonites (Fig. 3-3c). Due to its compatibility in biotite, TiO_2 is strongly controlled by biotite mode in the ultramafic cumulates, increasing from the phlogopite-poor to the phlogopite-rich cumulates and reaching 2.7 wt.% in the phlogopitite. TiO_2 then decreases with increasing SiO_2 in the monzogabbros and the monzonites (Fig. 3-3e). P_2O_5 contents in the ultramafic cumulates are controlled by apatite abundance with a maximum of 1.4 wt.% P_2O_5 in the apatite-rich phlogopitite sample, but decrease steadily with increasing degree of fractionation.

Amphibole-Dominated Sequence

The major element chemistry of the ultramafic amphibole cumulates mainly depends on the mode of clinopyroxene, amphibole, and, to a lesser extent, biotite. Only two primitive amphibole (+ minor phlogopite) clinopyroxenites (MO-10-398 and MO-10-373) were identified with Mg#'s of 85-86, SiO_2 contents of 53.5 wt.%, and Al_2O_3 of 1.7-3.4 wt.%. The next most primitive amphibole clinopyroxenites have Mg#s of 67-73 and SiO_2 contents of 48.5-52.8 wt.%. As the mode of hornblende increases, the Mg# of the cumulates decreases to ~50 and SiO_2 contents decrease to 38.1 wt.% in the hornblendites. In the amphibole-rich clinopyroxenites, Al_2O_3 contents are 7.9-12.5 wt.% (Fig. 3-3b) and FeO concentrations are high (10.4-18.3 wt.%). K_2O contents are lower in the amphibole-dominated clinopyroxenites than in the phlogopite-rich ultramafic lithologies, varying between 0.5 and 2.0 wt.% (Fig. 3-3d). Conversely, Na_2O contents are higher in the amphibole clinopyroxenites (2.4-4.7 wt.%.) than in the phlogopite clinopyroxenites. With the onset of feldspar crystallization in the amphibole gabbros and diorites, SiO_2 increases to 53.9 and 59.8 wt.%. In the more evolved rocks, Al_2O_3 contents are primarily a function of feldspar mode and reach a maximum of 19.5 wt.% in an amphibole gabbro (Fig. 3-3b). CaO decreases constantly with decreasing Mg#, due to the decrease in modal abundance of clinopyroxene, with the amphibole clinopyroxenites and monzogabbros containing 11.9-16.0 wt.% and 5.1-9.6 wt.% CaO,

respectively. TiO_2 concentrations are the highest in the amphibole clinopyroxenites (reaching 2.9 wt.% in sample MO-10-328) and generally decrease with increasing SiO_2 (Fig. 3-3e). P_2O_5 contents are generally high (up to 2.1 wt.%) in the amphibole clinopyroxenites due to high modal abundances of apatite, but then decrease with progressive fractionation.

3.4.2 Trace Element Chemistry

Biotite-Dominated Sequence

Ni and Cr are positively correlated with Mg# and strongly decrease with differentiation. This trend is concordant with early fractionation of olivine, clinopyroxene, and minor Cr-spinel. Ba enrichment in the ultramafic cumulates is controlled by phlogopite abundance, reaching 2290 ppm in the phlogopitite with 60 modal % phlogopite. In the evolved rocks, Ba concentrations remain uniformly high (750-1500 ppm) due to its compatibility with alkali feldspar. Rb follows trends similar to Ba. The ultramafic rocks mostly exhibit depleted Pb and Sr signatures and depletion in the HREE relative to LREE ($(La/Yb)_N$ = 2-12), (Fig. 3-4a-d). The more evolved feldspar-bearing rocks exhibit positive Pb anomalies and enrichment in LILEs, (Fig. 3-4e-h). No Eu enrichment is present in monzodiorites to quartz-monzonites, but there is strong Sr enrichment due to the presence of oligoclase to andesine (An_{16-40}) in these rocks (Fig. 3-4f,g). The evolved rocks are more enriched in LREE than the wehrlitic cumulates ($(La/Yb)_N$ = 8-25) (Fig. 3-4). Trace element patterns normalized to primitive mantle for the biotite-dominated sequence exhibit depletions in Nb, Ta, Zr, and Hf except for the quartz monzonites which have normalized Zr and Hf concentrations comparable to other incompatible elements (Fig. 3-4). Th and U are depleted in most, but not all, phlogopite-rich ultramafic cumulates and monzonites, while there is no distinct depletion in the felsic dikes.

Amphibole-Dominated Sequence

Ni and Cr contents are highest in the ultramafic cumulates (up to 208 and 1790 ppm, respectively) and are positively correlated with Mg#. Ba and Rb contents in the ultramafic lithologies of the amphibole-dominated sequence are controlled by the modal abundance of biotite and are therefore generally lower than that of the biotite-only fractionation sequence (Fig. 3-5a). The ultramafic amphibole-bearing cumulates are variably enriched or depleted in Pb with respect to other incompatible elements, have negative Sr signatures, and are depleted in HREE relative to LREE ($(La/Yb)_N$ = 7-22) (Fig. 3-5a). No Eu enrichment is present in the amphibole monzogabbros or diorites, but they generally exhibit a strong enrichment in Sr (Figs. 3-3f, 3-5b,c). The feldspar-bearing lithologies show a similar to slightly greater enrichment in LREE to HREE as the ultramafic cumulates ($(La/Yb)_N$ = 5-49) (Fig. 3-5). The feldspar-bearing amphibole monzogabbros and granitoids exhibit enrichments in Pb and LILE relative to other incompatible elements (Fig. 3-5b,c). Nb, Ta, Th, and U are all depleted relative to other incompatible elements, while Zr and |Hf are depleted in the ultramafic cumulates and monzogabbros but not in the more Si-rich intrusives

3.5 Discussion

3.5.1 Liquid Line of Descent (LLD) Modeling – Biotite-Dominated Series

Field relationships clearly indicate that quartz-monzonites that have biotite as the predominant hydrous mineral are intimately related to the biotite-dominated cumulate sequence (Chapter 2). Therefore, in order to test whether these evolved quartz-monzonites and late stage felsic dikes could be produced by fractionation of the biotite-bearing ultramafic and mafic cumulates from a primitive melt, we model the LLD and compare the results to bulk rock analyses. We do not model the LLD of the amphibole-dominated sequence due to the lack of primitive amphibole cumulates (Fig. 3-3a) and the incomplete characterization of more primitive fractionating lithologies.

Model Description

The LLD of the magma parental to the biotite-series cumulates was modeled by stepwise subtraction of cumulates of fixed composition following the method described in Jagoutz (2010) (see his equation 1). Fractionation steps were 1%. This model was chosen over more traditional methods utilizing mineral-melt partition coefficients and corresponding equations for fractional or equilibrium crystallization because the fractionating lithologies and the parental melt composition could be constrained from field observations and chemical analyses. In addition, this method is also independent of the choice of partition coefficients and fractionation mechanism (i.e. fractional versus equilibrium crystallization). The parental melt composition was constrained by averaging the composition of three primitive (Mg# = 67-74, Ni = 144-171 ppm, and Cr = 520-643 ppm) late-stage basaltic dikes with biotite as phenocrysts or in the groundmass that cross-cut the cumulate sequence (samples MO-11-19, MO-9-228, MO-9-230). These synmagmatic dikes have phenocrysts and groundmass mineralogy similar to the cumulate sequence (e.g., biotite and clinopyroxene) and trace element concentrations that are in equilibrium with clinopyroxenes from the most primitive phlogopite wehrlites (Chapter 2). The range of compositions of these dikes corresponds to a K-rich basalt (Na_2O = 1.84-2.66 wt.%, K_2O = 1.63-2.76 wt.%, 48.7-52.9 wt.% SiO_2).

Fractionating compositions were constrained by averaging 1 to 7 samples of representative cumulative lithologies (Table 1). Unaltered dunite (±clinopyroxene ±phlogopite) with clear relationships to the biotite fractionation sequence was not observed in the field, but such dunites have been documented as xenoliths in alkali magmas and early olivine-only crystallization intervals are observed in crystallization experiments on high-K melts (e.g., Righter & Carmichael, 1996). As the most primitive wehrlite sampled is in equilibrium with a melt of Mg# ~66 (all Fe as ferric Fe), we included 5% fractionation of the average of phlogopite-bearing dunite cumulate xenoliths from the Bear Paw Mountains (Downes et al. 2004) to account for the gap between the primitive melt (Mg# 71.6) and a melt in equilibrium with the Dariv wehrlites. We chose these dunites as a range of phlogopite-bearing

ultramafic cumulate xenoliths similar to the sequence in Dariv is observed in the Bear Paw Mountains (e.g., phlogopite wehrlites and clinopyroxenites) suggesting a similar crystallization sequence.

Evolved plutonic rocks may range from segregated cumulates to solidified bulk melts, which may be inferred from trace element systematics, such as positive or negative Eu anomalies. Although the evolved rocks do not display a positive Eu anomaly, this is not evidence against feldspar accumulation as all Eu was Eu^{3+} at the moderately elevated oxygen fugacity of +2 to +3 ΔFMQ (log-units above the fayalite-quartz-magnetite buffer) in this fractionation sequence (see Chapter 2). Instead, elevated Al/Si (>0.17) and Sr/Nd (>27) ratios were taken to indicate accumulation of feldspar and were used to identify the monzogabbros, monzodiorites, and monzonites of cumulate character.

As the areal extent of the various cumulate lithologies in the field is not necessarily representative of total volumes, the mass of each cumulate type crystallized was estimated by utilizing cumulate olivine and clinopyroxene Mg# to calculate the equilibrium melt Mg# and comparing that to the modeled melt Mg# (e.g., Greene et al. 2006) (Fig. 3-6). With approximately 35% of the total melt Fe present as Fe^{3+} (at the oxygen fugacity of the ultramafic cumulates of +2 to +3 Δ QFM), the modeled melt Mg# is similar to slightly lower than the melt Mg# calculated to be in equilibrium with olivine- and clinopyroxene from the cumulates (using $K_D^{Fe\text{-}Mg}$(olivine-melt) = 0.3 (Roedder & Emslie, 1970) and $K_D^{Fe\text{-}Mg}$(clinopyroxene-melt) = 0.23) (following findings of Sisson & Grove, 1993). In general, calculated equilibrium melt Mg# (including the Fe oxidation state adjustment) for the ultramafic cumulates range from ~70 to 55. We therefore allow for an interval of ultramafic cumulate fractionation until the modeled LLD Mg# reaches ~60. The equilibrium melt Mg# calculated from clinopyroxenes in the more evolved cumulates (monzogabbros, monzodiorites, and monzonites) is lower than that of the modeled LLD. This could be due to uncertainties in the oxidation state of these lithologies or the limited number of samples with clinopyroxene analyses. Within the constraints of Fe-Mg partitioning between melt and crystallizing phases, the amount of each cumulate type was varied iteratively until an optimal fit between the modeled LLD and more evolved lithologies was achieved. The final model fit yields the following cumulate mass percentages: 5% dunite, 3% wehrlite, 5% phlogopite-poor wehrlites (<0.3 wt.% K_2O in the bulk cumulate), 10% phlogopite-rich wehrlites (>0.7 wt.% K_2O in the bulk cumulate), 8% phlogopitite, 21% high Mg# monzogabbro (bulk Mg# > 65), 14% low Mg# monzogabbro (bulk Mg# < 59), 26% monzodiorite, 5% monzonite. Calculations were performed until 5% liquid mass remained. Furthermore, the composition of the average primitive melt from the three biotite-bearing primitive dikes was modified within error in order to optimally reproduce the geochemical trend defined by the bulk rocks. Oxides or trace elements were not modified more than ±25% of the average, with most to <10% and well within the $2\sigma_{SD}$ of the primitive dikes' average. Assimilation was not considered in the model, but we cannot exclude a minor contribution of this mechanism to the evolving plutonic series.

Uncertainties associated with this modeling approach are discussed in detail by Jagoutz (2010) and include variability in the composition of the primitive parental melt, estimates of the mass fraction of

each cumulate type crystallized, and the degree to which the samples used in the average bulk cumulate compositions are representative of the actual fractionating compositions and chemical variability in a given lithology. Our methods of reducing the first two uncertainties are discussed above and we use the best estimates possible from the available constraints. The last source of uncertainty is inherent to a finite whole rock geochemical dataset, but is mitigated by our division of cumulate lithologies into nine coherent geochemical groups.

Model Results

The major and trace element compositions of the derivative melt at 10% fractionation intervals are given in Table 2 and the calculated LLD and fractionated cumulate compositions are shown in Figs. 3, 6, & 7. Beginning with a primitive alkali-rich basalt composition, the model successfully reproduces the major and minor trace element characteristics observed in the most evolved monzonites and late-stage felsic dikes.

SiO_2 Enrichment

A general difficulty in producing silica-rich granitoids by magmatic differentiation alone is that fractionation of gabbros, which have similar SiO_2 contents as basaltic to basaltic andesite melts (48-54 wt%), is inefficient for producing volumetrically significant silica-rich derivative liquids (Annen et al. 2006; Jagoutz 2010). Thus, early appearance of plagioclase and clinopyroxene as fractionating phases does not result in the silica-enrichment observed in upper crustal granitoids. Rather, silica-enrichment requires the fractionation of cumulates dominated by SiO_2-poor minerals. For calc-alkaline basalts, the importance of hydrous, high-P fractionation of silica-poor minerals such as amphibole, garnet, oxides, and An-rich plagioclase is well documented experimentally (Müntener et al. 2001; Grove et al. 2003; Sisson et al. 2005; Alonso-Perez et al. 2009) and from field studies (Greene et al. 2006; Jagoutz et al. 2010; Dessimoz et al. 2012). For the high-K parental basalt in Dariv, the primary fractionating low SiO_2 mineral is biotite, (with ~35 wt.% SiO_2). The phlogopite-rich wehrlites and phlogopitites have the required low SiO_2 contents and their fractionation produces sufficient silica enrichment such that subsequent fractionation of monzogabbros and monzodiorites results in further SiO_2 enrichment (Figs. 3 & 6). The model reproduces the silica-content of the least evolved monzonites (55-60 wt.% SiO_2) with 24-63% melt remaining. The most evolved quartz-monzonites and late stage felsic dikes (63-75 wt.% SiO_2) can be produced through fractionation of cumulates when $\leq$16% of the melt remains. This amount of melt is in reasonable agreement with the volumes of (quartz-)monzonites and felsic dikes observed in the field. Interestingly, whereas moderate to high pressure fractionation has been demonstrated as an effective mechanism to produce SiO_2 enrichment in calc-alkaline basalts (Alonso-Perez et al. 2009; Jagoutz et al. 2011; Müntener et al. 2001), the fractionation sequence observed in Dariv occurred at relatively low pressures (< 0.2-0.4 GPa, see Chapter 2) and still resulted in significant SiO_2-enrichment. This is primarily due to the stability of biotite on the liquidus of these melts, but also to the protracted

fractionation of olivine resulting from a stability field increasing with decreasing pressure (Esperança and Holloway 1987; Righter and Carmichael 1996).

Other Major Elements

It is illustrative to inspect the behavior of several key oxides to determine the proportion and composition of cumulate lithologies as well as the parental magma composition. Al_2O_3 enrichment of fractionating melts to levels not observed in arc granitoids is a common problem in models of primitive arc magma fractionation (Annen et al. 2006; Blatter et al. 2013). One way to limit Al_2O_3 enrichment is for fractional crystallization to occur at greater pressures. Higher pH_2O stabilizes garnet (e.g., Alonso-Perez et al. 2009; Wolf and Wyllie 1994), aluminous amphibole (Grove et al. 2003) and anorthite-rich plagioclase (34-36 wt.% Al_2O_3) which all minimize Al_2O_3 enrichment in fractionating magmas (Annen et al. 2006; Jagoutz 2010). Nevertheless, it has been noted that deeper fractionation results in a larger interval of clinopyroxene crystallization and therefore an increases in the aluminum saturation index (ASI = Al/(2Ca+Na+K)) (Blatter et al., 2013). In Dariv, however, the observed alkaline sequence crystallized at relatively low pressures (0.2-0.4 GPa) and amphibole, garnet, and anorthitic plagioclase are not important fractionating phases in the biotite+clinopyroxene-dominated series. Due to its relatively high Al contents (13.5-16.8 wt.%), biotite crystallization limits Al-enrichment to some extent. The whole rock Al_2O_3 contents of the phlogopite ultramafic cumulates (1.0-10.8 wt.%, Fig. 3-3b), however, are still low compared to high pressure hornblendite and garnetite cumulates from other paleo-arc sequences (e.g., 15.0-22.5 wt.% Al_2O_3 (Jagoutz 2010)) and a further mechanism is required to limit Al-enrichment. An alternative would be a primitive melt that itself has relatively low Al_2O_3 (Annen et al. 2006). Primitive arc basalts have highly variable Al_2O_3 contents of 10-18 wt.% with most between 14-16 wt.%. Primitive high-K basalts from Dariv have Al_2O_3 contents between 12.3-15.3 wt.%. Using a slightly lower Al_2O_3 content (12.9 wt.%) than the average primitive basalt composition, Al-enrichment is sufficiently limited and the observed geochemical trends are reproduced well (Fig. 3-3b).

A decrease in TiO_2 with SiO_2-enrichment is observed in Dariv and other arc suites (Dessimoz et al. 2012; Greene et al. 2006; Jagoutz 2010). Initially, however, TiO_2 is incompatible during the fractionation of olivine- and pyroxene-rich cumulates. The observed decrease in TiO_2 must therefore be explained by crystallization of a TiO_2-rich phase. In the Kohistan and Talkeetna paleo-arcs amphibole and Fe-Ti oxides had sufficiently high TiO_2-contents to produce a decrease in TiO_2 concentrations with increasing fractionation (Greene et al., 2006; Jagoutz, 2010). In Dariv, the early crystallizing phlogopite has 2.1-4.9 wt.% TiO_2 and phlogopite-rich wehrlites and phlogopitites have the required high TiO_2 contents (1.3 and 2.8 wt.% on average, respectively), to drive fractionating liquids to lower TiO_2 contents (Fig. 3-3e). In addition, accessory titanomagnetite (with 3.5-23.0 wt.% TiO_2, see Chapter 2) contributes to the high TiO_2 concentrations of the phlogopite-rich wehrlites and phlogopitites.

The high K_2O contents of several of the fractionating lithologies (e.g., phlogopitite, monzonite) necessitate a primitive starting composition with high K_2O in order to yield the elevated K_2O contents of

the quartz-monzonites and late-stage felsic dikes. As we only have one phlogopitite sample (MO-11-10), it is somewhat uncertain how representative its K_2O content (4.5 wt.%) is of the actual fractionating composition. For example, 4.5 wt.% K_2O is high compared to the average 3.4 wt.% K_2O of phlogopite clinopyroxenite xenoliths from other localities. If the latter K_2O value is used, a primitive melt with 2.96 wt.% K_2O yields the K_2O concentrations of the late stage felsic dikes (Fig. 3-3d). This value is similar to two of the K-rich primitive dikes (2.8 wt.% K_2O). Therefore, we treat 2.96 wt.% K_2O in our primitive melt as the value necessary to reproduce the trends observed in the most silica-rich dikes.

Trace Elements

Fractionation of a few percent of dunite is required to reproduce the Ni contents of the most magnesian olivines (1135±82 ppm), which are lower than typical mantle olivine values (3500-4500 ppm) (Arai 1994; Sato 1977). Cr and Ni then decrease dramatically in the evolving melt with fractionation of olivine-rich wehrlites. LILE concentrations in the Dariv primitive melts are high (Ba: 561-1007 ppm; Rb: 30-79 ppm). Rb increases with progressive fractionation due to the high initial concentration of the primitive melt and comparatively low concentrations in the fractionating cumulates. Ba is 1.5-13 times more compatible than Rb in biotite crystallizing from alkali basalts, (Green et al. 2000; LaTourrette et al. 1995; Villemant et al. 1981) and therefore displays more gentle enrichment trends. All REE follow a similar trend. Initially they are incompatible in the olivine and biotite-dominated ultramafic cumulates and therefore increase in the fractionating melt. In the apatite-bearing cumulate assemblages, however, REE become compatible and their concentrations in the melt begin to decrease. REE concentrations of the "liquid-like" granitoids and felsic dikes are best reproduced between 20-40% and 10% melt remaining, respectively (Fig. 3-7). Sr displays a similar pattern, but decreases in evolved liquids due to plagioclase fractionation in the monzogabbros and monzodiorites (Fig. 3-3f). Nb and Ta concentrations are high in the primitive melt (~9 ppm, 0.53 ppm) and increase moderately with continued fractionation. Although the wehrlites and dunites contain little Nb or Ta, they are compatible in biotite, which moderates Nb and Ta enrichment in the evolving melt. For example, the phlogopitite and other phlogopite-rich cumulate xenoliths contain 2-7 ppm Nb.

3.5.2 Biotite- and Amphibole-Series in Arcs

Controls on Biotite and Amphibole Crystallization in Hydrous Arc Melts

In the Dariv Igneous Complex, two distinct alkaline fractionation sequences are observed: one with early saturation of biotite and much later crystallization of amphibole and the second with early saturation of amphibole accompanied by minor biotite. As such, an important question to address is which parameters control high temperature, early crystallization of biotite and/or amphibole in hydrous arc-related basalts. To investigate the influence of melt composition and H_2O-content we compiled major element data from experiments on hydrous basaltic to andesitic starting materials and from natural high

Mg# (>60) alkali-basalts and lamprophyres from the Mexican Volcanic Belt saturated with (i.e., had phenocrysts of) amphibole and/or biotite (Figs. 8 & 9). We take the high Mg# of the alkali-basalts as indicative of elevated liquidus temperatures and their phenocrysts assemblages as representative of near liquidus phases. The data set of lamprophyres from the Mexican Volcanic Belt is most useful because it constrains a variability of bulk compositions with amphibole and/or biotite phenocrysts including both very potassic and sodic types. We then compared this compiled dataset to the compositions of 13 high Mg# (>60) basaltic to andesitic dikes from the Dariv Igneous Complex. The primitive compositions used in the LLD modeling are included in this set, but not all of these dikes are primitive, but rather, were only selected by the elevated Mg# criterion. Three of these dikes contain biotite as phenocrysts or groundmass phase, seven contain amphibole as a groundmass phase or phenocrysts, and three contain biotite and amphibole in the groundmass.

For biotite, the dominant control on early crystallization is the major element composition, in particular K_2O, TiO_2, and Al_2O_3, of the melt. As to be expected, a high K_2O content and K_2O/Na_2O are critical in determining whether biotite will crystallize near the liquidus (Edgar and Arima, 1983). Biotites have K>>Na while igneous amphiboles have Na>K at crustal pressures. Consequently, higher K/(K+Na) values in a melt will favor biotite crystallization at higher temperatures. Expanding upon an early experimental compilation on high-K starting materials of Edgar and Arima (1983), Figure 8 shows K_2O and K_2O/Na_2O plotted against the difference between the liquidus and biotite crystallization temperatures ($\Delta T_{liq\text{-}bt}$) for various experiments on high-K hydrous basalts at pressures of 0.05-1.0 GPa. With increasing K_2O and K_2O/Na_2O, $\Delta T_{liq\text{-}bt}$ decreases at all pressures (Fig. 3-8a,b). This finding is supported by the fact that high Mg# lamprophyres with relatively high K_2O/Na_2O (> 0.8) have phenocrystic biotite (Fig. 3-8a). High TiO_2 contents also increase the thermal stability of biotite (Edgar and Arima 1983; Righter and Carmichael 1996), a fact which is reflected in a decrease in $\Delta T_{liq\text{-}bt}$ with increasing TiO_2 content (Fig. 3-8c). High Mg# lamprophyres with elevated TiO_2 contents (>1.2 wt.%) generally contain biotite, but not amphibole phenocrysts (Fig. 3-9c). In contrast, low Al_2O_3 concentrations in a melt appear to stabilize biotite (Fig. 3-8d). In support of this observation, high Mg# lamprophyres and experimental starting materials with biotite as a near liquidus phase tend to have lower Al_2O_3 contents (mostly <14 wt.%) than those with amphibole (generally >14 wt.%) (Fig. 3-9b). It is important to note that in the dataset several of the investigated compositional variables are correlated with each other. For example, K_2O and TiO_2 are positively correlated with K_2O/Na_2O, whereas Na_2O and Al_2O_3 are negatively correlated. F has been shown to stabilize biotite to significantly higher temperatures (Foley et al. 1986), however, as the biotites from Dariv do not have particularly high F contents (generally 0.2-0.6 wt.%) we do not explore the effect of this compositional parameter further.

In contrast, the water content of the melt is perhaps the strongest control on the appearance of amphibole. Numerous experimental studies have demonstrated that with increasing P_{H2O} the temperature difference between the liquidus and the onset of amphibole crystallization decreases (Grove et al. 2003;

Holloway and Burnham 1972; Krawczynski et al. 2012). Conversely, biotite may crystallize under strongly water-undersaturated conditions. For example, Naney (1983) on a granodioritic melt, found that amphibole crystallized only at relatively high water contents (4 wt.% H_2O at 0.2 GPa and 2.5 wt.% H_2O at 0.8 GPa) whereas biotite crystallized at significantly lower water concentrations (<0.5 wt.% H_2O). Further, in water under-saturated andesites at 0.8-1.2 GPa, 4 wt.% H_2O is required to stabilize amphibole at high temperatures (Alonso-Perez et al. 2009). Experimental studies on K-rich basaltic starting compositions have also found biotite as a stable phase under H_2O-undersaturated conditions (Barton and Hamilton 1979; Esperança and Holloway 1987). However, as biotite is a hydrous phase, some water is required for its crystallization and at very low pressures and thus low P_{H_2O}, biotite is depressed from the liquidus (e.g. at 0.05 GPa, Fig. 3-8).

Thus, while biotite crystallization strongly depends on the degree of K-enrichment in a melt, amphibole crystallization requires a certain H_2O-content. It is important to note that amphibole and biotite are not necessarily in direct 'competition' as crystallizing phases, their relative proximity to the basalt liquidus being controlled in part by different parameters. There is a critical threshold in K_2O/Na_2O and in TiO_2 and Al_2O_3 contents where near-liquidus biotite crystallization is strongly enhanced, rendering it the primary hydrous high temperature phase. At lower K_2O/Na_2O or TiO_2 and higher Al_2O_3 contents, amphibole, not biotite, is the stable hydrous phase at high temperatures. K_2O-concentration by itself does not lead to such a clear distinction: at >4 wt%, biotite is the near-liquidus hydrous phase, but at lower K_2O contents, low Al_2O_3 (< 14 wt.%) and/or high TiO_2 (>1.3 wt.%) result in biotite as the high temperature hydrous phase. Surprisingly, CaO concentrations or Na_2O/CaO ratios are of secondary importance within the range of natural magmas (Fig. 3-9d). SiO_2 concentrations are generally (though not exclusively) lower in the biotite- than amphibole-saturated melts. There is a range within these chemical parameters, i.e. near the thresholds of approximately 14 wt.% Al_2O_3, a K_2O/Na_2O of 0.7-0.9, increasing with Si-content, or 1.3 wt.% TiO_2, where the melt is compositionally appropriate for both early biotite and amphibole crystallization (Fig. 3-9). The few phenocrystic amphibole+biotite MVB lamprophyres and one experimental starting material characterized by high temperature crystallization of both amphibole and biotite fall in this range. Also, the high Mg#, biotite±amphibole-bearing dikes from Dariv are situated near these thresholds. As the Dariv high Mg# melt compositions are compositionally suitable for early biotite and amphibole crystallization, it is likely that the H_2O-concentrations of the Dariv primitive melts were critical in controlling whether biotite or amphibole crystallized close to the liquidus. Higher concentrations enhance while lower concentrations depress the amphibole crystallization temperature leading to biotite as the high temperature hydrous phase.

In Dariv, amphibole-crystallization occurs in the amphibole-dominated crystallization at much higher temperatures (i.e., in the ultramafic amphibole clinopyroxenites) than in the biotite-dominated sequence, where amphibole only appears in the monzodiorites and more evolved lithologies. Temperatures calculated from clinopyroxene or amphibole-plagioclase thermometry for the amphibole

clinopyroxenites and biotite monzodiorites are 1102-1165°C and 693-726°C, respectively (see Chapter 2). We note that the temperature estimates for the amphibole clinopyroxenites are at or above the experimentally established thermal stability of amphibole in hydrous basalts (~1050°C) (Grove et al. 2003; Krawczynski et al. 2012). This is likely due to errors associated with the clinopyroxene-only thermometer (±50°C), which would bring the estimates into accord with amphibole crystallization at 1050-1100°C. Clearly, the ultramafic amphibole clinopyroxenites crystallized at high temperatures suggesting that the melts crystallizing these cumulates had higher water contents than the parental melts of the biotite-dominated sequence. The high Mg# of amphibole (81.0-82.8) and clinopyroxene (84.4-86.2) in the most primitive amphibole clinopyroxenite (MO-10-398) suggest that when the fractionating melt reached Mg#'s of 57-59, H_2O-contents were ≥4 wt.% in the amphibole-dominated fractionation series. Using mineral-melt Fe-Mg equilibrium partitioning constraints, we calculate that the parental melts of the amphibole-dominated sequence crystallized ~10-11% clinopyroxene and olivine by mass to reach an Mg# of ~58. This requires that the parental melts of the amphibole-dominated sequence must have had ≥3.5-3.6 wt.% H_2O to reach 4 wt.% H_2O (the minimum amount of H_2O required for amphibole saturation) at a Mg# of 58. In contrast, using mass balance and constraints on the H_2O content required for amphibole crystallization, we calculated in Chapter 2 that the parental melt of the biotite-dominated sequence would contain 2.2-2.6 wt.% H_2O in order to saturate in amphibole when the fractionating melt reached a monzodioritic composition.

Effects of Biotite versus Amphibole Crystallization on the Geochemistry of Fractionating Arc-Related Melts

The Dariv alkaline arc series allows for the reconstruction of a LLD dominated by biotite fractionation. Amphibole fractionation has been previously well documented in the field and in experiments and is thought to constitute the dominant mechanism for generating the geochemical trends of calc-alkaline magmatic sequences (Cawthorn and O'Hara 1976; Dessimoz et al. 2012; Grove et al. 2003; Jagoutz 2010; Sisson and Grove 1993). As such, we are able to discuss the effect of biotite versus amphibole crystallization on the geochemistry of a fractionating primitive arc melt by comparing the high-K LLD modeled here with that ascertained for the calc-alkaline series.

Crystallization of biotite vs. amphibole each result in some key trends observed in arc magmatic sequences. First, as TiO_2 is compatible and SiO_2 contents are low in both minerals, their fractionation is able to produce the characteristic decrease in TiO_2 with increasing SiO_2 in arc related plutonic and volcanic rocks. Conversely, amphibole and biotite crystallization will result in distinctly different trends in terms of Na and K. This is most clearly seen in the K_2O/Na_2O ratio of the cumulates and evolving melts. The biotite ultramafic cumulates from Dariv reach 4.5 wt.% K_2O, depending on the mode of biotite. Conversely, Na_2O contents are <0.8 wt.% resulting in $K_2O/Na_2O > 1.4$ for the ultramafic phlogopite cumulates. K_2O/Na_2O ratios of the mafic biotite cumulates decrease to ~1, due to the crystallization of

oligoclase to andesine. Importantly, K-feldspar co-crystallizes with plagioclase (An_{13}-An_{40}) resulting in bulk K_2O/Na_2O ratios that do not decrease much further in the biotite-series. In contrast, hornblendites and hornblende gabbros from paleo-arc fractionation sequences have significantly higher Na_2O (typically 1.7-2.2 wt.%) whereas their K_2O content is almost at trace levels leading to K_2O/Na_2O ratios of <0.2 in bulk cumulates (Jagoutz, 2010). Consequently, biotite and K-feldspar crystallization will serve to moderate K_2O/Na_2O ratios in crystallizing melts that initially have K_2O/Na_2O of 1-2, whereas amphibole crystallization will increase this ratio in calc-alkaline series. The resulting convergence of K_2O/Na_2O ratios with fractionation is exemplified by comparing the Dariv high-K LLD to that of a modeled calc-alkaline LLD for the Kohistan paleo-island arc (Fig. 3-10). The primitive melts identified for the Dariv Igneous Complex have K_2O/ Na_2O ratios of 0.74-1.15. The modeled LLD does not deviate from this range of values, varying between 0.94-1.18 from 52-74 wt.% SiO_2. In contrast, the primitive melt identified for the Kohistan paleo-arc has a relatively low K_2O/Na_2O ratio (~0.25), but the modeled LLD results in a strong increase of this value with increasing SiO_2 content (to 0.76 at 69 wt.% SiO_2). Comparison to a compilation of arc-related granitoids from the Sierra Nevada, S. California, and the Peninsular Range Batholith reinforces these distinct trends resulting from biotite versus amphibole fractionation (Fig. 3-10). High-K or monzonitic granitoids generally have high K_2O/Na_2O (>0.6) values across a wide array of SiO_2 contents (50-75 wt.%) and are in good agreement with the Dariv high-K LLD. Conversely, calc-alkaline granitoids show a general trend of increasing K_2O/Na_2O with increasing SiO_2 content, indicative of fractionation of low K_2O/Na_2O cumulates, such as in magmatic hornblendites. Nevertheless, absolute K_2O, and consequently K_2O+Na_2O contents, are higher in the biotite-dominated monzonitic series than the calc-alkaline series (Fig. 3-3c,d).

Though not as distinct, trends similar to K_2O are observed for trace elements compatible in biotite, such as Rb and Ba. In the Dariv high-K LLD, these have high concentrations in the primitive melt, but because of their compatibility in biotite and also K-feldspar, their enrichment during fractionation is moderated with increasing SiO_2. As these elements are incompatible in amphibole (and other typical fractionating minerals in the calc-alkaline sequence), these elements show a distinct enrichment with increasing SiO_2 in the calc-alkaline LLD and granitoids. Another interesting feature is the general high levels of Sr in monzonitic series relative to the calc-alkaline series. Although both series generally display Sr depletion with increasing SiO_2 due to feldspar fractionation, the monzonitic trend is offset several hundred ppm higher from the calc-alkaline trend (Fig. 3-3f). This is mostly due to the elevated initial Sr concentrations in the primitive high-K basalts consistent with higher levels of addition of an also K-, Rb-, and Ba-rich subduction component.

Implications for the Mantle Wedge and Subduction Component

The amphibole- and biotite-series arise from two contrasting primary magma compositions. The normal calc-alkaline, amphibole series has a relatively sodic and H_2O-rich primitive melt as a parental

magma, while the biotite-series has a comparatively more potassic and LILE-rich, but less hydrous parental melt. Apparently, LILE (including K) and H_2O in the subduction component are decoupled for these two series and we envision two different scenarios for the generation of their parental melts in the mantle wedge.

For the the calc-alkaline amphibole series, the addition of a sodic subduction component concomitant with mantle wedge melting leads to common hydrous sodic primitive arc basalts as, for example, compiled in Jagoutz and Schmidt (2013). In this scenario, the subduction component is likely to be dominated by fluids (Stolper & Newman, 1994; Grove et al. 2002), but may also include a minor sediment melt component which is sodic at moderate pressures (to 3 GPa) and relatively hydrous slab melting conditions (Hermann and Spandler 2008).

For the high-K, biotite series, the subduction signature is increased, but the concentration of H_2O is decreased, leading to two possible scenarios. In the first scenario, one may decouple K+LILE from H_2O by an intermittent stage of crystallization in the mantle wedge. Phlogopite (<1200 °C) and possibly also amphibole (at <1050-1100 °C) could form in a mantle wedge with a temperature colder than that characteristic for primitive arc melts (1250-1350 °C, from multiple saturation experiments, Kushiro 1986, Tatsumi et al. 1994), leading to a sequestration of LILE in these phases, but to further ascent of remnant H_2O through the wedge. Upon heating and/or further fluid-input, this enriched mantle wedge may then deliver a potassic LILE-rich, moderately hydrous primitive arc melt. The first stage may occur when changes in subduction geometry lead to a relatively cooler mantle wedge, most likely causing a hiatus in arc magmatism. In principal, the first stage could also happen in the colder forearc of an active subduction zone, but more potassic magmatism is characteristic for the main or back arc regions (Kuno, 1965; Dickinson 1975), rendering biotite crystallization in the forearc mantle unlikely.

In the second scenario, a subduction component with a higher (K+LILE)/H_2O ratio than characteristic for normal calc-alkaline magmatism is required. A much less hydrous subduction signal results from slab melts instead of fluids. With increasing pressure sediment melts become highly potassic, particularly when little fluid is available for slab melting (Schmidt et al. 2004). In this scenario, the slab component addition and mantle wedge melting would occur concomitantly, but in contrast to normal calc-alkaline magmas, the slab-component would be dominated by deep (≥3.5 GPa) sediment melts.

For the Dariv Igneous Complex, neither the paleo-geometry of the slab nor the relative time difference between the biotite- and amphibole-series are well-constrained, hence we cannot distinguish which of the above scenarios lead to the spatially overlapping occurrence of the two series. In several modern arcs, potassic volcanism occurs towards the back-arc concomitantly with typical calc-alkaline volcanism in the main arc (e.g., Sunda, Sumatra, Wheller et al. 1987) favoring the second scenario. However, high-K, biotite-phenocrystic basalts in the Sierra Nevada and the Western Mexican Volcanic Belt have been suggested to have formed through a secondary melting event of a previously metasomatized mantle based on their occurrence after subduction had ceased and/or low trace element

ratios (e.g., B/Be) indicating little direct input of slab-derived fluids into their source region (Hochstaedter et al. 1996; Ducea and Saleeby, 1998; Farmer et al., 2002). Thus, both scenarios presented above may occur in arcs, depending on the specific geodynamic setting of a particular subduction zone.

3.5.3 Comparison of Hydrous Basalt LLDs to Quartz-Albite-Orthoclase Ternary Phase Relationships

The fractionation paths leading to evolved granitic melts both for the high-K and calc-alkaline LLDs are well illustrated in the melting diagram of the system Quartz-Albite-Orthoclase-H_2O (Qz-Ab-Or-H_2O, Fig. 3-11). This ternary system is well constrained over a range of pressures (0.05-1.0 GPa) and from dry to water-saturated conditions (Ebadi and Johannes 1991; Holtz et al. 1989; Luth et al. 1964; Tuttle and Bowen 1958). Notably, the Or/(Ab+Or) ratio of the minimum or eutectic melt increases markedly with decreasing water activity, whereas the normative Qz content remains almost invariant. Conversely, with increasing pressure normative Qz decreases dramatically.

Figure 11 shows CIPW normative compositions of feldspar-bearing lithologies of the Dariv alkaline fractionation sequence plotted onto the Qz-Ab-Or ternary. The monzogabbros, monzodiorites, and several of the monzonites plot just slightly into the silica-undersaturated side of the Ab-Or join. The modeled LLD is also plotted and follows the water-undersaturated (a_{H_2O} = 0.4-0.5) Ab-Or cotectic toward SiO_2-enrichment. A few monzonites and late stage felsic dikes fall along this cotectic suggesting that they are representative of liquid compositions. The LLD ultimately ends at the minimum/eutectic at 0.2-0.5 GPa where the majority of the late-stage granitic dikes plot. A pressure range of 0.2-0.5 GPa is in good agreement with intrusion pressures of the Dariv Igneous Complex (see Chapter 2). Alkali-rich granitoids from the upper crust of preserved arcs have compositions similar to the calculated LLD. For example, the feldspar-bearing lithologies and LLD of the Dariv alkaline sequence overlaps remarkably well with the compilation of California monzonites of Miller (1977) (Fig. 3-11b). Instead, amphibole-dominated fractionation sequences lie along the water-saturated cotectic, further supporting our conclusion that the amphibole-dominated fractionation sequence was characterized by higher H_2O contents. For comparison, we also show a compilation of calc-alkaline granitoids from the Sierra Nevada and the modeled calc-alkaline LLD for the Kohistan paleo-arc (Fig. 3-11b). In contrast to the Dariv LLD, the calc-alkaline granitoids and LLD follow a water-saturated trend towards the eutectic composition. In the Qz-Ab-Or ternary, the relationship of water content and amphibole versus biotite crystallization is directly visible: the calc-alkaline trends are near water-saturated and correspond to amphibole-dominated fractional crystallization, whereas those for the high-K LLD correspond to low water contents and are produced through biotite-dominated crystallization.

Conclusion

In contrast to the well-studied liquid lines of descent of calc-alkaline and tholeiitic primitive melts, high-K LLDs have received little attention, perhaps due to the lack of field exposure documenting the

cumulative counterpart to the evolving liquids. We present such a LLD based on actual cumulate compositions for the newly discovered alkaline Dariv Igneous Complex in Western Mongolia. We demonstrate that relatively low pressure (0.2-0.4 GPa), hydrous, but not water-saturated fractionation of a primitive alkaline arc magma produces a K-rich monzonitic granitoids series. Critically, fractionation of silica-poor biotite is required to derive such liquids. Although the biotite-dominated ultramafic and mafic cumulates are dominant in the Dariv Igneous Complex, there is a volumetrically subordinate second sequence characterized by early appearance of amphibole. The high temperature appearance of amphibole in this second sequence necessitates higher H_2O contents in its parental melt as compared to the biotite-dominated sequence. Biotite crystallization will moderate enrichments of K_2O and other LILEs with increasing SiO_2. These differences result in distinct geochemical signatures for a high-K LLD dominated by biotite crystallization versus a sequence controlled by amphibole fractionation, such as the common calc-alkaline magmatic series.

Although calc-alkaline plutons dominate batholiths in volcanic arcs, high-K granitoids are observed in many continental arcs. These high-K granitoids may critically contribute to the incompatible element budget of continental arcs and hence the bulk continental crust. Hypotheses on the origin of these high-K alkaline granitoids are numerous and include melting of a subducted alkali-rich quartz eclogite (Miller 1977; Miller 1978), partial melting of a garnet-bearing lower crust (Rapela and Pankhurst 1996), and melting of an enriched mantle (Sylvester et al. 1978). Here we document the generation of high-K granitoids through biotite- and clinopyroxene-dominated fractional crystallization of a primitive, alkali-enriched melt. The global spatial and temporal distribution of these high-K suites in relationship to calc-alkaline arc magmatism, however, has not been cohesively studied and remains essential to fully understand the magmatic and geochemical evolution of volcanic arcs.

References

Alonso-Perez R, Müntener O, Ulmer P (2009) Igneous garnet and amphibole fractionation in the roots of island arcs: experimental constraints on H2O undersaturated andesitic liquids. Contributions to Mineralogy and Petrology 157:541-558

Annen C, Blundy JD, Sparks RSJ (2006) The Genesis of Intermediate and Silicic Magmas in Deep Crustal Hot Zones. Journal of Petrology 47(3):505-539

Arai S (1994) Characterization of spinel peridotites by olivine-spinel compositional relationships: review and interpretation. Chemical Geology 113(3):191-204

Badarch G, Dickson Cunningham W, Windley BF (2002) A new terrane subdivision for Mongolia: implications for the Phanerozoic crustal growth of Central Asia. Journal of Asian Earth Sciences 21(1):87-110

Barclay J, Carmichael I (2004) A hornblende basalt from western Mexico: water-saturated phase relations constrain a pressure,Äìtemperature window of eruptibility. Journal of Petrology 45(3):485-506

Barth AP, Wooden JL (2006) Timing of magmatism following initial convergence at a passive margin, southwestern US Cordillera, and ages of lower crustal magma sources. The Journal of Geology 114(2):231-245

Barth MG, McDonough WF, Rudnick RL (2000) Tracking the budget of Nb and Ta in the continental crust. Chemical Geology 165(3):197-213

Barton M, Hamilton D (1978) Water-saturated melting relations to 5 kilobars of three Leucite Hills lavas. Contributions to Mineralogy and Petrology 66(1):41-49

Barton M, Hamilton DL (1979) The melting relationships of a madupite from the Leucite Hills, Wyoming, to 30 Kb. Contributions to Mineralogy and Petrology 69(2):133-142

Bateman PC (1961) Granitic formations in the east-central Sierra Nevada near Bishop, California. Geological Society of America Bulletin 72(10):1521-1537

Blatter DL, Sisson TW, Hankins WB (2013) Crystallization of oxidized, moderately hydrous arc basalt at mid-to lower-crustal pressures: implications for andesite genesis. Contributions to Mineralogy and Petrology 166(3):861-886

Blundy J, Cashman K (2001) Ascent-driven crystallisation of dacite magmas at Mount St Helens, 1980-1986. Contributions to Mineralogy and Petrology 140(6):631-650

Brantley S, Chesley J, Stillings L (1998) Isotopic ratios and release rates of strontium measured from weathering feldspars. Geochimica et Cosmochimica Acta 62(9):1493-1500

Brown G, Thorpe R, Webb P (1984) The geochemical characteristics of granitoids in contrasting arcs and comments on magma sources. Journal of the Geological Society 141(3):413-426

Buhlmann AL, Cavell P, Burwash RA, Creaser RA, Luth RW (2000) Minette bodies and cognate mica-clinopyroxenite xenoliths from the Milk River area, southern Alberta: records of a complex history of the northernmost part of the Archean Wyoming craton. Canadian Journal of Earth Sciences 37(11):1629-1650

Buslov MM, Saphonova IY, Watanabe T, Obut OT, Fujiwara Y, Iwata K, Semakov NN, Sugai Y, Smirnova LV, Kazansky AY (2001) Evolution of the Paleo-Asian Ocean (Altai-Sayan Region,

Central Asia) and collisions of possible Gondwana-derived terranes with the southern marginal part of the Siberian continent. Geoscience Journal 5(3):203-224

Cawthorn RG, O'Hara M (1976) Amphibole fractionation in calc-alkaline magma genesis. American Journal of Science 276(3):309-329

DeBari SM, Greene AR (2011) Vertical stratification of composition, density, and inferred magmatic processes in exposed arc crustal sections. In: Arc-continent collision, vol. Springer, pp 121-144

Dessimoz M, Müntener O, Ulmer P (2012) A case for hornblende dominated fractionation of arc magmas: the Chelan Complex (Washington Cascades). Contributions to Mineralogy and Petrology 163(4):567-589

Di Carlo I, Pichavant M, Rotolo SG, Scaillet B (2006) Experimental crystallization of a high-K arc basalt: the golden pumice, Stromboli volcano (Italy). Journal of Petrology 47(7):1317-1343

Dickinson WR (1975) Potash-Depth (K-h) Relations in Continental Margin and Intra-Oceanic Magmatic Arcs. Geol 3:53.

Dijkstra AH, Brouwer FM, Cunningham WD, Buchan C, Badarch G, Mason PRD (2006) Late Neoproterozoic proto-arc ocean crust in the Dariv Range, Western Mongolia: a supra-subduction zone end-member ophiolite. Journal of the Geological Society, London 163:363-373

Downes H, MacDonald R, Upton BGJ, Cox KG, Bodinier J-L, Mason PRD, James D, Hill PG, Hearn BC (2004) Ultramafic Xenoliths from the Bearpaw Mountains, Montana, USA: Evidence for Multiple Metasomatic Events in the Lithospheric Mantle beneath the Wyoming Craton. Journal of Petrology 45(8):1631-1662

Ducea M, Saleeby J (1998) A Case for Delamination of the Deep Batholithic Crust beneath the Sierra Nevada, California. International Geology Review 40:78–93. doi: 10.1080/00206819809465199

Ebadi A, Johannes W (1991) Beginning of melting and composition of first melts in the system Qz-Ab-Or-H_2O-CO_2. Contributions to Mineralogy and Petrology 106(3):286-295

Edgar A, Arima M (1983) Conditions of phlogopite crystallization in ultrapotassic volcanic rocks. Mineralogical Magazine 47(1):11-19

Elburg M, van Bergen MJ, Foden JD (2004) Subducted upper and lower continental crust contributes to magmatism in the collision sector of the Sunda-Banda arc, Indonesia. Geology 32(1):41-44

Esperança S, Holloway JR (1987) On the origin of some mica-lamprophyres: experimental evidence from a mafic minette. Contributions to Mineralogy and Petrology 95(2):207-216

Foley SF, Taylor WR, Green DH (1986) The effect of fluorine on phase relationships in the system $KAlSiO_4$-Mg_2SiO_4-SiO_2 at 28 kbar and the solution mechanism of fluorine in silicate melts. Contributions to Mineralogy and Petrology 93(1):46-55

Farmer GL, Glazner AF, Manley CR (2002) Did lithospheric delamination trigger late Cenozoic potassic volcanism in the southern Sierra Nevada, California? Geological Society of America Bulletin 114:754–768.

Fowler M, Henney P (1996) Mixed Caledonian appinite magmas: implications for lamprophyre fractionation and high Ba-Sr granite genesis. Contributions to Mineralogy and Petrology 126(1-2):199-215

Fowler M, Henney P, Darbyshire D, Greenwood P (2001) Petrogenesis of high Ba-Sr granites: the Rogart pluton, Sutherland. Journal of the Geological Society 158(3):521-534

Giannetti B, Luhr JF (1990) Phlogopite-clinopyroxenite nodules from high-K magmas, Roccamonfina Volcano, Italy: evidence for a low-pressure metasomatic origin. Earth and Planetary Science Letters 101:404-424

Green TH, Blundy JD, Adam J, Yaxley GM (2000) SIMS determination of trace element partition coefficients between garnet, clinopyroxene and hydrous basaltic liquids at 2-7.5 GPa and 1080-1200°C. Lithos 53:165-187

Greene AR, DeBari SM, Kelemen PB, Blusztajn J, Clift PD (2006) A Detailed Geochemical Study of Island Arc Crust: the Talkeetna Arc Section, South-Central Alaska. Journal of Petrology 47(6):1051-1093

Grove T, Parman S, Bowring S, et al. (2002) The role of an H2O-rich fluid component in the generation of primitive basaltic andesites and andesites from the Mt. Shasta region, N California. Contrib Mineral Petrol 142:375–396.

Grove TL, Elkins-Tanton LT, Parman SW, Chatterjee N, Müntener O, Gaetani GA (2003) Fractional crystallization and mantle-melting controls on calc-alkaline differentiation trends. Contributions to Mineralogy and Petrology 145:515-533

Hermann J, Spandler CJ (2008) Sediment Melts at Sub-arc Depths: an Experimental Study. Journal of Petrology 49:717–740.

Hochstaedter AG, Ryan JG, Luhr JF (1996) On B/Be ratios in the Mexican volcanic belt. ... et Cosmochimica Acta 60:613–628.

Holloway JR, Burnham CW (1972) Melting relations of basalt with equilibrium water pressure less than total pressure. Journal of Petrology 13(1):1-29

Holtz F, Barbey P, Johannes W, Pichavant M (1989) Composition and temperature at the minimum point in the Qz-Ab-Or system for H_2O-undersaturated conditions. Experimental investigation. Terra Cognita 1:271-272

Irvine TN, Baragar WRA (1971) A Guide to the Chemical Classification of the Common Volcanic Rocks. Canadian Journal of Earth Sciences 8(5):523-548

Jagoutz O, Müntener O, Schmidt MW, Burg J-P (2011) The roles of flux- and decompression melting and their respective fractionation lines for continental crust formation: Evidence from the Kohistan arc. Earth and Planetary Science Letters 303(1-2):25-36

Jagoutz O, Schmidt MW (2012) The formation and bulk composition of modern juvenile continental crust: The Kohistan arc. Chemical Geology 298-99:79-96

Jagoutz O, Schmidt MW (2013) The composition of the foundered complement to the continental crust and a re-evaluation of fluxes in arcs. Earth and Planetary Science Letters

Jagoutz OE (2010) Construction of the granitoid crust of an island arc. Part II: a quantitative petrogenetic model. Contributions to Mineralogy and Petrology 160:359-381

Janousek V, Farrow CM, Erban V (2006) Interpretation of whole-rock geochemical data in igneous geochemistry: introducing geochemical data toolkit (GCDkit). J Petrol 47:1255-1259.

Kelemen PB, Hanghoj K, Greene AR (2003) 3.18 - One View of the Geochemistry of Subduction-Related Magmatic Arcs, with an Emphasis on Primitive Andesite and Lower Crust. In: Editors-in-Chief: Heinrich DH, Karl KT (eds) Treatise on Geochemistry, vol. Pergamon, Oxford, pp 1-70

Khain EV, Bibikova EV, Salnikova EB, Kröner A, Gibsher AS, Didenko AN, Degtyarev KE, Fedotova AA (2003) The Palaeo-Asian ocean in the Neoproterozoic and early Palaeozoic: new geochronological data and palaeotectonic reconstructions. Precambrian Research 122:329-358

Kovalenko DV, Mongush, AA, Ageeva, OA, Eenzhin, G. (2014) Sources and Geodynamic Environments of Formation of Vendian-Early Paleozoic Magmatic Complexes in the Daribi Range, Western Mongolia. Petrology 22:389-417.

Kozakov IK, Salnikova EB, Khain EV, Kovach VP, Berezhnaya NG, Yakoleva SZ, Plotkina YV (2002) Early Caledonian Crystalline Rocks of the Lake Zone in Mongolia: Formation History and Tectonic Settings as Deduced from U-Pb and Sm-Nd Datings. Geotectonics 36(2):156-166

Krawczynski MJ, Grove TL, Behrens H (2012) Amphibole stability in primitive arc magmas: effects of temperature, H_2O content, and oxygen fugacity. Contributions to Mineralogy and Petrology 164(2):317-339

Kress VC, Carmichael, ISE (1991) The compressibility of silicate liquids containing Fe_2O_3 and the effect of composition, temperature, oxygen fugacity and pressure on their redox states. Contributions to Mineralogy and Petrology 108:82-92.

Kuno H (1966) Lateral variation of basalt magma type across continental margins and island arcs. Bulletin Volcanologique

Kushiro I (1987) A petrological model of the mantle wedge and lower crust in the Japanese island arcs. Physicochemical Principles. Geochem Soc Spec Publ, no. 1, ed. Mysen, BO.

Lackey JS, Valley JW, Chen JH, Stockli DF (2008) Dynamic magma systems, crustal recycling, and alteration in the central Sierra Nevada batholith: The oxygen isotope record. Journal of Petrology 49(7):1397-1426

Lameyre J, Bowden P (1982) Plutonic rock types series: discrimination of various granitoid series and related rocks. Journal of Volcanology and Geothermal Research 14(1):169-186

LaTourrette T, Hervig RL, Holloway JR (1995) Trace element partitioning between amphibole, phlogopite, and basanite melt. Earth and Planetary Science Letters 135:13-30

Le Bas MJ, Le Maitre RW, Streckeisen A, Zanettin B (1986) A Chemical Classification of Volcanic Rocks Based on the Total Alkali-Silica Diagram. Journal of Petrology 27(3):745-750

Lee C-TA, Morton DM, Kistler RW, Baird AK (2007) Petrology and tectonics of Phanerozoic continent formation: from island arcs to accretion and continental arc magmatism. Earth and Planetary Science Letters 263(3):370-387

Lobach-Zhuchenko SB, Rollinson H, Chekulaev VP, Savatenkov VM, Kovalenko AV, Martin H, Guseva NS, Arestova NA (2008) Petrology of a Late Archaean, Highly Potassic, Sanukitoid Pluton from the Baltic Shield: Insights into Late Archaean Mantle Metasomatism. Journal of Petrology 49(3):393-420

Luth WC, Jahns RH, Tuttle OF (1964) The granite system at pressures of 4 to 10 kilobars. Journal of geophysical research 69(4):759-773

Middlemost EAK (1994) Naming materials in the magma/igneous rock system. Earth-Science Reviews 37(3-4):215-224

Miller CF (1977) Early alkalic plutonism in the calc-alkalic batholithic belt of California. Geology 5(11):685-688

Miller CF (1978) Monzonitic plutons, California, and a model for generation of alkali-rich, near silica-saturated magmas. Contributions to Mineralogy and Petrology 67(4):349-355

Müntener O, Kelemen P, Grove T (2001) The role of H2O during crystallization of primitive arc magmas under uppermost mantle conditions and genesis of igneous pyroxenites: an experimental study. Contributions to Mineralogy and Petrology 141(6):643-658

Müntener O, Ulmer P (2006) Experimentally derived high-pressure cumulates from hydrous arc magmas and consequences for the seismic velocity structure of lower arc crust. Geophysical Research Letters 33(21):L21308

Nicholls I, Whitford D (1983) Potassium-rich volcanic rocks of the Muriah complex, Java, Indonesia: products of multiple magma sources? Journal of Volcanology and Geothermal Research 18(1):337-359

Peccerillo A, Taylor SR (1976) Geochemistry of eocene calc-alkaline volcanic rocks from the Kastamonu area, Northern Turkey. Contributions to Mineralogy and Petrology 58(1):63-81

Rapela C, Pankhurst R (1996) Monzonite suites: the innermost Cordilleran plutonism of Patagonia. Transactions of the Royal Society of Edinburgh-Earth Sciences 87(1):193-204

Righter K, Carmichael ISE (1996) Phase equilibria of phlogopite lamprophyres from western Mexico: biotite-liquid equilibria and P-T; estimates for biotite-bearing igneous rocks. Contributions to Mineralogy and Petrology 123(1):1-21

Roberts MP, Clemens JD (1993) Origin of high-potassium, calc-alkaline, I-type granitoids. Geology 21(9):825-828

Rudnick RL, Gao S (2003) The composition of the continental crust. In: Rudnick RL (ed) The Crust : Treatise on Geochemistry, vol. Elsevier, Oxford, pp 1-64

Sato H (1977) Nickel content of basaltic magmas: identification of primary magmas and a measure of the degree of olivine fractionation. Lithos 10(2):113-120

Schmidt MW, Vielzeuf D, Auzanneau E (2004) Melting and dissolution of subducting crust at high pressures: the key role of white mica. Earth and Planetary Science Letters 228:65–84.

Sengör AMC, Natalín BA, Burtman VS (1993) Evolution of the Altaid tectonic collage and Palaeozoic crustal growth in Eurasia. Nature 364:299-307

Sengör AMC, Natalín BA, Burtman VS (1994) Tectonic evolution of Altaides. Russian Geology and Geophysics 35:33-47

Sisson TW, Grove TL (1993) Experimental investigations of the role of H_2O in calc-alkaline differentiation and subduction zone magmatism. Contributions to Mineralogy and Petrology 113:143-166

Sisson TW, Ratajeski K, Hankins WB, Glazner AF (2005) Voluminous granitic magmas from common basaltic sources. Contributions to Mineralogy and Petrology 148:635-661

Stolper E, Newman S (1994) The role of water in the petrogenesis of Mariana trough magmas. Earth and Planetary Science Letters 121:293–325. doi: 10.1016/0012-821X(94)90074-4

Sun S, McDonough WF (1989) Chemical and isotopic systematics of oceanic basalts: implications for mantle composition and processes. Geological Society, London, Special Publications 42(1):313-345

Sylvester AG, Miller CF, Nelson C (1978) Monzonites of the White-Inyo Range, California, and their relation to the calc-alkalic Sierra Nevada batholith. Geological Society of America Bulletin 89(11):1677-1687

Sylvester PJ (1989) Post-collisional alkaline granites. The Journal of Geology:261-280

Tatsumi Y, Sakuyama M, Fukuyama H (1983) Generation of arc basalt magmas and thermal structure of the mantle wedge in subduction zones. Journal of Geophysical Research 88:5815–5825.

Taylor SR, McLennan SM (1985) The Continental Crust: Its Composition and Evolution. Blackwell, Oxford

Tuttle OF, Bowen NL (1958) Origin of Granite in the Light of Experimental Studies in the System $NaAlSi_3O_8$-$KAlSi_3O_8$-SiO_2-H_2O. Geological Society of America,

Villemant B, Jaffrezic H, Joron J-L, Treuil M (1981) Distribution coefficients of major and trace elements; fractional crystallization in the alkali basalt series of Chaîne des Puys (Massif Central, France). Geochimica et Cosmochimica Acta 45(11):1997-2016

Wheller GE, Varne R, Foden JD, Abbott MJ (1987) Geochemistry of Quaternary volcanism in the Sunda-Banda arc, Indonesia, and three-component genesis of island-arc basaltic magmas. Journal of Volcanology and Geothermal Research 32:137–160.

Wolf MB, Wyllie PJ (1994) Dehydration-melting of amphibolite at 10 kbar: the effects of temperature and time. Contributions to Mineralogy and Petrology 115(4):369-383

3.7 Figures and Captions

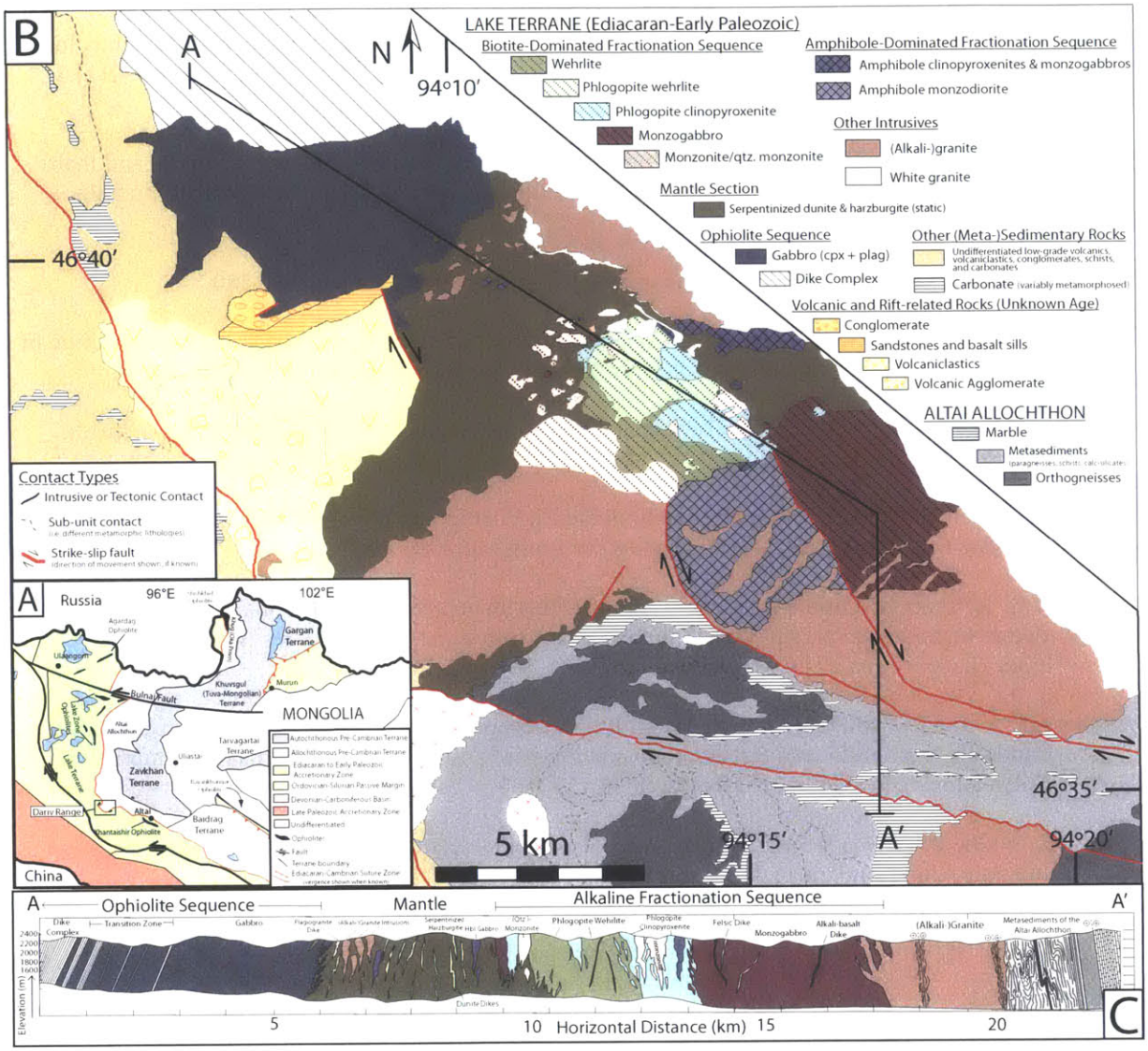

Fig. 3-1: (a) Simplified terrane map of Mongolia. Notably, Mongolia consists of Pre-Cambrian autochthonous terranes surrounded by accreted allochthonous terranes, ophiolites, and island arc-related units to the south and west. The Dariv Range is located at the boundary of the Pre-Cambrian Altai Allochthon and the Lake Terrane and is isolated from neighboring ranges by >25 km wide, mainly tertiary basins. (b) Geological map of the detailed study area in the NW part of the Dariv Range showing relationships between the Lake Terrane (the tholeiitic ophiolite sequence, the mantle section, the alkaline fractionation sequence, and low grade metasediments) and the metamorphic Altai Allochthon. The geologic map is based on own field mapping, interpretation of Landsat images, and previously constructed maps of the area (Dijkstra et al. 2006, Khain et al. 2003). (c) Cross-section through Dariv Range showing the overall structure and relationship between various units. Profile location is indicated in Fig. 3-1b. Note that most contacts in this profile are intrusive in nature. The only two major faults are within the red (alkali-)granites.

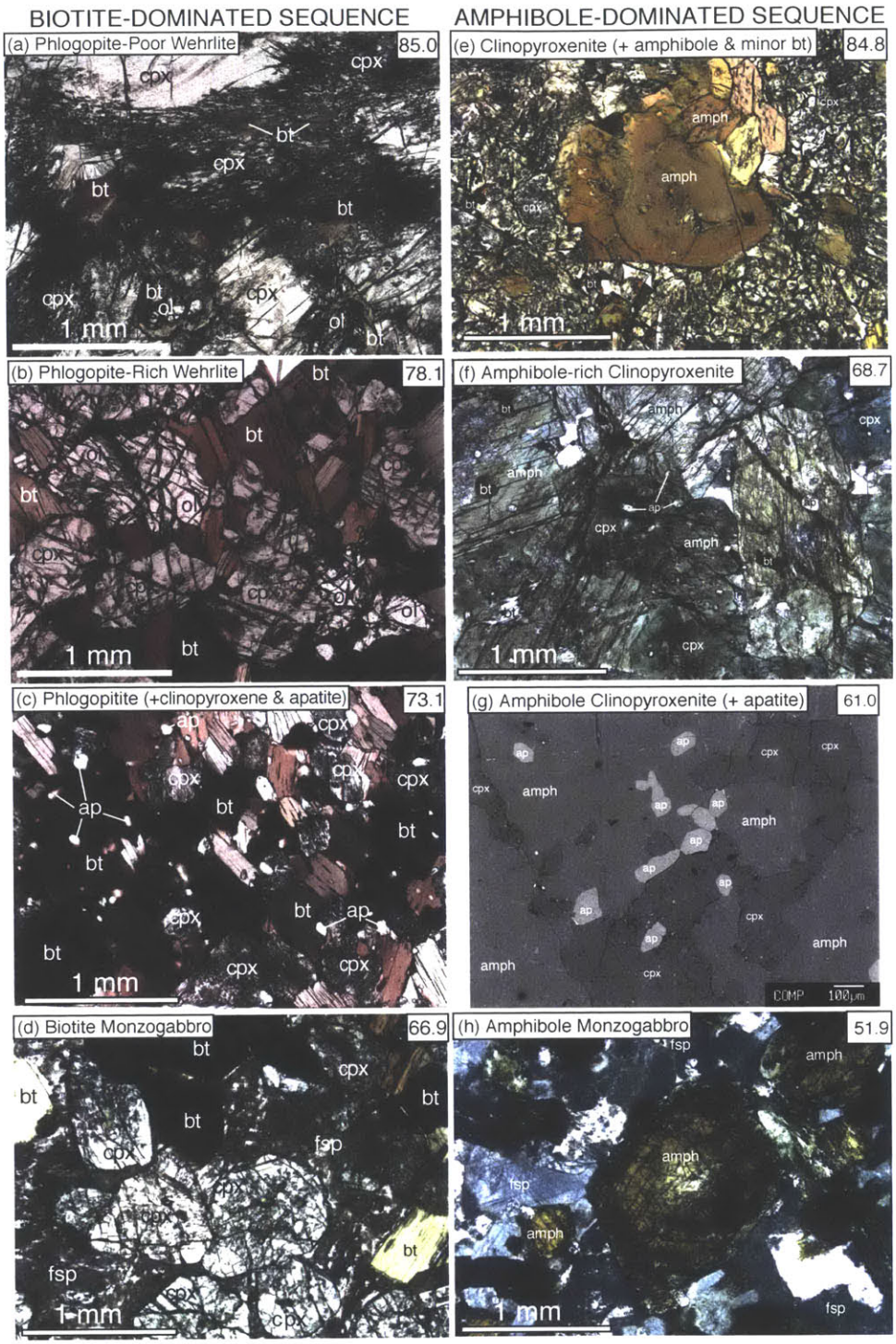

Fig. 3-2: Representative photomicrographs illustrating the ultramafic and mafic lithologies of the two studied fractionation sequences. Photomicrographs in the left column (a-d) are from the biotite-dominated sequence, whereas those in the right column (e-h) are from the amphibole-dominated sequence. Whole rock Mg# (molar $Mg/(Mg+Fe^T)$) are plotted in the upper right corners of the images. All images, except g, were taken in plane-polarized light. g is a backscattered electron image. All thin sections are 100 μm thick. Mineral abbreviations are as in Fig. 3-4. a) Phlogopite-poor wehrlite (MO-10-394). b) Phlogopite-rich wehrlite (MO-10-392) with increased modal percent of biotite. c) Clinopyroxene phlogopitite (MO-11-10) with abundant and large apatite crystals. d) Biotite monzogabbro (MO-11-12) with biotite, clinopyroxene, and feldspar. e) Clinopyroxenite with amphibole and minor biotite (MO-10-398). f) Amphibole-rich clinopyroxenite with apatite (MO-9-251). g) Amphibole clinopyroxenite with apatite (MO-10-329). h) Amphibole monzogabbro (MO-10-309a).

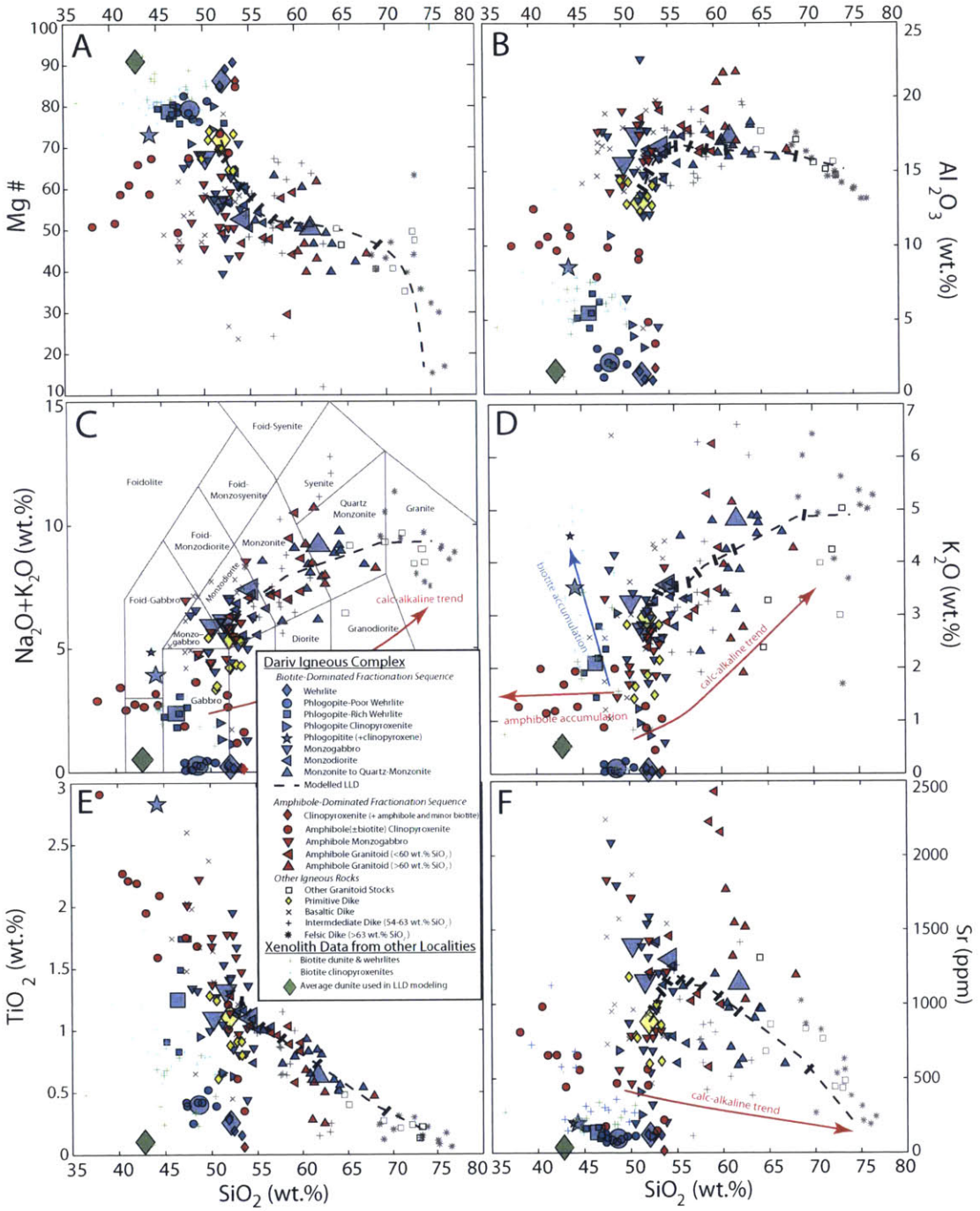

Fig. 3-3: Whole rock Mg#, major, and trace elements versus SiO_2 with results of the LLD model described in the text. All analyses are plotted on an anhydrous basis. The black dashed line marks the calculated LLD. Ticks on LLD indicate the melt composition at 10% intervals of melt remaining. Larger faded symbols indicate average cumulate compositions used in the LLD modeling. Red arrows represent the general trend for the calc-alkaline series based on whole rock data from the Sierra Nevada Batholith (Lackey et al., 2008) and the Kohistan Arc (Jagoutz (2010)). Xenolith data is from Buhlmann et al. (2000), Downes et al. (2004), and Giannetti and Luhr (1990). (a) Mg#, (b) Al_2O_3, (c) $Na_2O + K_2O$ (TAS plot modified for plutonic rocks (Le Bas et al. 1986; Middlemost 1994)) (d) K_2O, (e) TiO_2, (f) Sr.

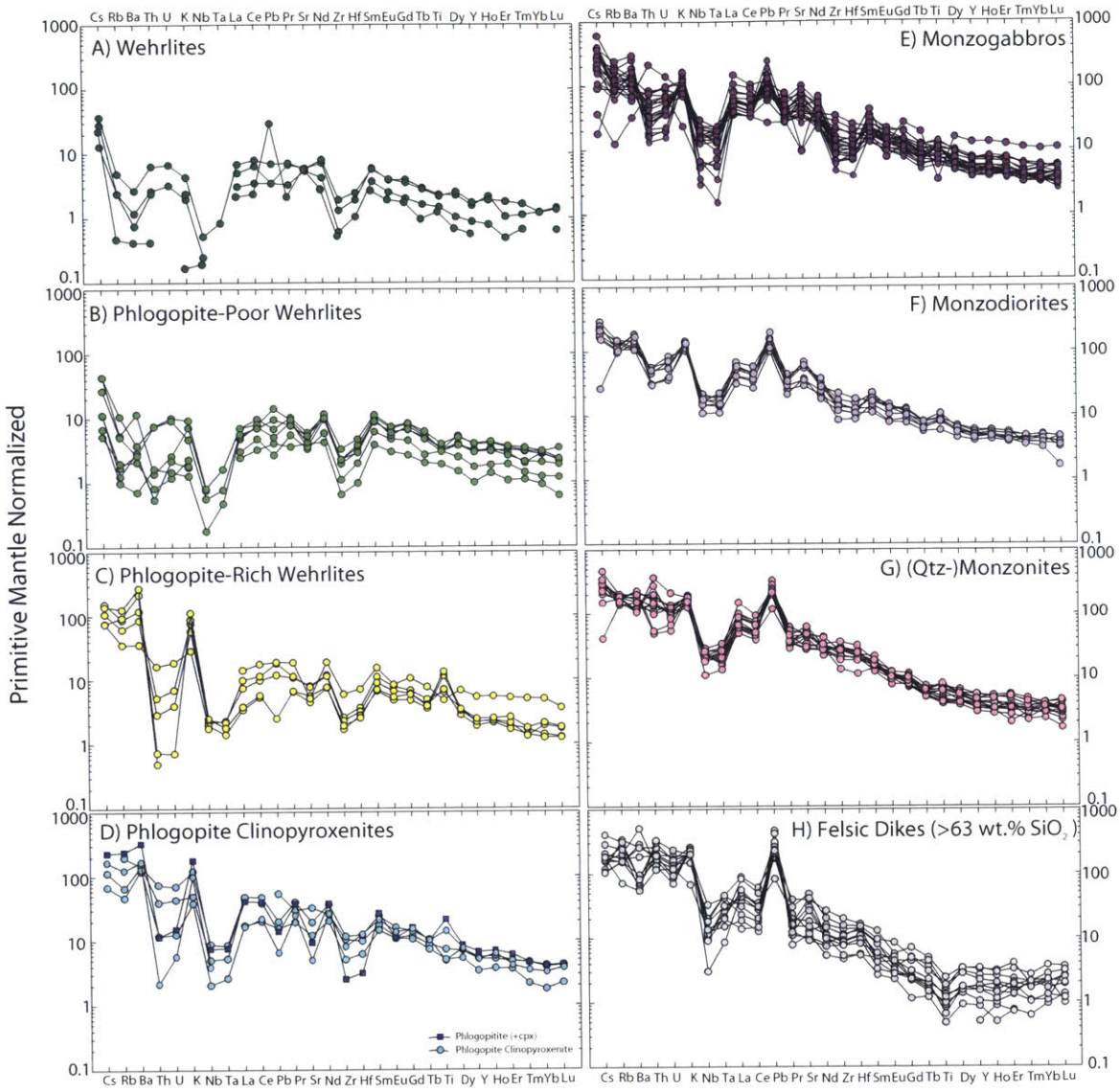

Fig. 3-4: Trace element spider diagrams normalized to primitive mantle for the biotite-dominated fractionation sequence, (Sun and McDonough 1989) for (a) wehrlites, (b) phlogopite-poor wehrlites, (c) phlogopite-rich wehrlites, (d) phlogopite clinopyroxenites and phlogopitite, (e) monzogabbros, (f) monzodiorites, (g) (quartz-)monzonites, and (h) late-stage felsic dikes.

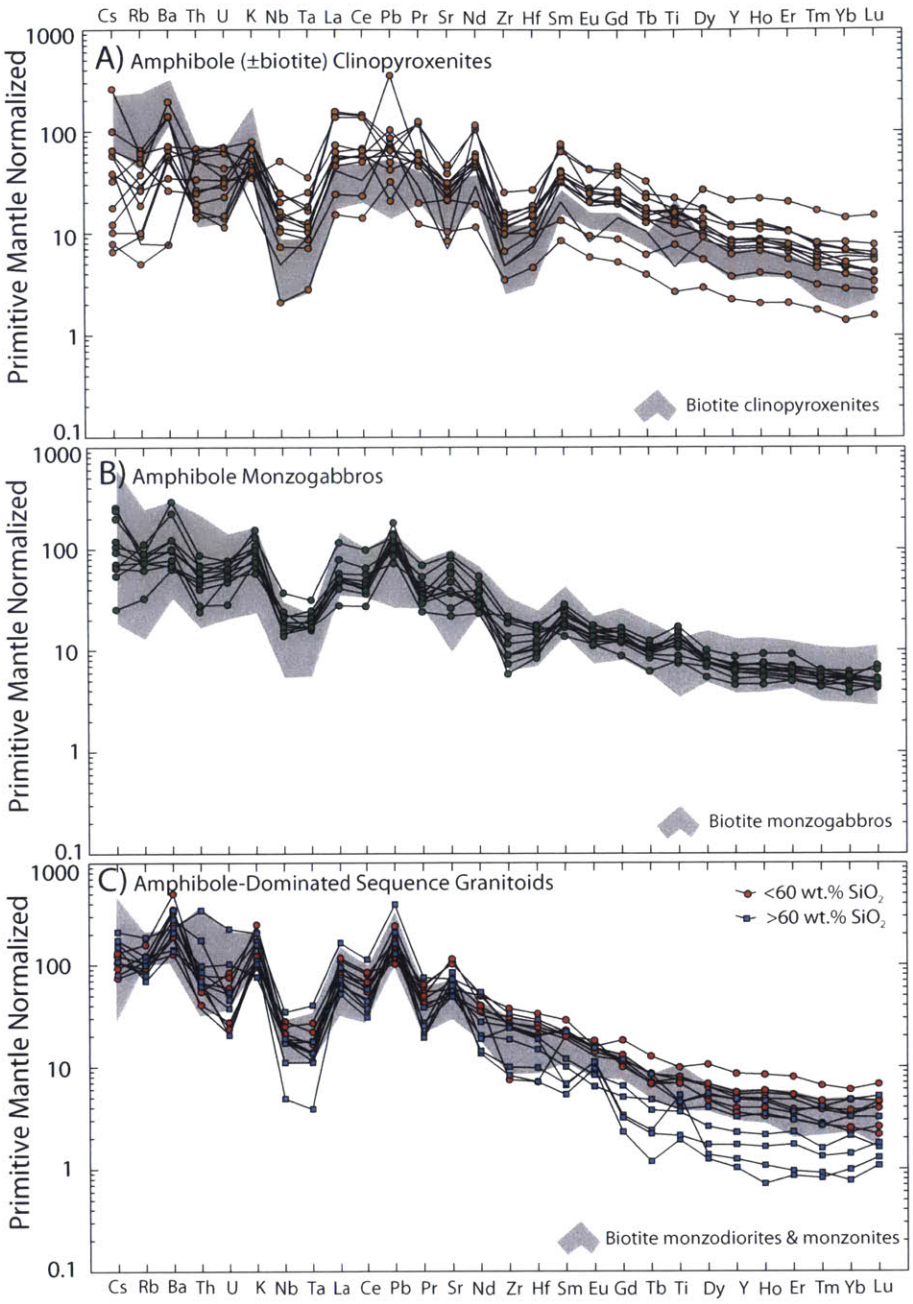

Fig. 3-5: Trace element spider diagrams normalized to primitive mantle for the amphibole-dominated fractionation sequence, (Sun and McDonough 1989) for (a) amphibole(±biotite) clinopyroxenites, (b) amphibole monzogabbros, and (c) granitoids divided based on SiO_2 content. Shaded gray areas indicate the range in composition for similar lithologies of the biotite-dominated sequence.

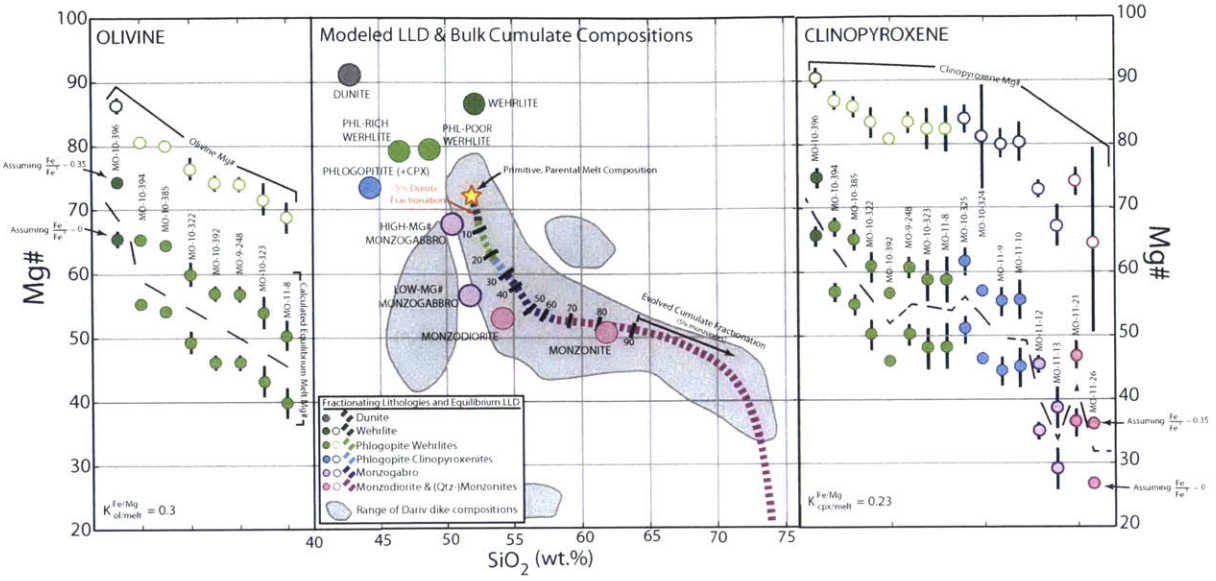

Fig. 3-6: Summary of Mg# constraints on LLD modeling. Central panel shows Mg# versus SiO_2 (wt.%) of modeled LLD (dashed line) which is colored according to which lithology is crystallizing. Ticks with increments of 10 adjacent to them represent the mass % crystallized at a given point in the LLD trajectory. Large colored circles are the average bulk compositions of the cumulate lithologies used in the model. "Phl" = phlogopite. The gray area indicates field of analyzed dike compositions from the Dariv Range, which are assumed to mostly represent liquid compositions. However, a few outlier dike groups from the main trend likely result from crystal accumulation. Adjacent panels show Mg# of olivine (left) and clinopyroxene (right), in addition to the Mg# of calculated equilibrium melts. Open colored circles are averages (with $2\sigma_{SD}$ error bars) of analyzed Mg# of olivine and clinopyroxene for available samples. Error bars are omitted for clinopyroxene calculated melts for clarity, but are equivalent to those shown for measured minerals. Filled symbols are the calculated equilibrium melt Mg#. The equilibrium melt Mg# was calculated assuming a K_d(Fe-Mg) of 0.3 for olivine-melt (Roeder & Emslie, 1970) and 0.23 for clinopyroxene-melt (Sisson and Grove (1993)). Two calculated melts are shown, one considering all Fe present as Fe^{2+} and the other assuming that $Fe^{3+}/Fe^{T} = 0.35$. This ratio value is equivalent to an oxygen fugacity of +2.3 ΔQFM at 1200°C and 3000 bars (Kress & Carmichael, 1991), an intermediate value for the estimated oxygen fugacity of crystallization for the phlogopite ultramafic cumulates (+1.8 to +3.2 ΔQFM). Lower and higher Fe^{3+}/Fe^{T} ratios would shift the calculated melt Mg# to lower and higher values, respectively. A black dashed line is included for clarity to separate the two different melt calculations.

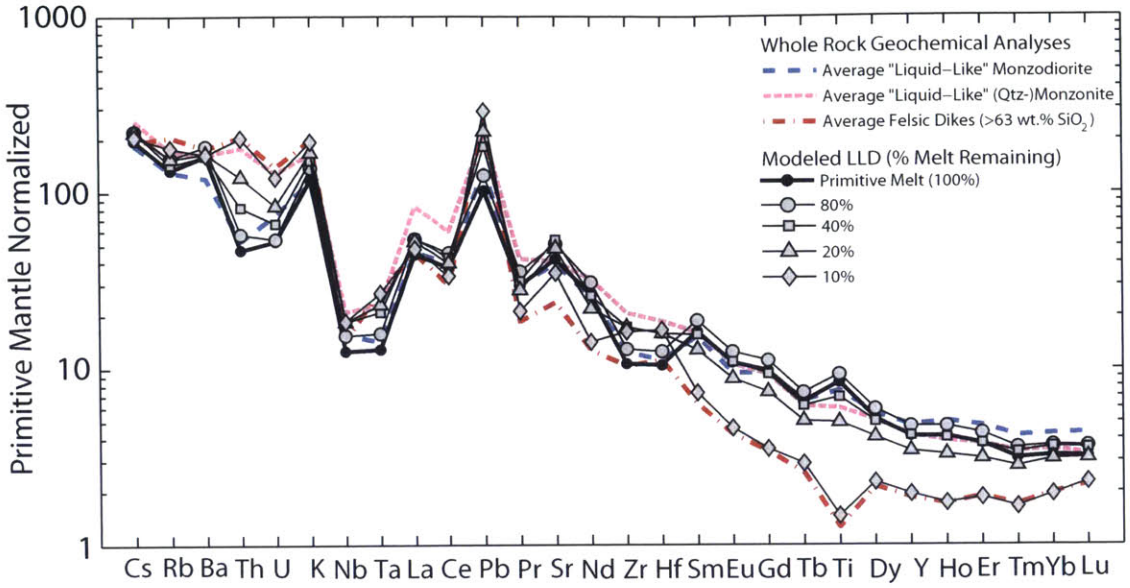

Fig. 3-7: Trace element spider diagram showing results of LLD modeling compared to "liquid-like" whole rock compositions of the biotite dominated fractionation sequence. "Liquid-like" feldspar-bearing samples were identified by their lack of cumulate signature as described in the text under "Model Description". Elements are normalized to primitive mantle composition (Sun and McDonough 1989). Modeled LLD are shown at 80, 40, 20, and 10% melt mass remaining.

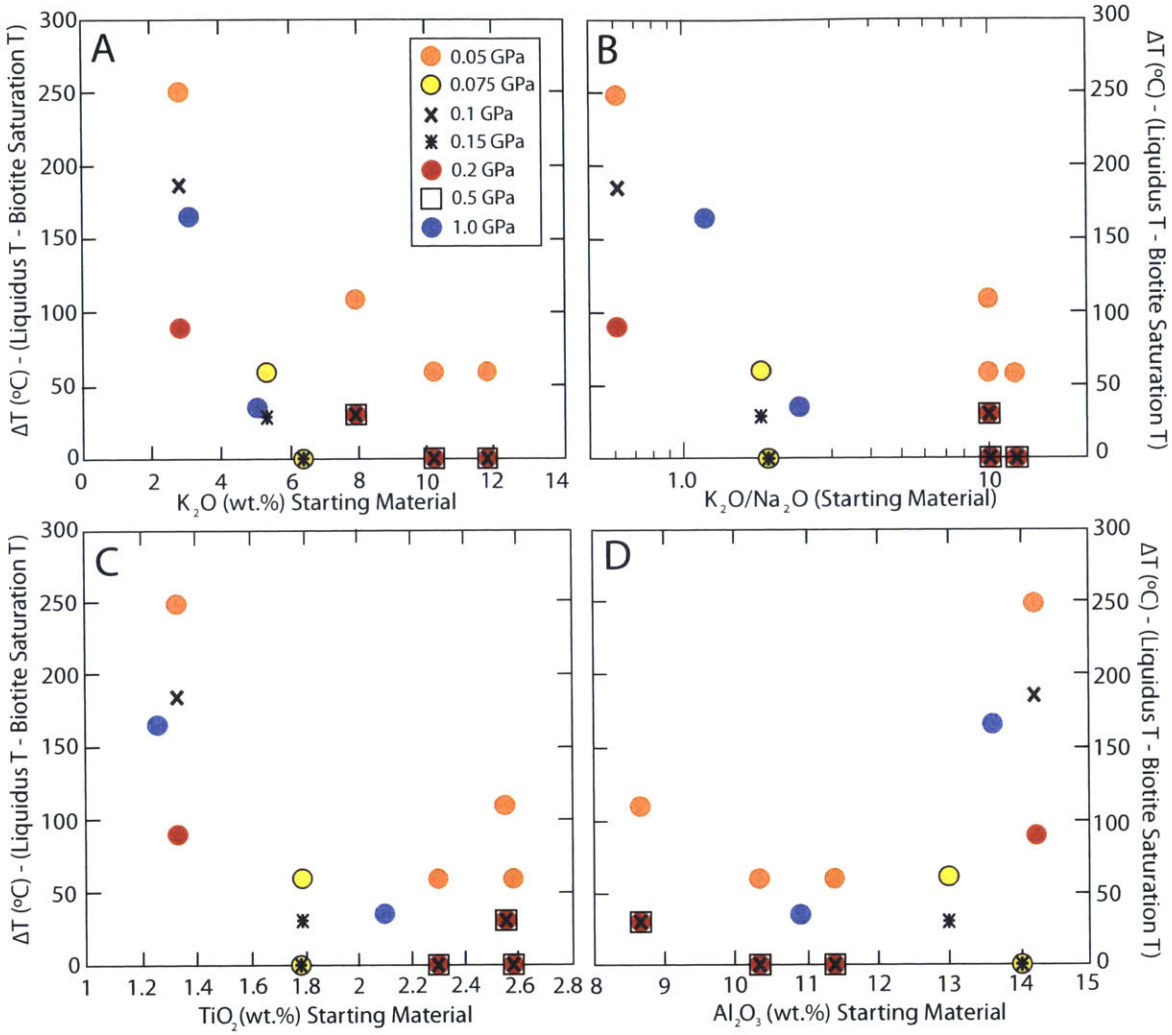

Fig. 3-8: Difference in temperature between the liquidus and biotite saturation versus various compositional parameters of high-K basaltic experimental starting materials at various pressures. Experimental data is from Barclay and Carmichael (2004), Barton and Hamilton (1978), Esperança and Holloway (1987), Nicholls and Whitford (1983), and Righter and Carmichael (1996). (Barclay and Carmichael 2004; Esperança and Holloway 1987; Nicholls and Whitford 1983; Righter and Carmichael 1996). $T_{liquidus}$ of the experiments vary between 1090-1230°C. (a) K_2O, (b) K_2O/Na_2O, (c) TiO_2, (d) Al_2O_3.

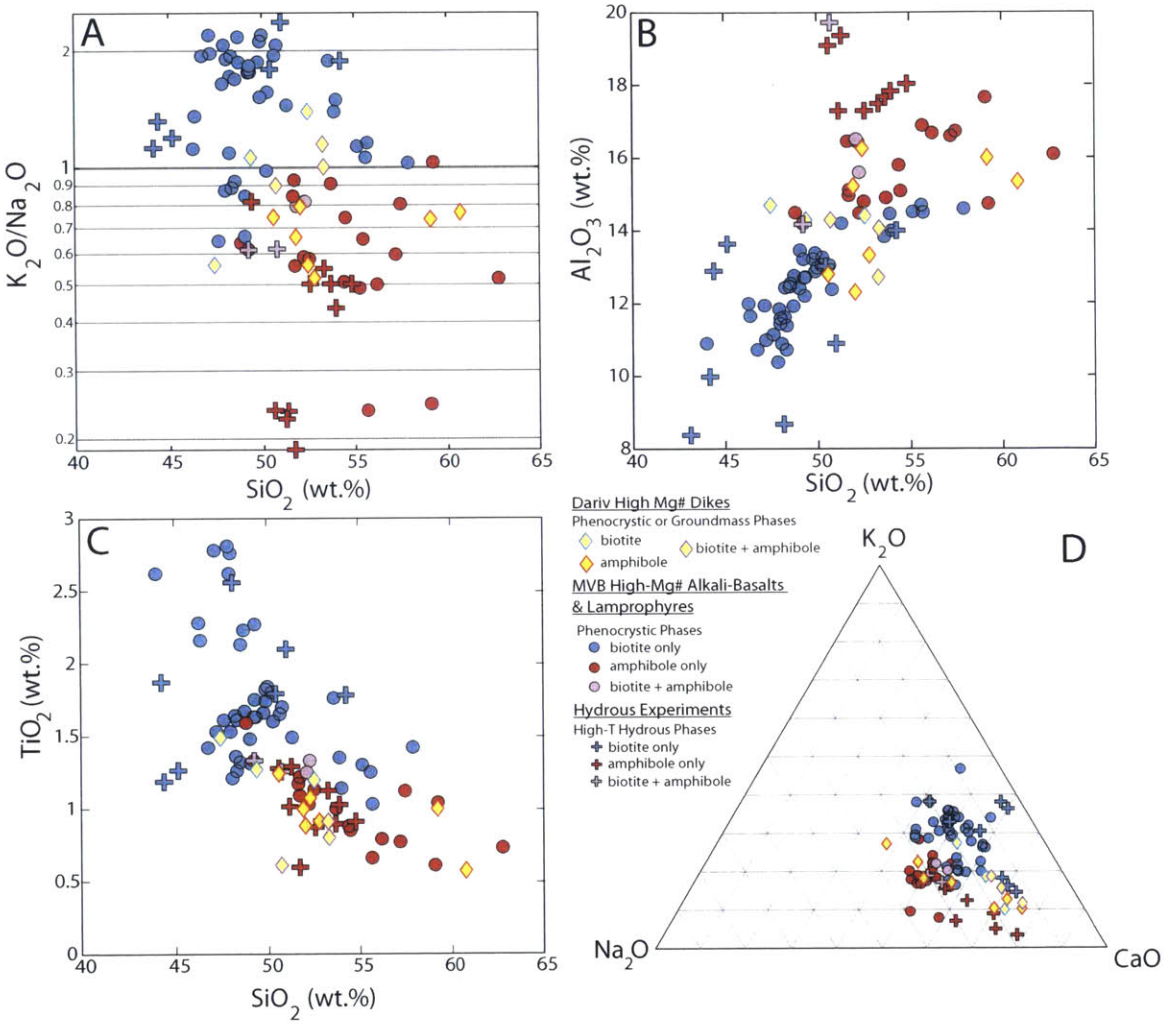

Fig. 3-9: Geochemistry of high-K basalts and hydrous experiments saturated with biotite and/or amphibole in comparison to the Dariv high-Mg# dike compositions. (a) K_2O/Na_2O v. SiO_2 (note that y-axis is a logarithmic scale), (b) Al_2O_3 v. SiO_2, (c) TiO_2 v. SiO_2, (d) CaO-NaO-K_2O. Mexican Volcanic Belt high Mg# alkali-basalts and lamprophyre data (colored circles) are from Allan and Carmichael (1984), Carmichael et al. (1996), Luhr et al. (1989), Luhr and Carmichael (1985), Maria and Luhr (2008), Ownby et al. (2008), Righter and Rosas-Elguera (2001), Vigouroux et al. (2008), Wallace and Carmichael (1989), and Wallace and Carmichael (1992). Amphibole-saturated experimental data (red crosses) are from Alonso-Perez et al. 2009, Di Carlo et al. 2006, Grove et al. 2003, Müntener et al. 2001, Sisson and Grove 1993, and Sisson et al. 2005. Biotite-saturated experimental data (blue crosses) are from Barton and Hamilton (1978), (1979), Edgar and Arima (1983); Edgar and Condliffe (1978), Edgar et al. (1976), Elkins-Tanton and Grove (2003), Esperança and Holloway (1987), Nicholls and Whitford (1983), and Righter and Carmichael (1996). The biotite- and amphibole-saturated experimental data (purple crosses) are from Barclay and Carmichael (2004) and Sisson et al. (2005).

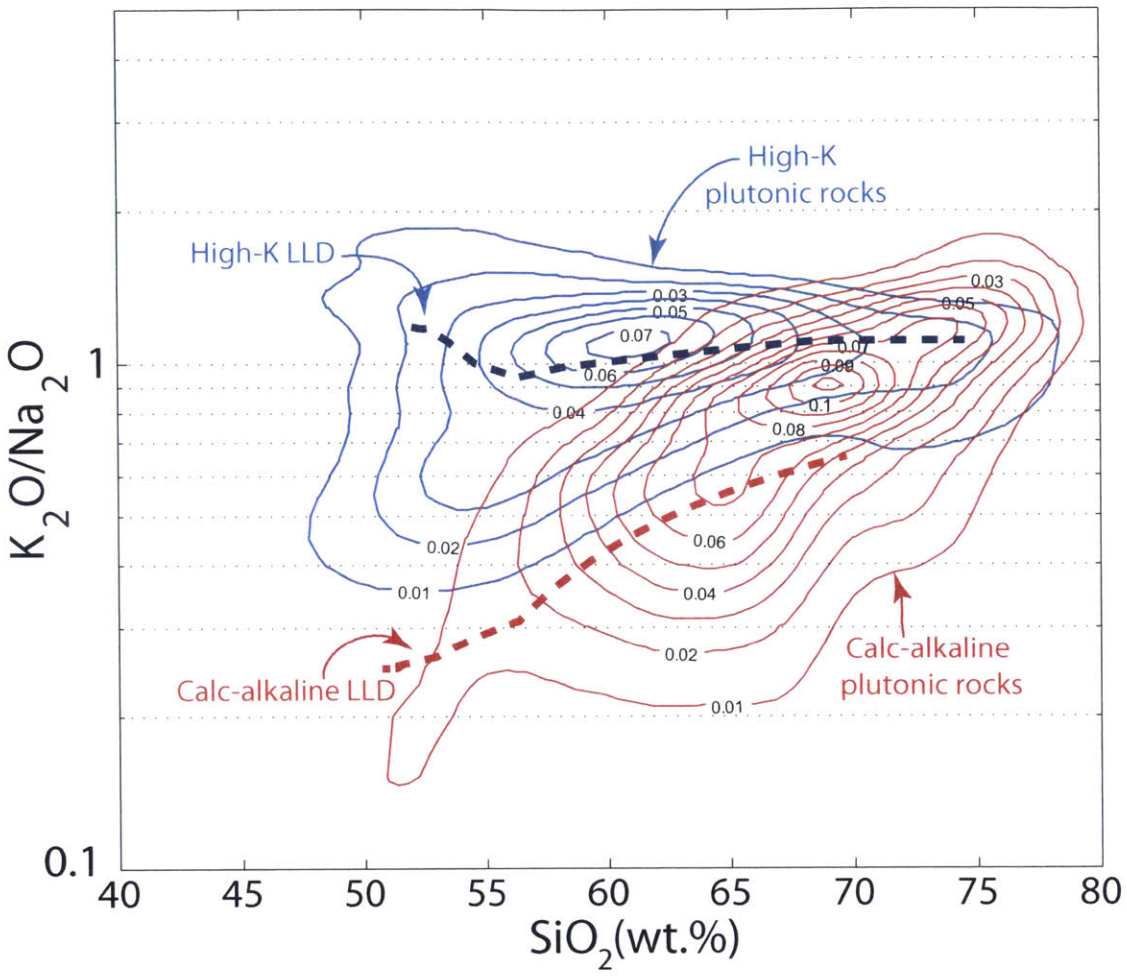

Fig. 3-10: Comparison of K_2O/Na_2O with SiO_2-enrichment for a high-K versus calc-alkaline LLD and arc-related plutonic rocks ($45 < SiO_2 < 80$ wt.%). Data is from the Sierra Nevada, the Peninsular Range Batholith, Southern California Permo-Triassic intrusion, and GEOROC database (http://georoc.mpch-mainz.gwdg.de/georoc/). High-K versus calc-alkaline designation is defined by the K_2O v. SiO_2 classification of Pecerillo and Taylor (1976). Sierra Nevada data is from Lackey et al. (2008) and Bateman (1961) . Peninsular Range Batholith data is from Lee et al. (2007). Southern California Permo-Triassic granitoid data is from Barth and Wooden (2006). Arc-related monzodiorites, monzonites, and quartz-monzonites are from the GEOROC database. Note that y-axis is shown with a logarithmic scale. Probability density function contours are plotted using GCDKit 2.3 (Janousek et al., 2006).

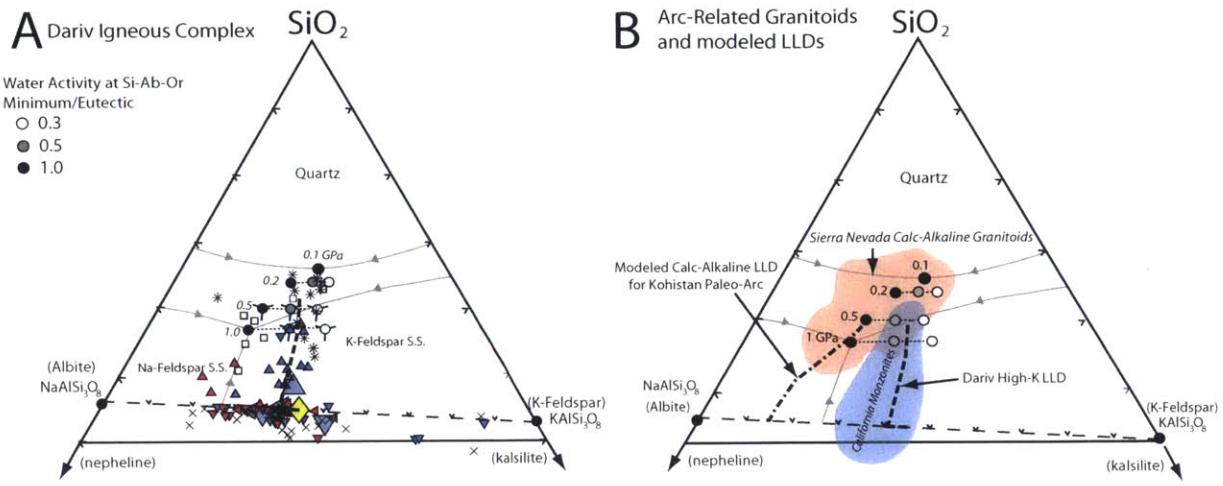

Fig. 3-11: Ternary phase diagram in nepheline-kalsilite-quartz system. Figures are zoomed into the section containing the end members albite-K-feldspar-quartz (Ab-Or-Qz). Phase boundaries are from Ebadi and Johannes (1991), Holtz et al. (1989), (1991), Luth et al. (1964), and Tuttle and Bowen (1958). The position of the minimum/euctectic at different water activities are shown by white, gray, and black circles for water activities of 0.3, 0.5, and 1.0, respectively. Minimum/eutectic positions are shown for pressures of 0.1, 0.2, 0.5, and 1.0 GPa. (a) Projected whole rock data from the Dariv Igneous Complex in the $SiO_2 \geq 60\%$ portion of the Qz-Ne-Ks ternary. Data is projected using calculated CIPW norm compositions (mass %) following the projection scheme of Blundy and Cashman (2001) to account for normative anorthite component. For both the amphibole-dominated and biotite-dominated sequence, monzogabbros mostly have >35 wt.% Qz-Ks-Ne (including Or + Ab recalculated into Qz, Ks, and Ne). Biotite monzodiorites and amphibole sequence granitoids with <60 wt.% SiO_2 have 40-52 wt.% and 47-74 wt.% Qz-Ks-Ne, respectively. (Qtz-)monzonites, amphibole sequence granitoids with >60 wt.% SiO_2, and late stage felsic dikes have 60-95 wt.% Qz-Ks-Ne. All symbols as in Fig. 3-3. The primitive melt composition (yellow diamond) used in the LLD model (dashed line) is shown for reference. Bulk cumulate compositions used in LLD model are shown as larger faded symbols. Cotectics at water-saturated conditions at 0.1 and 1.0 GPa are shown as gray lines with arrows. (b) Modeled Dariv high-K LLD and Kohistan paleo-arc calc-alkaline LLD compared to arc-related granitoids in the Qz-Ab-Or ternary. Blue field of California monzonites is from Miller (1977). Red field for calc-alkaline granitoids from the Sierra Nevada is from compilation described in Fig. 3-10.

3.8 TABLES

Table 3-1 Compositions used in LLD model.

	PARENTAL MELT		FRACTIONATED CUMULATE COMPOSITIONS																	
			***Phlogopite Dunite			Wehrlite		Phlogopite-Poor Wehrlite		Phlogopite-Rich Wehrlite		Phlogopite-Rich Clinopyroxenite	High Mg# Monzogabbro		Low Mg# Monzogabbro		Monzodiorite		Monzonite	
	Model Composition**	Average (N=3)*	2σ	N=3*	2σ	N=3*	2σ	N=7*	2σ	N=4*	2σ	N=1*	N=5*	2σ	N=5*	2σ	N=4*	2σ	N=3*	2σ
SiO_2	52.00	51.35	3.57	42.81	1.32	52.07	0.66	48.62	2.33	46.38	1.54	44.25	50.23	3.75	51.57	2.24	54.27	2.81	61.69	5.55
TiO_2	1.10	0.90	0.56	0.10	0.04	0.26	0.12	0.40	0.16	1.25	0.88	2.83	1.10	0.44	1.32	0.36	1.10	0.14	0.63	0.29
Al_2O_3	12.90	14.28	1.59	1.55	0.64	1.34	0.62	2.12	1.33	5.46	1.95	8.55	15.55	4.02	17.53	2.61	16.68	1.17	17.34	2.09
FeO	7.85	7.66	1.59	8.06	1.99	5.60	1.98	10.26	2.21	9.94	2.82	10.60	8.08	0.91	8.14	1.48	7.69	1.37	4.52	1.93
MnO	0.16	0.18	0.05	0.12	0.04	0.14	0.05	0.24	0.05	0.20	0.06	0.19	0.17	0.02	0.17	0.06	0.16	0.04	0.08	0.03
MgO	11.26	10.83	2.88	45.45	1.74	19.74	1.21	21.94	5.34	20.65	4.46	16.14	9.47	1.86	5.98	1.72	4.80	1.77	2.58	1.82
CaO	8.70	9.96	1.12	1.01	0.23	20.34	1.01	15.96	4.10	13.51	3.04	11.97	8.85	1.58	8.54	1.42	7.31	2.02	3.67	2.09
Na_2O	2.50	2.21	0.72	-	-	0.15	0.10	0.17	0.20	0.29	0.16	0.41	2.68	0.44	3.39	0.95	3.83	0.44	4.36	0.92
K_2O	2.96	2.21	1.14	0.52	0.17	0.07	0.06	0.10	0.16	2.09	1.13	3.52	3.25	1.58	2.73	1.14	3.57	1.46	4.82	0.12
P_2O_5	0.49	0.40	0.39	0.06	0.02	0.02	0.01	0.02	0.01	0.05	0.13	1.43	0.56	0.28	0.60	0.22	0.59	0.14	0.30	0.21
Cr2O3	0.08	0.03	0.09	0.32	-	0.28	0.18	0.16	0.22	0.19	0.06	0.11	0.06	0.07	0.03	0.04	0.02	0.01	0.01	0.01
Total	100.00	100.00	-	100.00	-	100.00	-	100.00	-	100.00	-	100.00	100.00	-	100.00	-	100.00	-	100.00	-
Mg#	71.9	71.50	9.35	91.0	2.3	86.3	4.9	79.1	4.5	78.8	2.9	73.1	67.6	3.4	56.6	3.1	52.7	4.2	50.4	12.2
Sc	24.3	25.3	6.0	4.7	1.2	47.2	12.0	51.4	19.1	44.2	17.6	40.6	22.9	2.7	20.6	5.0	18.6	7.9	7.3	6.4
V	203	172	58	28	22	85	56	186	122	267	213	558	189	63	189	77	200	86	64	61
Cr	579	602	241	2967	800	1750	1139	1262	653	1206	384	739	390	451	185	194	151	32	50	59
Ni	239	160	127	2330	81	208	15	355	244	331	233	289	120	116	50	30	53	11	17	29
Zn	59.0	62.8	10.7	55.7	26.1	25.0	14.4	53.3	25.2	51.2	10.5	64.0	63.1	14.1	66.9	14.5	68.1	9.6	46.8	13.5
Rb	85	71	25	23	8	2	2	2	4	58	33	152	105	83	84	47	83	41	116	6
Sr	889	856	478	36	4	121	13	96	42	137	73	197	1397	1199	1154	786	1300	287	1139	419
Y	18.9	21.8	8.3	1.9	1.0	6.3	4.1	12.7	10.0	10.0	2.1	30.4	23.3	11.5	23.5	8.8	22.2	6.6	14.9	3.2
Zr	120	159	153	7	4	14	15	22	19	24	9	28	102	48	165	186	204	139	293	85
Nb	9.0	9.3	10.8	0.6	0.2	0.2	0.4	0.2	0.5	1.6	0.3	5.3	9.3	8.4	13.4	5.7	13.0	3.2	14.9	2.5
Cs	1.55	1.83	1.41	1.15	0.92	0.20	0.19	0.17	0.26	0.94	0.56	1.80	1.88	3.92	1.65	0.54	1.83	1.05	2.10	1.58
Ba	1125	766	516	197	71	11	14	27	50	1217	1227	2287	1382	1060	797	689	1173	557	1421	587
La	30.7	42.4	27.4	1.7	0.7	3.4	2.6	3.5	2.4	4.2	4.3	28.2	43.8	24.6	38.5	8.7	39.7	9.1	47.1	35.8
Ce	67.0	87.7	56.6	3.7	1.9	10.5	8.0	12.1	7.7	14.4	10.8	70.8	101.9	61.0	80.5	18.4	81.9	13.4	89.6	58.8
Pr	8.2	10.3	6.7	-	-	1.6	1.2	2.1	1.3	2.4	1.4	10.3	12.8	8.1	9.9	2.9	9.6	1.0	9.7	4.7
Nd	35.6	42.4	26.4	2.2	1.5	8.8	5.3	12.2	7.6	13.1	6.4	51.3	54.8	34.0	42.2	14.5	40.3	4.5	36.4	12.8
Sm	7.22	7.65	4.46	0.55	0.38	2.27	1.10	3.73	2.29	3.77	1.82	11.84	10.17	6.01	8.36	3.17	8.12	1.86	6.22	0.74
Eu	1.82	1.93	1.06	0.17	0.16	0.58	0.27	0.94	0.49	1.04	0.45	1.83	2.72	1.59	2.28	0.97	2.17	0.45	1.83	0.46
Gd	5.80	6.04	2.68	-	-	1.87	1.19	3.75	2.45	3.52	0.98	9.49	7.78	4.98	6.92	2.68	6.69	1.54	4.38	0.31
Tb	0.700	0.791	0.364	0.068	0.047	0.264	0.156	0.483	0.333	0.446	0.123	1.085	0.949	0.532	0.810	0.236	0.777	0.161	0.591	0.092
Dy	3.85	4.18	1.84	0.42	0.27	1.42	1.16	2.69	1.94	2.41	0.44	6.25	4.96	2.57	4.55	1.73	4.36	0.91	3.00	0.42
Ho	0.680	0.810	0.210	-	-	0.262	0.236	0.488	0.346	0.378	0.049	1.139	0.847	0.483	0.863	0.325	0.785	0.222	0.500	0.084
Er	1.81	2.15	0.81	-	-	0.53	0.62	1.27	0.87	1.00	0.38	2.92	2.23	0.98	2.37	0.86	2.08	0.71	1.44	0.33
Tm	0.230	0.282	0.177	-	-	0.084	0.072	0.169	0.131	0.114	0.032	0.337	0.272	0.077	0.287	0.099	0.291	0.164	0.203	0.074
Yb	1.58	1.80	0.75	0.19	0.04	0.40	0.68	1.10	0.85	0.82	0.41	2.02	1.82	0.72	1.98	0.99	2.06	0.78	1.38	0.49
Lu	0.235	0.281	0.135	0.032	0.006	0.084	0.063	0.145	0.132	0.112	0.044	0.313	0.266	0.086	0.311	0.117	0.291	0.086	0.154	0.057
Hf	3.25	3.81	3.34	0.25	0.01	0.56	0.44	0.92	0.75	0.95	0.31	0.97	2.68	0.97	5.48	3.24	4.71	2.61	6.82	1.90
Ta	0.53	0.57	0.67	0.03	0.01	0.01	0.04	0.02	0.05	0.08	0.03	0.31	0.43	0.43	0.69	0.21	0.80	0.18	0.80	0.28
Pb	7.3	5.0	4.9	2.0	1.1	0.3	0.3	0.4	0.7	0.6	1.2	1.0	5.6	6.2	7.5	2.8	11.0	6.7	20.9	4.5
Th	4.0	7.6	5.3	0.6	0.2	0.3	0.4	0.2	0.5	0.2	0.4	1.0	3.3	4.4	4.2	4.9	3.4	1.8	8.9	9.1
U	1.11	1.82	0.12	3.81	2.87	0.07	0.14	0.08	0.17	0.06	0.14	0.32	1.02	1.39	1.28	1.24	0.97	0.45	2.02	1.18

* N equals the number of samples of a lithology included in average. Analyses recalculated on an anhydrous basis with all Fe calculated as FeO^T.
** Composition used in LLD model.
*** Average of WC-232, WC-253, & WC-251 from Downes *et al.* (2004)

Table 3-2 Calculated LLD Compositions

% Melt Remaining	*0.90*	*0.80*	*0.70*	*0.60*	*0.50*	*0.40*	*0.30*	*0.20*	*0.10*
SiO_2	52.56	53.28	54.47	55.28	56.28	57.48	58.98	61.31	68.36
TiO_2	1.18	1.20	1.03	1.00	0.98	0.90	0.80	0.64	0.19
Al_2O_3	14.10	15.31	16.36	16.59	16.79	16.66	16.52	16.44	16.19
FeO	7.86	7.58	7.18	7.00	6.78	6.45	5.96	5.11	2.54
MnO	0.16	0.15	0.15	0.14	0.14	0.13	0.12	0.10	0.04
MgO	8.93	7.38	6.01	5.33	4.51	4.05	3.62	3.04	1.28
CaO	8.61	7.89	7.27	6.96	6.59	6.10	5.50	4.60	1.90
Na_2O	2.76	3.08	3.45	3.62	3.80	3.92	4.02	4.11	4.39
K_2O	3.24	3.45	3.49	3.53	3.59	3.79	4.00	4.21	4.85
P_2O_5	0.53	0.60	0.53	0.51	0.50	0.48	0.45	0.38	0.17
Cr2O3	0.06	0.05	0.03	0.03	0.02	0.02	0.02	0.01	0.00
Total	100	100	100	100	100	100	100	100	100
Mg#	66.9	63.5	59.9	57.6	54.2	52.8	52.0	51.5	47.4
Sc	24.1	21.3	18.5	17.5	16.4	15.3	13.9	11.6	4.5
V	217	213	174	168	163	157	144	117	33
Cr	399	294	216	181	140	124	109	89	27
Ni	124	97	69	58	46	43	40	33	14
Zn	60.4	61.5	61.5	61.3	60.9	59.5	56.8	51.2	34.3
Rb	93	99	95	92	90	91	93	98	113
Sr	975	1084	1210	1191	1151	1144	1113	1021	741
Y	20.3	21.5	21.0	20.5	19.9	19.0	17.7	15.5	8.9
Zr	131	145	162	173	187	194	197	193	183
Nb	9.9	11.0	11.9	12.5	13.1	13.1	13.1	13.1	13.2
Cs	1.64	1.76	1.78	1.76	1.74	1.76	1.76	1.72	1.62
Ba	1232	1274	1169	1121	1070	1123	1163	1158	1142
La	33.7	37.5	39.6	39.0	38.1	37.8	37.4	36.3	32.9
Ce	73.3	80.9	84.3	81.5	77.5	76.2	74.5	70.8	59.8
Pr	9.0	9.9	10.1	9.6	9.0	8.7	8.4	7.7	5.9
Nd	38.7	42.0	42.0	39.9	36.9	35.3	33.3	29.8	19.3
Sm	7.81	8.33	8.11	7.73	7.25	6.93	6.49	5.68	3.24
Eu	1.97	2.09	2.15	2.06	1.93	1.84	1.71	1.47	0.77
Gd	6.28	6.62	6.43	6.17	5.85	5.56	5.15	4.39	2.09
Tb	0.752	0.790	0.771	0.738	0.696	0.665	0.622	0.545	0.312
Dy	4.14	4.35	4.21	4.06	3.89	3.71	3.46	3.02	1.67
Ho	0.734	0.776	0.751	0.730	0.707	0.669	0.618	0.535	0.284
Er	1.96	2.07	2.02	1.97	1.92	1.82	1.68	1.49	0.89
Tm	0.248	0.264	0.261	0.258	0.256	0.248	0.235	0.207	0.122
Yb	1.70	1.81	1.82	1.81	1.81	1.77	1.69	1.51	0.96
Lu	0.253	0.269	0.270	0.270	0.271	0.263	0.250	0.230	0.168
Hf	3.54	3.88	4.29	4.59	4.96	4.91	4.85	4.93	5.14
Ta	0.58	0.65	0.71	0.76	0.82	0.86	0.90	0.95	1.10
Pb	7.9	8.9	10.0	10.8	11.9	13.0	14.2	15.8	20.6
Th	4.4	4.9	5.5	5.9	6.4	7.0	8.0	10.3	17.3
U	1.02	1.14	1.26	1.31	1.37	1.40	1.50	1.76	2.55

CHAPTER 4:
Oxygen Isotope Trajectories of Crystallizing Melts

Abstract

Elevated oxygen isotope values in igneous rocks are often used to fingerprint supracrustal alteration or assimilation of material that once resided near the surface of the earth. The $\delta^{18}O$ value of a melt, however, can also increase through closed-system fractional crystallization. In order to quantify the change in melt $\delta^{18}O$ due to crystallization, we develop a mass balance modeling method that incorporates variable temperatures of crystallization, melt compositions, and crystallizing mineralogy. For comparison with our model, we measured $\delta^{18}O$ values of mineral separates from a relatively dry, tholeiitic sequence from the Upper and Upper Main Zones (UUMZ) of the Bushveld Complex (South Africa) and a high-K, hydrous sequence from the arc-related Dariv Igneous Complex (Mongolia). We calculated equilibrium melt $\delta^{18}O$ values using the measured mineral $\delta^{18}O$ values in combination with previously constrained liquid lines of descent (LLDs) and magmatic temperatures. Increases of 2-3‰ and 1-1.5‰ in the equilibrium melts are observed for the Dariv Igneous Complex and the Bushveld Complex, respectively. Our new modeling method reproduces the 1‰ increase observed in the equilibrium melt $\delta^{18}O$ for the Bushveld UUMZ, whereas for the Dariv Igneous Complex, a single assimilation step (resulting in an increase in the melt of 1.2‰) must be incorporated to account for the increase in melt $\delta^{18}O$ values. We demonstrate that melt fraction-temperature-SiO_2 relationships of crystallizing melts, which are strongly a function of magmatic water content, will control the specific $\delta^{18}O$ path of a crystallizing melt. Hydrous, calc-alkaline melts undergo larger increases in $\delta^{18}O$ during early stages of crystallization due to their lower magmatic temperatures, greater initial increases in SiO_2 content, and high temperature stability of low $\delta^{18}O$ phases, such as oxides, amphibole, and anorthitic plagioclase. Conversely, relatively dry, tholeiitic melts only experience significant enrichment in $\delta^{18}O$ at melt fractions less than ~0.2. Total calculated increases in melt $\delta^{18}O$ of 1.0 to 1.8‰ can be attributed to crystallization from ~50 to 70 wt.% SiO_2 for modeled LLDs. As primitive basalts produced at subduction zones have values from ~5.7-8.0‰, whole rock $\delta^{18}O$ values of ~7-9.8‰ in granites can be explained through fractional crystallization of mantle-derived melts alone without invoking intracrustal assimilation of high $\delta^{18}O$ material. Lastly, our model results demonstrate that it is critical to consider the effect of specific temperature-SiO_2 relationships of a crystallizing melt on mineral-melt fractionations when using mineral $\delta^{18}O$ analyses, such as zircon, to calculate bulk magmatic $\delta^{18}O$ values.

4.1 Introduction

As oxygen is the most abundant element in the silicate Earth, oxygen isotopes are a powerful and widely used tool to study the source and magmatic evolution of igneous rocks. In particular, enrichments or depletion in $\delta^{18}O$ values of igneous rocks and minerals can yield information about the degree of

mantle versus crustal material involved in their origin. The standard interpretation is that igneous rocks enriched in ^{18}O compared to basalts from mid-ocean ridges ($\delta^{18}O$[1] = 5.7±0.2‰) must have interacted with material that resided on or near the surface of the earth, either through contamination of the mantle by subduction of surface materials or through direct assimilation in the crust (Bindeman, 2008; Eiler, 2001; Harmon and Hoefs, 1995; Taylor and Sheppard, 1986).

Elevated $\delta^{18}O$ melt values, however, may also arise through closed-system fractional crystallization if the crystallizing mineral assemblage is dominated by minerals depleted in ^{18}O relative to the melt. In general, equilibrium $\delta^{18}O$ values of igneous minerals decrease in the following order: quartz > alkali-feldspar > calcic plagioclase > biotite > apatite > orthopyroxene > zircon > clinopyroxene > amphibole > garnet > olivine > oxides (see summary in Eiler, 2001; Valley, 2003). Minerals such as olivine, magnetite, garnet, pyroxenes, and hornblende have lower $\delta^{18}O$ values than basaltic melts at magmatic temperatures (Fig. 4-1a) and crystallizing mineral assemblages dominated by these minerals will enrich the residual melt with ^{18}O (Fig. 4-1b). Conversely, crystallization and fractionation of quartz or feldspars from a melt can result in ^{18}O depletion. Increases or decreases in melt $\delta^{18}O$ values will be enhanced at lower crystallization temperatures where mineral-melt fractionations are larger (Fig. 4-1a). Thus the magnitude of change during fractional crystallization of a melt will be strongly dependent on both the crystallizing mineral assemblages and temperature, which are in turn controlled by a number of factors, including melt composition and water content, as well as, the pressure and oxidation state of crystallization.

As melts from different tectonic settings are characterized by distinct melt compositions and conditions of crystallization, it may be expected that the changes in melt $\delta^{18}O$ values during fractional crystallization could be variable in these different locations. For example, anhydrous tholeiitic basalts from mid-ocean ridges are dominated by olivine, clinopyroxene, and plagioclase crystallization at relatively high magmatic temperatures (1330-900°C) (Grove et al., 1992; Stolper, 1980; Villiger et al., 2004; Walker et al., 1979; Whitaker et al., 2007). Relatively limited enrichments in ^{18}O in a crystallizing tholeiitic melt would be expected due to the high temperatures of crystallization and a crystallizing assemblage rich in plagioclase. In contrast, hydrous calc-alkaline basalts typical of subduction zones are characterized by crystallization of anorthite-rich plagioclase, hornblende, pyroxenes, oxides, and garnet at relatively lower temperatures (1200-650°C) (Alonso-Perez et al., 2009; Jagoutz, 2010; Melekhova et al., 2015; Müntener et al., 2001; Nandedkar et al., 2014; Sisson and Grove, 1993; Sisson et al., 2005). Fractional crystallization of such low $\delta^{18}O$ mineral assemblages at low magmatic temperatures would be expected to produce more pronounced enrichments in melt $\delta^{18}O$ values of crystallizing calc-alkaline melts.

---

[1] $\delta^{18}O$ values reported in this chapter are always relative to Standard Mean Ocean Water (SMOW). $\Delta^{18}O_{A\text{-}B}$ is the isotopic fractionation between phase A and B and is equal to $\delta^{18}O_A - \delta^{18}O_B$. We use subscripts after $\delta^{18}O$, $\Delta^{18}O$, and Mg# to indicate a mineral, melt, or whole rock sample. The following abbreviations are used: plagioclase (plag), clinopyroxene (cpx), orthopyroxene (opx), pyroxene (pyx), olivine (ol), fayalite (fay), zircon (zrc), qtz (quartz), whole rock (WR), mineral (min).

Consequently, liquid lines of descent (LLDs) defined by contrasting melt compositions and physical conditions of crystallization (e.g., tholeiitic versus calc-alkaline) may have distinctly different $\delta^{18}O_{melt}$ trajectories.

Although qualitative conclusions about the $\delta^{18}O_{melt}$ trajectory along different LLDs may be deduced from the above relationships, there has been no study that systematically addresses the effect of variable melt composition, crystallization conditions, and crystallizing mineralogy. Here we study the $\delta^{18}O$ trajectories of fractionally crystallizing melts ranging from dry, tholeiitic basalts to hydrous, calc-alkaline basalts to constrain the effect which closed-system magmatic differentiation can have on $\delta^{18}O_{melt}$ trajectories. We present a two-pronged approach to this problem. First, we develop a model for closed system crystallizing melt $\delta^{18}O$ trajectories based on incremental stepwise subtraction of calculated bulk cumulate $\delta^{18}O$ compositions from a known melt composition. To compare the model results to natural data, we present high precision mineral $\delta^{18}O$ data from two well-documented fractionation sequences, the Upper and Upper Main Zones of the Bushveld Complex (South Africa) and the Dariv Igneous Complex, (Mongolia). These sequences are comprised of rocks representing both cumulates and solidified melts that resulted from the crystallization of a parental low-H_2O, tholeiitic basalt (VanTongeren et al., 2010) and a hydrous high-K basalt (Chapters 2 & 3). Consequently, oxygen isotope analyses of minerals from these two sequences yield insight into the $\delta^{18}O$ trajectories of end-member LLDs. We compare the results of the closed-system fractional crystallization modeling to mineral $\delta^{18}O$ data to assess whether the two natural sequences represent closed systems or whether they experienced assimilation of material with a distinct $\delta^{18}O$ value. In light of our data and modeling results, we discuss the factors controlling the $\delta^{18}O_{melt}$ trajectories along different LLDs, highlighting the importance of magmatic water content. Further, we apply our modeling results to the zircon and igneous rock $\delta^{18}O$ record to constrain the range in $\delta^{18}O$ values permissible through closed-system fractional crystallization of mantle-derived melts alone. Lastly, we demonstrate that it is critical to consider variable melt trajectories when using $\delta^{18}O_{zrc}$ to calculate equilibrium $\delta^{18}O_{melt}$ values.

4.2 Background

4.2.1 Previous Studies on the Effects of Fractional Crystallization on Melt $\delta^{18}O$ Values

Although the effect of fractional crystallization on the $\delta^{18}O$ values of derivative melts has been the focus of numerous studies, there is no consensus on the magnitude of increases expected (Bindeman et al., 2004; Harris et al., 2000; Muehlenbachs and Byerly, 1982; Sheppard and Harris, 1985). Broadly, past investigations can be divided into two groups based on methodology; i.e., 1) those studying natural samples of either whole-rock powders or phenocrysts of extrusive rocks or minerals from layered mafic intrusions or 2) modeling studies based on calculated or experimental melt compositions and crystallized mineral phases. Below, we briefly review the findings of previous studies.

The oxygen isotope ratios of layered mafic intrusions classically received attention as they could potentially provide examples of closed-system differentiation of a single magma body. Although hydrothermal exchange obscured magmatic $\delta^{18}O$ whole rock and mineral values for the Skaergaard Intrusion (Taylor and Epstein, 1963; Taylor and Forester, 1979) and the Muskox Intrusion (Taylor, 1968), the Kiglapait Intrusion demonstrated close-system behavior with respect to oxygen isotopes (Kalamarides, 1984). Whole rock and mineral $\delta^{18}O$ data in the Kiglapait intrusion suggests negligible changes in $\delta^{18}O$ of derivative liquids formed by crystal fractionation of an anhydrous olivine tholeiite (< 0.1‰). The oxygen isotope variations in cogenetic suites of volcanic rocks have also been investigated. Studied systems include LLDs of tholeiitic basalts, (e.g., the Kiluaea Iki Lava Lake (Clayton et al., 1989) and the Galapagos Spreading Center (Muehlenbachs and Byerly, 1982)), ocean island alkali basalts (e.g., Ascension Island (Sheppard and Harris, 1985) and Tristan de Cunha and Gough Island (Harris et al., 2000)), hydrous calc-alkaline basalts (the Lesser Antilles (Tollan et al., 2012)), and volcanic rocks from Honshu and Hokkaido, Japan (Matsuhisa, 1979; Matsuhisa et al., 1973). These studies found positive, but ≤1‰ increases in $\delta^{18}O$ at 80% fractionation (Fig. 4-2). For the Galapagos Spreading Center, slightly more pronounced increases up to ~1.2‰ at 90% crystallization were observed, due to titanomagnetite crystallization and marked silica enrichment in the melt at late stages of differentiation of a Fe-Ti basalt (Muehlenbachs and Byerly, 1982).

Alternatively, modeling studies have investigated the effect of crystallization on melt $\delta^{18}O$ using experimentally-constrained (Eiler, 2001) or MELTS-calculated (Bindeman et al., 2004; Cooper et al., 2004) melt compositions, crystallizing mineralogy, and temperatures. Eiler (2001) calculated an increase of 0.6‰ over a SiO_2 range of 52-67 wt.% for equilibrium crystallization experiments on tholeiitic basalts from the Galapagos and the Kane Fracture Zone (Juster et al., 1989). Notably, significant increases in $\delta^{18}O$ occurred when the equilibrium melt SiO_2 content began to appreciably increase, resulting in preferential partitioning of ^{18}O into the melt rather than plagioclase. Cooper et al., (2004) modeled small increases (0.13-0.22‰) in $\delta^{18}O$ for crystallizing mid-ocean ridge basalts crystallizing over a limited range of SiO_2 between 48.5-54.3 wt.% (Fig. 4-2). Bindeman et al., (2004) presented a MELTS-based modeling study of several parental melt compositions including high-Mg basalts, tholeiitic basalts, shoshonites, and high-Al basalts with up to 1 wt.% H_2O. Their modeling results indicated a <0.4‰ increase in $\delta^{18}O$ over a melt SiO_2 content of 50-75 wt.% (Fig. 4-2).

Although these past studies provide an initial framework for assessing the effect of fractional crystallization on melt $\delta^{18}O$, they are limited in the number of different LLDs investigated and many are based on whole rock geochemical analyses, which are susceptible to secondary alteration. For example, existing studies of natural samples have focused primarily on $\delta^{18}O$ changes in crystallizing relatively dry tholeiitic basalts and alkali-basalts. Studies focusing on arc-related LLDs have been limited to tholeiitic trends (Matsuhisa, 1979; Matsuhisa et al., 1973), or have only quantified the effects at high melt fractions (~50% melt remaining) before significant melt SiO_2-enrichment has occurred (Tollan et al., 2012).

Similarly, modeling studies have been limited to tholeiitic trends (Cooper et al., 2004; Eiler, 2001) or minimally hydrous basalts (Bindeman et al., 2004). In this study, we provide a more comprehensive approach to the problem by modeling a number of melts with variable compositions, temperatures, and crystallized mineral assemblages. Further, we combine our modeling approach with mineral data from two end-member crystallization sequences. First, we provide a background on the two natural sequences selected for this study and describe our analytical methods before discussing the details of the model.

4.2.2. Geologic Setting, Petrology, and Previous Oxygen Isotope Investigations of Studied Sequences

Bushveld Complex, South Africa

The Rustenberg Layered Suite (RLS) of the Bushveld Complex, South Africa constitutes a complete, approximately 8 km thick stratigraphic section of progressively more evolved cumulate lithologies, from harzburgite near the base to fayalite and apatite-bearing diorite at the top (Cameron, 1980; 1978; Gruenewaldt, 1973; Molyneux, 1974). The RLS was emplaced in four main pulses of magma, roughly corresponding to the start of the Lower Zone, Critical Zone, Main Zone, and Upper Zone. The last major pulse of magma into the RLS occurred just below the level of the Pyroxenite Marker (Cawthorn et al., 1991; VanTongeren and Mathez, 2013). At this level a major reversal in major and trace element composition occurs coincidently with a break in $^{87}Sr/^{86}Sr$ values (Kruger et al., 1987; Sharpe, 1985). Above the Pyroxenite Marker, the observed cumulate phase assemblage indicates a crystallization sequence of pyroxene (pyx) + plagioclase (plg) → pyx + plg + magnetite (mgt) → pyx + plg + mgt + fayalite (fay) → pyx+ plg+ mt+ fay+ apatite. Fe-Mg silicate minerals become less magnesian and plagioclase more albite-rich towards the roof of the Upper Zone with no major reversals (Molyneux, 1974; Tegner et al., 2006; VanTongeren et al., 2010), suggesting no volumetrically significant additional input of magma or assimilation during crystallization. On the basis of this geochemical distinction, VanTongeren et al. (2010) interpreted the stratigraphic interval above the Pyroxenite Marker as a single tholeiitic fractionation sequence and termed it the combined Upper and Upper Main Zone (UUMZ). The volcanic rocks of the Rooiberg Group, the intrusive Rashoop Granophyre Suite (e.g. Stavoren Granophyre), and the Lebowa and Nebo Granites overly the RLS. VanTongeren et al. (2010) and Mathez et al. (2013) suggested that some portions of the felsic volcanic rocks of the Rooiberg Group and/or the Rashoop Granophyre are cogenetic with the RLS and represent the residual liquids from the prolonged fractionation of the UUMZ parental magma. In particular, Mathez et al. (2013) suggest that the highly ferroan, metaluminous Stavoren Granophyre is the best candidate for the escaped residual liquid after fractional crystallization of the UUMZ cumulate lithologies. Evidence supporting this hypothesis includes 1) their ε_{Nd} values (Twist and Harmer, 1987; Buchanan et al., 2004), oxygen isotope compositions (Fourie and Harris, 2011), and ages (e.g. Scoates et al., 2012) are similar to those of the RLS; and 2) quantitative geochemical modeling and mass balance calculations demonstrate that they are an appropriate melt counterpart to cumulates of the UUMZ (VanTongeren et al., 2010; VanTongeren and Mathez, 2012).

Data from previous oxygen isotope studies of the UUMZ relative to their stratigraphic height above the PM are shown in Figure 4-3. Plagioclase and pyroxene $\delta^{18}O$ values vary between 6.0-8.3‰ and 5.8-6.7‰, respectively, across the sequence (Harris and Chaumba, 2001; Harris et al., 2005; Schiffries and Rye, 1989). These mineral values correspond to $\delta^{18}O$ values of 6.8‰ and 7.3‰ for the parental melts in the Main/Critical and Upper Zones, respectively, suggesting that the parental magmas of the Bushveld Complex were enriched in ^{18}O compared to typical mantle-derived melts and required at least 10% of its oxygen to be derived from isotopically heavier crustal material (assuming an assimilant value of 15‰) (Schiffries and Rye, 1989). Analysis of quartz and zircon $\delta^{18}O$ values from the overlying granites and granophyres of the Bushveld Complex yield estimates of 6.6-6.9‰ for the original silicic magmas (Fourie and Harris, 2011).

A few points are important to note from these previous studies. First, multiple studies have demonstrated that the $\delta^{18}O$ values of the RLS magmas are ~1-1.5‰ higher than that of the typical value of mantle-derived melts (~5.7‰) (Harris and Chaumba, 2001; Reid et al., 1993; Schiffries and Rye, 1989). Second, the UUMZ in the Northern Limb differs from the Eastern and Western Limb of the RLS in its absence of a thick Pyroxenite Marker and therefore may have crystallized from a distinct magma. Therefore, differences between the data of the Northern Limb UUMZ analyses of Harris et al. (2005) and Harris and Chaumba (2001) and data presented in this study from the Eastern Limb UUMZ may be due to different mineralogy and melt compositions.

Dariv Igneous Complex, Western Mongolia

The Dariv Range of western Mongolia exposes the contact between the Proterozoic high-grade metamorphic rocks of the Altai Allochthon and the Lake Terrane, an Ediacaran to Early Paleozoic island arc system comprised of ophiolites and arc-related plutonic and volcano-sedimentary rocks (Badarch and Cunningham, 2002; Dijkstra et al., 2006; Khain, 2003). The km-scale, middle Cambrian Dariv Igneous Complex belongs to the latter and is comprised of a suite of high-K plutonic rocks, including phlogopite-bearing cumulative wehrlites and clinopyroxenites, mafic monzogabbro and monzodiorites, and (quartz-)monzonites that are cross-cut by late-stage high-SiO_2 and lamprophyre dikes (see Chapters 2 & 3 for detailed field and petrographic descriptions). The observed lithological variability, petrographic observations, mineral and whole rock geochemistry suggest that the plutonic rocks can be ascribed to a common fractionation sequence defined by a progression of crystallizing major mineralogy in the order of olivine + clinopyroxene (cpx) + phlogopite (phl) → cpx + phl + apatite → cpx + biotite (bt) + K-feldspar (kfsp) + plagioclase (plg) → cpx + bt + kfsp + plg + amphibole + quartz. Several primitive high-K basaltic dikes have compositions appropriate to be parental to the observed cumulate lithologies and the LLD of their average composition has been quantitatively modeled (Chapter 3). Although feldspar-bearing plutonic lithologies can range from cumulative to liquid-like in character, most quartz-monzonites and all of the aplite dikes have major and trace element compositions appropriate for liquid-dominated

plutonics representative of late-stage differentiated melts in the fractionation sequence. No previous oxygen isotope data has been reported for Dariv Igneous Complex.

4.3 Sample Selection and Analytical Methods

4.3.1 Sample Selection

Nine samples from the UUMZ of the Eastern Limb of the RLS were selected for analysis. These samples include gabbronorites to olivine-magnetite gabbros with whole rock Mg# (molar $Mg/(Mg+Fe_{total})*100$) varying from 74.7 to 9.2. Whole rock and mineral geochemistry for these samples are reported in VanTongeren et al. (2010). Stratigraphic height (in meters) is relative to the Pyroxenite Marker. Seventeen samples from the Dariv Igneous Complex were chosen from ultramafic phlogopite wehrlites to evolved quartz monzonites and felsic dikes. Whole rock Mg#'s range from 90.7 in the most primitive wehrlite to 32.2 in a felsic dike.

4.3.2 Infrared Laser Fluorination Analyses

Mineral separates and a whole rock powder were analyzed for $\delta^{18}O$ values by infrared laser fluorination technique (ILFT) with a CO_2 laser at Yale University. This method has been previously described by Eiler et al., (1996) and Wang et al., (2011), and is based on methods developed by Sharp (1990) and Valley et al., (1995). Whole rock samples were crushed either by hand or by disc mill to a grain size of <500 μm and sieved to obtain grain sizes between 150-500 μm. Samples were then ultrasonically cleaned in distilled water, separated using a Franz magnetic separator, and handpicked under a binocular microscope. Crystals with visible inclusions and/or alteration were discarded. For one sample of the host lithology of the Dariv Igneous Complex (MO-11-2, serpentinized harzburgite), a whole rock powder was prepared in an agate mill and pressed into a pellet for analysis. The total number of analyzed aliquots for different minerals and whole rock powders from the Dariv Igneous Complex are as follows: 6 olivine, 11 clinopyroxene, 13 phlogopite/biotite, 4 alkali-feldspar, 2 quartz, and 1 whole rock powder. For the Bushveld Complex, 3 clinopyroxene, 3 orthopyroxene, 9 plagioclase, and 3 fayalitic olivine aliquots were analyzed. All mineral aliquots were analyzed at least in duplicate to ensure reproducibility. Measurement of both garnet (UWG-2, Gore Mountain Garnet from New York) and olivine (KHX-1, Kilbourne Hole olivine from New Mexico) standards were interspersed between every four unknown measurements. Long term reproducibility of the standards are UWG-2 = 5.84 ± 0.10‰, KHX-1 = 5.27 ± 0.08‰, which compare favorably with the accepted values (UWG-2 = 5.80‰, (Valley et al., 1995), KHX-1 = 5.23‰, (Sharp, 1990), (see Appendix D). All oxygen isotope measurements of unknowns were corrected by the difference between the measured and accepted values for the standards bracketing their analysis. Average analytical precision was (~0.01‰, 1σ). For the Dariv Igneous Complex mineral separates, average 1σ per mil reproducibility is as follows for various minerals: olivine (0.03), clinopyroxene (0.04), biotite (0.06), and quartz (0.11). Feldspar duplicates were not reproducible. For the

Bushveld Complex, the range of 1σ per mil reproducibility is 0.04-0.20 for olivine, 0.02-0.12 for clinopyroxene, 0.01-0.07 for orthopyroxene, and 0.01-0.11 for feldspar.

4.3.3 SIMS Analyses

Zircons from six samples from the Dariv Igneous Complex were analyzed for *in situ* oxygen isotope ratios using the CAMECA IMS-1280 ion microprobe at the WiscSIMS Laboratory, University of Wisconsin-Madison. Zircons were separated through mechanical crushing using a disc mill, Frantz magnetic separation, and heavy liquid techniques. Hand-picked zircons were then mounted with zircon standard KIM-5 ($\delta^{18}O_{VSMOW}$ = 5.09‰; (Valley, 2003)) in in the center of a 1" epoxy mount and polished to expose centers of zircons. All grains were imaged by transmitted and reflected light on a petrographic microscope, and cathodoluminescence (CL) on the JEOL-JXA-733 electron microprobe at MIT to identify internal structures, exposed inclusions, and physical defects prior to selecting locations for SIMS analyses. The mount was sonicated in distilled water and ethanol prior to gold coating. Analytical procedures are described briefly below and in more detail elsewhere (e.g., Kita et al., 2009; Valley and Kita, 2009).

^{16}O, ^{18}O, and $^{16}O^{1}H$ were analyzed simultaneously on different Faraday cups. A $^{133}Cs^{+}$ primary ion beam (20 keV total impact voltage, 1.84-2.07 nA) was focused to an oval area of ~10 μm^2. A single measurement consisted of 10 s of pre-sputtering, 120 s of automatic tuning of the secondary beam, and 80 s of analysis, for a total of 3.5 minutes. Every 10-14 sample analyses were bracketed by 8 standard analyses to calibrate for instrumental fractionations and drift. As internal precision for a single spot (commonly <0.2‰) is not a good indicator of analytical quality of stable isotope ratios measure by SIMS (Kita et al., 2009; Valley and Kita, 2009), precision of individual $\delta^{18}O$ analyses is estimated to be the two standard deviations (2σ) of the reproducibility of bracket zircon standards. The average $2\sigma_{SD}$ precision for groups of 8 bracketing standard analyses is 0.3‰. Full details of both standard and sample analyses are given in Appendix D. Following oxygen isotope analysis, each pit was inspected using an optical microscope at high magnification. Any analyses that intersected cracks or defects in the zircons were considered unreliable due to possible contamination and discarded.

4.4 Analytical Results

Results from ILFT and SIMS oxygen isotope analyses are reported in Tables 1 & 2. In addition, whole rock Mg# & SiO_2, mineral Mg# for constituent ferromagnesian silicate minerals, and anorthite contents of plagioclase are given where available.

4.4.1. $\delta^{18}O$ Values of the Bushveld Complex

In the UUMZ, $\delta^{18}O_{plag}$ remains fairly constant with increasing stratigraphic height and decreasing Mg# with only a slight increase from 6.67-6.77‰ in the two stratigraphically lowest samples (122 & 572 m, $Mg\#_{WR}$ 74.7 & 67.1) to 6.81-7.26‰ in the higher samples ($Mg\#_{WR}$ 41.8-9.2) (Fig. 4-4a). Pyroxene

values also show little variation with increasing stratigraphic height with $\delta^{18}O_{opx}$ varying between 6.08-6.18‰ and $\delta^{18}O_{cpx}$ ranging from 5.76-5.96‰. $\delta^{18}O_{fay}$ decreases slightly with increasing stratigraphic height from 5.42‰ ($Fo_{46.1}$) at 1312 m to 5.21‰ ($Fo_{10.3}$) at 2327 m.

4.4.2. $\delta^{18}O$ Values of the Dariv Igneous Complex

Across the fractionation sequence there is a general increase in mineral $\delta^{18}O$ with decreasing whole rock and mineral Mg# (Fig. 4-4b). $\delta^{18}O_{ol}$ in the (phlogopite-)wehrlites increases from 6.51 to 7.53‰ as olivine Mg# decreases from 90 to 69 from the most to least primitive samples. Across the same set of ultramafic samples, clinopyroxene increases from 6.64 to 8.16‰. Clinopyroxene $\delta^{18}O$ continues to increase in the mafic cumulates, reaching 9.15‰ in monzogabbro sample MO-11-12. Biotite shows no systematic trends across the sequence with values between 6.98-9.44‰. The two analyzed quartz separates from (quartz-) monzonites have high $\delta^{18}O$ values (13.43 and 14.61‰). The $\delta^{18}O$ value of a bulk serpentinite sample, which is the host lithology of the Dariv Igneous Complex, is 3.87±0.04‰.

$\delta^{18}O_{zcn}$ values were analyzed from a primitive lamprophyre dike (Mg# = 67), a cumulative monzogabbro (MO-11-12), liquid-like monzodiorites to (quartz-)monzonites (MO-11-14, MO-11-23, & MO-11-26), and a granitic dike (MO-11-16). The average $\delta^{18}O_{zcn}$ value from the lamprophyre dike is 7.87 ± 0.10‰ ($1\sigma_{SD}$, n = 14). In the mafic plutonic lithologies, $\delta^{18}O_{zcn}$ values are 8.35 ± 0.11‰ (n = 15) in the monzodiorite and 9.37 ± 0.21‰ (n = 16) in a cumulative monzogabbro. The average $\delta^{18}O_{zcn}$ values from the two (quartz-)monzonites are indistinguishable at 9.09 ± 0.12‰ (n = 16) and 9.12 ± 0.15‰ (n = 17). The zircons from the granitic dike cluster in three populations of $\delta^{18}O_{zcn}$ values from relatively low values of dark cores (8.48 ± 0.09‰, n = 9) to higher values of sector zoned zircons (8.91 ± 0.11‰, n = 5) and oscillatory zoned rims (9.33 ± 0.07‰, n = 6). Other than the granitic dike, no other samples demonstrate intra-grain zoning of $\delta^{18}O_{zrc}$ values.

4.5 Modeling of $\delta^{18}O$ Melt Trajectories due to Fractional Crystallization

4.5.1. Model Description

We developed a new mass balance model to calculate the possible effects of closed system fractional crystallization on the oxygen isotope composition of an evolving melt. Our aim is to provide a theoretical basis to compare with mineral data from igneous rocks, which allows for us to better quantify the relative role of assimilation and magmatic differentiation in producing mineral or melt $\delta^{18}O$ values. This model is applicable to any crystallizing melt for which the melt composition, temperature, and modal amounts of crystallizing minerals is known. A detailed derivation and description of the model is available in Appendix D.

We used melt compositions from constrained LLDs for both the UUMZ of the Bushveld Complex (VanTongeren et al., 2010) and the Dariv Igneous Complex (Chapter 3), which start with a parental basalt and evolve towards granitic compositions at low melt fractions. Modal percentages of crystallized minerals were constrained from modal abundances from studied samples across the sequences. Melt temperatures across the LLDs were estimated using temperature estimates from mineral

geothermometers (Liang et al., 2013; Sun et al., 2013; Chapter 2), and comparison to temperature paths of experimentally determined LLDs with similar parental melts (i.e., Whitaker et al., 2007 and Righter & Carmichael, 1996). From an initially defined parental melt $\delta^{18}O$ value, we subtract bulk cumulate $\delta^{18}O$ values in a stepwise fashion from the crystallizing melt. Bulk cumulate-melt fractionations are calculated knowing the modal percentage (converted to mass percent) of the crystallized minerals at each fractionation step and calculated mineral-melt fractionation factors. Using estimated melt temperatures, treating the melt as a mixture of CIPW normative minerals, and using experimentally determined $\Delta^{18}O_{min\text{-}min}$, we calculated the temperature and melt composition-dependent mineral-melt fractionations ($\Delta_n^{i+1}(T)$) at each fractionation step $i+1$ and for each crystallization mineral n. Bulk cumulate-melt per mil fractionations can then be calculated as:

$$\Delta^{i+1} = \delta^{18}O_{cumulate}^{i+1} - \delta^{18}O_{melt}^{i+1} = \sum(M_n^{i+1} \times \Delta_n^{i+1}(T)) \quad (1)$$

where M_n^{i+1} is the fraction of total cumulate oxygen contained in crystallizing mineral n at fractionation step $i+1$. The anorthite composition of plagioclase and its effect on $\Delta_{plag-melt}(T)$ was explicitly considered in the model. Using mass balance constraints and making the simplification that the melt and bulk cumulate compositions have approximately equal mass percentages of oxygen (in general, 40-50 wt.% O):

$$\delta^{18}O_{melt}^{i} = (\delta^{18}O_{melt}^{i+1})(X^{i+1}) + (\delta^{18}O_{cumulate}^{i+1})(1 - X^{i+1}) \quad (2)$$

where X^{i+1} is the fraction of melt remaining at step $i+1$ and accounts for decreasing melt mass during fractionation and is defined as $X^{i+1} = F^{i+1}/F^{i}$. Combining Eqs. (1) and (2), $\delta^{18}O_{melt}$ at the next fractionation step $i + 1$ can then be calculated as:

$$\delta^{18}O_{melt}^{i+1} = \delta^{18}O_{melt}^{i} - \Delta^{i+1}(1 - X^{i+1}) \quad (3)$$

We estimated a range of $\delta^{18}O$ values of the initial parental melts ($\delta^{18}O_{melt}^{1}$) to be in equilibrium with $\delta^{18}O_{min}$ in the least evolved cumulates from the two sequences (samples B06-062, $Mg\#_{WR}$ = 74.7 and MO-12-21, $Mg\#_{WR}$ = 91.5). Parental melt $\delta^{18}O$ values of 6.1-6.5‰ and 7.2-8.0‰ were used for the UUMZ of the Bushveld Complex and the Dariv Igneous Complex, respectively. It is important to note, however, that the relative magnitude of the $\delta^{18}O$ trajectory of the crystallizing melt is independent of this initial melt value. Further, the choice of the parental $\delta^{18}O_{melt}$ value is the only dependency this model has on the mineral data obtained from the two plutonic sequences.

To explore the effects of fractional crystallization on $\delta^{18}O$ values of melts with an array of starting major element compositions, water contents, crystallized mineral modes, and pressure and temperature conditions, we applied our model to a number of experimental and natural LLDs (Table 3). Three fractional crystallization experimental studies were selected for starting materials and conditions including a hydrous basalt at 0.7 GPa (Nandedkhar et al., 2014), a dry basalt at 1.0 GPa (Villiger et al.,

2004), and a basalt with initially 0.4 wt.% H_2O at 0.4 GPa (Whitaker et al., 2007). The experimental models have the distinct advantage of having well constrained melt compositions, magmatic temperatures, pressures, and water content, as well as, crystallizing mineralogy. We also modeled the LLD constrained for the accreted Kohistan Arc (Pakistan), which is representative of a moderate-to-high pressure fractional crystallization of a primitive, hydrous calc-alkaline basalt (Jagoutz, 2010).

4.4.2 Uncertainties Associated with Model

There are several sources of uncertainties associated with the model that must be considered before interpreting its results. Input parameters for the experimentally determined LLDs are generally better constrained than the natural LLDs in terms of melt composition, crystallized mineralogy, and temperature. For natural LLDs these parameters must be determined through indirect methods. First, the composition of the crystallizing melts has been previously constrained either through mass balance modeling (Chapter 3; Jagoutz, 2010) or MELTS thermodynamic modeling (VanTongeren et al., 2010), both of which have inherent uncertainties. Uncertainties associated with mass balance modeling have been previously discussed (Jagoutz, 2010) and primarily arise from assuming an average composition for each cumulate lithology, as well as, the initial parental melt composition. A second uncertainty with the natural modeled LLDs are the magmatic temperatures used. We attempted to limit such uncertainties through implementing temperature constraints from mineral geothermometers (e.g., from Chapter 2 and Sun et al., 2013) and comparison to temperature paths of experimentally determined LLDs with similar parental melts.

Due to poor constraints on oxygen isotope fractionations involving silicate melts and minerals, our model approximates the melt as a mixture of CIPW normative minerals, as first proposed by Eiler et al., (2001). A general similarity between isotope fractionations for experimental melt compositions and chemically similar minerals suggest that this is the best available approach to estimate mineral-melt fractionations for melt compositions that have not been examined experimentally (Appora et al., 2003; Eiler, 2001; Matthews et al., 1994; Palin et al., 1996). However, the CIPW normative calculations do not consider the water content of the melt. As no study of isotopic fractionations involving significantly hydrous silicate melts exist, it is unclear how dissolved water would affect mineral-melt fractionations. Minerals and melts with high ratios of network-forming cations (e.g., Si and Al) to network-modifying cations (e.g., Na, Ca, and Mg) preferentially favor ^{18}O (Appora et al., 2003). As interaction of dissolved H_2O with bridging oxygen in the melt framework produces OH^- groups and a less polymerized melt (Mysen et al., 1980), it is possible that increased water contents would limit the enrichment of ^{18}O in the melt. Further experimental work on hydrous melts must be done to rigorously quantify the effects of dissolved H_2O on oxygen isotope fractionations between melts and minerals.

4.6 Interpretation of Data

4.6.1 Preservation of Magmatic $\delta^{18}O$ Values in Natural Samples

When minerals preserve their magmatic $\delta^{18}O$ values their oxygen isotope compositions are better indicators of the $\delta^{18}O$ value of the coexisting melt than whole rock $\delta^{18}O$ values. For example, the $\delta^{18}O$ value of the whole rock sample could deviate from that of melt if the rock sample either 1) represents accumulated minerals or 2) has experienced secondary alteration by surface waters, a metasomatic melt, or a supercritical fluid. Previous studies show, however, that sub-solidus re-equilibration of oxygen isotopes among constituent minerals can occur in slowly cooled plutonic rocks through diffusive exchange (Eiler et al., 1992; 1993; Giletti, 1986; Valley, 2001). The ability of a mineral to preserve its magmatic $\delta^{18}O$ value depends on the cooling rate, the self-diffusivity of oxygen in the mineral, the grain size and shape of the mineral, and the mineral modal abundance. In general, refractory minerals such as olivine, zircon, and garnet with low oxygen self-diffusivities are more likely to preserve magmatic $\delta^{18}O$ values than minerals such as K-feldspar, plagioclase, and biotite in which oxygen diffuses more rapidly (Bindeman, 2008). For example, unaltered forsteritic olivine and zircon are characterized by low oxygen diffusivities (e.g., 3.3 $x10^{-20}$ m^2/s (Dohmen et al., 2002) and 1.9 x 10^{-19} m^2/s (Watson and Cherniak, 1997) at 1200°C, respectively). Clinopyroxene has slightly higher oxygen self-diffusivities than olivine at a given temperature ($6.6x10^{-20}$ and m^2/s at 1200°C, (Ingrin et al., 2001)), whereas feldspar, quartz, and biotite have much higher oxygen self-diffusivities (10^{-16} to 10^{-18} m^2/s at 500 to 900°C) (Fortier and Giletti, 1991; Giletti et al., 1978; Giletti and Yund, 1984). Orthopyroxene oxygen self-diffusivities have not been thoroughly investigated.

Dodson's concept of a closure or blocking temperature below which diffusive exchange effectively ceases may be applied to oxygen isotopes (Dodson, 1973; Giletti, 1986). Although, this concept was established based on significantly simplified assumptions and more sophisticated Fast Grain Boundary models have been developed (Eiler et al., 1992), closure temperatures can place first order constraints on isotopic equilibration potential among different minerals. Closure temperatures will be higher for minerals with smaller oxygen diffusivities and larger grain sizes that experience rapid cooling. Calculated closure temperatures for olivine and clinopyroxene grains of 0.1-0.5 mm in radius, typical of that observed in the studied sequences, at relatively slow cooling rates for upper crustal intrusions of 10-100°C per million years are ~1060-1340 °C for olivine and ~970-1310°C for clinopyroxene. Similarly, for a zircon approximated as a 50 μm thick slab, calculated closure temperatures are 1190-1290°C at the same range of cooling rates. Conversely, similarly sized grains of quartz, biotite, and albite cooled at the same rates have much lower closure temperatures of ~340-640°C. Therefore, in the analyzed ultramafic samples from the Dariv Igneous Complex, olivine was the first mineral to close to isotopic exchange, then clinopyroxene, and lastly biotite. In the more evolved lithologies, zircon is the most robust recorder of magmatic $\delta^{18}O$ values. Likely none of the measured fractionations between minerals from Dariv and Bushveld record crystallization temperatures, as all the minerals (with the exception of potentially olivine and zircon) formed above their closure temperatures. Indeed, temperatures calculated from mineral-mineral fractionations are generally not in agreement between different mineral pairs from the same

sample and do not yield appropriate crystallization temperatures, suggesting subsolidus equilibration of some minerals.

It is the goal of this study to assess which minerals are the most likely to preserve magmatic oxygen isotope values in order to reconstruct the oxygen isotope evolution of melts. Due to variability in O diffusivities and thus closure temperatures, the reliability of $\delta^{18}O$ values of minerals to reflect that of coexisting melt is in the order of zircon ≅ olivine > clinopyroxene/orthopyroxene > quartz > feldspar > biotite. Preservation of magmatic $\delta^{18}O$ values in olivine and pyroxene would have been enhanced by their relatively large crystal size (0.5-1 mm in diameter). Further, there is no evidence for other subsolidus processes, such as hydrothermal exchange or deformation, which may enhance oxygen isotope exchange of olivine and pyroxene. In both the Bushveld UUMZ and Dariv Igneous Complex, olivine and pyroxene show little evidence for alteration, as identified through optical hand-picking and electron microprobe analyses with robust totals. Zircon has been shown to preserve a reliable record for magmatic oxygen isotope ratios if radiation damage is limited (Valley, 2003; Wang et al., 2014; Gao et al., 2014). Unpublished in-situ U-Pb LA-ICPMS analyzes for zircons from the Dariv Igneous Complex yield predominantly concordant ages (>95% of analyses), suggesting limited loss of Pb due to radiation damage. Further, SIMS analyses were focused on domains of bright oscillatory magmatic zoning observed in CL imagery and darker regions characteristic of radiation damage were avoided. Analyses with elevated $^{16}OH/^{16}O$ ratios, potentially indicative of radiation-damaged domains in zircons (Wang et al., 2014), were discarded and not included in averages. We, therefore, place greatest confidence in the $\delta^{18}O_{ol}$ and $\delta^{18}O_{pyx}$ values in the mafic and ultramafic rocks and $\delta^{18}O_{zrc}$ values in the more evolved lithologies as being indicative of magmatic values.

4.6.2 $\delta^{18}O$ Values of Equilibrium Melt

A few of the more evolved samples from the Dariv Igneous Complex were suggested to be solidified melts based on trace element systematics suggesting a lack of feldspar accumulation. Therefore, their whole rock compositions can be considered as representative of equilibrium melt compositions. However, for minerals analyzed from cumulate samples, we used an indirect method to calculate the equilibrium melt major element composition and $\delta^{18}O$. First, we estimated the equilibrium major element melt compositions using previously constrained LLDs for the Dariv Igneous Complex (Chapter 3) and the UUMZ of the Bushveld Complex (VanTongeren et al., 2010). We then implemented mineral-melt Fe/Mg exchange coefficients of 0.3 for olivine (Roeder and Emslie, 1970) and 0.23 for clinopyroxene (Sisson and Grove, 1993), to estimate an equilibrium melt Mg# for each analyzed cumulate sample. For example, sample MO-12-21 from the Dariv Igneous Complex has $Mg\#_{cpx}$ of 91.4, corresponding to an equilibrium melt composition from the LLD with an Mg# of ~71. Similar to the formulation in our model, we treated the melt composition as a mixture of CIPW normative minerals to calculate $\Delta^{18}O_{min\text{-}melt}$. Then, using the calculated equilibrium melt $\Delta^{18}O_{min\text{-}melt}$ and the analyzed $\delta^{18}O_{min}$, we calculated an equilibrium $\delta^{18}O_{melt}$.

The results of our calculations indicate that equilibrium $\delta^{18}O_{melt}$ values increases by 1-1.5‰ and ~2-3‰ with increasing SiO_2 content of the melt from 50 to ~70 wt.% for the Bushveld Complex and Dariv Igneous Complex, respectively (Fig. 4-5b&d). For the Bushveld Complex, there is an initially flat trajectory in $\delta^{18}O_{melt}$ as the melt Mg# decreases from 40 to ~25, in agreement with crystallization of phases with $\delta^{18}O$ values similar to that of the equilibrium melt (plagioclase (An = ~50-70) and pyroxenes). At lower Mg# the slope of the $\delta^{18}O_{melt}$ trajectory increases significantly, due to higher SiO_2 contents in the melt, as well as, fayalite and magnetite crystallization. Conversely, an abrupt increase in the calculated $\delta^{18}O_{melt}$ of 1-2‰ is observed at a melt Mg# of 50-55 (Fig. 4-5d) for the Dariv Igneous Complex. This increase coincides with an increase in SiO_2 content of the melt from ~55 to 60 wt.% which would serve to enrich the melt in ^{18}O, but a decrease the proportion of crystallizing mafic, relatively low $\delta^{18}O$ minerals, which would have the opposite effect.

4.6.3 Modeling Results Compared to Data

Beginning with a parental $\delta^{18}O_{melt}$ value of 6.0-6.5‰, the closed-system fractional crystallization model reproduces the ~1.0‰ increase in $\delta^{18}O_{melt}$ inferred from minerals for the UUMZ (Fig. 4-5b). The consistency between our model of closed-system fractionation and the mineral data suggests that the UUMZ of the Bushveld Complex did not experience significant input of material with distinctive $\delta^{18}O$ values from the crystallizing melt, consistent with previous Sr isotopic studies of the complex (Sharpe, 1985; Kruger et al., 1987).

For the Dariv Igneous Complex, the closed-system fractional crystallization model is not able to reproduce the ~2-3‰ increase observed for the calculated $\delta^{18}O_{melt}$ as its silica content increases from ~50 to 70 wt.%. This indicates that either (1) olivine, clinopyroxene, and zircon data in the more evolved lithologies were preferentially affected by subsolidus equilibration or alteration resulting in higher $\delta^{18}O$ values or (2) that the crystallizing melt may have assimilated high $\delta^{18}O$ material during the latter stages of its fractionation. Although we cannot rule out option 1, significant subsolidus equilibration is unlikely due to the refractory nature of the minerals and their high closure temperatures. To simulate option 2, we incorporate a single, late-stage assimilation step resulting in a 1.2‰ increase in the melt when 27% of the crystallizing melt remaining (Fig. 4-5d). Inclusion of this assimilation step is able to replicate the calculated $\delta^{18}O_{melt}$ value from mineral data. Based on the geology of the area and field relationships there are no obvious candidates for the high $\delta^{18}O$ assimilated material. In particular, the exposed Dariv Igneous Complex intrudes serpentinized harzburgite-dunite with low SiO_2 and a bulk rock $\delta^{18}O$ of 3.87‰, which would produce decreasing $\delta^{18}O$ and SiO_2 trends. One possibility is that late stage recharge by a high-$\delta^{18}O$ melt is responsible for the observed increase in $\delta^{18}O$, but the field and whole rock geochemical evidence for it is cryptic.

Applying our model to the rock suites of this study demonstrates the potential to identify whether cogenetic igneous suites can be explained through a dominantly closed-system fractional crystallization

process (e.g. Bushveld Complex, UUMZ) or whether assimilation of material with a distinct $\delta^{18}O$ value must be evoked (e.g. Dariv Igneous Complex). Our model is applicable to any cogenetic suite of igneous rocks where fractional crystallization played an important role and a LLD is constrained.

4.7 Discussion

4.7.1 Controls on Trajectory of $\delta^{18}O$ in Crystallizing Melts

The modeled closed system parental melt crystallization trajectories for the Dariv Igneous Complex and the Bushveld Complex UUMZ, in combination with the other modeled experimental systems allows us to assess controls on $\delta^{18}O$ variations during fractional crystallization of different parental melts. Our results indicate that $\delta^{18}O_{melt}$ values increase significantly by ~1.0-1.8‰ as melt SiO_2 changes from ~50 to 70 wt.% SiO_2. The specific $\delta^{18}O$ trajectory of a crystallizing melt will depend on (1) the temperature of crystallization, (2) the composition of the evolving melt (and thus the degree of differentiation), and (3) the crystallized mineralogy.

(1) The temperature of crystallization is critically important as mineral-melt fractionations increase in absolute magnitude with decreasing temperature. Liquidus and solidus temperatures for melts vary greatly depending on the major element composition of the melt, but also critically the water content. For example, an addition of 3 wt.% H_2O to a basaltic melt will reduce the liquidus temperature by ~100°C (Médard and Grove, 2007). Similarly the solidus of a eutectic granite may vary from ~900°C for an anhydrous granite to ~650°C for a water-saturated one (Ebadi and Johannes, 1991; Holtz and Johannes, 1994). In general, mineral-melt fractionations will be larger at lower temperatures (Fig. 4-1). If bulk mineral-melt fractionations are negative, crystallizing wet, cooler melts will result in larger increases in $\delta^{18}O$ per degree of crystallization than for dry, hot melts.

(2) The trajectory of $\delta^{18}O_{melt}$ v. melt fraction (F) will depend on the composition of the remaining melt and, in particular, when enrichment in its silica content occurs. Increases in melt SiO_2 content will result in preferential enrichment of ^{18}O in the melt relative to crystallized minerals. In tholeiitic systems silica-enrichment generally happens late in the fractionation process ($F \leq 0.20$), whereas for the calc-alkaline trend silica-enrichment occurs earlier (Miyashiro, 1974) (Fig. 4-6a). Relatively early silica enrichment during fractional crystallization is driven by the crystallization of silica-poor minerals such as hornblende, garnet, An-rich plagioclase, and oxides for the calc-alkaline series (Alonso-Perez et al., 2009; Jagoutz, 2010; Melekhova et al., 2015; Müntener et al., 2001; Nandedkar et al., 2014; Sisson and Grove, 1993; Sisson et al., 2005) or biotite, apatite, and oxides from high-K hydrous melts (Esperança and Holloway, 1987; Righter and Carmichael, 1996). Often silica enrichment occurs rather rapidly upon multiple saturation of these low-Si minerals with other crystallized phases (e.g., plagioclase or pyroxenes) (Blatter et al., 2013; Melekhova et al., 2013; Nandedkar et al., 2014). The effect of an early increase in silica content is observed in the increase of modeled $\delta^{18}O$ of hydrous basalts at higher F (Fig. 4-6b). Conversely, significant ^{18}O-enrichment in dry/water-poor systems occurs in the late stages of crystallization ($F \leq 0.20$).

(3) A number of factors including melt composition and water content, as well as the temperature, pressure, and oxidation state of crystallization will affect the crystallized mineral assemblage, which in turn affects the magnitude of $\delta^{18}O$ increase. Higher water contents generally increase the thermal stability of low $\delta^{18}O$ minerals, such as olivine, Fe-Ti oxides, garnet, and hornblende, whereas the stability of relatively $\delta^{18}O$-enriched plagioclase decreases (Alonso-Perez et al., 2009; Müntener et al., 2001; Nicholls and Ringwood, 1973; Sisson and Grove, 1993). In addition, high water contents lead to the crystallization of anorthitic plagioclase, which will have lower $\delta^{18}O$ values than coexisting albitic plagioclase (Sisson and Grove, 1993). Elevated crystallization pressures will stabilize garnet while suppressing plagioclase and olivine crystallization, thereby having variable effects on the magnitude of fractionation between cumulate minerals and the crystallizing melt (Alonso-Perez et al., 2009; Müntener et al., 2001; Sisson and Grove, 1993). The oxidation state of a crystallizing melt will also variably affect the thermal stability of ^{18}O-depleted minerals as higher oxygen fugacities reduce the stabilities of olivine and Fe-rich amphibole, but increase that of magnetite (Nitsan, 1974; Sisson et al., 2005; Toplis and Carroll, 1995). Notably, fayalitic olivine crystallizes at relatively low temperatures and melt fractions in the UUMZ of the Bushveld Complex and in experiments on relatively dry tholeiitic basalts (Whitaker et al., 2007). Low temperature crystallization of olivine from melts having relatively high SiO_2 contents causes pronounced increases in $\delta^{18}O_{melt}$ at low melt fractions in these systems.

In summary, first order differences in the trajectory of $\delta^{18}O$ increases during differentiation can be deduced for hydrous versus dry melts due to differences in T-SiO_2-F relationships. Hydrous melts, typical of calc-alkaline arc magmatism, will generally show large, earlier (i.e., at higher F) increases in $\delta^{18}O$ during fractional crystallization due to enhanced high temperature stability of low $\delta^{18}O$ phases, lower magmatic temperatures, and early silica-enrichment as compared to dry melts. Dry tholeiitic sequences only experience large increases in $\delta^{18}O$ during the late stages of crystallization.

4.7.2. Using Zircon $\delta^{18}O$ to Calculate Melt $\delta^{18}O$

Zircon is often selected to study oxygen isotope compositions of igneous rocks as it is highly retentive of magmatic $\delta^{18}O$, offering an alternative approach to analyzing whole rock samples which may be affected by low temperature alteration (Bindeman, 2008; Page et al., 2007; Valley, 2003). In addition, although $\delta^{18}O_{melt}$ will increase with progressive fractionation, $\delta^{18}O_{zircon}$ will stay relatively constant due to the increase in $\Delta^{18}O_{melt\text{-}zrc}$ as melt temperature decreases and its SiO_2 content increases. For example, in the Tuolumne Suite of the Sierra Nevada $\delta^{18}O_{zrc}$ values remain relatively constant at (~6.1-6.3‰) while $\delta^{18}O_{WR}$ values vary from ~7 to 9‰ from 57-76 wt.% SiO_2 (Lackey et al., 2008). In order to use zircon as a proxy to estimate whole rock $\delta^{18}O$, $\Delta^{18}O_{WR\text{-}zrc}$ must be known at various magmatic temperatures and melt compositions. Lackey et al., (2008) present an empirical equation relating $\Delta^{18}O_{WR\text{-}zrc}$ to bulk rock SiO_2 wt.% based on 297 rocks from the Sierra Nevada Batholith for which mineral modes, SiO_2 content, and $\delta^{18}O_{zrc}$ were constrained. Knowing the abundance and equilibrium fractionation factors for the constituent minerals they calculated $\Delta^{18}O_{WR\text{-}zrc}$ using a linearly extrapolated relationship between solidus

temperature and SiO_2 content. Importantly, they assumed that solidus temperatures decreased linearly from 900°C at 45 wt.% SiO_2 to 650°C at 78 wt.% SiO_2 (Fig. 4-7a).

Although this was a good initial attempt to address $\Delta^{18}O_{WR\text{-}zircon}$ variations for different melt compositions and temperatures, calculating $\Delta^{18}O_{WR\text{-}zircon}$ in natural systems is more nuanced than the approach presented by Lackey et al., (2008). First, a linear correlation between SiO_2 content and melt temperature is not observed from experimental studies, rather melt T-SiO_2 relationships are generally non-linear and are variable between melts of different compositions (Fig. 4-7a). Due to the assumed linearity between melt SiO_2 and temperature and the proportionality of mineral-melt fractionation factors to $1/T^2$, it is not surprising that the Lackey et al., (2008) model produces a strong positive correlation between $\Delta^{18}O_{WR\text{-}zircon}$ and SiO_2 content ($r^2 = 0.98$). Secondly, the solidus temperatures chosen for a low-silica gabbro (900°C) versus a granite (650°C) are in reality highly variable depending on pressure and water contents. For example, granite solidi can vary from 650-900°C depending on the water content of the granitic melt (Holtz and Johannes, 1994).

In Figure 4-7b, we show the $\Delta^{18}O_{WR\text{-}zircon}$ relationship derived by Lackey et al., (2008) compared to those calculated using the model presented in this study. Notably, using the correlation proposed by Lackey et al., (2008) generally predicts larger $\Delta^{18}O_{WR\text{-}zircon}$ values than those using our model. This is primarily due to the significantly lower temperature at a given SiO_2 content used by Lackey et al., (2008), which arises from their use of solidus temperatures rather than liquidus temperatures for melt compositions along a LLD, as used in this study (Fig. 4-7a). In natural systems zircon crystallization will occur somewhere between the liquidus and solidus temperatures depending on the melt composition and Zr content (Watson and Harrison, 1983). Implementing experimentally constrained T-SiO_2 relationships, we calculate $\Delta^{18}O_{melt\text{-}zrc}$ values of 0.75‰ and 1.5‰ for hot, dry and "cool", water-saturated granodioritic melts, respectively. $\Delta^{18}O_{melt\text{-}zrc}$ fractionations, therefore, are strongly controlled not only by the SiO_2 content of the melt, but also the temperature. Applying the equation of Lackey et al., (2008) will lead to erroneous magmatic $\delta^{18}O$ values if the actual temperature of the crystallizing melt at zircon saturation varies from the linear extrapolation they assumed (Fig. 4-7a).

In order to calculate appropriate temperatures for mineral-melt fractionations, estimates of crystallization temperature can be obtained from geothermometry (Anderson et al., 2008), including Ti-in-zircon thermometry (Ferry and Watson, 2007; Fu et al., 2008; Watson et al., 2006), or estimates through zircon saturation temperatures (Hanchar and Watson, 2003; Watson and Harrison, 1983). Water contents of granitic melts may also be determined using experimentally determined plagioclase-liquid hygrometers (Lange et al., 2009) which can then help to constrain magmatic temperatures when used in conjunction with the T-H_2O relationships for granitic melts (Ebadi and Johannes, 1991; Holtz and Johannes, 1994).

Once constituent mineralogy or bulk composition and magmatic temperatures are known for a plutonic rock, $\Delta^{18}O_{melt\text{-}zrc}$ may be calculated in a relatively straightforward manner. The bulk rock

composition may be assumed to be the melt composition and be treated as a mixture of CIPW minerals. This assumption is valid as long as the rock is not cumulative in nature nor does it contain abundant phenocrysts. For high silica rocks, the primary CIPW normative mineralogy will be albite, anorthite, orthoclase, and quartz with lesser hypersthene, corundum, or oxides. Using experimentally or empirically determined coefficients between CIPW normative minerals and zircon ($A_{Min-Zrc}$) to calculate mineral-zircon fractionations ($\Delta_{min-zrc}$), bulk melt-zircon fractionation may be calculated as:

$$\Delta_{melt-zrc} \approx \sum(A_{i-zrc} * X_i) * (\frac{10^6}{T^2}) \qquad (3)$$

where X_i indicates the CIPW normative mass percent of mineral *i* and T (in K) indicates the temperature of zircon crystallization. Consider a water-saturated and a dry granite, both with $X_{qtz} = 0.31$, $X_{Ab} = 0.32$, $X_{An} = 0.11$, $X_{Or} = 0.19$, $X_{Hyp} = 0.07$, $X_{Ilm} = 0.006$, but with eutectic or minimum temperatures of 650 and 900°C, respectively. The differing crystallization temperatures of these two granites will result in markedly different $\Delta_{melt-zrc}$ values varying from 2.04‰ for the wet granite to 1.13‰ for the dry granite. This example demonstrates that only knowing the SiO_2 content of a rock, or even its modal mineralogy or bulk composition, is not adequate to calculate $\Delta_{melt-zrc}$ and that it is critical to also constrain the temperature of crystallization.

4.7.3. $\delta^{18}O$ Values of Granites Permissible through Closed-System Fractional Crystallization

Our model also allows us to calculate the range of $\delta^{18}O_{melt}$ values admissible through fractional crystallization of mantle-derived melts and compare this to $\delta^{18}O$ values observed in upper crustal granitoids. In order to apply our model to the natural rock record, we must first constrain the initial $\delta^{18}O$ values of crystallizing mantle-derived melts. Mid-ocean ridge basalts have limited $\delta^{18}O$ values of 5.7±0.3‰ corresponding to equilibrium olivine values of 5.2 ± 0.3‰ (Eiler, 2001; Eiler et al., 2000b). Early studies of oceanic arcs confirmed this rather restricted range of mantle-derived values for supra-subduction zone mantle (Eiler et al., 2000a). More recent studies of continental arcs, however, have demonstrated a much larger range in $\delta^{18}O$ values of primitive arc basalts (Auer et al., 2009; Eiler et al., 2005; Johnson et al., 2009; Martin et al., 2011; Ruscitto et al., 2010; 2011). For example, olivine phenocrysts from high-Mg lavas (MgO > 9 wt.%) from Klyuchevskoy Volcano in Kamchatka have $\delta^{18}O$ values ranging from ~5.6-7.6‰ corresponding to an equilibrium melt composition of 6.3-8.0‰ (Auer et al., 2009; Dorendorf et al., 2000). Similarly, elevated $\delta^{18}O_{olivine}$ values of up to 6.1‰ have been reported for high-Mg lavas from the South Cascades (Martin et al., 2011), Central Oregon (Ruscitto et al., 2011; 2010), Mexico (Johnson et al., 2009), and Central America (Eiler et al., 2005). Further, zircons from the primitive dike analyzed from this study (MO-11-19, whole rock Mg# = 67.2, Cr = 520 ppm, & Ni = 144 ppm) have an average $\delta^{18}O$ value of 7.90 ± 0.14‰. Due to the near primitive nature of these lavas or melts, elevation of $\delta^{18}O$ values through intra-crustal contamination (i.e., within the crustal column) is not likely. As such, these are primary features of the lavas with a high $\delta^{18}O$ contribution from subducted

crustal material introduced to the mantle wedge.

Therefore, the assumption that mantle-derived melts must fall in the range of 5.7 ± 0.2‰ and that minerals in equilibrium with these melts must have specific values (e.g. olivine 5.3 ± 0.3‰ and zircon 5.2 ± 0.5‰) must be broadened to include a wider range of values for primitive arc melts. If a range of $\delta^{18}O$ values for primitive arc melts of 5.7 to 8.0‰ exists and increases in $\delta^{18}O$ of 1.0-1.8‰ during fractional crystallization can occur, high silica melts with $\delta^{18}O$ values of 6.7 to 9.8‰ can be produced through closed-system fractional crystallization alone (Fig. 4-8a). This range in $\delta^{18}O$ covers the majority of values from analyzed "A-" and "I-type" granites, which are generally <10‰ (Harris et al., 1997; Taylor, 1978). Higher $\delta^{18}O$ values than this would require intra-crustal assimilation of high-$\delta^{18}O$ material, such as (meta-)sediments, that originally precipitated from or equilibrated with water at surface temperatures. This finding is in agreement with the elevated $\delta^{18}O$ values (10-13‰) generally observed in peraluminous "S-type" granites, which are widely assumed to be largely derived from intra-crustal melting of sedimentary rocks (Harris et al., 1997; Lackey et al., 2006; O'Neil et al., 1977).

For example, $\delta^{18}O_{zrc}$ and $\delta^{18}O_{WR}$ values from peraluminous granites of the Central Sierra (Lackey et al., 2006), are elevated above the maximum $\delta^{18}O$ values permissible through fractional crystallization of primitive arc melts alone (~7.5-9.8‰). As such, the elevated $\delta^{18}O_{zrc}$ (>~7.6‰) and $\delta^{18}O_{WR}$ (>9.8‰) for these granites must be derived directly from or through significant assimilation of crustal material (Fig. 4-8a). Although lower $\delta^{18}O_{zrc}$ values of ~6 to 7.6‰ do not preclude intra-crustal assimilation, $\delta^{18}O_{zrc}$ values elevated above the canonical "mantle" zircon values of (5.3±0.6‰) (Valley, 2003; Valley et al., 1994) is not on its own evidence of significant assimilation after extraction from the mantle. In order to assess whether intra-crustal assimilation of high $\delta^{18}O$ material has occurred to produce more evolved lithologies characteristic of volcanic arcs, one must look for stepwise increases in $\delta^{18}O$ (and other geochemical and/or isotopic indices of assimilation) across a cogenetic suite of rocks formed through a common LLD (Fig. 4-8b). For example, the effect of combined fractional crystallization and assimilation was demonstrated for the Dariv Igneous Complex in this study (Fig. 4-5c,d).

4.8 Concluding Remarks

Our study demonstrates that although oxygen isotopes are a critical tool to understanding the origin of igneous rocks, the interpretation of the igneous oxygen isotope record must be done in the context of fundamental igneous processes. It is important to consider not only how the source region or assimilated materials contribute to the $\delta^{18}O$ values of igneous rocks and minerals, but also how processes such as fractional crystallization may affect the $\delta^{18}O$ values of melts. We have constrained the $\delta^{18}O$ trajectory of fractionally crystallizing melts through combining detailed mass balance modeling and analysis of oxygen isotope compositions of minerals from two end-member fractionation sequences. Oxygen isotope trajectories of crystallizing melts will strongly depend on the specific melt fraction-temperature-SiO_2 relationships and crystallizing mineralogy. This dependence allows for a distinction between the $\delta^{18}O$ paths of crystallizing hydrous, calc-alkaline versus dry, tholeiitic melts. Calc-alkaline

melts undergo greater increases in $\delta^{18}O$ at higher melt fractions compared to tholeiitic melts due to their lower temperatures, higher SiO_2 contents, and greater abundance of low $\delta^{18}O$ crystallizing minerals. Absolute increases in $\delta^{18}O$ as a melt crystallizes over a SiO_2 interval of ~50 to 70 wt.% may vary between 1.0-1.8‰. These increases are sufficient to explain $\delta^{18}O$ values of granites and other similarly high silica melts up to ~9.8‰ through fractional crystallization of mantle-derived parental basalts alone. Our modeling results also demonstrate that it is critical to consider specific T-SiO_2 relationships for crystallizing melts when using zircon $\delta^{18}O$ values to calculate bulk melt $\delta^{18}O$ due to the strong dependence of zircon-melt fractionations on these two variables. Accordingly, wet, "cool" granitic melts will have larger zircon-melt fractionations than hot, "dry" granites.

Lastly, we emphasize that the assumption that the mantle is homogeneous in terms of oxygen isotopes (i.e., "mantle" zircon $\delta^{18}O = 5.3 \pm 0.6$‰) must be used cautiously. Several recent studies of arc volcanics have shown that enrichment in ^{18}O of the mantle wedge may occur through fluid fluxing or partial melting of subducting slabs and overlying sediments, resulting in primary mantle melts with elevated $\delta^{18}O$ values above those found at mid-ocean ridges (up to ~8.0‰). We have demonstrated that this expanded range of "mantle" values will strongly control the absolute values of melts crystallizing in the crustal column after extraction from the mantle. Importantly, this newly expanded range of mantle $\delta^{18}O$ values has significant implications for studies addressing crustal growth and recycling through interpretation of zircon $\delta^{18}O$ values. In general, these studies assume that high $\delta^{18}O$ results from intracrustal reworking, indicating no new input of material from the mantle. Future investigations into the extent of $\delta^{18}O$ enrichment in terms of the absolute range of mantle values, as well as, the spatial and temporal existence of such domains, will be critical in order to understand crustal growth and recycling throughout Earth's history.

REFERENCES

Alonso-Perez, R., Muntener, O., Ulmer, P., 2009. Igneous garnet and amphibole fractionation in the roots of island arcs: experimental constraints on andesitic liquids. Contributions to Mineralogy and Petrology. doi:10.1007/s00410-008-0351-8

Anderson, J.L., Barth, A.P., Wooden, J.L., Mazdab, F., 2008. Thermometers and Thermobarometers in Granitic Systems. Reviews in Mineralogy and Geochemistry 69, 121–142. doi:10.2138/rmg.2008.69.4

Appora, I., Eiler, J.M., Matthews, A., Stolper, E.M., 2003. Experimental determination of oxygen isotope fractionations between CO_2 vapor and soda-melilite melt. Geochimica et Cosmochimica Acta 67, 459–471. doi:10.1016/S0016-7037(02)01090-6

Auer, S., Bindeman, I., Wallace, P., Ponomareva, V., Portnyagin, M., 2009. The origin of hydrous, high-$\delta^{18}O$ voluminous volcanism: diverse oxygen isotope values and high magmatic water contents within the volcanic record of Klyuchevskoy volcano, Kamchatka, Russia. Contrib Mineral Petrol 157, 209–230. doi:10.1007/s00410-008-0330-0

Badarch, G., Cunningham, W.D., 2002. A new terrane subdivision for Mongolia: implications for the Phanerozoic crustal growth of Central Asia. Journal of Asian Earth ... 21, 87–110. doi:10.1016/S1367-9120(02)00017-2

Bindeman, I., 2008. Oxygen Isotopes in Mantle and Crustal Magmas as Revealed by Single Crystal Analysis. Reviews in Mineralogy and Geochemistry 69, 445–478. doi:10.2138/rmg.2008.69.12

Bindeman, I.N., Ponomareva, V.V., Bailey, J.C., Valley, J.W., 2004. Volcanic arc of Kamchatka: a province with high-$\delta^{18}O$ magma sources and large-scale $^{18}O/^{16}O$ depletion of the upper crust. Geochimica et Cosmochimica Acta 68, 841–865. doi:10.1016/j.gca.2003.07.009

Blatter, D.L., Sisson, T.W., Hankins, W.B., 2013. Crystallization of oxidized, moderately hydrous arc basalt at mid- to lower-crustal pressures: implications for andesite genesis. Contrib Mineral Petrol 166, 861–886. doi:10.1007/s00410-013-0920-3

Cameron, E.N., 1978. The Lower Zone of the Eastern Bushveld Complex in the Olifants River Trough. Journal of Petrology 19, 437–462. doi:10.1093/petrology/19.3.437

Cameron, E.N., 1980. Evolution of the Lower Critical Zone, central sector, eastern Bushveld Complex, and its chromite deposits. Economic Geology 75, 845–871. doi:10.2113/gsecongeo.75.6.845

Cawthorn, R.G., Meyer, P.S., Kruger, F.J., 1991. Major Addition of Magma at the Pyroxenite Marker in the Western Bushveld Complex, South Africa. Journal of Petrology 32, 739–763. doi:10.1093/petrology/32.4.739

Clayton, R.N., Goldsmith, J.R., Mayeda, T.K., 1989. Oxygen isotope fractionation in quartz, albite, anorthite and calcite. Geochimica et Cosmochimica Acta.

Cooper, K.M., Eiler, J.M., Asimow, P.D., 2004. Oxygen isotope evidence for the origin of enriched mantle beneath the mid-Atlantic ridge. Earth and Planetary Science Letters. doi:10.1016/S0012821X04000585

Dijkstra, A.H., Brouwer, F.M., Cunningham, W.D., Buchan, C., Badarch, G., Mason, P.R.D., 2006. Late Neoproterozoic proto-arc ocean crust in the Dariv Range, Western Mongolia: a supra-subduction zone end-member ophiolite. Journal of the Geological Society 163, 363–373. doi:10.1144/0016-764904-156

Dodson, M.H., 1973. Closure temperature in cooling geochronological and petrological systems. Contrib Mineral Petrol 40, 259–274. doi:10.1007/BF00373790

Dorendorf, F., Wiechert, U., Wörner, G., 2000. Hydrated sub-arc mantle: a source for the Kluchevskoy volcano, Kamchatka/Russia. Earth and Planetary Science Letters.

Ebadi, A., Johannes, W., 1991. Beginning of melting and composition of first melts in the system Qz-Ab-Or-H_2O-CO_2. Contrib Mineral Petrol.

Eiler, J.M., 2001. Oxygen Isotope Variations of Basaltic Lavas and Upper Mantle Rocks. Reviews in Mineralogy and Geochemistry 43, 319–364. doi:10.2138/gsrmg.43.1.319

Eiler, J.M., Baumgartner, L.P., Valley, J.W., 1992. Intercrystalline stable isotope diffusion: a fast grain boundary model. Contrib Mineral Petrol 112, 543–557. doi:10.1007/BF00310783

Eiler, J.M., Carr, M.J., Reagan, M., 2005. Oxygen isotope constraints on the sources of Central American arc lavas. Geochemistry.

Eiler, J.M., Crawford, A., Elliott, T., Farley, K.A., Valley, J.W., Stolper, E.M., 2000a. Oxygen Isotope Geochemistry of Oceanic-Arc Lavas. Journal of Petrology 41, 229–256. doi:10.1093/petrology/41.2.229

Eiler, J.M., Schiano, P., Kitchen, N., Stolper, E.M., 2000b. Oxygen-isotope evidence for recycled crust in the sources of mid-ocean-ridge basalts
. Nature 403, 530–534.

Eiler, J.M., Valley, J.W., Baumgartner, L.P., 1993. A new look at stable isotope thermometry. Geochimica et Cosmochimica Acta 57, 2571–2583. doi:10.1016/0016-7037(93)90418-V

Esperança, S., Holloway, J.R., 1987. On the origin of some mica-lamprophyres: experimental evidence from a mafic minette. Contrib Mineral Petrol.

Ferry, J.M., Watson, E.B., 2007. New thermodynamic models and revised calibrations for the Ti-in-zircon and Zr-in-rutile thermometers. Contrib Mineral Petrol 154, 429–437. doi:10.1007/s00410-007-0201-0

Fortier, S.M., Giletti, B.J., 1991. Volume self-diffusion of oxygen in biotite, muscovite, and phlogopite micas. Geochimica et Cosmochimica Acta.

Fourie, D.S., Harris, C., 2011. O-isotope Study of the Bushveld Complex Granites and Granophyres: Constraints on Source Composition, and Assimilation. Journal of Petrology 52, 2221–2242. doi:10.1093/petrology/egr045

Fu, B., Page, F.Z., Cavosie, A.J., Fournelle, J., Kita, N.T., Lackey, J.S., Wilde, S.A., Valley, J.W., 2008. Ti-in-zircon thermometry: applications and limitations. Contrib Mineral Petrol 156, 197–215.

doi:10.1007/s00410-008-0281-5
Giletti, B.J., 1986. Diffusion effects on oxygen isotope temperatures of slowly cooled igneous and metamorphic rocks. Earth and Planetary Science Letters.
Giletti, B.J., Semet, M.P., Yund, R.A., 1978. Studies in diffusion—III. Oxygen in feldspars: an ion microprobe determination. Geochimica et Cosmochimica Acta 42, 45–57. doi:10.1016/0016-7037(78)90215-6
Giletti, B.J., Yund, R.A., 1984. Oxygen diffusion in quartz. Journal of Geophysical Research: Solid Earth (1978–2012) 89, 4039–4046. doi:10.1029/JB089iB06p04039
Grove, T.L., Kinzler, R.J., Bryan, W.B., 1992. Fractionation of Mid-Ocean Ridge Basalt (MORB), in:. pp. 281–310.
Gruenewaldt, Von, G., 1973. The main and upper zones of the Bushveld Complex in the Roossenekal area, eastern Transvaal. Transactions of the Geological Society of South Africa.
Hanchar, J.M., Watson, E.B., 2003. Zircon saturation thermometry. Reviews in Mineralogy and Geochemistry 53, 89–112.
Harmon, R.S., Hoefs, J., 1995. Oxygen isotope heterogeneity of the mantle deduced from global 18O systematics of basalts from different geotectonic settings. Contrib Mineral Petrol.
Harris, C., Chaumba, J.B., 2001. Crustal Contamination and Fluid–Rock Interaction during the Formation of the Platreef, Northern Limb of the Bushveld Complex, South Africa. Journal of Petrology 42, 1321–1347. doi:10.1093/petrology/42.7.1321
Harris, C., Faure, K., Diamond, R.E., Scheepers, R., 1997. Oxygen and hydrogen isotope geochemistry of S- and I-type granitoids: the Cape Granite suite, South Africa. Chemical Geology 143, 95–114. doi:10.1016/S0009-2541(97)00103-4
Harris, C., Pronost, J., Ashwal, L.D., 2005. Oxygen and hydrogen isotope stratigraphy of the Rustenburg Layered Suite, Bushveld Complex: constraints on crustal contamination. Journal of Petrology. doi:10.1093/petrology/egh089
Harris, C., Smith, H.S., le Roex, A.P., 2000. Oxygen isotope composition of phenocrysts from Tristan da Cunha and Gough Island lavas: variation with fractional crystallization and evidence for assimilation. Contrib Mineral Petrol 138, 164–175. doi:10.1007/s004100050015
Holtz, F., Johannes, W., 1994. Maximum and minimum water contents of granitic melts: implications for chemical and physical properties of ascending magmas. Lithos.
Ingrin, J., Pacaud, L., Jaoul, O., 2001. Anisotropy of oxygen diffusion in diopside. Earth and Planetary Science Letters 192, 347–361. doi:10.1016/S0012-821X(01)00460-5
Jagoutz, O.E., 2010. Construction of the granitoid crust of an island arc. Part II: a quantitative petrogenetic model. Contrib Mineral Petrol 160, 359–381. doi:10.1007/s00410-009-0482-6
Johnson, E.R., Wallace, P.J., Delgado Granados, H., Manea, V.C., Kent, A.J.R., Bindeman, I.N., Donegan, C.S., 2009. Subduction-related Volatile Recycling and Magma Generation beneath Central Mexico: Insights from Melt Inclusions, Oxygen Isotopes and Geodynamic Models. Journal of Petrology 50, 1729–1764. doi:10.1093/petrology/egp051
Juster, T.C., Grove, T.L., Perfit, M.R., 1989. Experimental constraints on the generation of FeTi basalts, andesites, and rhyodacites at the Galapagos Spreading Center, 85 W and 95 W. Journal of Geophysical Research: Solid Earth (1978–2012). doi:10.1029/JB094iB07p09251
Kalamarides, R.I., 1984. Kiglapait Geochemistry VI: Oxygen Isotopes. Geochimica et Cosmochimica Acta 48, 1827–1836.
Khain, E., 2003. The Palaeo-Asian ocean in the Neoproterozoic and early Palaeozoic: new geochronologic data and palaeotectonic reconstructions. Precambrian Research 122, 329–358. doi:10.1016/S0301-9268(02)00218-8
Kruger, F.J., Cawthorn, R.G., Walsh, K.L., 1987. Strontium isotopic evidence against magma addition in the Upper Zone of the Bushveld Complex. Earth and Planetary Science Letters.
Lackey, J.S., Valley, J.W., Chen, J.H., Stockli, D.F., 2008. Dynamic Magma Systems, Crustal Recycling, and Alteration in the Central Sierra Nevada Batholith: the Oxygen Isotope Record. Journal of Petrology 49, 1397–1426. doi:10.1093/petrology/egn030
Lackey, J.S., Valley, J.W., Hinke, H.J., 2006. Deciphering the source and contamination history of peraluminous magmas using δ18O of accessory minerals: examples from garnet-bearing plutons of the Sierra Nevada batholith. Contrib Mineral Petrol 151, 20–44. doi:10.1007/s00410-005-0043-6

Lange, R.A., Frey, H.M., Hector, J., 2009. A thermodynamic model for the plagioclase-liquid hygrometer/thermometer. American Mineralogist 94, 494–506. doi:10.2138/am.2009.3011

Liang, Y., Sun, C., Ashwal, L.D., VanTongeren, J.A., 2013. Spatial variations in temperature across the Bushveld layered intrusion revealed by REE-in-plagioclase-pyroxene thermometers with implications for magma chamber processes, in:. Presented at the AGU Fall Meeting Abstracts, San Francisco, CA.

Martin, E., Bindeman, I., Grove, T.L., 2011. The origin of high-Mg magmas in Mt Shasta and Medicine Lake volcanoes, Cascade Arc (California): higher and lower than mantle oxygen isotope signatures attributed to current and past subduction. Contrib Mineral Petrol 162, 945–960. doi:10.1007/s00410-011-0633-4

Matsuhisa, Y., 1979. Oxygen isotopic compositions of volcanic rocks from the East Japan island arcs and their bearing on petrogenesis. Journal of Volcanology and Geothermal Research 5, 271–296. doi:10.1016/0377-0273(79)90020-9

Matsuhisa, Y., Matsubaya, O., Sakai, H., 1973. Oxygen isotope variations in magmatic differentiation processes of the volcanic rocks in Japan. Contrib Mineral Petrol 39, 277–288. doi:10.1007/BF00376468

Matthews, A., Palin, J.M., Epstein, S., Stolper, E.M., 1994. Experimental study of $^{18}O/^{16}O$ partitioning between crystalline albite, albitic glass and CO_2 gas. Geochemica et Cosmoschimica Acta.

Melekhova, E., Annen, C., Blundy, J., 2013. Compositional gaps in igneous rock suites controlled by magma system heat and water content. Nature Geosci 6, 1–5. doi:10.1038/ngeo1781

Melekhova, E., Blundy, J., Robertson, R., Humphreys, M.C.S., 2015. Experimental Evidence for Polybaric Differentiation of Primitive Arc Basalt beneath St. Vincent, Lesser Antilles. Journal of Petrology 56, 161–192. doi:10.1093/petrology/egu074

Médard, E., Grove, T.L., 2007. The effect of H_2O on the olivine liquidus of basaltic melts: experiments and thermodynamic models. Contrib Mineral Petrol 155, 417–432. doi:10.1007/s00410-007-0250-4

Miyashiro, A., 1974. Volcanic rock series in island arcs and active continental margins. American Journal of Science 274, 321–355. doi:10.2475/ajs.274.4.321

Molyneux, T.G., 1974. A geological investigation of the Bushveld Complex in Sekhukhuneland and part of the Steelpoort valley. Transactions of the Geological Society of South Africa.

Muehlenbachs, K., Byerly, G., 1982. ^{18}O-Enrichment of silicic magmas caused by crystal fractionation at the Galapagos Spreading Center. Contrib Mineral Petrol 79, 76–79. doi:10.1007/BF00376963

Müntener, O., Kelemen, P.B., Grove, T.L., 2001. The role of H2O during crystallization of primitive arc magmas under uppermost mantle conditions and genesis of igneous pyroxenites: an experimental study. Contrib Mineral Petrol 141, 643–658. doi:10.1007/s004100100266

Mysen, B.O., Virgo, D., Harrison, W.J., Scarfe, C.M., 1980. Solubility mechanisms of H_2O in silicate melts at high pressures and temperatures: a Raman spectroscopic study. American Mineralogist.

Nandedkar, R.H., Ulmer, P., Müntener, O., 2014. Fractional crystallization of primitive, hydrous arc magmas: an experimental study at 0.7 GPa. Contrib Mineral Petrol 167, 1015. doi:10.1007/s00410-014-1015-5

Nicholls, I.A., Ringwood, A.E., 1973. Effect of water on olivine stability in tholeiites and the production of silica-saturated magmas in the island-arc environment. The Journal of Geology.

Nitsan, U., 1974. Stability field of olivine with respect to oxidation and reduction. Journal of Geophysical Research: Solid Earth (1978–2012) 79, 706–711. doi:10.1029/JB079i005p00706

O'Neil, J.R., Shaw, S.E., Flood, R.H., 1977. Oxygen and hydrogen isotope compositions as indicators of granite genesis in the New England Batholith, Australia. Contrib Mineral Petrol 62, 313–328. doi:10.1007/BF00371018

Page, F.Z., Ushikubo, T., Kita, N.T., Riciputi, L.R., 2007. High-precision oxygen isotope analysis of picogram samples reveals 2 μm gradients and slow diffusion in zircon. American Mineralogist 92, 1772–1775.

Palin, J.M., Epstein, S., Stolper, E.M., 1996. Oxygen isotope partitioning between rhyolitic glass/melt and CO_2: An experimental study at 550–950° C and 1 bar. Geochimica et Cosmochimica Acta 60, 1963–1973. doi:10.1016/0016-7037(96)00072-5

Reid, D.L., Cawthorn, R.G., Kruger, F.J., Tredoux, M., 1993. Isotope and trace-element patterns below the Merensky Reef, Bushveld Complex, South Africa: evidence for fluids? Chemical Geology 106,

171–186. doi:10.1016/0009-2541(93)90171-E
Righter, K., Carmichael, I.S.E., 1996. Phase equilibria of phlogopite lamprophyres from western Mexico: biotite-liquid equilibria and P-T estimates for biotite-bearing igneous rocks. Contrib Mineral Petrol 123, 1–21. doi:10.1007/s004100050140
Roeder, P.L., Emslie, R.F., 1970. Olivine-liquid equilibrium. Contrib Mineral Petrol 29, 275–289.
Ruscitto, D.M., Wallace, P.J., Johnson, E.R., Kent, A.J.R., Bindeman, I.N., 2010. Volatile contents of mafic magmas from cinder cones in the Central Oregon High Cascades: Implications for magma formation and mantle conditions in a hot arc. Earth and Planetary Science Letters 298, 153–161. doi:10.1016/j.epsl.2010.07.037
Ruscitto, D.M., Wallace, P.J., Kent, A.J.R., 2011. Revisiting the compositions and volatile contents of olivine-hosted melt inclusions from the Mount Shasta region: implications for the formation of high-Mg andesites. Contrib Mineral Petrol 162, 109–132. doi:10.1007/s00410-010-0587-y
Schiffries, C.M., Rye, D.M., 1989. Stable isotopic systematics of the Bushveld Complex; I, Constraints of magmatic processes in layered intrusions. American Journal of Science.
Sharp, Z.D., 1990. A laser-based microanalytical method for the *in situ* determination of oxygen isotope ratios of silicates and oxides. Geochimica et Cosmochimica Acta.
Sharpe, M.R., 1985. Strontium isotope evidence for preserved density stratification in the main zone of the Bushveld Complex, South Africa. Nature.
Sheppard, S.M.F., Harris, C., 1985. Hydrogen and oxygen isotope geochemistry of Ascension Island lavas and granites: variation with crystal fractionation and interaction with sea water. Contrib Mineral Petrol 91, 74–81. doi:10.1007/BF00429429
Sisson, T.W., Grove, T.L., 1993. Experimental investigations of the role of H2O in calc-alkaline differentiation and subduction zone magmatism. Contrib Mineral Petrol 113, 143–166. doi:10.1007/BF00283225
Sisson, T.W., Ratajeski, K., Hankins, W.B., Glazner, A.F., 2005. Voluminous granitic magmas from common basaltic sources. Contrib Mineral Petrol 148, 635–661. doi:10.1007/s00410-004-0632-9
Stolper, E., 1980. A phase diagram for mid-ocean ridge basalts: Preliminary results and implications for petrogenesis. Contrib Mineral Petrol 74, 13–27.
Sun, C., Liang, Y., Ashwal, L., VanTongeren, J., 2013. Temperature Variations Along Stratigraphic Height Across the Bushveld Complex with Implications for Magma Chamber Processes in Layered Intrusions, in:. Presented at the 2013 GSA Annual ..., Denver, CO.
Taylor, H.P., Epstein, S., 1963. O^{18}/O^{16} ratios in rocks and coexisting minerals of the Skaergaard intrusion, east Greenland. Journal of Petrology.
Taylor, H.P., Forester, R.W., 1979. An oxygen and hydrogen isotope study of the Skaergaard intrusion and its country rocks: a description of a 55 my old fossil hydrothermal system. Journal of Petrology.
Taylor, H.P., Jr, 1968. The oxygen isotope geochemistry of igneous rocks. Contrib Mineral Petrol 19, 1–71. doi:10.1007/BF00371729
Taylor, H.P., Jr, 1978. Oxygen and hydrogen isotope studies of plutonic granitic rocks. Earth and Planetary Science Letters.
Taylor, H.P., Sheppard, S.M.F., 1986. Igneous rocks; I, Processes of isotopic fractionation and isotope systematics. Reviews in Mineralogy and Geochemistry 16, 227–271.
Tegner, C., Cawthorn, R.G., Kruger, F.J., 2006. Cyclicity in the Main and Upper Zones of the Bushveld Complex, South Africa: Crystallization from a Zoned Magma Sheet. Journal of Petrology 47, 2257–2279. doi:10.1093/petrology/egl043
Tollan, P.M.E., Bindeman, I., Blundy, J.D., 2012. Cumulate xenoliths from St. Vincent, Lesser Antilles Island Arc: a window into upper crustal differentiation of mantle-derived basalts. Contrib Mineral Petrol 163, 189–208. doi:10.1007/s00410-011-0665-9
Toplis, M.J., Carroll, M.R., 1995. An Experimental Study of the Influence of Oxygen Fugacity on Fe-Ti Oxide Stability, Phase Relations, and Mineral—Melt Equilibria in Ferro-Basaltic Systems. Journal of Petrology 36, 1137–1170. doi:10.1093/petrology/36.5.1137
Valley, J.W., 2001. Stable Isotope Thermometry at High Temperatures. Reviews in Mineralogy and Geochemistry 43, 365–413. doi:10.2138/gsrmg.43.1.365
Valley, J.W., 2003. Oxygen isotopes in zircon. Reviews in Mineralogy and Geochemistry.
Valley, J.W., Chiarenzelli, J.R., McLelland, J.M., 1994. Oxygen isotope geochemistry of zircon. Earth

and Planetary Science ....
Valley, J.W., Kitchen, N., Kohn, M.J., Niendorf, C.R., 1995. UWG-2, a garnet standard for oxygen isotope ratios: strategies for high precision and accuracy with laser heating. Geochemica et Cosmoschimica Acta 59, 5223–5231. doi:10.1016/0016-7037(95)00386-X
VanTongeren, J.A., Mathez, E.A., 2012. Large-scale liquid immiscibility at the top of the Bushveld Complex, South Africa. Geol.
VanTongeren, J.A., Mathez, E.A., 2013. Incoming Magma Composition and Style of Recharge below the Pyroxenite Marker, Eastern Bushveld Complex, South Africa. Journal of Petrology 54, 1585–1605. doi:10.1093/petrology/egt024
VanTongeren, J.A., Mathez, E.A., Kelemen, P.B., 2010. A Felsic End to Bushveld Differentiation. Journal of Petrology 51, 1891–1912. doi:10.1093/petrology/egq042
Villiger, S., Ulmer, P., Müntener, O., Thompson, A.B., 2004. The Liquid Line of Descent of Anhydrous, Mantle-Derived, Tholeiitic Liquids by Fractional and Equilibrium Crystallization - an Experimental Study at 1.0 GPa. Journal of Petrology 45, 2369–2388. doi:10.1093/petrology/egh042
Walker, D., Shibata, T., DeLong, S.E., 1979. Abyssal Tholeiites From the Oceanographer Fracture Zone. II. Phase Equilibra and Mixing. Contributions to Mineralogy and Petrology 70, 111–125.
Wang, X.-L., Coble, M.A., Valley, J.W., Shu, X.-J., Kitajima, K., Spicuzza, M.J., Sun, T., 2014. Influence of radiation damage on Late Jurassic zircon from southern China: Evidence from in situ measurements of oxygen isotopes, laser Raman, U–Pb ages, and trace elements. Chemical Geology 389, 122–136. doi:10.1016/j.chemgeo.2014.09.013
Wang, Z., Bucholz, C., Skinner, B., Shimizu, N., Eiler, J., 2011. Oxygen isotope constraints on the origin of high-Cr garnets from kimberlites. Earth and Planetary Science Letters 312, 337–347. doi:10.1016/j.epsl.2011.09.061
Watson, E.B., Cherniak, D.J., 1997. Oxygen diffusion in zircon. Earth and Planetary Science Letters.
Watson, E.B., Harrison, T.M., 1983. Zircon saturation revisited: temperature and composition effects in a variety of crustal magma types. Earth and Planetary Science Letters.
Watson, E.B., Wark, D.A., Thomas, J.B., 2006. Crystallization thermometers for zircon and rutile. Contrib Mineral Petrol 151, 413–433. doi:10.1007/s00410-006-0068-5
Whitaker, M.L., Nekvasil, H., Lindsley, D.H., McCurry, M., 2007. Can crystallization of olivine tholeiite give rise to potassic rhyolites?—an experimental investigation. Bull Volcanol 70, 417–434. doi:10.1007/s00445-007-0146-1

4.9 Figures and Captions

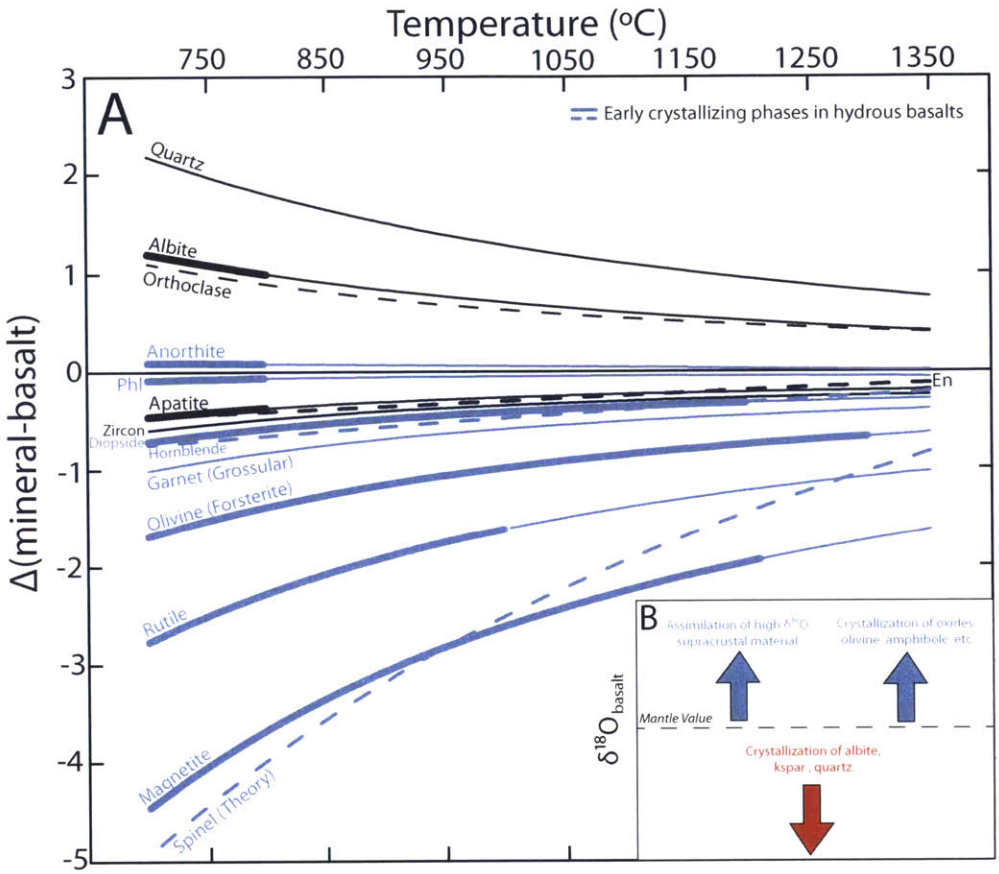

Fig. 4-1: (a) Calculated equilibrium per mil $\delta^{18}O$ fractionations between minerals and basalt. Fractionations are calculated treating the basalt as a mixture of its CIPW normative mineral constituents, as described in text. The basalt composition used in the calculations is 51.62 wt.% SiO_2, 0.90 wt.% TiO_2, 17.65 wt.% Al_2O_3, 8.66 wt.% FeO, 0.18 wt.% MnO, 7.25 wt.% MgO, 10.35 wt.% CaO, 2.71 wt.% Na_2O, and 0.68 wt.% K_2O. Sources and values for temperature-dependent mineral-mineral fractionations are provided in Appendix D. Thick curves indicate temperature range over which mineral fractionations have been experimentally constrained. Thin curve segments are extrapolations or empirical estimates. Dashed curves are calculated theoretical fractionations. Minerals typical of hydrous crystallization ("calc-alkaline") sequences are shown in blue. (b) Schematic of processes affecting oxygen isotope composition of basalt after extraction from the mantle. Assimilation of high $\delta^{18}O$ material in the crustal column or crystallization of ^{18}O-poor phases, such as olivine, amphibole, or oxides, will result in increases in $\delta^{18}O_{melt}$, whereas crystallization of ^{18}O-rich phases such as albite or K-feldspar will result in decreases in $\delta^{18}O_{melt}$.

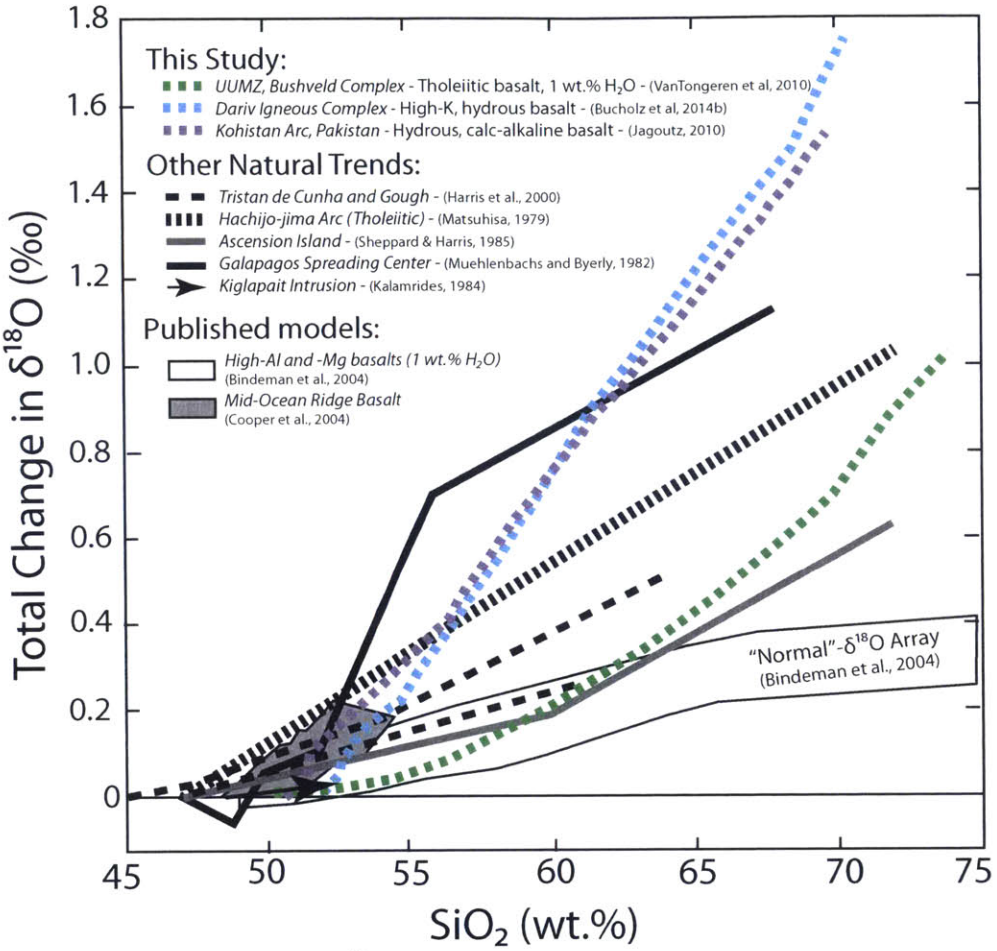

Fig. 4-2: Comparison of total increase in $\delta^{18}O_{melt}$ versus SiO_2 for crystallizing melts from various natural and modeling studies. Results shown for this study are modeled $\delta^{18}O_{melt}$ trajectories for the parental melts of the Dariv Igneous Complex, the UUMZ of the Bushveld Complex, and the Kohistan Arc, Pakistan.

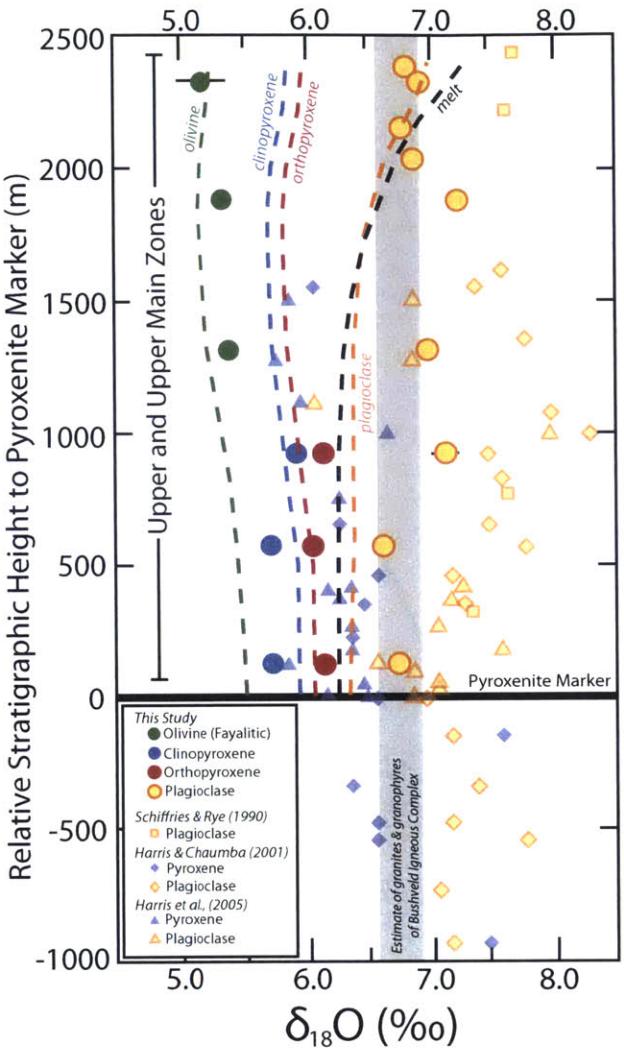

Fig. 4-3: Stratigraphic height versus mineral $\delta^{18}O$ for the Upper and Upper Main Zones of the Bushveld Complex, South Africa. Stratigraphic height is relative to the Pyroxenite Marker (PM). Mineral $\delta^{18}O$ analyses from previous studies are shown from the Eastern Limb (Schiffries & Rye, 1990) and the Northern Limb (Harris & Chaumba, 2001; Harris et al., 2005). Dashed lines indicate modeling results for minerals and equilibrium melt from this study assuming an initial melt value of 6.3‰. The gray shaded region is the range in estimated $\delta^{18}O$ values of granites and granophyres of the Bushveld Igneous Complex overlying the Rustenberg Layered Suite (6.6-6.9‰; Fourie and Harris, 2011).

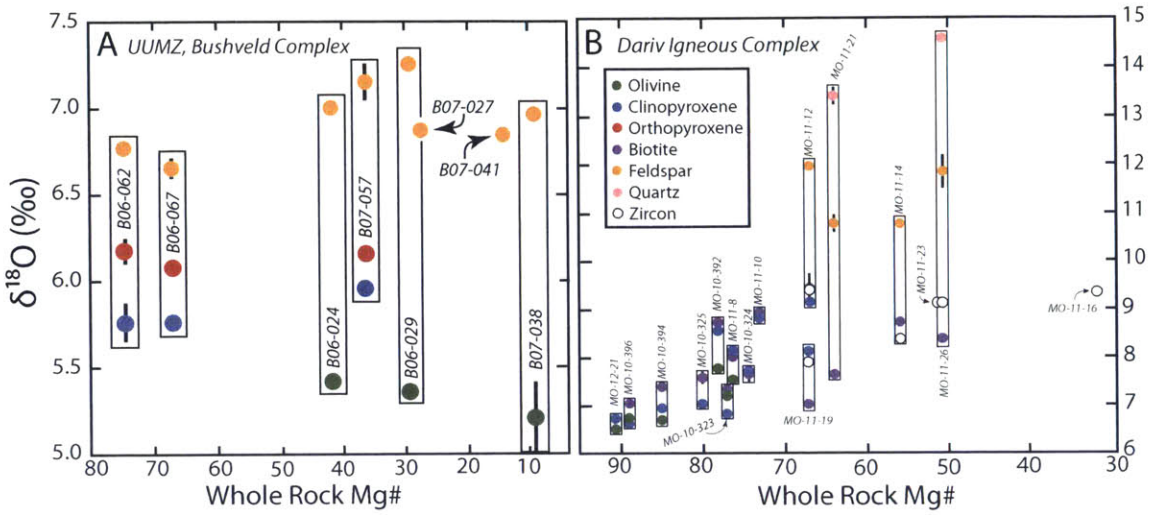

Fig. 4-4: Mineral $\delta^{18}O$ versus whole rock Mg# (molar $Mg/(Fe^{2+}+Mg)x100$) for a) the UUMZ of the Bushveld Complex b) the Dariv Igneous Complex. Whole rock Mg# are from Chapter 3 and VanTongeren et al., 2010. Error bars indicate 1σ analytical uncertainties. Mineral separates from the same samples are grouped in boxes with sample numbers indicated. For MO-11-16, only *in-situ* analyses of bright, oscillatory magmatic zoning from zircons are shown. Plagioclase data for sample B06-055 is not shown as no whole rock Mg# is available.

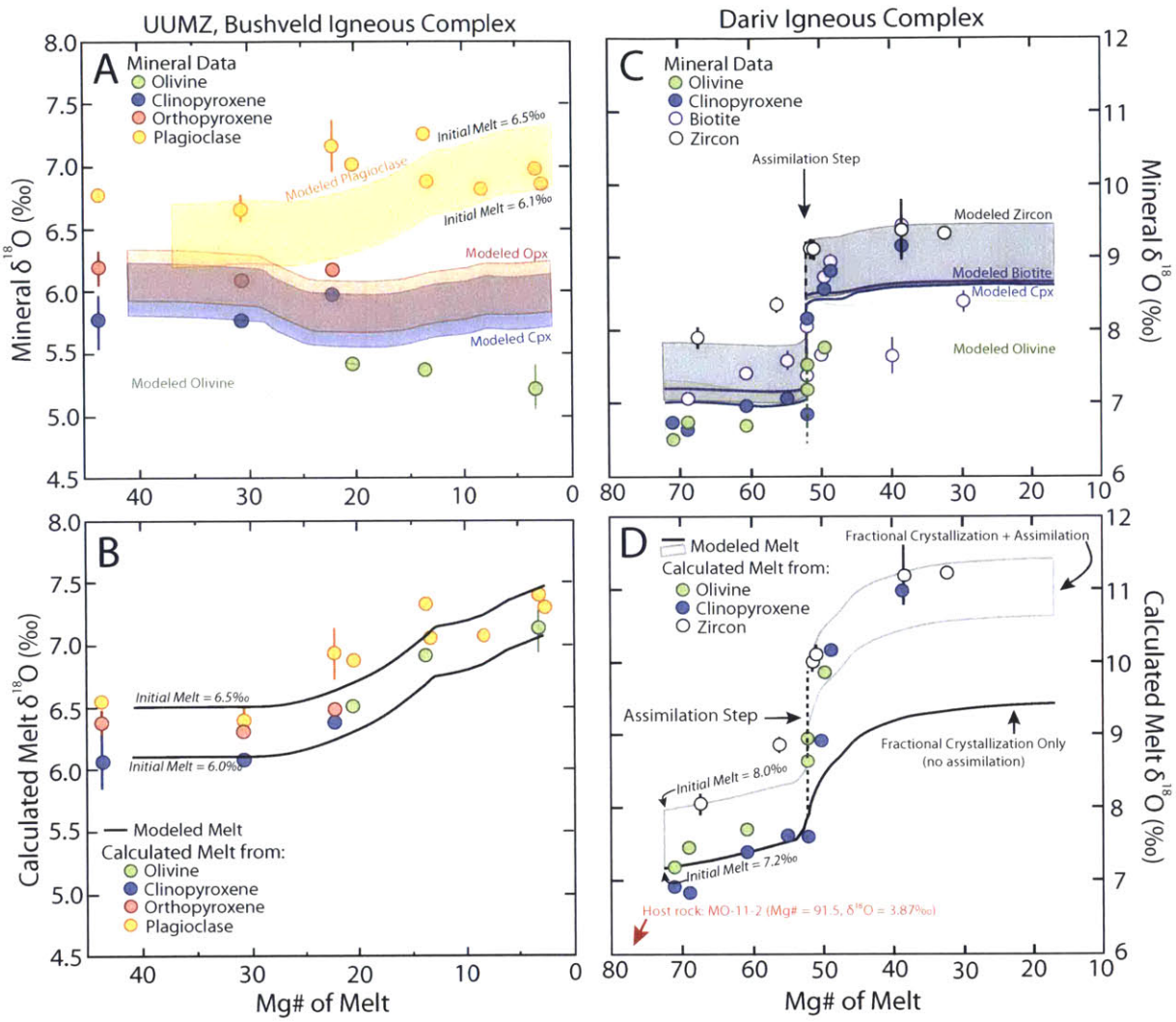

Fig. 4-5: Mineral and calculated melt $\delta^{18}O$ values versus melt Mg# for the Bushveld Complex (a & b) and Dariv Igneous Complex (c & d). Calculated equilibrium melt Mg# for mineral data from cumulate sample is based on Fe/Mg partitioning between clinopyroxene or olivine and melt. For samples representative of solidified melts, the whole rock Mg# is used. 2σ error bars for mineral data are shown where they exceed the size of the symbol. In a and c, modeled mineral values are shown as different colored lines or shaded regions. A range of modeled mineral (a,c) and melt values (b,d) are shown for the Bushveld UMMZ for initial melt compositions of 6.1-6.5‰ and 7.2-8.0‰, respectively. Changing the initial melt value results in a linear shift of model curves. In d, model results for the Dariv Igneous Complex are shown for both the scenario of fractional crystallization only and for a single assimilation step increasing the melt $\delta^{18}O$ value by 1.2‰ at a melt Mg# of ~50 (% melt remaining = 0.27). In c, only the fractional crystallization + assimilation model results are shown for clarity.

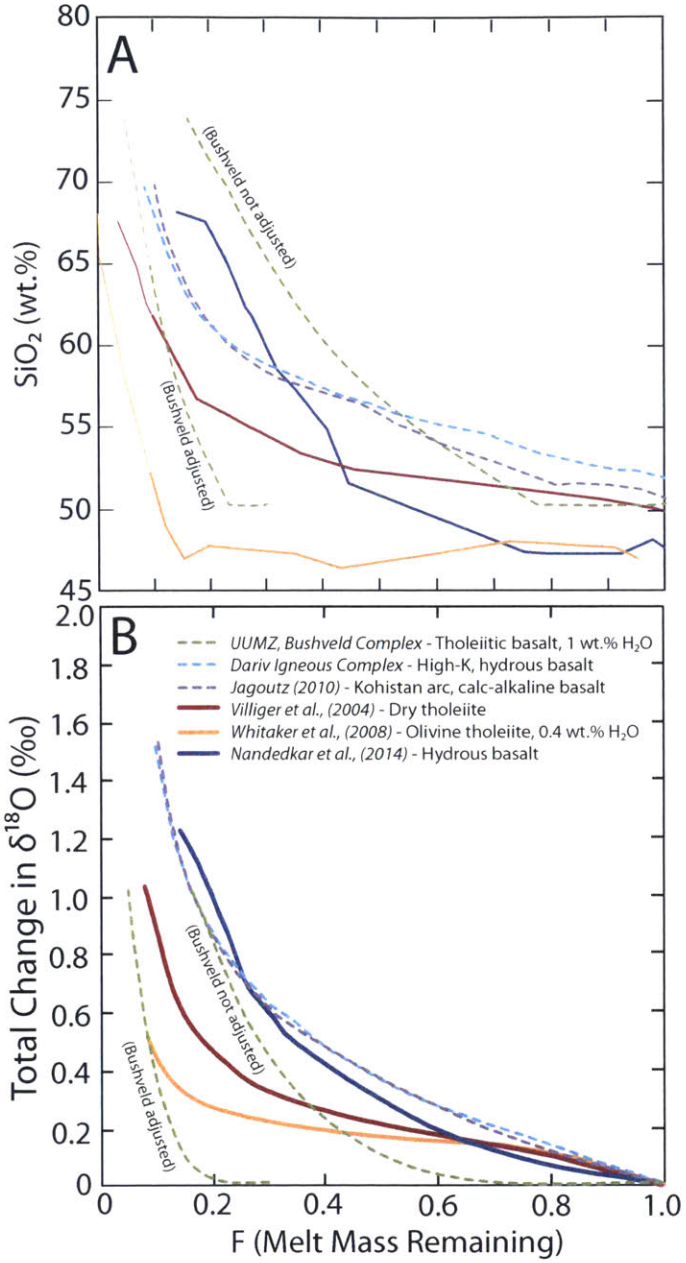

Fig. 4-6: a) SiO_2 (wt.%) and b) total change in $\delta^{18}O$ of modeled LLDs versus mass of melt remaining (F). Modeled LLD (F = 1 to 0.1) are shown for naturally and experimentally constrained LLDs for parental melts of a variety of compositions, including a tholeiitic parental melt with 1 wt.% H_2O for the UUMZ of the Bushveld Complex (VanTongeren et al., 2010), a high-K, hydrous primitive basalt from the Dariv Igneous Complex (see Chapter 3), a hydrous, calc-alkaline basalt for the Kohistan paleo-arc, Pakistan (Jagoutz, 2010), a dry tholeiitic basalt at 1.0 GPa (Villiger et al., 2004), an olivine tholeiite with 0.4 wt.% H_2O at 0.4 GPa (Whitaker et al., 2008), and a hydrous (3.6 wt.% H_2O), near primary olivine tholeiite at 0.7 GPa (Nandedkar et al., 2014). Modeled experimental and natural LLDs are shown in solid and dashed lines, respectively. The green dashed line for the Bushveld LLD trend is shown both as total melt fraction and also adjusted to lower melt fractions to account for the lower Mg# (~41) of the parental melt compared to the other modeled LLDs (64-77).

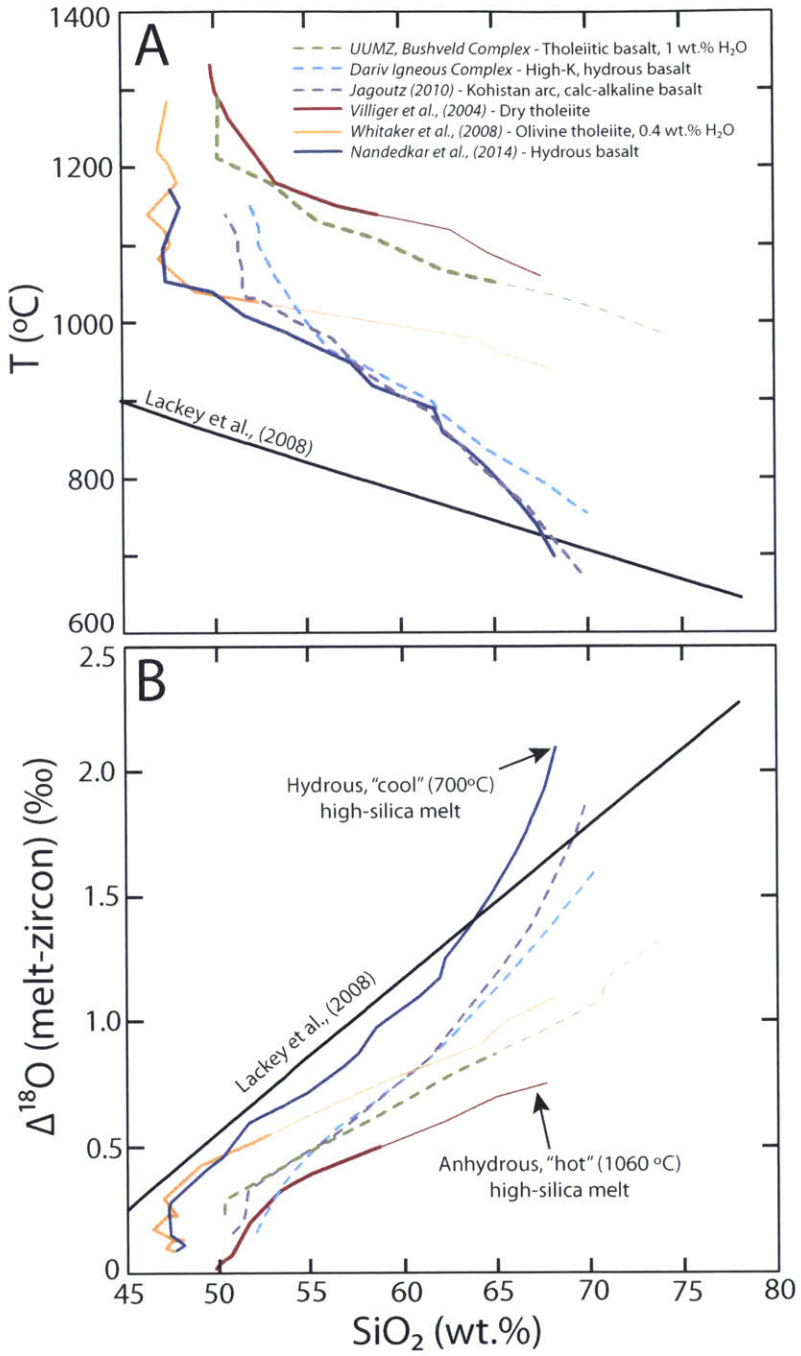

Fig. 4-7: Variations in a) temperature (°C) and b) per mil melt-zircon $\delta^{18}O$ fractionation with melt SiO_2 (wt.%) for modeled LLDs and relationship used in Lackey et al., (2008). Modeled LLDs are the same as in Fig. 4-5. Lackey et al., (2008) assumed a linear relationship between solidus temperature and SiO_2 content from 900°C at 45 wt.% to 650°C at 78 wt.% SiO_2. Note Lackey et al., (2008) chose to use solidus temperatures, whereas modeled LLDs from this study represent liquidus temperatures. Heavy and light lines are shown for melt fractions greater and less than 0.1, respectively.

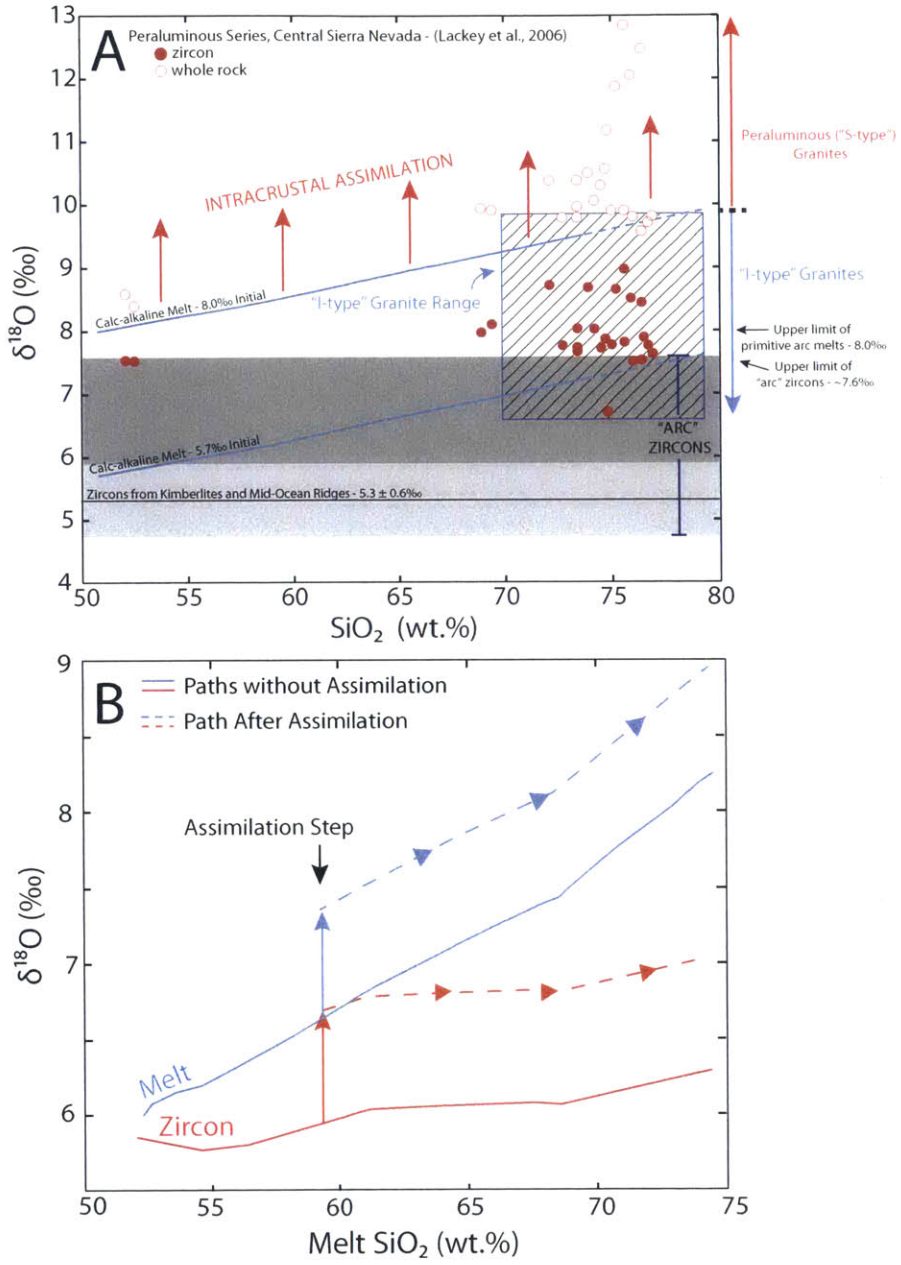

Fig. 4-8: $\delta^{18}O$ v. melt/whole rock SiO_2. a) Modeled calc-alkaline melt and zircon trajectories are shown in comparison to whole rock (open circles) and zircon (filled circles) data for peraluminous granites from the Sierra Nevada, California from Lackey et al., (2006). $\delta^{18}O$ trajectories for a hydrous, calc-alkaline LLD typical of primitive arc melts (using the modeled LLD of Jagoutz et al., 2010 for the Kohistan Arc) are shown in blue lines starting with initial values of 5.7 and 8.0‰. The light gray shaded region indicates "mantle" zircon $\delta^{18}O$ range (5.3±0.6‰) based on zircon analyses from kimberlites (Valley et al., 1998) and mid-ocean ridge plagiogranites (Grimes et al., 2011). The dark gray shaded region indicates extended range of zircon $\delta^{18}O$ permissible for mantle-derived arc melts (up to 7.6‰), using $\delta^{18}O$ values of high-Mg basalts from arcs. Range of "I-type" granites is from Harris et al., 1997. Although contamination by high $\delta^{18}O$ crustal material is necessary to extend the range of $\delta^{18}O_{zircon}$ above the "mantle" zircon range of 5.3 ± 0.6‰, it may occur solely through subducted crustal contributions to the sub-arc mantle. b) Modeled example of the affect of fractional crystallization on melt (blue lines) and zircon (red lines) $\delta^{18}O$ with (solid lines) and without (dashed lines) assimilation across a single LLD. A single assimilation event, which results in an increase of 0.7‰ in the melt $\delta^{18}O$ value, is incorporated when the melt reaches ~60 wt.% SiO_2.

4.10 Tables

Table 4-1: Oxygen isotope composition of minerals from the Bushveld Igneous Complex, South Africa

Sample	Rock Type	Height above PM (m)	SiO_2 (WR)	Mg# (WR)	Mineral (n)	Olivine Mg#	Cpx Mg#	Opx Mg#	Plg X_{An}	$\delta^{18}O_{Ol}$	$\delta^{18}O_{Cpx}$	$\delta^{18}O_{Opx}$	$\delta^{18}O_{Plg}$
B06-062	Gabbronorite	125	52.32	74.7	Cpx(4), Opx(4), Plg(2)		80.30	73.73	72.71		5.76 (0.12)	6.18 (0.07)	6.77 (0.01)
B06-067	Gabbronorite	575	51.58	67.1	Cpx(2), Opx(2), Plg(2)		73.38	63.85	62.66		5.76 (0.02)	6.08 (0.01)	6.65 (0.06)
B07-057	Magnetite Gabbro	922	46.81	36.4	Cpx(2), Opx(2), Plg(2)		62.00		59.5		5.96 (0.03)	6.17 (0.03)	7.15 (0.11)
B06-024	Troctolite	1315	42.77	41.8	Ol(2), Plg(2)	46.05	65.00	57.49	54.4	5.42 (0.04)			7.01 (0.00)
B06-029	Olivine-Magnetite Gabbro	1883	39.14	29.2	Ol(4), Plg(2)	34.59	58.11		45.3	5.37 (0.03)			7.26 (0.01)
B07-027	Olivine-Magnetite Gabbro	2032	40.69	27.1	Plg(2)	33.92	59.92		47.1				6.88 (0.01)
B06-055	Olivine-Magnetite Gabbro	2155			Plg(2)	23.66			49.1				6.81 (0.03)
B07-038	Olivine-Magnetite Gabbro	2330	49.51	9.2	Ol(2), Plg(4)	10.25	38.86	24.91	46.3	5.21 (0.20)			6.91 (0.09)
B07-041	Olivine-Magnetite Gabbro	2390	47.00	14.2	Plg(2)	8.8	29.43		40.7				6.85 (0.03)

Abbreviations: Ol (olivine), Cpx (clinopyroxene), Opx (orthopyroxene), Plg (plagioclase), WR (whole rock), An (anorthite).
All $\delta^{18}O$ values are relative to Vienna Standard Mean Ocean Water (VSMOW). n is the number of replicate analyses. Value in parentheses behind mineral values are 1σ on averages.
Whole rock and mineral chemistry data is from Vantongeren et al. (2010)

Table 4-2: Oxygen isotope composition of minerals from the Dariv Igneous Complex

Sample	Rock Type	SiO_2 (WR)	Mg# (WR)	Mineral (n)	Olivine Mg#	Cpx Mg#	$\delta^{18}O_{Ol}$	$\delta^{18}O_{Cpx}$	$\delta^{18}O_{Bt}$	$\delta^{18}O_{Fsp}$	$\delta^{18}O_{Qtz}$	$\delta^{18}O_{Zrc}$	$\delta^{18}O_{WR}$
MO-11-2	Serpentinite	44.14	91.5	WR(2)									3.87 (0.04)
MO-12-21	Wehrlite	52.67	90.7	Ol (2), Cpx (2)	87.0	91.4	6.51 (0.01)	6.73 (0.01)					
MO-10-396	Phlogopite Wehrlite	51.86	89.1	Ol (4), Cpx (4), Bt (2)	86.3	90.6	6.74 (0.03)	6.64 (0.08)	7.06 (0.05)				
MO-10-394	Phlogopite Wehrlite	51.02	85.0	Ol (2), Cpx (2), Bt (2)	80.6	87.0	6.69 (0.04)	6.96 (0.01)	7.40 (0.04)				
MO-10-392	Phlogopite Wehrlite	46.69	78.1	Ol (2), Cpx (2), Bt (2)	74.1	81.0	7.78 (0.01)	8.56 (0.03)	8.73 (0.02)				
MO-10-323	Phlogopite Wehrlite	45.76	77.1	Ol (2), Cpx (4), Bt (2)	71.7	82.4	7.20 (0.06)	6.84 (0.06)	7.36 (0.06)				
MO-11-8	Phlogopite Wehrlite	48.43	76.3	Ol (2), Cpx (2), Bt (4)	68.7	82.4	7.53 (0.04)	8.16 (0.04)	8.04 (0.01)				
MO-10-325	Phlogopite Clinopyroxenite	50.36	80.1	Cpx(2), Bt(2)		84.0		7.05 (0.06)	7.58 (0.07)				
MO-10-324	Phlogopite Clinopyroxenite	50.31	74.4	Cpx(2), Bt(4)		81.3		7.73 (0.01)	7.65 (0.06)				
MO-11-10	Phlogopitite	42.71	73.1	Cpx(2), Bt(2)		80.4		8.81 (0.03)	8.93 (0.03)				
MO-11-12	Monzogabbro	49.25	66.9	Cpx(2), Bt(2), Fsp(1), Zrc(16)		73.0		9.15 (0.04)	9.44 (0.05)	11.97		9.38 (0.21)	
MO-11-14	Monzodiorite	53.24	56.0	Bt(2), Fsp(1), Zrc(15)					8.72 (0.07)	10.75		8.35 (0.11)	
MO-11-16	Felsic Dike	74.58	32.2	Zrc(9,5,6)*								8.48 (0.09); 8.91 (0.11), 9.33 (0.07)	
MO-11-19	Lamprophyre	48.69	67.2	Cpx(2), Bt(4), Zrc(14)		75.3		8.04 (0.10)	6.98 (0.07)			7.87 (0.10)	
MO-11-21	Monzonite	52.47	64.0	Bt(2), Fsp(2), Qtz(2)		74.2			7.65 (0.11)	10.78 (0.17)	13.43 (0.17)		
MO-11-23	Monzonite	57.80	51.2	Zrc(16)								9.09 (0.12)	
MO-11-26	Quartz Monzonite	59.75	50.8	Cpx(2), Bt(2), Fsp(2), Qtz(2), Zrc(17)		64.7			8.39 (0.13)	11.85 (0.33)	14.61 (0.05)	9.12 (0.15)	

Abbreviations: Ol (olivine), Cpx (clinopyroxene), Bt (biotite), Fsp (feldspar), Qtz (quartz), Zrc (zircon), WR (whole rock powder).
All $\delta^{18}O$ values are relative to Vienna Standard Mean Ocean Water (VSMOW). n is the number of replicate analyses. Value in parentheses behind mineral values are 1σ of averages.
Whole rock and mineral chemistry data is from Bucholz et al., (2014a,b)
*Zircon analyses for MO-11-16 reported for cores, sectors zones, and oscillatory zoned rims, respectively.

Table 4-3: Modeled Fractional Crystallization Studies

									Parental Melt Major Element Composition (Anhydrous Totals)													
Reference	**Study Type**	**Locality or Source of Starting Material**	**Parental Melt**	**Initial H_2O (wt.%)**	**Temperature Range (°C)**	**Pressure (GPa)**	**Crystallizing Mineralogy***	**Melt Fraction Range**	**SiO_2**	**TiO_2**	**Al_2O_3**	**Cr_2O_3**	**Fe_2O_3**	**FeO**	**MnO**	**MgO**	**CaO**	**Na_2O**	**K_2O**	**P_2O_5**	**TOTAL**	**Mg#**
Vantongeren et al., (2010)	Field Based	Bushveld UUMZ, South Africa	Tholeiitic Basalt	1	1150-707	0.2	Opx, Pig, Cpx, Plag, Mgt, Ap, Bt, Alkali Fsp	1.0-0.18	50.83	1.54	15.87	0.00	1.98	12.08	0.19	5.35	8.22	2.51	1.08	0.34	100.00	40.8
Bucholz et al., (2014b)	Field Based	Dariv Igneous Complex, Western Mongolia	Primitive High-K Basalt	2.5	1150-700	0.3-0.5	Ol, Cpx, Phl, Mgt, Ap, Alkali Fsp, Plag, Amph, Qtz	1.0-0.07	52.00	1.10	12.90	0.08	0.00	7.85	0.16	11.26	8.70	2.50	2.96	0.49	100.00	71.9
Jagoutz (2010)	Field Based	Kohistan, Pakistan	Primitive Calc-alkaline Basalt	3	1137-670	1.0	Ol, Cpx, Opx, Grt, Amph, Mgt, Plag, Qtz	1.0-0.1	50.72	0.80	15.67	0.06	0.00	8.60	0.17	10.87	9.88	2.43	0.61	0.19	100.00	69.3
Nandekhar et al., (2014)	Experimental	Adamello Batholith, Italy	Synthetic near-primary olivine tholeiite (RDC156)	3.6	1170-700	0.7	Ol, Cpx, Opx, Oxides (Mgt, Usp, Sp), Amph, Plag, Ap, Bt, Qtz	1-0.14	50.27	0.73	15.05	0.00	0.00	8.77	0.19	10.16	12.13	1.95	0.64	0.11	100.00	67.4
Villiger et al., (2004)	Experimental	Partial Melting Experiments of Hirose & Kushiro (1993)	Synthetic Primitive Tholeiitic Basalt (HK#19)	0	1200-1060	1.0	Ol, Opx, Cpx, Sp, Ilm, Plag, Qtz	1.0-0.06	49.43	0.68	15.03	0.35	0.00	6.68	0.16	12.99	12.68	1.94	0.07	0.00	100.00	77.6
Whitaker et al., (2008)	Experimental	Snake River Plain, USA	Primitve Olivine Tholeiite (1260)	0.4	1280	0.4	Ol, Cpx, Plag, Ilm, Ap, Pig	1.0-0.02	48.13	1.45	15.22	0.00	1.78	9.06	0.16	10.59	10.70	2.21	0.43	0.26	100.00	63.9

***Mineral Abbreviations**: Ol: olivine, Cpx: clinopyroxene, Opx: orthopyroxene, Pig: pigeonite, Ap: apatite, Plag: plagioclase, Ilm: ilmenite, Mgt: magnetite, Sp: spinel, Alkali Fsp: alkali feldspar, Bt: biotite, Amph: Amphibole, Qtz: Quartz.

CHAPTER 5:
Constraining the Timescales of Magmatic Differentiation with U-Pb Zircon Geochronology

Abstract

Quantifying the timescales of magmatic differentiation is critical to understand the rate at which silicic plutonic and volcanic rocks can form. However, directly dating this process is difficult because locations with both clear evidence for fractional crystallization and the accessory phases necessary for radiometric dating are rare. This study focuses on the Dariv Igneous Complex in western Mongolia where early saturation of zircon in a suite of cogenetic, upper crustal (<0.5 GPa) igneous rocks ranging from ultramafic cumulates through to evolved granitoids and late stage felsic dikes allows for dating of magmatic differentiation through U-Pb geochronology for the first time. Crystallization ages from Th-corrected $^{206}Pb/^{238}U$ dates of zircons from five samples across the sequence indicate that magmatic fractionation from a basalt to high silica (>65 wt.% SiO_2) melt occurred in ≤300 ka. As early zircon saturation could be characteristic of alkaline melts similar to the parental basalts of the Dariv Igneous Complex, younger alkaline plutonic sequences may be excellent localities to resolves the duration of magmatic fractionation to shorter timescales.

5.1 Introduction

Differentiation of mantle-derived, basaltic magmas to produce more silicic compositions is an essential process in the compositional stratification of the continental crust. One process by which differentiation occurs is fractional crystallization, or the physical segregation of silica-poor minerals to produce silica-enriched residual liquids. The process is well-studied both experimentally (Sisson and Grove, 1993; Blatter et al., 2013; Nandedkar et al., 2014; Melekhova et al., 2015) and through field-based studies of crustal sections (Greene, 2006; Jagoutz, 2010) and individual intrusions (McBirney, 1996; VanTongeren et al., 2010). However, the timescales over which differentiation occurs remains uncertain. This question has been addressed primarily through U-series disequilibrium in modern (<300 ka) volcanic rocks (see Hawkesworth et al., 2000 & 2004 for a review). The U-series method relies on the fact that minerals may preferentially sequester certain U-series nuclides, resulting in disequilibrium between the parent and daughter nuclides in a crystallizing melt. However, there are numerous assumptions underlying this method that produce uncertainty in the timescales of magmatic differentiation. For example, basaltic and more evolved volcanic samples are assumed to be derived from the same batch of crystallizing magma even though evidence for this may be ambiguous. Further, the origin of U-series disequilibria must be presumed to be due solely to crystallization although other processes such as assimilation of crustal material or mixing with isotopically distinct melts will also affect disequilibria.

Lastly, the inferred timescales of fractionation are strongly dependent on variables, such as partition coefficients and crystallization models, which are often not well constrained.

In exhumed plutonic rocks, the evolution of a crystallizing melt and the connection between residual melts and cumulates has the potential to be more clear. However, few locations preserve unambiguous differentiation sequences and contain the accessory minerals (e.g. zircon) needed to obtain radiometric dates from rocks representing a wide range of melt SiO_2. The Dariv Igneous Complex in Western Mongolia affords the unique opportunity to address timescales associated with fractional crystallization through U-Pb geochronology as it satisfies the above two requirements. First, field relationships as well as, detailed mineral and whole rock geochemistry, provide clear evidence that the complex preserves a cogenetic sequence of ultramafic and mafic cumulates through to evolved granitoids that represent the differentiation products of a primitive high-K basalt (Chapters 2 & 3). Second, zircon is an early crystallizing phase, first appearing the ultramafic cumulates, and thereby affords a unique opportunity to utilize U-Pb geochronology to constrain the timescales of magmatic differentiation over a wide range of melt SiO_2 contents. Here we present high precision U-Pb zircon CA-IDTIMS ages from the Dariv Igneous Complex in Western Mongolia in order to constrain the timescales of fractional crystallization.

5.2 Geologic Setting, Field Relationships, and Petrography

The Dariv Range of southwestern Mongolia exposes the contact between Proterozoic high-grade metamorphic rocks of the Altai Allochthon and the Lake Terrane, an Ediacaran to Early Paleozoic island arc system (Khain, 2003; Dijkstra et al., 2006). The km-scale Dariv Igneous Complex belongs to the latter and is comprised of a suite of high-K plutonic rocks, including phlogopite-bearing wehrlites and clinopyroxenites, monzogabbros, monzodiorites, (quartz-)monzonites, and late-stage felsic and lamprophyre dikes that were emplaced at 0.2-0.5 GPa (see Chapter 2 for detailed field and petrographic descriptions). The observed lithological variability, petrographic observations, and mineral and whole rock geochemistry suggest that the plutonic rocks can be ascribed to a common fractionation sequence defined by olivine + clinopyroxene ± Fe-Ti oxides → phlogopite + apatite ± titanite ± zircon → K-feldspar + plagioclase → amphibole + quartz (Fig. 5-1, Chapter 2). Several primitive lamprophyre dikes have compositions appropriate to be parental to the observed cumulate lithologies and their liquid line of descent is quantitatively modeled in Chapter 3. Although feldspar-bearing plutonic lithologies can range from cumulative to liquid-like in character, some of the monzodiorites, most of the quartz-monzonites, and all of the aplite dikes have major and trace element compositions that suggest they are liquid-like and represent late-stage differentiated melts within the fractionation sequence. Oxygen and Hf isotopes in zircons from the sequence suggest that assimilation of material enriched in ^{18}O and characterized by non-radiogenic Hf isotopic compositions occurred during the late stages of differentiation (Chapter 4), but the major and trace element trends of the sequence are dominantly controlled by fractional crystallization.

Notably, zircon is an early crystallizing mineral in the Dariv Igneous Complex, first appearing in the ultramafic phlogopite clinopyroxenites (Fig. 5-2a). Textural observations, such as enclosure within clinopyroxene and biotite, confirm that zircon is magmatic in origin and crystallized either before or contemporaneously with the volumetrically dominant mineral phases (Fig. 5-2).

5.3 Sample Selection and Description

Five samples were selected for U-Pb zircon geochronology from a ca. 250m thick section of the Dariv Igneous Complex with continuous exposure of ultramafic cumulates to quartz monzonites (Figs. 1 & 3). Although zircons were observed in biotite clinopyroxenites (Fig. 5-2a), they are rare and small (≤20 μm) and we could not separate grains for analysis. Samples from which zircons were successfully extracted and analyzed include one cumulate monzogabbro sample (MO-11-12) and four liquid-like samples, including a monzodiorite (MO-11-14), a quartz monzonite (MO-11-26), a felsic dike (MO-11-16), and a primitive lamprophyre dike (MO-11-19). The order of magmatic evolution for the samples from least to most evolved is MO-11-19, MO-11-12, MO-11-14, MO-11-26, and MO-11-16. Below we give detailed petrographic descriptions of the samples.

MO-10-324: Phlogopite Clinopyroxenite

This sample is comprised of subrounded clinopyroxene (70%) with interstitial phlogopite (20%) and minor plagioclase (5%) (Fig. 5-2a). Accessory phases include apatite (up to 500 μm in diameter), hemo-ilmenite, titanite, and zircon. Subhedral titanite is found both enclosed by biotite and clinopyroxene and along grain boundaries between these major phases. Zircon occurs as 10-20 μm grains enclosed within clinopyroxene and sometimes growing in association with allanite. Note, this sample was not analyzed for zircon geochronology, but we describe it here to illustrate the early saturation of zircon in the Dariv Igneous Complex.

MO-11-19: Lamprophyre Dike

The main mineral phases are biotite, plagioclase, and clinopyroxene with accessory apatite, zircon, and hematite (Fig. 5-2b). Biotite (50%) occurs in 100-200 μm long blocky laths often enclosing zircon and hematite. Subhedral, rounded 20-100 μm clinopyroxene crystals (5%) are surrounded by plagioclase (45%). Plagioclase crystals display irregular margins and appear to have crystallized after biotite. Zircon is an abundant accessory phase occurring as 20-150 μm long prismatic crystals within both plagioclase and biotite. Zircons are euhedral and prismatic and vary from 200-400 μm in length. CL imaging shows oscillatory zoning typical of igneous zircons, though a few of the grains have rounded cores, possibly reflecting resorption of an entrained zircon and followed by a main phase of magmatic growth.

MO-11-12: Biotite Monzogabbro

This sample is composed of alkali-feldspar and plagioclase (together 30%), phlogopite (30%), and clinopyroxene (35%) with accessory subhedral titanite, apatite, zircon, and hemo-ilmenite (Fig. 5-2c). Phlogopite grows both interstitially and in large laths (1-2 cm in length), occasionally poikilitically enclosing titanite and apatite. Oligoclase (An ~20) and alkali-feldspar occur together in patchy intergrowths. Apatite occurs as stubby, subhedral 1-2 mm long crystals often, but not exclusively, within clinopyroxene and biotite. Zircons are euhedral and vary from being stubby to elongate. CL imaging reveals clear oscillatory zoning typical of igneous zircons. The zircons are generally 300-400 μm in length, but vary between 200-500 μm.

MO-11-14: Biotite Monzodiorite

Clinopyroxene (10%), biotite (15%), plagioclase (25%), K-feldspar (30%), amphibole (10%), and quartz (10%) constitute the major mineral phases (Fig. 5-2d). Apatite, hematite-ilmenite solid solution Fe-Ti oxides, zircon are present as accessory phases. Clinopyroxene is anhedral, with irregular margins, and contains abundant subequant apatite inclusions (up to 200 μm in length). Biotite occurs as subhedral blocky laths and also contains abundant apatite inclusions. Secondary green actinolite often replaces clinopyroxene, particularly along the rims. Na-rich plagioclase and alkali-feldspar occur together in patchy intergrowths. Zircons are subhedral and vary in length from 150-300 μm. CL images show sector and igneous zoning. A few contain inclusions of brighter phases, but these were excluded from the CA-IDTIMS analysis. Some zircons also display thin (<5 μm) bright rims.

MO-11-26: Quartz Monzonite

This sample is characterized by large (1-2 cm) alkali-feldspar megacrysts surrounded by smaller crystals of albite, quartz, biotite, amphibole, and clinopyroxene as major constituents and with accessory apatite, titanite, zircon, and hemo-ilmenite (Fig. 5-2e). Quartz displays interlobate grain boundaries. Biotite occurs as stubby laths, 1-4 mm in length and contains inclusions of Fe-Ti oxides and apatite. Secondary green actinolite extensively replaces clinopyroxene. Clinopyroxene contains both biotite and numerous apatite inclusions (5-100 μm diameter). Zircons are equant to subequant, stubby to elongate, and vary in size between 100-200 μm. CL images show that the zircons have clear oscillatory, igneous zoning. A few zircons have inclusions of bright phases.

MO-11-16: Felsic Dike

This sample is a fine-grained dike composed primarily of albite (30%), K-feldspar (35%), quartz (30%), and biotite (5%) with accessory Fe-Ti oxides, monazite, and zircon (Fig. 5-2f). Albite grains are subhedral and up to ~1 mm in their longest dimension. Smaller (100-300 μm) anhedral K-feldspar and rounded quartz grains surround the larger albite crystals. Biotite occurs in short laths up to 300 μm in length. Zircons are generally <100 μm in length and subequant. No CL images were obtained for the

zircons analyzed in this study, however CL images of other zircons from this sample demonstrate that they have weak oscillatory zoning and often display dark cores.

5.4 U-Pb Zircon Geochronology

Zircons were analyzed via thermal ionization mass spectrometry (TIMS) following a procedure slightly modified from Mattinson (2005). This procedure is described in detail in the supplementary material for Rioux et al. (2012). All isotopic measurements are presented in Table 1 and were made on the Sector 54 TIMS at the Massachusetts Institute of Technology (MIT). Pb isotopes were measured by peak hopping on a Daly detector and corrected for fractionation based on repeat analyses of the NBS 981 Pb isotopic standard. U was measured statically on Faraday cups and corrected for fractionation using the known ratio of ^{233}U to ^{235}U in the EARTHTIME ^{205}Pb-^{233}U-^{235}U isotopic tracer. Data reduction was done using the U-Pb_Redux software package (Bowring et al., 2011) and the decay constants for ^{238}U and ^{235}U presented in Jaffey et al. (1971).

We assume that zircon does not incorporate Pb during crystallization and that all measured ^{204}Pb comes from laboratory blank (Pb_c). The mass of Pb_c in the zircon analyses reported in this chapter is consistent with the range of Pb_c seen in total procedural blanks produced at MIT, providing strong support for this assumption. We corrected all Pb isotopic ratios for the addition of this Pb using a Pb_c isotopic composition of $^{206}Pb/^{204}Pb = 17.911 \pm 0.372$, $^{207}Pb/^{204}Pb = 15.205 \pm 0.262$, and $^{208}Pb/^{204}Pb = 36.842 \pm 0.726$ (1σ, absolute) based on 53 total procedural blank measurements run between August 2013 and January 2015 (Fig. 5-4). Calculated dates are insensitive to the Pb_c isotopic composition when the mass of radiogenic Pb (Pb*) is much greater than the mass of Pb_c. However, the effect of this correction on the calculated date is much greater when this ratio is small ($Pb^*/Pb_c < 15$). Some zircons from MO-11-16 and MO-11-26 have low Pb* and correspondingly low Pb^*/Pb_c. These grains have Th-corrected $^{238}U/^{206}Pb$ dates that are older than the main population of grains in each sample (Table 1), raising the possibility that the difference between these dates is an artifact of the Pb_c correction. However, a $^{206}Pb/^{204}Pb \sim 19$-$20$ is needed to reduce dispersion in these samples, and this value is higher than those measured in total procedural blanks. Therefore, we believe that the dispersion in zircon dates seen in these two samples is real and results from either protracted crystallization or the incorporation of antecrysts into the melt.

Zircon excludes Th during crystallization and this can lead to initial disequilibrium in the ^{238}U-^{206}Pb decay chain. The resulting deficiency in radiogenic ^{206}Pb can leads to $^{238}U/^{206}Pb$ dates up to ca. 100 kyr too young. We correct for initial disequilibrium (exclusion of ^{230}Th during crystallization) using a calculated Th/U for the zircon and an assumed Th/U for the magma from which it crystallized. We consider samples MO-11-16, MO-11-26, MO-11-19, and MO-11-14 to approximate liquid compositions and use the whole rock trace element data presented in Chapter 3 to calculate $[Th/U]_{magma}$ and arbitrarily apply an uncertainty of ± 1 (2σ). Our values are consistent with the range of Th/U seen in 14925 volcanic rocks of the trachytic series from the EarthChem database (http://www.earthchem.org/), providing further

justification for their use (Fig. 5-5). The $[Th/U]_{magma}$ for sample MO-11-12 is more difficult to determine. This sample is a mafic cumulate and likely remained in equilibrium with a range of melt compositions during magmatic differentiation. Clinopyroxene from this sample is in equilibrium with a melt with a Mg# = 38.5 ± 1.5, which corresponds to a magma with a Th/U of 7.70 using the modeled liquid line of descent for the Dariv Igneous Complex presented in Chapter 3. However, this likely represents the last melt in equilibrium with this phase and we believe that an average of the Th/U for MO-11-14 and MO-11-26 (Th/U = 4.30) is probably more representative of the equilibrium melt for MO-11-12 during the majority of its crystallization period. Further, the LLD presented in Chapter 3 reproduces the upper range of Th/U values observed in liquid-like plutonics and dikes of the Dariv Igneous Complex, which have [Th/U] values between 4-8.

5.5 CA-IDTIMS Geochronology Results

Since the ^{238}U-^{206}Pb isotopic system gives the most precise date for rocks of this age, we use Th-corrected $^{206}Pb/^{238}U$ dates for all of our interpretations and present 34 single grain analyses in Fig. 5-6 and in Table 1. The mean square weighted deviation is a useful tool for determining whether a population of zircon dates is indistinguishable within analytical uncertainty (MSWD $\approx$ 1) or contains resolvable differences (MSWD >> 1). We use the expected 2σ variability (Wendt and Carl, 1991) in the MSWD for different size populations to determine whether or not zircon dates from individual samples are statistically indistinguishable. The monzogabbro (MO-11-12) and monzodiorite (MO-11-14) yield zircon populations with a weighted means of 502.48 ± 0.12 (n=5, MSWD = 0.52) and 502.58 ± 0.12 (n=5, MSWD = 0.48) (Fig. 5-6a). However, zircon dates from the quartz monzonite (MO-11-26), felsic dike (MO-11-16), and lamprophyre (MO-11-19) demonstrate dispersion beyond that which can be explained by analytical uncertainty alone. Youngest zircons dates from these samples are 502.33 ± 0.27 (MO-11-26), 502.52 ± 0.27 (MO-11-16), and 502.33 ± 0.25 (MO-11-19), respectively (Fig. 5-6a).

5.6 Discussion

5.6.1 Spread of Zircon Ages within Single Samples

Increased age precision in U-Pb IDTIMS geochronology has revealed that populations of zircons from a single hand sample may record dispersion in dates over 10^4-10^6 years (Lissenberg et al., 2009; Schaltegger et al., 2009; Schoene et al., 2012). To interpret these ages in the context of magmatic events, analytical artifacts and post-crystallization Pb-loss must be ruled out. We discuss and exclude analytical biases in the section 5.4, and although Pb-loss cannot be entirely eliminated as a possibility, the chemical abrasion technique employed in this study has been shown to be extremely effective at removing zircon domains that have experienced Pb-loss (Mattinson, 2005; Rioux et al., 2012). Thus, we are confident that the observed spread in dates should be interpreted in the context of the dynamic magma systems from which the zircons crystallized. The range in ages may result from incorporation of xenocrysts (zircons

inherited from fully solidified country rock), antecrysts (zircons inherited by the magma but that originated in broadly the same magmatic system), protracted autocrystic zircon growth, or a combination of all of these processes (see Miller et al., 2007 for detailed discussion). For the 34 zircons analyzed by CA-IDTIMS in this study, none appear to be true xenocrysts based solely on age. Rather, the analyzed zircons appear to be either auto- or antecrysts.

Field evidence for high-temperature mechanical mixing of multiple melt generations is abundant in the quartz monzonite (MO-11-26) and in felsic dikes (e.g. MO-11-16), including abundant mafic lamprophyre enclaves, diffuse intrusive contacts, and K-feldspar xenocrysts (Fig. 5-3). Additionally, zircon O isotope data (Chapter 4) indicates that there was incorporation of high $\delta^{18}O$ material during the end stages of fractionation. We, therefore, consider the range of zircon dates observed in the quartz monzonite (MO-11-26) and felsic dike (MO-11-16) to result primarily from incorporation of antecrysts. Likewise, protracted crystallization in the lamprophyre dike is unlikely and we consider the oldest zircons in this sample to be antecrysts as well.

5.6.2 Timescales of Magmatic Fractionation

We interpret the weighted mean age of the monzogabbro and monzodiorite and the youngest zircon date from the three other samples to be the age of final crystallization for each sample (Fig. 5-6). Using these ages we can bracket the total duration of crystallization between the monzogabbro (MO-11-12) and the monzonite (MO-11-26) as ~230 kyr. Further, the youngest zircons from the lamprophyre and felsic dikes that intrude the cumulate sequence have indistinguishable ages from the cumulate monzogabbro, providing clear field relationships indicating that fractionation occurred on timescales comparable to the 2σ uncertainty of the crystallization ages added in quadrature (~280-300 kyr). Estimates for differentiation timescales based on U-series disequilibria range from thousands (Lundstrom et al., 2003; Rogers, 2004; Johansen et al., 2005) to tens of thousands (Widom et al., 1992; Lowenstern et al., 2006) to hundreds of thousands of years (Allegre and Condomines, 1976; Bourdon et al., 1994; Reagan et al., 2003) and are within the analytical uncertainties of the dates obtained in this study. Our precision is limited by the age of the rocks and we are not able to constrain fractionation timescales to durations shorter than 10^5 years. However, we emphasize that this is the first to use U-Pb zircon CA-IDTIMS geochronology to directly date a suite of rocks with clear field, petrographic, and geochemical relationships indicating an origin through fractional crystallization.

Assuming that crystal settling is efficient process in low viscosity basaltic melts and occurs on timescales more rapid than that of crystallization (Martin and Nokes, 1988; Fig. 5-7), the rate of cooling is the primary control on the timescales associated with fractional crystallization. To place time constraints on the cooling history of the Dariv Igneous Complex, we modeled the closed-system thermal evolution of a 500 to 1000 m-thick sheet-like magma body emplaced at an initial temperature of 1200°C into a country rock at 400 °C. The results of this modeling suggest that ~5-15 kyr are required to cool the magma body

to near its solidus temperature at ~700°C (Fig. 5-7), which is in agreement with more complex models of closed-system, similarly-sized basaltic magma reservoirs that suggest hundreds to tens of thousands of years are required for solidification (Spera, 1980; Hort, 1997; Hawkesworth et al., 2000). 5-15 kyr represents the minimum time requirement for fractional crystallization to occur due to the assumed closed nature of the system and the fact that our model ignores the latent heat of crystallization. The modeled cooling timescale of tens of thousands of years is within the uncertainties associated with our U-Pb zircon geochronology constraints on duration of fractional crystallization.

If crystallization rates in crustal intrusions are primarily a function of cooling and the effects of decompression are negligible, rates of fractionation will be strongly dependent on the size and depth of the magmatic system, as well as, the dynamics of magma chamber replenishment (Annen et al., 2006; Annen, 2009; Gelman et al., 2013). Thus, the Dariv Igneous Complex, which crystallized at relatively shallow (0.2-0.5 GPa) and cool levels in the crust represents an end-member constraint for fractional crystallization of a basaltic melt. Fractional crystallization of mantle-derived basalts in the lower crust may occur on more protracted timescales due to greater ambient temperatures at depth within the crust and repeated influx of hot basalts (Dufek and Bergantz, 2005; Annen et al., 2006).

5.6.3 Early Zircon Saturation

Early saturation of zircon in the Dariv Igneous Complex permits the direct dating of magmatic fractionation from gabbroic cumulates to quartz-bearing lithologies. However, estimated primitive, parental melts for the Dariv fractionation sequence have high M values ($M = (Na + K + 2Ca)/(Al \cdot Si) =$ 2.8-3.7), indicating low polymerization and conditions unfavorable for zircon saturation (Watson and Harrison, 1983). Calculated zircon saturation temperatures for these melts are 630-700°C and well below their solidi. We note, however, the zircon solubility model of Watson and Harrison (1983) is only characterized for experiments at <1020°C and much lower M values (~1-2) and is not directly applicable to the basaltic melt compositions in this study. A subsequent study investigated more mafic lithologies and suggested similarly high Zr solubilities using new experimental, analytical, and statistical methods (Boehnke et al., 2013). However, no reversals were done on the mafic starting materials to ensure equilibrium and the systematics of zircon saturation in mafic melts remains poorly constrained. The Dariv Igneous Complex provides an interesting natural example where zircon saturation occurred in a melt with presumably low polymerization, indicating that other factors may ultimately control zircon saturation in mafic melts.

We consider the elevated concentrations of Zr in the parental high-K basalts (90-264 ppm, Chapter 2 and 3) to be an important driver of early zircon saturation. Indeed, lamprophyres and other high-K primitive melts are generally enriched in Zr and often contain magmatic zircons (Bergman, 1987; Rock, 1987; Scarrow et al., 2009). Further, closed-system crystallization of a melt prior to zircon saturation results in increases in melt Zr concentration and polymerization, driving the melt composition

towards conditions favorable for zircon crystallization. Thus, zircon saturation temperatures based on bulk rock chemistry of the lamprophyre dike could significantly underestimate the temperature of initial zircon crystallization (Harrison et al., 2007). Other high-K intrusive suites, similar to the Dariv Igneous Complex, may also exhibit early saturation of zircon and prove useful in further studies on timescales of magmatic fractionation. In particular, younger complexes (<100 Ma) could yield even more precise ages, reducing the uncertainty in fractionation timescales to the 10 ka timescale.

5.6.5 Concluding Remarks

High-precision CA-IDTIMS U-Pb zircon ages from the Dariv Igneous Complex of Western Mongolia indicate that fractional crystallization of basaltic melts to produce more evolved granites in the upper crust can occur in <300 ka and possibly shorter timescales. Our data indicate that the segregation of silica-poor minerals from a basaltic melt is an efficient process and that evolved melts may be generated on relatively rapid time scales. Once produced, however, intermediate to silicic mushes/melts may reside in the crust for prolonged periods (10^5-10^6 years) at near eutectic conditions (Halliday et al., 1989; Reid et al., 1997; Vazquez and Reid, 2002). Temporal and spatial constraints on the production, extraction, and residence of upper crustal silicic plutonics and volcanics are critical to decipher the processes underpinning the construction and stratification of the continental crust. Further detailed field studies, particularly of high-K intrusive suites demonstrating early saturation of zircon, combined with high precision U-Pb zircon geochronology are necessary to obtain higher resolution temporal these constraints.

References

Allegre, C.J., and Condomines, M., 1976, Fine chronology of volcanic processes using ^{238}U-^{230}Th systematics: Earth and Planetary Science Letters.

Annen, C., 2009, From plutons to magma chambers: Thermal constraints on the accumulation of eruptible silicic magma in the upper crust: Earth and Planetary Science Letters, v. 284, no. 3-4, p. 409–416, doi: 10.1016/j.epsl.2009.05.006.

Annen, C., Blundy, J.D., and Sparks, R.S.J., 2006, The Genesis of Intermediate and Silicic Magmas in Deep Crustal Hot Zones: Journal of Petrology, v. 47, no. 3, p. 505–539, doi: 10.1093/petrology/egi084.

Bachmann, O., & Bergantz, G. W. (2004). On the origin of crystal-poor rhyolites: extracted from batholithic crystal mushes. *Journal of Petrology*, *45*(8), 1565-1582.

Bergman, S.C., 1987, Lamproites and other potassium-rich igneous rocks: a review of their occurrence, mineralogy and geochemistry: Geological Society, London, Special Publications, v. 30, no. 1, p. 103–190, doi: 10.1144/GSL.SP.1987.030.01.08.

Blatter, D.L., Sisson, T.W., and Hankins, W.B., 2013, Crystallization of oxidized, moderately hydrous arc basalt at mid- to lower-crustal pressures: implications for andesite genesis: Contributions to Mineralogy and Petrology, v. 166, no. 3, p. 861–886, doi: 10.1007/s00410-013-0920-3.

Boehnke, P., Watson, E.B., Trail, D., Harrison, T.M., and Schmitt, A.K., 2013, Zircon saturation re-

revisited: Chemical Geology, v. 351, no. C, p. 324–334, doi: 10.1016/j.chemgeo.2013.05.028.

Bourdon, B., Zindler, A., and Wörner, G., 1994, Evolution of the Laacher See magma chamber: Evidence from SIMS and TIMS measurements of U-Th disequilibria in minerals and glasses: Earth and Planetary Science Letters, v. 126, no. 1-3, p. 75–90, doi: 10.1016/0012-821X(94)90243-7.

Bowring, J.F., McLean, N.M., and Bowring, S.A., 2011, Engineering cyber infrastructure for U-Pb geochronology: Tripoli and U-Pb_Redux: Geochemistry, Geophysics, and Geosystems, v. 12, doi: 10.1029/2010GC003479.

Carslaw, H. S., and J. C. Jaeger, 1959, *Conduction of Heat in Solids*, Oxford Univ. Press, London, 510 pp.

Dijkstra, A.H., Brouwer, F.M., Cunningham, W.D., Buchan, C., Badarch, G., and Mason, P.R.D., 2006, Late Neoproterozoic proto-arc ocean crust in the Dariv Range, Western Mongolia: a supra-subduction zone end-member ophiolite: Journal of the Geological Society, v. 163, no. 2, p. 363–373, doi: 10.1144/0016-764904-156.

Dufek, J., and Bergantz, G.W., 2005, Lower Crustal Magma Genesis and Preservation: a Stochastic Framework for the Evaluation of Basalt-Crust Interaction: Journal of Petrology, v. 46, no. 11, p. 2167–2195, doi: 10.1093/petrology/egi049.

Gelman, S.E., Gutierrez, F.J., and Bachmann, O., 2013, On the longevity of large upper crustal silicic magma reservoirs: Geology, v. 41, no. 7, p. 759–762, doi: 10.1130/G34241.1.

Greene, A.R., 2006, A Detailed Geochemical Study of Island Arc Crust: the Talkeetna Arc Section, South-Central Alaska: Journal of Petrology, v. 47, no. 6, p. 1051–1093, doi: 10.1093/petrology/egl002.

Halliday, A.N., Mahood, G.A., Holden, P., Metz, J.M., Dempster, T.J., and Davidson, J.P., 1989, Evidence for long residence times of rhyolitic magma in the Long Valley magmatic system: the isotopic record in precaldera lavas of Glass Mountain: Earth and Planetary Science Letters, v. 94, no. 3-4, p. 274–290, doi: 10.1016/0012-821X(89)90146-5.

Harrison, T.M., Watson, E.B., and Aikman, A.B., 2007, Temperature spectra of zircon crystallization in plutonic rocks: Geology, v. 35, no. 7, p. 635–4, doi: 10.1130/G23505A.1.

Hawkesworth, C., George, R., Turner, S., and Zellmer, G., 2004, Time scales of magmatic processes: Earth and Planetary Science Letters, v. 218, no. 1-2, p. 1–16, doi: 10.1016/S0012-821X(03)00634-4.

Hawkesworth, C.J., Blake, S., Evans, P., Hughes, R., Macdonald, R., Thomas, L.E., Turner, S.P., and Zellmer, G., 2000, Time scales of crystal fractionation in magma chambers—integrating physical, isotopic and geochemical perspectives: Journal of Petrology, v. 41, no. 7, p. 991–1006.

Hort, M., 1997, Cooling and crystallization in sheet-like magma bodies revisited: Journal of Volcanology and Geothermal Research, v. 76, no. 3-4, p. 297–317, doi: 10.1016/S0377-0273(96)00079-0.

Jaffey, A.H., Flynn, K.F., Glendenin, L.E., Bentley, W.C., Essling, A.M., 1971, Precision measurement of half-lives and specific activities of 235U and 38U: Physical Review C, v. 4, p. 1889-1906, doi: 10.1103/PhysRevC.4.1889.

Jagoutz, O.E., 2010, Construction of the granitoid crust of an island arc. Part II: a quantitative petrogenetic model: Contributions to Mineralogy and Petrology, v. 160, no. 3, p. 359–381, doi: 10.1007/s00410-009-0482-6.

Johansen, T.S., Hauff, F., Hoernle, K., Klügel, A., and Kokfelt, T.F., 2005, Basanite to phonolite

differentiation within 1550–1750 yr: U-Th-Ra isotopic evidence from the A.D. 1585 eruption on La Palma, Canary Islands: Geology, v. 33, no. 11, p. 897–900, doi: 10.1130/G21663.1.

Khain, E., 2003, The Palaeo-Asian ocean in the Neoproterozoic and early Palaeozoic: new geochronologic data and palaeotectonic reconstructions: Precambrian Research, v. 122, no. 1-4, p. 329–358, doi: 10.1016/S0301-9268(02)00218-8.

Le Bas, M.J., Le Maitre, R.W., Streckeisen, A., Zanettin, B., 1986, A chemical classification of volcanic rocks based on the total alkali-silica diagram: Journal of Petrology, v. 27, p. 745-750.

Lissenberg, C.J., Rioux, M., Shimizu, N., and Bowring, S.A., 2009, Zircon dating of oceanic crustal accretion: Science,, doi: 10.1126/science.1165675.

Lowenstern, J.B., Charlier, B.L.A., Clynne, M.A., and Wooden, J.L., 2006, Extreme U-Th Disequilibrium in Rift-Related Basalts, Rhyolites and Granophyric Granite and the Timescale of Rhyolite Generation, Intrusion and Crystallization at Alid Volcanic Center, Eritrea: Journal of Petrology, v. 47, no. 11, p. 2105–2122, doi: 10.1093/petrology/egl038.

Lundstrom, C.C., Hoernle, K., and Gill, J., 2003, U-series disequilibria in volcanic rocks from the Canary Islands: Plume versus lithospheric melting: Geochimica et Cosmochimica Acta, v. 67, no. 21, p. 4153–4177, doi: 10.1016/S0016-7037(03)00308-9.

Martin, D., and Nokes, R., 1988, Crystal settling in a vigorously converting magma chamber: Nature, v. 332, p. 534–536, doi: 10.1038/332534a0.

Mattinson, J.M., 2005, Zircon U–Pb chemical abrasion ("CA-TIMS") method: Combined annealing and multi-step partial dissolution analysis for improved precision and accuracy of zircon ages: Chemical Geology, v. 220, no. 1-2, p. 47–66, doi: 10.1016/j.chemgeo.2005.03.011.

McBirney, A.R., 1996, The Skaergaard Intrusion: Developments in Petrology, v. 15, p. 147–180.

Melekhova, E., Blundy, J., Robertson, R., and Humphreys, M.C.S., 2015, Experimental Evidence for Polybaric Differentiation of Primitive Arc Basalt beneath St. Vincent, Lesser Antilles: Journal of Petrology, v. 56, no. 1, p. 161–192, doi: 10.1093/petrology/egu074.

Miller, J.S., Matzel, J.E.P., Miller, C.F., Burgess, S.D., and Miller, R.B., 2007, Zircon growth and recycling during the assembly of large, composite arc plutons: Journal of Volcanology and Geothermal Research, v. 167, no. 1-4, p. 282–299, doi: 10.1016/j.jvolgeores.2007.04.019.

Nandedkar, R.H., Ulmer, P., and Müntener, O., 2014, Fractional crystallization of primitive, hydrous arc magmas: an experimental study at 0.7 GPa: Contributions to Mineralogy and Petrology, v. 167, no. 6, p. 1015, doi: 10.1007/s00410-014-1015-5.

Reagan, M.K., Sims, K.W.W., Erich, J., Thomas, R.B., Cheng, H., Edwards, R.L., Layne, G., and Ball, L., 2003, Time-scales of Differentiation from Mafic Parents to Rhyolite in North American Continental Arcs: Journal of Petrology, v. 44, no. 9, p. 1703–1726, doi: 10.1093/petrology/egg057.

Reid, M.R., Coath, C.D., Mark Harrison, T., and McKeegan, K.D., 1997, Prolonged residence times for the youngest rhyolites associated with Long Valley Caldera:230Th—238U ion microprobe dating of young zircons: Earth and Planetary Science Letters, v. 150, no. 1-2, p. 27–39, doi: 10.1016/S0012-821X(97)00077-0.

Rioux, M., Lissenberg, C.J., McLean, N.M., Bowring, S.A., MacLeod, C.J., Hellebrand, E., and Shimizu, N., 2012, Protracted timescales of lower crustal growth at the fast-spreading East Pacific Rise: Nature Geoscience, v. 5, no. 4, p. 275–278, doi: 10.1038/ngeo1378.

Rock, N.M.S., 1987, The nature and origin of lamprophyres: an overview: Geological Society, London, Special Publications, v. 30, no. 1, p. 191–226, doi: 10.1144/GSL.SP.1987.030.01.09.

Rogers, N.W., 2004, Rates and Timescales of Fractional Crystallization from ^{238}U-^{230}Th-^{226}Ra Disequilibria in Trachyte Lavas from Longonot Volcano, Kenya: Journal of Petrology, v. 45, no. 9, p. 1747–1776, doi: 10.1093/petrology/egh032.

Scarrow, J.H., Bea, F., Montero, P., and Molina, J.F., 2009, Shoshonites, vaugnerites and potassic lamprophyres: similarities and differences between "ultra-"high-K rocks: Earth and Environmental Science Transactions of the Royal Society of Edinburgh, v. 99, no. 3-4, p. 159, doi: 10.1017/S1755691009008032.

Schaltegger, U., Brack, P., Ovtcharova, M., Peytcheva, I., Schoene, B., Stracke, A., Marocchi, M., and Bargossi, G.M., 2009, Zircon and titanite recording 1.5million years of magma accretion, crystallization and initial cooling in a composite pluton (southern Adamello batholith, northern Italy): Earth and Planetary Science Letters, v. 286, no. 1-2, p. 208–218, doi: 10.1016/j.epsl.2009.06.028.

Schoene, B., Schaltegger, U., Brack, P., Latkoczy, C., Stracke, A., and Günther, D., 2012, Rates of magma differentiation and emplacement in a ballooning pluton recorded by U–Pb TIMS-TEA, Adamello batholith, Italy: Earth and Planetary Science Letters, v. 355-356, p. 162–173, doi: 10.1016/j.epsl.2012.08.019.

Sisson, T.W., and Grove, T.L., 1993, Experimental investigations of the role of H2O in calc-alkaline differentiation and subduction zone magmatism: Contributions to Mineralogy and Petrology, v. 113, no. 2, p. 143–166, doi: 10.1007/BF00283225.

Spera, F., 1980, Thermal evolution of plutons: a parameterized approach: Science, v. 207, 299-301.

Trommsdorff V, Connolly JA (1996) The ultramafic contact aureole about the Bregaglia (Bergell) tonalite: isograds and a thermal model. Schweiz Mineral Petrogr Mitt 76(3): 537–547.

VanTongeren, J.A., Mathez, E.A., and Kelemen, P.B., 2010, A Felsic End to Bushveld Differentiation: Journal of Petrology, v. 51, no. 9, p. 1891–1912, doi: 10.1093/petrology/egq042.

Vazquez, J.A., and Reid, M.R., 2002, Time scales of magma storage and differentiation of voluminous high-silica rhyolites at Yellowstone caldera, Wyoming: Contributions to Mineralogy and Petrology, v. 144, no. 3, p. 274–285, doi: 10.1007/s00410-002-0400-7.

Vermeesch, P., 2010, HelioPlot, and the treatment of overdispersed (U–Th–Sm)/He data: Chemical Geology, v. 271, no. 3-4, p. 108–111, doi: 10.1016/j.chemgeo.2010.01.002.

Wendt, I., and Carl, C., 1991, The statistical distribution of the mean squared weighted deviation: Chemical Geology: Isotope Geoscience Section, v. 86, no. 4, p. 275–285, doi: 10.1016/0168-9622(91)90010-T.

Widom, E., Schmincke, H.U., and Gill, J.B., 1992, Processes and timescales in the evolution of a chemically zoned trachyte: Fogo A, Sao Miguel, Azores: Contributions to Mineralogy and Petrology, v. 111, no. 3, p. 311–328, doi: 10.1007/BF00311194.

5.7 Figures and Captions

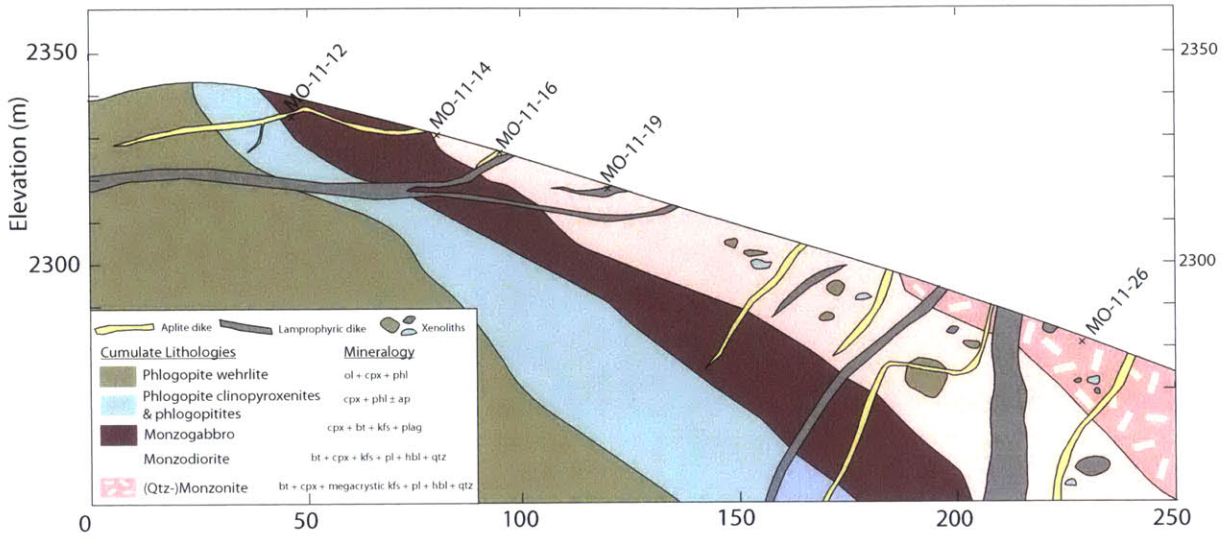

Fig. 5-1: Detailed cross-section across alkaline fractionation sequence from which U-Pb geochronology samples were taken. Lithologies become more evolved left to right, starting with phlogopite wehrlites and grading into clinopyroxene-bear quartz monzonites. Contacts are drawn as sharp lines for clarity, but boundaries between lithologies are gradational. Mineral abbreviations: *ol* olivine, *cpx* clinopyroxene, *phl* phlogopite, *ap* apatite, *bt* biotite, *ksp* K-feldspar, *pl* plagioclase, *hbl* hornblende, *qtz* quartz

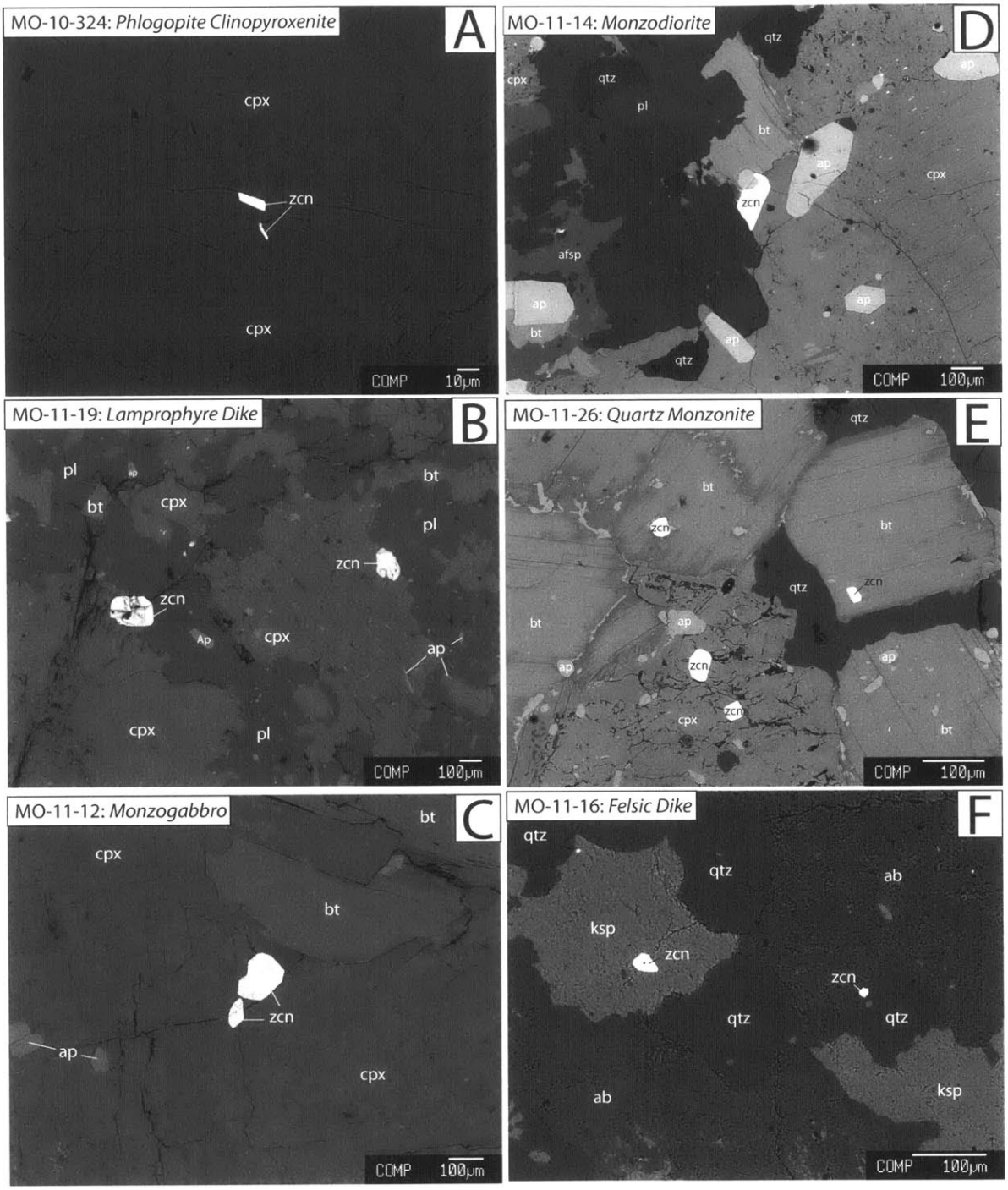

Fig. 5-2: Backscatter electron photomicrographs of samples from the Dariv Igneous Complex showing zircon textural relationships with other phases. Abbreviations used: zcn = zircon, bt = biotite, cpx = clinopyroxene, pl = plagioclase, ab = albite, ksp = K-feldspar, qtz = quartz, ap = apatite. A) MO-10-324 (phlogopite clinopyroxenite): Small (~10 µm) zircon enclosed within cpx ($Mg\#_{cpx}$ = 81.2). Zircon not analyzed in this study. B) MO-11-19 (primitive lamprophyre dike) and C) MO-11-12 (monzogabbro): Late crystallization of zircon on grain boundaries with bt and cpx. D) MO-11-14 (monzodiorite): Zircon crystallizing on grain boundaries of plag, bt, cpx, and ap. E) MO-11-26 (quartz monzonite): Early crystallization of zircon within both cpx and bt. F) Zircon crystallization within ksp and along grain boundaries of qtz and ab.

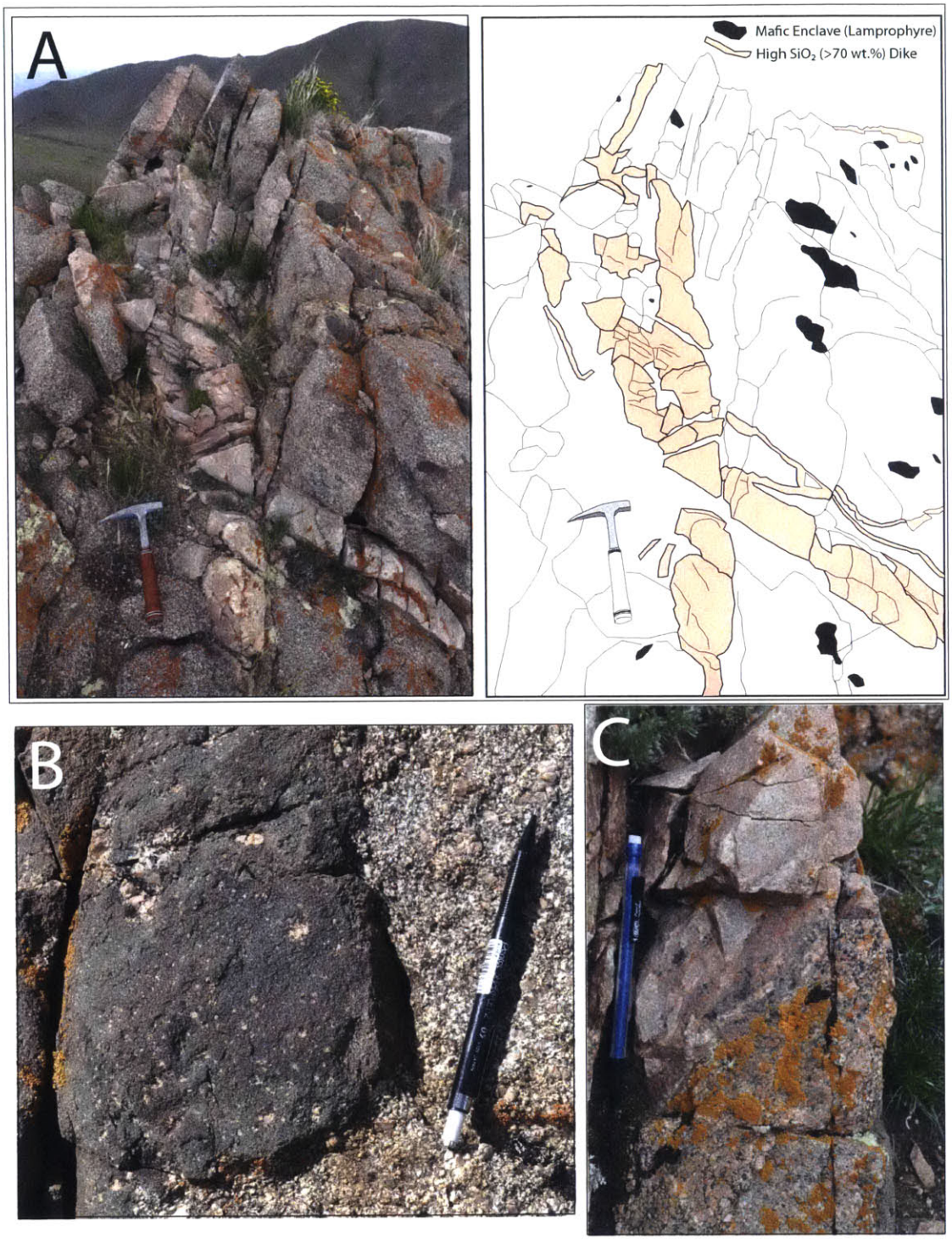

Fig. 5-3: Field relationships indicating magma mixing and mingling in more evolved lithologies. A) Left panel shows field photo of multiple felsic dikes cross-cutting a quartz monzonite, which contains numerous mafic enclaves of disaggregated lamprophyre dikes/melts. B) Lamprophyre enclave with K-feldspar xenocrysts in monzonite. Pencil is 13.5 cm long. C) Diffuse contact between monzonite and late stage felsic dike indicating comagmatic formation and interaction between the two melts.

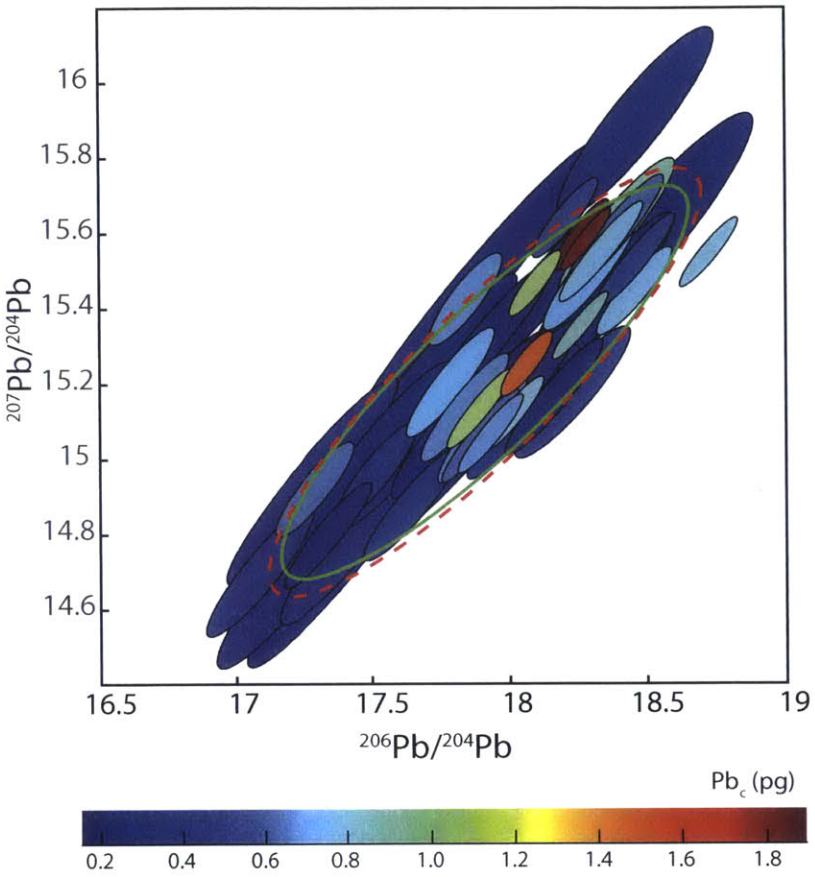

Fig. 5-4: The $^{206}Pb/^{204}Pb$ and $^{207}Pb/^{204}Pb$ compositions of 53 total procedural blanks produced in the MIT Isotope Geochemistry Laboratory between August 2013 and January 2015. Filled ellipses represent individual analyses and are color coded by mass of Pb_c. The red dashed ellipse is the mean and covariance of the measured data points and includes both measurement uncertainty and variability in blank isotopic composition. The green ellipse is the calculated over-dispersion within the data and represents the best estimate of the long-term variability in the isotopic composition of Pb_c.

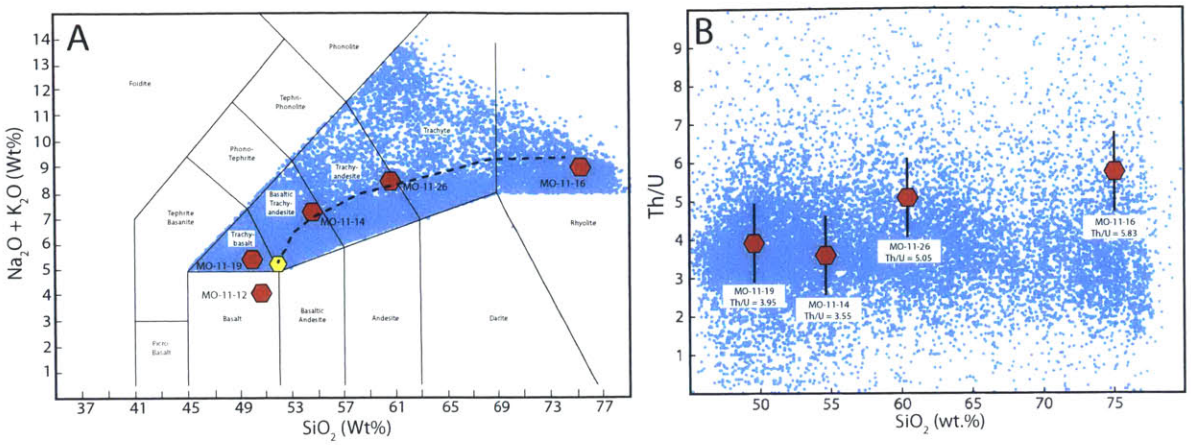

Fig. 5-5: Th/U melt values used in Th-corrected $^{206}Pb/^{238}U$ dates. A) Comparison between the compositions of 14925 whole rock analyses downloaded from Earthchem and the parental melt (yellow hexagon) and liquid line of descent (heavy black line) of rocks from the Dariv Complex (Chapter 3). TAS plot is modified from Le Bas et al. (1986). B) Comparison between the Th/U ratios of the volcanic rocks shown in A and the Th/U of samples MO-11-19, MO-11-14, MO-11-26, and MO-11-16. See text for discussion of the $[Th/U]_{magma}$ used for MO-11-12.

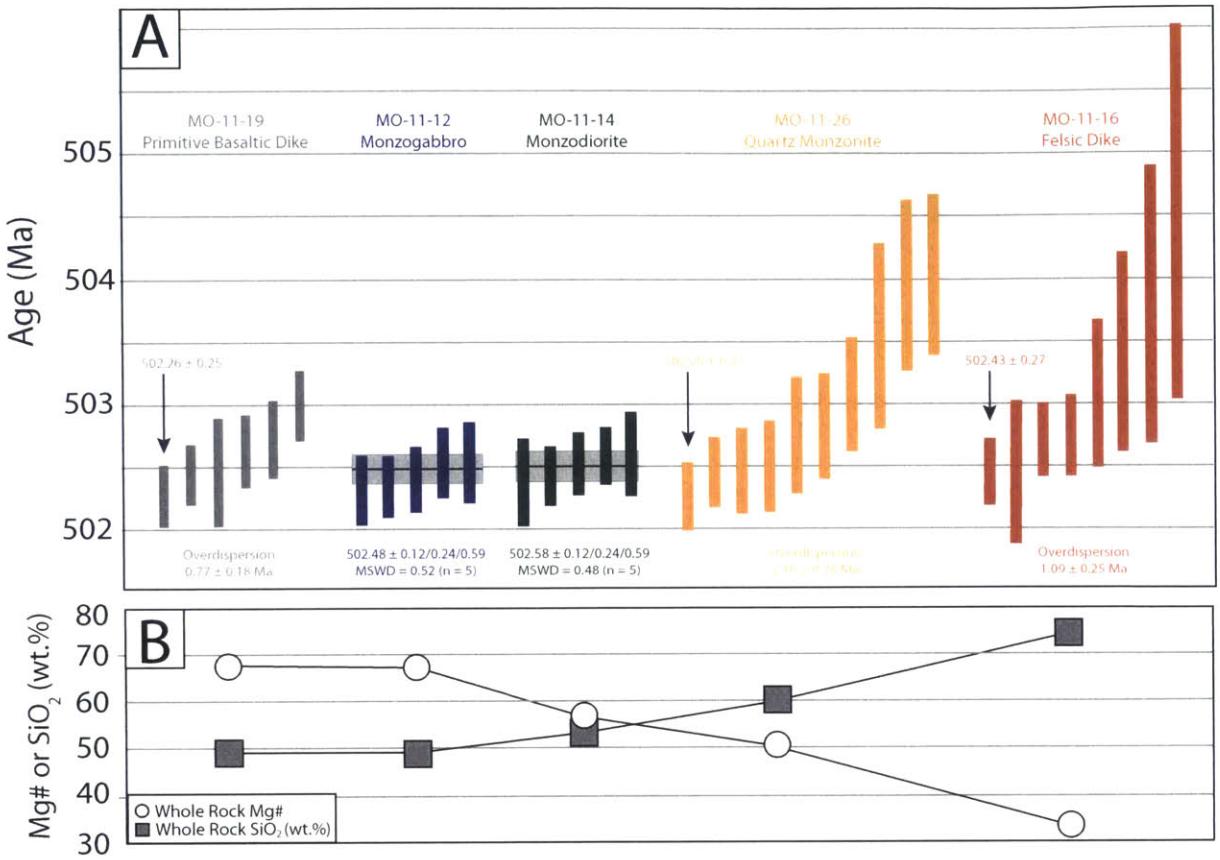

Fig. 5-6: A) U-Pb geochronology data showing Th-corrected $^{206}Pb/^{238}U$ dates for individual zircons. Each bar is an individual analysis and represents 2σ uncertainty. Weighted means for samples with acceptable MSWD's (MO-11-12 & MO-11-14) are shown with internal uncertainties/with tracer calibration uncertainties/with decay constant uncertainties. MSWD's for MO-11-19, MO-11-26, and MO-11-16 indicate that they are not a single population. For these samples, overdispersion and crystallization ages for youngest zircons are shown. Overdispersion indicates the amount of time represented by each population that cannot be accounted for using analytical uncertainty and is calculated using equations in Vermeesch, 2010. B) Whole rock Mg# and SiO_2 of analyzed samples (see Chapter 3).

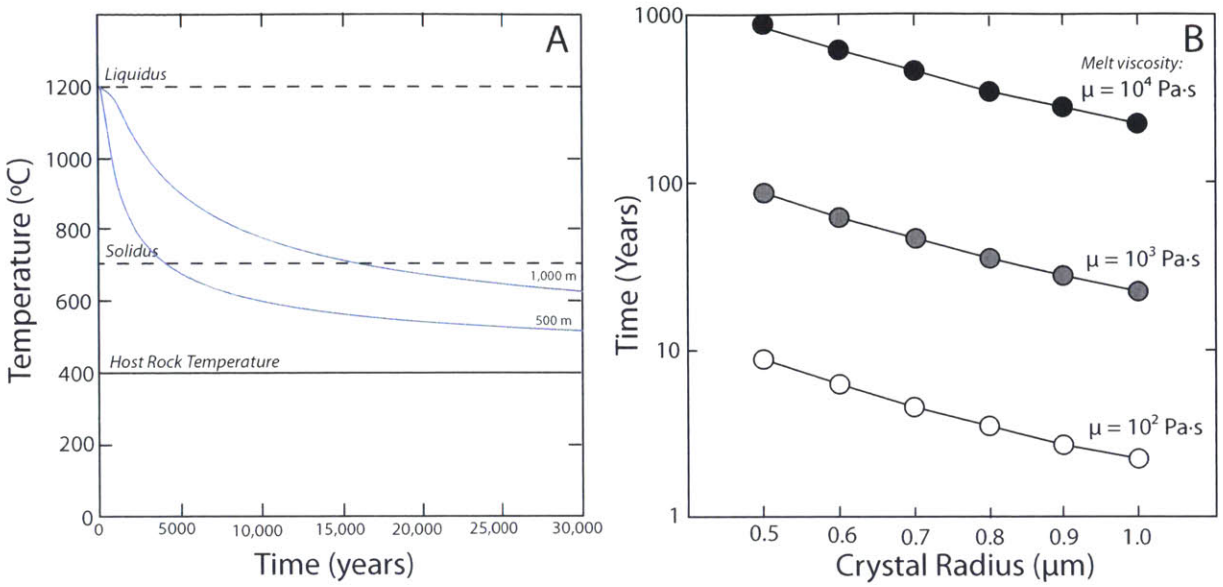

Fig. 5-7: Timescales associated with cooling and crystal settling. A) Temperature evolution of sheet-like bodies with thicknesses of 500 and 1000 m, an initial uniform temperature of 1200°C, and external contact temperatures held at 400°C (see Carslaw and Jaeger, p. 100). This model assumes that during cooling no additional heat (e.g., radiogenic or latent heat) was produced or added to the system (e.g., magmatic recharge events) and that heat loss was entirely from the sides. T_0 was set at 1200°C using previously estimated magmatic temperatures for the most primitive cumulates in the Dariv Igneous Complex (Chapter 2). T_h was chosen to be 400 °C based on the observed assemblage of brucite+serpentine in the host serpentinites, which is limited to 360–390°C (at 0.3–0.5 GPa) (Trommsdorff and Connolly 1996). B) Hindered crystal settling timescales for varying magmatic viscosities and crystallizing grain sizes following the equations 2, 3, & 4 of Bachmann & Bergantz (2004). A crystal-melt density difference ($\Delta\rho$) of 400 kg/m^3, a crystallinity of 0.1, and settling distance of 500 m were used. The calculated timescales are much more rapid than those calculated for cooling and solidification, therefore crystal settling is an efficient fractionation mechanism during crystallization of relatively low viscosity basaltic melts. In more evolved silicic melts, characterized by higher viscosities and smaller $\Delta\rho$ values, crystal settling velocities will be lower. In these melts, crystal settling may not be a viable fractionation mechanism (Hawkesworth et al., 2000).

5.8 Tables

TABLE 5-1: CA-IDTIMS U-Pb ZIRCON GEOCHRONOLOGY RESULTS

Frac.	Dates $^{206}Pb/^{238}U^{*}$	2σ abs.	$^{207}Pb/^{235}U^{\dagger}$	2σ abs.	$^{207}Pb/^{206}Pb^{\dagger}$	2σ abs.	% Disc.[§]	Corr. Coef.	Composition Th/U[#]	Pb_c (pg)[**]	Pb*/Pb_c[††]	Isotopic Ratios $^{206}Pb/^{204}Pb$[§§]	$^{208}Pb/^{206}Pb$[#,#]	$^{206}Pb/^{238}U^{*,\#\#}$	2σ %	$^{207}Pb/^{235}U^{\#\#}$	2σ %	$^{207}Pb/^{206}Pb^{*,\#\#}$	2σ %
MO-11-12																			
z4	502.38	0.28	502.36	0.40	502.7	1.4	0.07	0.815	0.59	0.39	926	53159	0.184	0.081035	0.057	0.64009	0.10	0.057314	0.056
z10	502.48	0.26	502.72	0.42	504.2	1.5	0.36	0.813	0.45	0.33	762	45391	0.140	0.081051	0.054	0.64066	0.11	0.057354	0.062
z11	502.61	0.32	502.83	0.42	504.3	1.3	0.34	0.875	0.57	0.37	564	32575	0.177	0.081072	0.067	0.64085	0.11	0.057356	0.047
z14	502.61	0.28	503.08	0.46	505.6	1.5	0.61	0.890	0.70	0.29	338	18848	0.220	0.081073	0.059	0.64125	0.12	0.057391	0.062
z16	502.42	0.25	502.68	0.43	504.2	1.7	0.38	0.743	0.50	0.51	476	27953	0.157	0.081041	0.051	0.64060	0.11	0.057356	0.072
MO-11-14																			
z7	502.66	0.24	502.72	0.47	503.3	2.0	0.15	0.721	0.76	0.37	344	18974	0.236	0.081082	0.050	0.64066	0.12	0.057332	0.083
z14	502.49	0.24	502.40	0.44	502.4	1.7	-0.01	0.823	0.85	0.33	488	26276	0.266	0.081054	0.049	0.64016	0.11	0.057307	0.068
z16	502.67	0.34	502.79	0.61	503.7	2.6	0.22	0.668	0.83	0.87	200	10830	0.260	0.081084	0.070	0.64078	0.15	0.057341	0.11
z18	502.60	0.26	502.76	0.41	503.9	1.6	0.27	0.731	0.70	0.33	759	42428	0.218	0.081072	0.054	0.64073	0.10	0.057345	0.066
z19	502.45	0.35	502.49	0.44	503.0	1.3	0.13	0.860	0.71	0.32	1255	69981	0.220	0.081046	0.072	0.64029	0.11	0.057324	0.051
MO-11-16																			
z2	503.52	0.80	505.1	3.4	513	18	1.80	0.319	0.68	0.36	21	1178	0.212	0.08123	0.16	0.6445	0.84	0.05758	0.80
z15	504.7	1.5	504	11	502	62	-0.57	0.326	0.52	0.39	6	356	0.162	0.08142	0.31	0.643	2.9	0.0573	2.8
z17	503.18	0.58	502.5	1.2	499.6	6.1	-0.69	0.393	0.59	0.28	75	4299	0.184	0.081168	0.12	0.6403	0.30	0.05724	0.28
z19	502.52	0.27	502.89	0.73	505.0	3.6	0.50	0.515	0.66	0.58	121	6849	0.204	0.081058	0.057	0.6409	0.18	0.057374	0.16
z21	503.9	1.1	512.0	9.6	549	51	8.16	0.325	0.72	1.01	7	407	0.223	0.08129	0.23	0.656	2.4	0.0585	2.3
z22	502.82	0.32	502.84	0.52	503.4	2.1	0.12	0.719	0.50	0.22	342	20094	0.155	0.081107	0.067	0.64086	0.13	0.057332	0.089
z23	502.79	0.29	503.46	0.67	506.9	3.3	0.83	0.491	0.57	0.20	240	13858	0.178	0.081103	0.060	0.6419	0.17	0.057425	0.15
z24	502.53	0.57	502.56	0.88	503.1	4.0	0.13	0.567	0.44	0.31	127	7609	0.139	0.081059	0.12	0.6404	0.22	0.05733	0.18
MO-11-19																			
z17	502.33	0.25	502.89	0.79	505.8	4.0	0.69	0.443	1.15	0.38	119	5994	0.358	0.081029	0.051	0.6409	0.20	0.05740	0.18
z23	502.53	0.43	502.44	0.52	502.4	1.5	-0.01	0.875	1.00	0.39	438	22759	0.313	0.081061	0.089	0.64022	0.13	0.057308	0.060
z29	503.05	0.28	503.03	0.58	503.3	2.7	0.06	0.600	0.84	0.41	222	12020	0.262	0.081149	0.057	0.64117	0.15	0.057331	0.12
z37	502.79	0.31	502.88	0.47	503.6	2.0	0.18	0.648	1.11	0.40	337	17120	0.347	0.081105	0.065	0.64093	0.12	0.057340	0.085
z45	502.69	0.29	502.5	1.0	501.8	5.3	-0.15	0.325	1.21	0.23	90	4475	0.376	0.081088	0.061	0.6403	0.26	0.05729	0.24
z46	502.51	0.25	502.35	0.43	501.9	1.7	-0.10	0.756	1.11	0.36	676	34303	0.346	0.081058	0.052	0.64006	0.11	0.057295	0.069
MO-11-26																			
z0	504.03	0.69	507.1	4.1	521	22	3.35	0.298	0.54	0.69	16	974	0.170	0.08131	0.14	0.6478	1.0	0.05781	1.0
z5	504.12	0.65	505.2	4.8	511	26	1.30	0.278	0.48	0.25	15	883	0.150	0.08132	0.13	0.6447	1.2	0.05752	1.2
z13	502.88	0.43	504.3	2.0	511	11	1.66	0.306	0.55	0.34	36	2375	0.173	0.081117	0.090	0.6433	0.50	0.05754	0.48
z14	503.62	0.75	504.3	6.8	508	37	0.87	0.278	0.51	0.54	10	574	0.160	0.08124	0.15	0.643	1.7	0.05745	1.7
z15	502.57	0.37	503.6	2.2	509	12	1.28	0.359	0.49	0.50	31	1868	0.152	0.081065	0.077	0.6422	0.56	0.05748	0.54
z28	503.13	0.46	501.7	2.4	496	13	-1.51	0.327	0.50	0.25	30	1803	0.157	0.081159	0.095	0.6390	0.61	0.05713	0.59
z32	502.81	0.47	505.5	3.8	518	21	3.02	0.252	0.51	0.54	18	1044	0.158	0.081106	0.098	0.6452	0.96	0.05773	0.94
z40	502.33	0.27	502.59	0.53	504.2	2.3	0.38	0.683	0.79	0.33	187	10220	0.246	0.081027	0.056	0.64046	0.13	0.057353	0.10
z43	502.53	0.28	502.7	1.5	503.8	7.6	0.28	0.442	0.54	0.51	50	2927	0.167	0.081059	0.058	0.6406	0.37	0.05735	0.34
z47	502.55	0.35	503.1	1.7	506.0	9.0	0.71	0.167	0.54	0.51	41	2423	0.167	0.081062	0.072	0.6413	0.42	0.05740	0.41

[*] Corrected for initial Th/U disequilibrium using radiogenic ^{208}Pb and $Th/U_{[Magma]}$ of MO-11-12=4.30, MO-11-14=4.65, MO-11-16=5.83, MO-11-19=3.95, and MO-11-26=5.05. All uncertainties are ± 1 (2σ)

[†] Isotopic dates calculated using the decay constants λ238 = 1.55125E-10 and λ235 = 9.8485E-10 (Jaffey et al. 1971).

[§] % discordance = 100 - (100 * ($^{206}Pb/^{238}U$ date) / ($^{207}Pb/^{206}Pb$ date))

[#] Th contents calculated from radiogenic ^{208}Pb and the $^{207}Pb/^{206}Pb$ date of the sample, assuming concordance between U-Th and Pb systems.

[**] Total mass of common Pb.

[††] Ratio of radiogenic Pb (including ^{208}Pb) to common Pb.

[§§] Measured ratio corrected for fractionation and spike contribution only.

[#,#] Measured ratios corrected for fractionation, tracer and blank.

APPENDIX A: Map of Fieldwork Localities

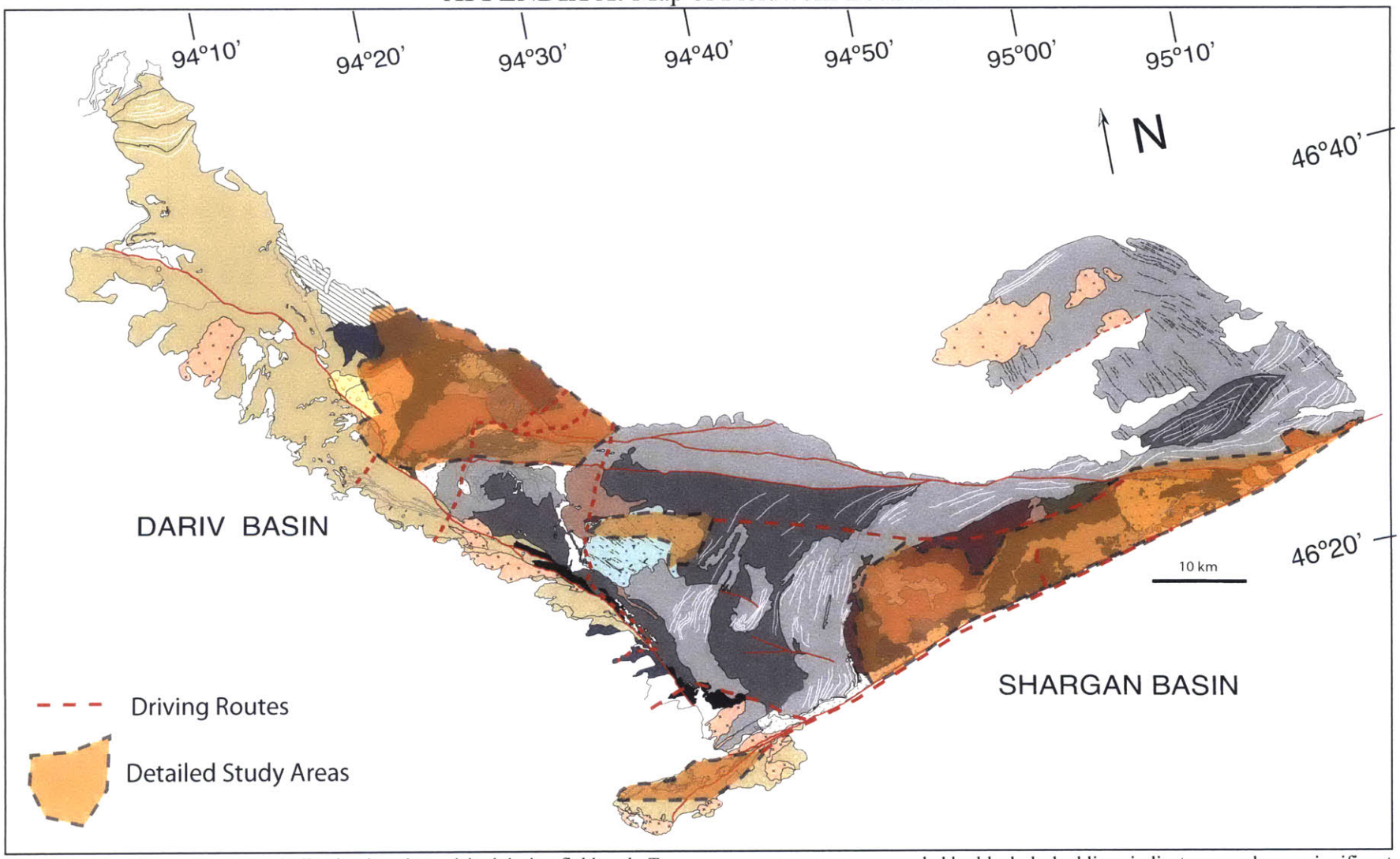

Fig. A-1 Map of the Dariv Range indicating locations visited during fieldwork. Transparent orange areas surrounded by black dashed lines indicate area where a significant amount of time mapping and sampling was spent. Dashed red line indicates routes driven across the mountain range. During the drives frequent stops to observe the lithologies and field relationships were taken.

APPENDIX B:
Mineral Major and Trace Element Compositions

Table B-1: Average major element concentrations (wt.%) in olivine

Sample	MO-10-396 (n=6)			MO-10-394 (n=13)			MO-10-385 (n=8)		
	Average	$2\sigma_{SD}$	$2\sigma_{SE}$	Average	$2\sigma_{SD}$	$2\sigma_{SE}$	Average	$2\sigma_{SD}$	$2\sigma_{SE}$
SiO_2	39.66	0.40	0.16	39.27	0.81	0.22	38.84	1.87	0.66
TiO_2	0.02	0.02	0.01	0.01	0.03	0.01	0.00	0.02	0.01
Cr_2O_3	0.00	0.01	0.00	0.00	0.00	0.00	0.01	0.02	0.01
Al_2O_3	0.00	0.00	0.00	0.00	0.01	0.00	0.01	0.02	0.01
FeO	13.18	1.05	0.43	18.34	0.76	0.21	18.99	0.40	0.14
MnO	0.20	0.06	0.02	0.26	0.06	0.02	0.33	0.04	0.01
NiO	0.18	0.04	0.02	0.12	0.08	0.02	0.02	0.09	0.03
MgO	46.75	1.80	0.73	42.81	0.82	0.23	42.67	0.47	0.17
CaO	0.03	0.02	0.01	0.01	0.03	0.01	0.03	0.03	0.01
Total	100.02			100.82			100.91		
Si	86.34	1.28	0.52	0.99	0.01	0.00	0.98	0.04	0.01
Ti	0.99	0.02	0.01	0.00	0.00	0.00	0.00	0.00	0.00
Cr	0.00	0.00	0.00	0.00	0.00	0.00	0.00	0.00	0.00
Al	0.00	0.00	0.00	0.00	0.00	0.00	0.00	0.00	0.00
Fe	0.00	0.00	0.00	0.39	0.02	0.00	0.40	0.01	0.00
Mn	0.27	0.02	0.01	0.01	0.00	0.00	0.01	0.00	0.00
Ni	0.00	0.00	0.00	0.00	0.00	0.00	0.00	0.00	0.00
Mg	0.00	0.00	0.00	1.61	0.02	0.00	1.61	0.03	0.01
Ca	1.73	0.04	0.01	0.00	0.00	0.00	0.00	0.00	0.00
Mg#	86.34	1.28	0.52	80.62	0.83	0.23	80.02	0.26	0.09

Sample	MO-10-392 (n=12)			MO-10-323 (n=13)			MO-11-8 (n=11)		
	Average	$2\sigma_{SD}$	$2\sigma_{SE}$	Average	$2\sigma_{SD}$	$2\sigma_{SE}$	Average	$2\sigma_{SD}$	$2\sigma_{SE}$
SiO_2	37.94	0.87	0.25	37.40	1.26	0.35	37.04	0.53	0.16
TiO_2	0.01	0.02	0.01	0.01	0.02	0.01	0.01	0.01	0.00
Cr_2O_3	0.01	0.03	0.01	0.00	0.00	0.00	0.01	0.01	0.00
Al_2O_3	0.00	0.01	0.00	0.00	0.01	0.00	0.00	0.01	0.00
FeO	24.00	1.19	0.34	25.81	2.28	0.63	27.96	1.41	0.43
MnO	0.41	0.06	0.02	0.47	0.09	0.03	0.46	0.05	0.02
NiO	0.05	0.10	0.03	0.13	0.06	0.02	0.11	0.05	0.01
MgO	38.51	0.99	0.29	36.71	1.47	0.41	34.48	2.16	0.65
CaO	0.02	0.03	0.01	0.01	0.03	0.01	0.03	0.02	0.01
Total	100.96			100.55			100.09		
Si	0.98	0.01	0.00	0.98	0.02	0.00	0.99	0.03	0.01
Ti	0.00	0.00	0.00	0.00	0.00	0.00	0.00	0.00	0.00
Cr	0.00	0.00	0.00	0.00	0.00	0.00	0.00	0.00	0.00
Al	0.00	0.00	0.00	0.00	0.00	0.00	0.00	0.00	0.00
Fe	0.52	0.02	0.01	0.57	0.05	0.01	0.62	0.04	0.01
Mn	0.01	0.00	0.00	0.01	0.00	0.00	0.01	0.00	0.00
Ni	0.00	0.00	0.00	0.00	0.00	0.00	0.00	0.00	0.00
Mg	1.49	0.03	0.01	1.44	0.05	0.01	1.37	0.06	0.02
Ca	0.00	0.00	0.00	0.00	0.00	0.00	0.00	0.00	0.00
Mg#	74.10	1.22	0.35	71.72	2.55	0.71	68.72	2.37	0.71

APPENDIX B: *Mineral Chemistry*

Table B-2: Average major element concentrations (wt.%) in clinopyroxene

Sample	MO-10-396 (n=16)			MO-10-394 (n = 14)			MO-10-385 (n = 13)			MO-10-392 (n = 6)		
	Average	$2\sigma_{SD}$	$2\sigma_{SE}$	Average	$2\sigma_{SD}$	$2\sigma_{SE}$	Average	$2\sigma_{SD}$	$2\sigma_{SE}$	Average	$2\sigma_{SD}$	$2\sigma_{SE}$
SiO_2	54.66	1.19	0.30	53.20	1.65	0.44	52.77	1.29	0.36	51.95	0.94	0.39
TiO_2	0.19	0.07	0.02	0.27	0.09	0.02	0.31	0.14	0.04	0.46	0.25	0.10
Cr_2O_3	0.49	0.15	0.04	0.32	0.10	0.03	0.24	0.14	0.04	0.10	0.05	0.02
Al_2O_3	0.84	0.32	0.08	1.33	0.36	0.10	1.38	0.58	0.16	2.47	0.64	0.26
FeO	3.32	0.60	0.15	4.47	0.49	0.13	4.71	0.60	0.17	6.58	0.30	0.12
MnO	0.12	0.05	0.01	0.11	0.04	0.01	0.12	0.04	0.01	0.19	0.01	0.01
NiO	-	-	-	0.01	0.02	0.01	0.02	0.02	0.01	-	-	-
MgO	17.88	0.36	0.09	16.71	0.45	0.12	16.15	0.43	0.12	15.70	0.46	0.19
CaO	23.21	0.62	0.15	22.44	0.61	0.16	23.94	1.42	0.39	22.67	1.22	0.50
Na_2O	0.21	0.06	0.01	0.28	0.09	0.02	0.24	0.15	0.04	0.25	0.09	0.04
K_2O	0.01	0.01	0.00	0.00	0.01	0.00	0.01	0.02	0.00	0.01	0.01	0.00
Total	100.93			99.14			99.88			100.37		
Si	1.97	0.02	0.00	1.96	0.03	0.01	1.94	0.03	0.01	1.90	0.03	0.01
Ti	0.01	0.00	0.00	0.01	0.00	0.00	0.01	0.00	0.00	0.01	0.01	0.00
Cr	0.01	0.00	0.00	0.01	0.00	0.00	0.01	0.00	0.00	0.00	0.00	0.00
Al	0.04	0.01	0.00	0.06	0.02	0.00	0.06	0.03	0.01	0.11	0.03	0.01
Fe^{3+}	0.02	0.03	0.01	0.02	0.05	0.01	0.06	0.05	0.01	0.07	0.05	0.02
Fe^{2+}	0.08	0.04	0.01	0.12	0.05	0.01	0.08	0.04	0.01	0.13	0.05	0.02
Mn	0.00	0.00	0.00	0.00	0.00	0.00	0.00	0.00	0.00	0.01	0.00	0.00
Ni	-	-	-	0.00	0.00	0.00	0.00	0.00	0.00	-	-	-
Mg	0.96	0.02	0.00	0.92	0.03	0.01	0.88	0.02	0.01	0.86	0.02	0.01
Ca	0.90	0.02	0.01	0.89	0.02	0.01	0.94	0.05	0.01	0.89	0.04	0.02
Na	0.01	0.00	0.00	0.02	0.01	0.00	0.02	0.01	0.00	0.02	0.01	0.00
K	0.00	0.00	0.00	0.00	0.00	0.00	0.00	0.00	0.00	0.00	0.00	0.00
Mg#	90.57	1.58	0.39	86.95	1.45	0.39	85.96	1.67	0.46	80.97	0.37	0.15
En	0.48	0.01	0.00	0.46	0.02	0.00	0.44	0.01	0.00	0.43	0.01	0.00
Fs	0.04	0.02	0.00	0.06	0.02	0.01	0.04	0.02	0.01	0.06	0.03	0.01
Wo	0.44	0.01	0.00	0.43	0.01	0.00	0.45	0.03	0.01	0.40	0.01	0.00

Sample	MO-10-323 (n = 9)			MO-11-8 (n = 8)			MO-10-325 (n = 10)			MO-10-324 (n = 8)		
	Average	$2\sigma_{SD}$	$2\sigma_{SE}$	Average	$2\sigma_{SD}$	$2\sigma_{SE}$	Average	$2\sigma_{SD}$	$2\sigma_{SE}$	Average	$2\sigma_{SD}$	$2\sigma_{SE}$
SiO_2	52.17	0.97	0.32	52.93	3.27	1.16	52.32	1.76	0.56	52.82	1.72	0.61
TiO_2	0.48	0.13	0.04	0.24	0.51	0.18	0.39	0.25	0.08	0.38	0.32	0.11
Cr_2O_3	0.32	0.41	0.14	0.13	0.20	0.07	0.05	0.07	0.02	0.13	0.09	0.03
Al_2O_3	2.28	0.82	0.27	1.07	2.34	0.83	1.72	0.78	0.25	1.96	0.74	0.26
FeO	5.76	1.03	0.34	5.91	1.23	0.43	5.28	0.51	0.16	6.08	2.65	0.94
MnO	0.14	0.05	0.02	0.24	0.05	0.02	0.13	0.04	0.01	0.18	0.16	0.06
NiO	-	-	-	0.03	0.02	0.01	0.06	-	-	-	-	-
MgO	15.13	0.73	0.24	15.57	0.82	0.29	15.56	1.16	0.37	14.77	1.53	0.54
CaO	23.08	0.73	0.24	23.53	3.03	1.07	24.12	1.70	0.54	23.29	1.63	0.57
Na_2O	0.32	0.09	0.03	0.11	0.26	0.09	0.26	0.08	0.03	0.43	0.23	0.08
K_2O	0.01	0.02	0.01	0.00	0.00	0.00	0.01	0.01	0.00	0.04	0.18	0.07
Total	99.69			99.73			99.86			100.08		
Si	1.93	0.02	0.01	1.96	0.07	0.03	1.92	0.04	0.01	1.95	0.05	0.02
Ti	0.01	0.00	0.00	0.01	0.01	0.01	0.01	0.01	0.00	0.01	0.01	0.00
Cr	0.01	0.01	0.00	0.00	0.01	0.00	0.00	0.00	0.00	0.00	0.00	0.00
Al	0.10	0.04	0.01	0.05	0.10	0.04	0.07	0.03	0.01	0.09	0.03	0.01
Fe^{3+}	0.03	0.02	0.01	0.03	0.03	0.01	0.07	0.06	0.02	0.04	0.05	0.02
Fe^{2+}	0.14	0.04	0.01	0.15	0.02	0.01	0.09	0.06	0.02	0.15	0.11	0.04
Mn	0.00	0.00	0.00	0.01	0.00	0.00	0.00	0.00	0.00	0.01	0.00	0.00
Ni	-	-	-	0.00	0.00	0.00	0.00	-	-	-	-	-
Mg	0.83	0.03	0.01	0.86	0.04	0.01	0.85	0.07	0.02	0.81	0.09	0.03
Ca	0.91	0.02	0.01	0.93	0.10	0.03	0.95	0.06	0.02	0.92	0.07	0.02
Na	0.02	0.01	0.00	0.01	0.02	0.01	0.02	0.01	0.00	0.03	0.02	0.01
K	0.00	0.00	0.00	0.00	0.00	0.00	0.00	0.00	0.00	0.00	0.01	0.00
Mg#	82.40	3.18	1.06	82.44	3.58	1.27	83.99	2.18	0.69	81.25	8.16	2.88
En	0.42	0.02	0.01	0.43	0.02	0.01	0.43	0.04	0.01	0.41	0.04	0.02
Fs	0.07	0.02	0.01	0.08	0.01	0.00	0.04	0.03	0.01	0.07	0.05	0.02
Wo	0.43	0.02	0.01	0.45	0.08	0.03	0.45	0.03	0.01	0.44	0.03	0.01

APPENDIX B: *Mineral Chemistry*

Sample	MO-11-9 (n = 9)			MO-11-10 (n = 5)			MO-11-12 (n=5)			MO-11-13 (n=8)		
	Average	$2\sigma_{SD}$	$2\sigma_{SE}$	Average	$2\sigma_{SD}$	$2\sigma_{SE}$	Average	$2\sigma_{SD}$	$2\sigma_{SE}$	Average	$2\sigma_{SD}$	$2\sigma_{SE}$
SiO_2	52.93	1.75	0.58	53.45	1.26	0.56	53.23	0.32	0.14	52.76	0.89	0.40
TiO_2	0.22	0.28	0.09	0.20	0.37	0.17	0.07	0.05	0.02	0.05	0.06	0.02
Cr_2O_3	0.13	0.08	0.03	0.06	0.03	0.01	0.06	0.01	0.01	0.03	0.04	0.01
Al_2O_3	1.19	1.27	0.42	0.93	1.41	0.63	0.46	0.35	0.16	0.47	0.56	0.20
FeO	6.80	1.10	0.37	6.54	0.94	0.42	8.92	0.41	0.18	10.75	1.51	0.53
MnO	0.20	0.07	0.02	0.24	0.08	0.03	0.39	0.03	0.01	0.49	0.09	0.03
NiO	0.04	0.04	0.01	-	-	-	-	-	-	0.00	0.01	0.00
MgO	15.40	0.47	0.16	15.07	0.93	0.42	13.56	0.44	0.20	12.39	0.48	0.17
CaO	21.96	1.37	0.46	23.26	1.85	0.83	23.58	0.63	0.28	22.86	1.73	0.61
Na_2O	0.30	0.15	0.05	0.30	0.36	0.16	0.22	0.07	0.03	0.22	0.14	0.05
K_2O	0.00	0.01	0.00	-	-	-	-	-	-	0.00	0.00	0.00
Total	99.12			100.05			100.48			100.33		
Si	1.97	0.04	0.01	1.97	0.05	0.02	1.98	0.01	0.00	1.98	0.01	0.01
Ti	0.01	0.01	0.00	0.01	0.01	0.00	0.00	0.00	0.00	0.00	0.00	0.00
Cr	0.00	0.00	0.00	0.00	0.00	0.00	0.00	0.00	0.00	0.00	0.00	0.00
Al	0.05	0.06	0.02	0.04	0.06	0.03	0.02	0.02	0.01	0.02	0.02	0.01
Fe^{3+}	0.02	0.04	0.01	0.03	0.04	0.02	0.03	0.01	0.00	0.05	0.07	0.02
Fe^{2+}	0.19	0.04	0.01	0.18	0.05	0.02	0.25	0.01	0.01	0.30	0.09	0.03
Mn	0.01	0.00	0.00	0.01	0.00	0.00	0.01	0.00	0.00	0.02	0.00	0.00
Ni	0.00	0.00	0.00	-	-	-	-	-	-	0.00	0.00	0.00
Mg	0.85	0.02	0.01	0.83	0.04	0.02	0.75	0.02	0.01	0.70	0.03	0.01
Ca	0.88	0.05	0.02	0.92	0.07	0.03	0.94	0.03	0.01	0.93	0.08	0.03
Na	0.02	0.02	0.01	0.02	0.03	0.01	0.02	0.00	0.00	0.02	0.01	0.00
K	0.00	0.00	0.00	-	-	-	-	-	-	0.00	0.00	0.00
Mg#	80.16	2.29	0.76	80.41	3.07	1.37	73.04	1.40	0.62	67.28	3.27	1.16
En	0.43	0.01	0.00	0.41	0.02	0.01	0.38	0.01	0.00	0.35	0.01	0.00
Fs	0.10	0.02	0.01	0.09	0.03	0.01	0.12	0.01	0.00	0.15	0.04	0.02
Wo	0.42	0.04	0.01	0.45	0.05	0.02	0.46	0.02	0.01	0.46	0.05	0.02

Sample	MO-11-21 (n = 6)			MO-11-26 (n = 8)			MO-11-19 (n = 10)		
	Average	$2\sigma_{SD}$	$2\sigma_{SE}$	Average	$2\sigma_{SD}$	$2\sigma_{SE}$	Average	$2\sigma_{SD}$	$2\sigma_{SE}$
SiO_2	52.81	0.76	0.44	52.82	1.62	0.93	52.28	2.91	0.92
TiO_2	0.14	0.10	0.04	0.08	0.07	0.02	0.32	0.50	0.16
Cr_2O_3	0.02	0.05	0.02	0.03	0.15	0.05	0.15	0.49	0.15
Al_2O_3	0.81	0.33	0.13	0.50	0.51	0.18	2.02	2.20	0.70
FeO	8.65	0.50	0.20	11.66	4.53	1.60	8.21	1.29	0.41
MnO	0.40	0.06	0.02	0.61	0.33	0.12	0.37	0.08	0.03
NiO	0.00	0.01	0.01	0.01	0.03	0.01	-	-	-
MgO	13.96	0.84	0.34	12.02	3.39	1.20	14.01	0.77	0.24
CaO	22.31	1.02	0.42	22.09	1.90	0.67	22.02	2.43	0.77
Na_2O	0.36	0.09	0.04	0.27	0.05	0.02	0.55	0.32	0.10
K_2O	0.00	0.01	0.00	0.00	0.00	0.00	0.05	0.21	0.07
Total	99.82			100.96			100.07	1.45	0.46
Si	1.97	0.00	0.00	1.98	0.05	0.03	1.94	0.09	0.03
Ti	0.00	0.00	0.00	0.00	0.00	0.00	0.01	0.01	0.00
Cr	0.00	0.00	0.00	0.00	0.00	0.00	0.00	0.01	0.00
Al	0.04	0.01	0.01	0.02	0.02	0.01	0.09	0.10	0.03
Fe^{3+}	0.07	0.07	0.03	0.06	0.06	0.02	0.05	0.09	0.03
Fe^{2+}	0.20	0.06	0.03	0.31	0.17	0.06	0.20	0.06	0.02
Mn	0.01	0.00	0.00	0.02	0.01	0.00	0.01	0.00	0.00
Ni	0.00	0.00	0.00	0.00	0.00	0.00	0.00	0.00	0.00
Mg	0.79	0.05	0.02	0.69	0.18	0.07	0.77	0.03	0.01
Ca	0.90	0.03	0.01	0.91	0.07	0.02	0.88	0.09	0.03
Na	0.03	0.01	0.00	0.02	0.00	0.00	0.04	0.02	0.01
K	0.00	0.00	0.00	0.00	0.00	0.00	0.00	0.01	0.00
Mg#	74.18	2.23	0.91	64.65	14.48	5.12	75.28	3.22	1.02
En	0.39	0.03	0.01	0.34	0.09	0.03	0.39	0.02	0.01
Fs	0.10	0.03	0.01	0.16	0.08	0.03	0.10	0.03	0.01
Wo	0.44	0.02	0.01	0.44	0.04	0.02	0.41	0.08	0.03

Table B-3: Average major element concentrations (wt.%) in biotite

Sample	MO-10-396 (n = 5)			MO-10-394 (n = 11)			MO-10-385 (n=5)			MO-10-392 (n = 15)		
	Average	$2\sigma_{SD}$	$2\sigma_{SE}$	Average	$2\sigma_{SD}$	$2\sigma_{SE}$	Average	$2\sigma_{SD}$	$2\sigma_{SE}$	Average	$2\sigma_{SD}$	$2\sigma_{SE}$
SiO_2	38.64	0.55	0.25	38.00	1.14	0.34	38.32	0.30	0.14	36.93	0.83	0.21
TiO_2	2.32	0.76	0.34	3.64	1.55	0.47	3.83	0.14	0.06	4.63	0.27	0.07
Cr_2O_3	0.90	0.45	0.20	0.45	0.41	0.12	1.00	0.09	0.04	0.36	0.12	0.03
Al_2O_3	15.97	1.37	0.61	14.81	0.88	0.27	14.31	0.37	0.17	15.29	0.68	0.18
FeO	8.13	1.49	0.66	8.45	2.82	0.85	5.91	0.45	0.20	8.75	0.41	0.10
MnO	0.08	0.02	0.01	0.04	0.06	0.02	0.03	0.01	0.01	0.03	0.03	0.01
NiO	-	-	-	0.06	0.07	0.02	0.07	0.04	0.02	0.06	0.04	0.02
MgO	19.55	1.30	0.58	19.17	2.65	0.80	21.23	0.52	0.23	18.60	0.60	0.16
CaO	0.05	0.07	0.03	0.01	0.02	0.01	0.01	0.03	0.01	0.01	0.02	0.00
Na_2O	0.12	0.06	0.03	0.33	0.44	0.13	0.49	0.09	0.04	0.61	0.11	0.03
K_2O	9.61	1.65	0.74	9.20	0.89	0.27	9.16	0.37	0.17	9.18	0.23	0.06
SrO	-	-	-	0.18	0.05	0.02	-	-	-	-	-	-
BaO	-	-	-	0.18	0.30	0.09	-	-	-	-	-	-
F	-	-	-	0.03	0.12	0.04	-	-	-	0.53	0.23	0.07
Cl	-	-	-	0.05	0.05	0.02	-	-	-	0.02	0.02	0.01
Total	95.39	-	-	94.42	-	-	94.37	-	-	94.80	-	-
Si	5.58	0.07	0.03	5.57	0.08	0.02	5.55	0.05	0.02	5.42	0.08	0.02
Al^{iv}	2.42	0.07	0.03	2.43	0.08	0.02	2.44	0.05	0.02	2.58	0.07	0.02
Al^{vi}	0.30	0.24	0.11	0.12	0.12	0.04	0.00	0.01	0.00	0.07	0.10	0.02
Ti	0.25	0.08	0.04	0.40	0.17	0.05	0.42	0.01	0.01	0.51	0.03	0.01
Cr	0.10	0.05	0.02	0.05	0.05	0.01	0.11	0.01	0.00	0.04	0.01	0.00
Fe	0.98	0.19	0.08	1.04	0.36	0.11	0.72	0.05	0.02	1.08	0.05	0.01
Mn	0.01	0.00	0.00	0.00	0.01	0.00	0.00	0.00	0.00	0.00	0.00	0.00
Mg	4.21	0.26	0.11	4.18	0.52	0.16	4.58	0.11	0.05	4.07	0.14	0.04
Ni	-	-	-	0.01	0.01	0.00	0.01	0.00	0.00	0.01	0.00	0.00
Ca	0.01	0.01	0.01	0.00	0.00	0.00	0.00	0.00	0.00	0.00	0.00	0.00
Na	0.03	0.02	0.01	0.09	0.12	0.04	0.14	0.02	0.01	0.17	0.03	0.01
K	1.77	0.31	0.14	1.72	0.18	0.05	1.69	0.06	0.03	1.72	0.04	0.01
Sr	0.00	0.00	0.00	0.02	0.00	0.00	-	-	-	0.00	0.00	0.00
Ba	0.00	0.00	0.00	0.01	0.02	0.01	-	-	-	0.00	0.00	0.00
OH*	-	-	-	3.97	0.05	0.02	-	-	-	3.75	0.11	0.03
F	-	-	-	0.02	0.05	0.02	-	-	-	0.25	0.11	0.03
Cl	-	-	-	0.01	0.01	0.00	-	-	-	0.00	0.00	0.00
Mg#	81.08	3.22	1.44	80.11	7.31	2.20	86.49	1.05	0.47	79.11	1.06	0.27

Sample	MO-10-323 (n = 12)			MO-11-8 (n = 9)			MO-10-325 (n = 20)			MO-10-324 (n = 9)		
	Average	$2\sigma_{SD}$	$2\sigma_{SE}$	Average	$2\sigma_{SD}$	$2\sigma_{SE}$	Average	$2\sigma_{SD}$	$2\sigma_{SE}$	Average	$2\sigma_{SD}$	$2\sigma_{SE}$
SiO_2	37.91	2.20	0.63	36.06	2.17	0.72	37.13	0.51	0.11	37.01	0.77	0.26
TiO_2	2.64	0.54	0.16	3.11	0.35	0.12	2.90	0.49	0.11	2.92	0.73	0.24
Cr_2O_3	0.26	0.32	0.09	0.38	0.10	0.03	0.11	0.06	0.01	0.17	0.05	0.02
Al_2O_3	14.79	0.93	0.27	15.24	0.55	0.18	15.46	0.96	0.21	15.42	0.50	0.17
FeO	8.06	1.38	0.40	9.70	2.44	0.81	12.31	1.01	0.23	14.78	1.44	0.48
MnO	0.03	0.03	0.01	0.08	0.07	0.02	0.09	0.03	0.01	0.15	0.05	0.02
NiO	0.08	0.04	0.02	0.05	0.00	0.00	0.07	0.03	0.01	-	-	-
MgO	20.42	1.60	0.46	18.96	1.91	0.64	16.68	0.99	0.22	15.17	1.14	0.38
CaO	0.00	0.01	0.00	0.01	0.03	0.01	0.01	0.01	0.00	0.01	0.02	0.01
Na_2O	0.80	0.20	0.06	0.23	0.24	0.08	0.34	0.08	0.02	0.35	0.07	0.02
K_2O	8.61	0.41	0.12	9.07	0.50	0.17	9.34	0.41	0.09	8.78	0.20	0.07
SrO	0.18	0.04	0.02	0.09	0.05	0.02	-	-	-	0.19	0.02	0.01
BaO	0.41	0.12	0.05	0.20	0.28	0.11	-	-	-	0.57	0.10	0.03
F	0.16	0.12	0.05	0.13	0.08	0.03	0.23	0.11	0.03	0.29	0.10	0.03
Cl	0.01	0.02	0.01	0.01	0.01	0.00	0.04	0.02	0.01	0.05	0.03	0.01
Total	93.95	-	-	93.13	-	-	94.54	-	-	95.86	-	-
Si	5.56	0.19	0.05	5.40	0.15	0.05	5.53	0.06	0.01	5.53	0.08	0.03
Al^{iv}	2.44	0.19	0.05	2.60	0.15	0.05	2.47	0.06	0.01	2.47	0.08	0.03
Al^{vi}	0.12	0.09	0.03	0.10	0.04	0.01	0.25	0.11	0.02	0.24	0.04	0.01
Ti	0.29	0.06	0.02	0.35	0.03	0.01	0.33	0.06	0.01	0.33	0.08	0.03
Cr	0.03	0.04	0.01	0.04	0.01	0.00	0.01	0.01	0.00	0.02	0.01	0.00
Fe	0.99	0.17	0.05	1.22	0.34	0.11	1.53	0.12	0.03	1.85	0.19	0.06
Mn	0.00	0.00	0.00	0.01	0.01	0.00	0.01	0.00	0.00	0.02	0.01	0.00

Mg	4.47	0.33	0.10	4.23	0.31	0.10	3.71	0.24	0.05	3.38	0.24	0.08
Ni	0.01	0.01	0.00	0.01	0.00	0.00	0.01	0.00	0.00	-	-	-
Ca	0.00	0.00	0.00	0.00	0.01	0.00	0.00	0.00	0.00	0.00	0.00	0.00
Na	0.23	0.06	0.02	0.07	0.07	0.02	0.10	0.02	0.01	0.10	0.02	0.01
K	1.61	0.06	0.02	1.73	0.08	0.03	1.78	0.06	0.01	1.67	0.03	0.01
Sr	0.02	0.00	0.00	0.01	0.00	0.00	0.00	0.00	0.00	0.02	0.00	0.00
Ba	0.02	0.01	0.00	0.01	0.02	0.01	0.00	0.00	0.00	0.03	0.01	0.00
OH*	3.92	0.06	0.02	3.93	0.04	0.01	3.88	0.05	0.02	3.85	0.04	0.01
F	0.07	0.05	0.02	0.06	0.04	0.01	0.11	0.05	0.02	0.14	0.05	0.02
Cl	0.00	0.01	0.00	0.00	0.00	0.00	0.01	0.01	0.00	0.01	0.01	0.00
Mg#	81.85	3.61	1.04	77.66	6.07	2.02	70.72	2.73	0.61	64.65	3.74	1.25

Sample	**MO-11-9 (n = 4)**			**MO-11-10 (n = 13)**			**MO-11-12 (n = 14)**			**MO-11-13 (n = 11)**		
	Average	$2\sigma_{SD}$	$2\sigma_{SE}$	Average	$2\sigma_{SD}$	$2\sigma_{SE}$	Average	$2\sigma_{SD}$	$2\sigma_{SE}$	Average	$2\sigma_{SD}$	$2\sigma_{SE}$
SiO_2	35.41	0.46	0.08	35.77	1.58	0.44	35.76	1.71	0.46	34.89	0.95	0.29
TiO_2	4.53	0.46	0.08	4.30	0.63	0.17	3.88	0.29	0.08	3.64	0.45	0.13
Cr_2O_3	0.39	0.03	0.01	0.18	0.05	0.01	0.16	0.10	0.03	0.05	0.06	0.02
Al_2O_3	14.24	0.95	0.16	14.42	1.10	0.30	13.23	1.00	0.27	13.78	0.91	0.28
FeO	12.15	1.30	0.22	12.14	0.58	0.16	16.45	1.38	0.37	19.48	1.08	0.32
MnO	0.09	0.05	0.01	0.09	0.06	0.02	0.16	0.05	0.01	0.20	0.05	0.01
NiO	-	-	-	-	-	-	-	-	-	-	-	-
MgO	16.71	0.55	0.09	16.72	0.42	0.12	13.86	0.74	0.20	11.84	0.54	0.16
CaO	0.04	0.06	0.01	0.01	0.02	0.01	0.01	0.01	0.00	0.01	0.03	0.01
Na_2O	0.37	0.17	0.03	0.42	0.10	0.03	0.11	0.05	0.01	0.10	0.06	0.02
K_2O	8.30	0.31	0.05	8.86	0.64	0.18	9.27	0.70	0.19	9.28	0.70	0.21
SrO	0.10	0.03	0.00	0.10	0.04	0.01	0.10	0.02	0.01	0.10	0.01	0.00
BaO	0.40	0.30	0.05	0.50	0.22	0.06	0.28	0.28	0.10	0.27	0.23	0.07
F	0.29	0.11	0.02	0.55	0.06	0.02	0.51	0.07	0.03	0.46	0.09	0.03
Cl	0.04	0.04	0.01	0.02	0.01	0.00	0.08	0.01	0.00	0.11	0.01	0.00
Total	92.93	-	-	93.52	-	-	93.29	-	-	93.61	-	-
Si	5.40	0.07	0.01	5.42	0.18	0.05	5.55	0.20	0.05	5.49	0.14	0.04
Al^{iv}	2.55	0.14	0.02	2.55	0.20	0.06	2.42	0.20	0.05	2.51	0.14	0.04
Al^{vi}	0.01	0.03	0.00	0.02	0.06	0.02	0.01	0.04	0.01	0.04	0.06	0.02
Ti	0.52	0.06	0.01	0.49	0.07	0.02	0.45	0.03	0.01	0.43	0.05	0.02
Cr	0.05	0.00	0.00	0.02	0.01	0.00	0.02	0.01	0.00	0.01	0.01	0.00
Fe	1.55	0.16	0.03	1.54	0.08	0.02	2.14	0.20	0.05	2.56	0.13	0.04
Mn	0.01	0.01	0.00	0.01	0.01	0.00	0.02	0.01	0.00	0.03	0.01	0.00
Mg	3.80	0.12	0.02	3.78	0.10	0.03	3.21	0.14	0.04	2.77	0.11	0.03
Ni	-	-	-	-	-	-	-	-	-	-	-	-
Ca	0.01	0.01	0.00	0.00	0.00	0.00	0.00	0.00	0.00	0.00	0.01	0.00
Na	0.11	0.05	0.01	0.12	0.03	0.01	0.03	0.02	0.00	0.03	0.02	0.01
K	1.61	0.06	0.01	1.71	0.11	0.03	1.84	0.12	0.03	1.86	0.15	0.05
Sr	0.01	0.00	0.00	0.01	0.00	0.00	0.01	0.00	0.00	0.01	0.00	0.00
Ba	0.02	0.02	0.00	0.03	0.01	0.00	0.02	0.02	0.01	0.02	0.01	0.00
OH*	3.85	0.06	0.01	3.73	0.03	0.01	3.73	0.04	0.01	3.74	0.05	0.01
F	0.14	0.05	0.01	0.26	0.03	0.01	0.25	0.03	0.01	0.23	0.05	0.01
Cl	0.01	0.01	0.00	0.01	0.00	0.00	0.02	0.00	0.00	0.03	0.00	0.00
Mg#	71.03	1.99	0.33	71.06	1.14	0.32	60.03	3.09	0.83	52.00	1.76	0.53

Sample	**MO-11-14 (n = 10)**			**MO-11-15 (n = 7)**			**MO-11-21 (n = 7)**			**MO-11-23 (n = 6)**		
	Average	$2\sigma_{SD}$	$2\sigma_{SE}$	Average	$2\sigma_{SD}$	$2\sigma_{SE}$	Average	$2\sigma_{SD}$	$2\sigma_{SE}$	Average	$2\sigma_{SD}$	$2\sigma_{SE}$
SiO_2	34.74	1.23	0.39	35.84	1.49	0.56	36.27	0.44	0.17	36.19	0.98	0.40
TiO_2	4.12	0.46	0.15	4.10	0.46	0.17	4.10	0.37	0.14	3.92	0.57	0.23
Cr_2O_3	0.05	0.05	0.02	0.09	0.08	0.03	0.13	0.08	0.03	0.06	0.04	0.02
Al_2O_3	13.59	0.91	0.29	14.06	0.31	0.12	14.07	0.41	0.15	13.56	0.22	0.09
FeO	20.30	0.84	0.27	20.34	0.49	0.18	17.46	0.65	0.24	21.78	0.89	0.36
MnO	0.23	0.10	0.03	0.18	0.08	0.03	0.18	0.04	0.02	0.27	0.06	0.03
NiO	-	-	-	-	-	-	-	-	-	-	-	-
MgO	10.85	0.74	0.23	11.22	0.48	0.18	13.11	0.62	0.23	10.58	0.65	0.27
CaO	0.01	0.02	0.01	0.02	0.10	0.04	0.01	0.01	0.01	0.02	0.07	0.03
Na_2O	0.10	0.07	0.02	0.11	0.02	0.01	0.15	0.04	0.02	0.08	0.04	0.02
K_2O	9.20	0.70	0.22	8.71	0.43	0.16	8.84	0.20	0.08	8.54	1.01	0.41
SrO	0.11	0.02	0.01	0.14	0.03	0.01	0.15	0.02	0.01	0.14	0.01	0.01

BaO	0.12	0.09	0.03	0.21	0.19	0.07	0.54	0.64	0.24	0.25	0.37	0.15
F	0.46	0.12	0.04	0.25	0.06	0.02	0.40	0.12	0.04	0.52	0.08	0.03
Cl	0.10	0.02	0.00	0.07	0.02	0.01	0.10	0.02	0.01	0.10	0.02	0.01
Total	93.49	-	-	95.23	-	-	95.30	-	-	95.78	-	-
Si	5.49	0.15	0.05	5.53	0.11	0.04	5.54	0.04	0.01	5.60	0.05	0.02
Al^{iv}	2.50	0.16	0.05	2.47	0.11	0.04	2.46	0.04	0.01	2.40	0.05	0.02
Al^{vi}	0.03	0.07	0.02	0.09	0.08	0.03	0.07	0.05	0.02	0.07	0.04	0.02
Ti	0.49	0.05	0.02	0.48	0.06	0.02	0.47	0.04	0.02	0.46	0.07	0.03
Cr	0.01	0.01	0.00	0.01	0.01	0.00	0.02	0.01	0.00	0.01	0.01	0.00
Fe	2.68	0.13	0.04	2.63	0.11	0.04	2.23	0.07	0.03	2.82	0.08	0.03
Mn	0.03	0.01	0.00	0.02	0.01	0.00	0.02	0.01	0.00	0.04	0.01	0.00
Mg	2.56	0.16	0.05	2.58	0.08	0.03	2.98	0.15	0.06	2.44	0.16	0.06
Ni	-	-	-	-	-	-	-	-	-	-	-	-
Ca	0.00	0.00	0.00	0.00	0.02	0.01	0.00	0.00	0.00	0.00	0.01	0.00
Na	0.03	0.02	0.01	0.03	0.01	0.00	0.04	0.01	0.00	0.02	0.01	0.00
K	1.86	0.13	0.04	1.71	0.06	0.02	1.72	0.05	0.02	1.68	0.19	0.08
Sr	0.01	0.00	0.00	0.01	0.00	0.00	0.01	0.00	0.00	0.01	0.00	0.00
Ba	0.01	0.01	0.00	0.01	0.01	0.00	0.03	0.04	0.01	0.02	0.02	0.01
OH*	3.74	0.06	0.02	3.86	0.03	0.01	3.78	0.06	0.02	3.72	0.04	0.01
F	0.23	0.06	0.02	0.12	0.03	0.01	0.19	0.06	0.02	0.26	0.04	0.02
Cl	0.03	0.00	0.00	0.02	0.00	0.00	0.03	0.00	0.00	0.03	0.01	0.00
Mg#	48.79	2.57	0.81	49.58	1.61	0.61	57.22	1.95	0.74	46.40	1.56	0.64

Sample	**MO-11-26 (n = 12)**			**MO-10-386 (n = 10)**			**MO-11-19 (n = 19)**		
	Average	$2\sigma_{SD}$	$2\sigma_{SE}$	Average	$2\sigma_{SD}$	$2\sigma_{SE}$	Average	$2\sigma_{SD}$	$2\sigma_{SE}$
SiO_2	36.04	1.08	0.18	36.84	0.77	0.24	37.52	2.20	0.61
TiO_2	4.05	0.52	0.09	4.20	0.50	0.16	3.37	0.44	0.12
Cr_2O_3	0.06	0.05	0.02	0.06	0.02	0.01	0.17	0.30	0.08
Al_2O_3	13.29	0.91	0.15	13.96	0.47	0.15	15.05	1.64	0.45
FeO	20.68	1.11	0.18	21.81	0.60	0.19	15.46	0.80	0.22
MnO	0.25	0.07	0.01	0.30	0.04	0.01	0.16	0.04	0.01
NiO	-	-	-	-	-	-	-	-	-
MgO	10.72	0.35	0.06	9.99	0.41	0.13	14.75	1.63	0.45
CaO	0.00	0.01	0.00	0.01	0.03	0.01	0.32	0.70	0.19
Na_2O	0.08	0.04	0.01	0.09	0.04	0.01	0.11	0.16	0.04
K_2O	9.16	0.64	0.11	8.88	0.25	0.08	8.54	1.94	0.54
SrO	0.15	0.01	0.01	0.20	0.03	0.01	-	-	-
BaO	0.21	0.32	0.13	0.17	0.21	0.07	-	-	-
F	0.52	0.11	0.05	0.57	0.16	0.05	0.49	0.45	0.13
Cl	0.11	0.03	0.01	0.10	0.02	0.01	0.06	0.01	0.00
Total	94.28	-	-	97.17	1.11	0.35	95.98	3.04	0.84
Si	5.61	0.04	0.01	5.63	0.07	0.02	5.60	0.14	0.04
Al^{iv}	2.38	0.04	0.01	2.37	0.07	0.02	2.40	0.13	0.04
Al^{vi}	0.05	0.10	0.02	0.14	0.09	0.03	0.25	0.30	0.08
Ti	0.47	0.07	0.01	0.48	0.06	0.02	0.38	0.05	0.01
Cr	0.01	0.01	0.00	0.01	0.00	0.00	0.02	0.03	0.01
Fe	2.69	0.09	0.02	2.78	0.08	0.03	1.91	0.11	0.03
Mn	0.03	0.01	0.00	0.04	0.01	0.00	0.02	0.01	0.00
Mg	2.49	0.11	0.02	2.27	0.09	0.03	3.24	0.39	0.11
Ni	-	-	-	-	-	-	-	-	-
Ca	0.00	0.00	0.00	0.00	0.01	0.00	0.05	0.12	0.03
Na	0.03	0.01	0.00	0.03	0.01	0.00	0.03	0.04	0.01
K	1.82	0.17	0.03	1.73	0.04	0.01	1.65	0.24	0.07
Sr	0.01	0.00	0.00	0.02	0.00	0.00	-	-	-
Ba	0.01	0.02	0.01	0.01	0.01	0.00	-	-	-
OH*	3.72	0.05	0.02	3.70	0.08	0.03	3.76	0.23	0.06
F	0.25	0.06	0.02	0.28	0.08	0.03	0.22	0.23	0.06
Cl	0.03	0.01	0.00	0.03	0.01	0.00	0.01	0.00	0.00
Mg#	48.03	1.69	0.28	44.95	1.34	0.42	62.94	3.04	0.84

*Stoichiometric formulas calculated assuming Tindle & Webb (1990) ignoring Li_2O.

Table B-4: Average major element concentrations (wt.%) in plagioclase

Sample	MO-11-12 (n = 3)			MO-11-13 (n = 4)			MO-11-14 (n = 4)			MO-11-15 (n = 6)		
	Average	$2\sigma_{SD}$	$2\sigma_{SE}$	Average	$2\sigma_{SD}$	$2\sigma_{SE}$	Average	$2\sigma_{SD}$	$2\sigma_{SE}$	Average	$2\sigma_{SD}$	$2\sigma_{SE}$
SiO_2	63.67	1.01	0.58	58.26	1.86	0.93	60.51	2.73	1.36	60.16	1.69	0.69
Al_2O_3	22.94	1.17	0.68	26.06	1.19	0.59	25.16	2.62	1.31	25.05	2.43	0.99
FeO	0.08	0.05	0.03	0.08	0.01	0.01	0.05	0.07	0.03	0.14	0.14	0.06
MgO	0.01	0.01	0.01	0.01	0.01	0.00	0.01	0.01	0.01	0.00	0.01	0.00
CaO	3.71	0.38	0.22	7.76	1.49	0.75	6.48	1.95	0.97	6.35	0.89	0.36
Na_2O	9.61	0.47	0.27	7.09	0.85	0.43	8.07	1.36	0.68	8.01	0.78	0.32
K_2O	0.22	0.04	0.03	0.24	0.08	0.04	0.21	0.14	0.07	0.18	0.10	0.04
Total	100.24			99.50			100.48			99.87		
Si	2.80	0.02	0.01	2.61	0.07	0.03	2.68	0.11	0.06	2.68	0.06	0.02
Al	1.19	0.04	0.02	1.38	0.07	0.03	1.31	0.14	0.07	1.31	0.09	0.04
Fe^{3-}	0.00	0.00	0.00	0.00	0.00	0.00	0.00	0.00	0.00	0.00	0.01	0.00
Fe^{2-}	0.00	0.00	0.00	0.00	0.00	0.00	0.00	0.00	0.00	0.00	0.00	0.00
Mg	0.00	0.00	0.00	0.00	0.00	0.00	0.00	0.00	0.00	0.00	0.00	0.00
Ca	0.17	0.02	0.01	0.37	0.07	0.04	0.31	0.09	0.05	0.30	0.05	0.02
Na	0.82	0.03	0.02	0.62	0.07	0.04	0.69	0.12	0.06	0.69	0.06	0.03
K	0.01	0.00	0.00	0.01	0.00	0.00	0.01	0.01	0.00	0.01	0.01	0.00
$CaAl_2Si_2O_8$ (An)	0.17	0.02	0.01	0.37	0.07	0.04	0.30	0.10	0.05	0.30	0.05	0.02
$NaAlSi_3O_8$ (Ab)	0.81	0.02	0.01	0.61	0.07	0.04	0.68	0.10	0.05	0.69	0.05	0.02
$KAlSi_3O_8$ (Or)	0.01	0.00	0.00	0.01	0.00	0.00	0.01	0.01	0.00	0.01	0.01	0.00

Sample	MO-11-23 (n = 5)			MO-11-26 (n = 3)			MO-10-386 (n = 6)			MO-11-19 (n = 16)		
	Average	$2\sigma_{SD}$	$2\sigma_{SE}$	Average	$2\sigma_{SD}$	$2\sigma_{SE}$	Average	$2\sigma_{SD}$	$2\sigma_{SE}$	Average	$2\sigma_{SD}$	$2\sigma_{SE}$
SiO_2	62.59	0.90	0.40	62.43	1.94	1.12	64.26	1.72	0.70	58.78	2.45	0.61
Al_2O_3	24.12	2.90	1.30	24.52	3.57	2.06	23.64	0.71	0.29	26.08	1.60	0.40
FeO	0.11	0.15	0.07	0.09	0.09	0.05	0.09	0.04	0.02	0.11	0.07	0.02
MgO	0.00	0.01	0.01	0.00	0.00	0.00	0.00	0.00	0.00	0.01	0.02	0.01
CaO	4.63	0.79	0.35	4.82	1.02	0.59	4.20	0.93	0.38	7.46	1.86	0.46
Na_2O	9.08	0.78	0.35	8.73	0.85	0.49	9.34	0.54	0.22	7.27	1.10	0.28
K_2O	0.20	0.16	0.07	0.27	0.15	0.09	0.21	0.07	0.03	0.14	0.11	0.03
Total	100.72			100.87			101.73			99.85		
Si	2.75	0.07	0.03	2.74	0.13	0.07	2.79	0.06	0.02	2.63	0.09	0.02
Al	1.25	0.12	0.05	1.27	0.16	0.09	1.21	0.04	0.02	1.37	0.09	0.02
Fe^{3-}	0.00	0.01	0.00	0.00	0.01	0.00	0.00	0.00	0.00	0.00	0.00	0.00
Fe^{2-}	0.00	0.00	0.00	0.00	0.00	0.00	0.00	0.00	0.00	0.00	0.00	0.00
Mg	0.00	0.00	0.00	0.00	0.00	0.00	0.00	0.00	0.00	0.00	0.00	0.00
Ca	0.22	0.03	0.01	0.23	0.04	0.03	0.20	0.04	0.02	0.36	0.09	0.02
Na	0.77	0.08	0.04	0.74	0.09	0.05	0.79	0.04	0.02	0.63	0.09	0.02
K	0.01	0.01	0.00	0.01	0.01	0.00	0.01	0.00	0.00	0.01	0.01	0.00
$CaAl_2Si_2O_8$ (An)	0.22	0.04	0.02	0.23	0.05	0.03	0.20	0.04	0.02	0.36	0.09	0.02
$NaAlSi_3O_8$ (Ab)	0.77	0.04	0.02	0.75	0.06	0.03	0.79	0.05	0.02	0.63	0.09	0.02
$KAlSi_3O_8$ (Or)	0.01	0.01	0.00	0.02	0.01	0.01	0.01	0.00	0.00	0.01	0.01	0.00

Table B-5: Average major element concentrations (wt.%) in K-feldspar

Sample	MO-11-12 (n = 3)			MO-11-13 (n = 2)			MO-11-14 (n = 4)			MO-11-15 (n = 2)		
	Average	$2\sigma_{SD}$	$2\sigma_{SE}$	Average	$2\sigma_{SD}$	$2\sigma_{SE}$	Average	$2\sigma_{SD}$	$2\sigma_{SE}$	Average	$2\sigma_{SD}$	$2\sigma_{SE}$
SiO_2	64.17	0.66	0.38	64.01	1.05	0.74	64.46	0.97	0.49	65.61	0.64	0.45
Al_2O_3	18.54	0.42	0.24	18.40	0.20	0.14	18.81	1.07	0.54	20.25	0.42	0.30
FeO	0.04	0.02	0.01	0.05	0.07	0.05	0.04	0.07	0.03	0.06	0.07	0.05
MgO	0.01	0.01	0.01	0.01	0.01	0.01	0.01	0.01	0.00	0.00	0.01	0.01
CaO	0.06	0.02	0.01	0.05	0.04	0.03	0.07	0.07	0.03	0.03	0.05	0.03
Na_2O	1.01	0.46	0.27	0.84	0.30	0.21	1.07	0.42	0.21	0.98	0.16	0.11
K_2O	13.83	0.63	0.36	13.79	0.58	0.41	13.56	0.50	0.25	14.09	0.34	0.24
Total	97.67	1.04	0.60	97.15	1.00	0.71	98.00	1.08	0.54	101.02	0.74	0.52
Si	3.03	0.01	0.01	3.05	0.03	0.02	3.04	0.03	0.01	3.00	0.01	0.00
Al	1.03	0.02	0.01	1.03	0.02	0.01	1.04	0.06	0.03	1.09	0.03	0.02
Fe^{3+}	0.00	0.00	0.00	0.00	0.00	0.00	0.00	0.00	0.00	0.00	0.00	0.00
Fe^{2+}	0.00	0.00	0.00	0.00	0.00	0.00	0.00	0.00	0.00	0.00	0.00	0.00
Mg	0.00	0.00	0.00	0.00	0.00	0.00	0.00	0.00	0.00	0.00	0.00	0.00
Ca	0.00	0.00	0.00	0.00	0.00	0.00	0.00	0.00	0.00	0.00	0.00	0.00
Na	0.09	0.04	0.02	0.08	0.03	0.02	0.10	0.04	0.02	0.09	0.01	0.01
K	0.83	0.04	0.02	0.84	0.03	0.02	0.81	0.03	0.01	0.82	0.01	0.01
$CaAl_2Si_2O_8$ (An)	0.00	0.00	0.00	0.00	0.00	0.00	0.00	0.00	0.00	0.00	0.00	0.00
$NaAlSi_3O_8$ (Ab)	0.10	0.05	0.03	0.08	0.03	0.02	0.11	0.04	0.02	0.10	0.01	0.01
$KAlSi_3O_8$ (Or)	0.90	0.05	0.03	0.91	0.03	0.02	0.89	0.04	0.02	0.90	0.01	0.01

Sample	MO-11-21 (n = 2)			MO-11-23 (n = 5)			MO-11-26 (n = 4)			MO-10-386 (n = 10)		
	Average	$2\sigma_{SD}$	$2\sigma_{SE}$	Average	$2\sigma_{SD}$	$2\sigma_{SE}$	Average	$2\sigma_{SD}$	$2\sigma_{SE}$	Average	$2\sigma_{SD}$	$2\sigma_{SE}$
SiO_2	64.32	1.41	1.00	64.71	0.96	0.43	65.17	1.25	0.62	65.45	1.31	0.42
Al_2O_3	19.28	2.59	1.83	18.86	1.70	0.76	19.68	1.56	0.78	18.86	0.40	0.13
FeO	0.05	0.06	0.04	0.05	0.02	0.01	0.07	0.06	0.03	0.06	0.06	0.02
MgO	0.01	0.03	0.02	0.00	0.00	0.00	0.01	0.01	0.01	0.00	0.00	0.00
CaO	0.02	0.00	0.00	0.03	0.03	0.01	0.04	0.06	0.03	0.05	0.07	0.02
Na_2O	0.71	0.02	0.01	1.00	0.60	0.27	0.95	0.48	0.24	0.82	0.42	0.13
K_2O	14.24	0.04	0.03	14.06	0.84	0.37	14.00	0.90	0.45	14.43	0.54	0.17
Total	98.62			98.71			99.93			99.67		
Si	3.02	0.06	0.04	3.03	0.04	0.02	3.01	0.03	0.01	3.04	0.02	0.01
Al	1.06	0.10	0.07	1.04	0.06	0.03	1.07	0.06	0.03	1.03	0.02	0.01
Fe^{3+}	0.00	0.00	0.00	0.00	0.00	0.00	0.00	0.00	0.00	0.00	0.00	0.00
Fe^{2+}	0.00	0.00	0.00	0.00	0.00	0.00	0.00	0.00	0.00	0.00	0.00	0.00
Mg	0.00	0.00	0.00	0.00	0.00	0.00	0.00	0.00	0.00	0.00	0.00	0.00
Ca	0.00	0.00	0.00	0.00	0.00	0.00	0.00	0.00	0.00	0.00	0.00	0.00
Na	0.06	0.00	0.00	0.09	0.05	0.02	0.09	0.04	0.02	0.07	0.04	0.01
K	0.85	0.03	0.02	0.84	0.06	0.03	0.83	0.06	0.03	0.85	0.04	0.01
$CaAl_2Si_2O_8$ (An)	0.00	0.00	0.00	0.00	0.00	0.00	0.00	0.00	0.00	0.00	0.00	0.00
$NaAlSi_3O_8$ (Ab)	0.07	0.00	0.00	0.10	0.06	0.03	0.09	0.05	0.02	0.08	0.04	0.01
$KAlSi_3O_8$ (Or)	0.93	0.00	0.00	0.90	0.06	0.03	0.90	0.05	0.02	0.92	0.04	0.01

Table B-6: Average major element concentrations (wt.%) in amphibole

Sample	MO-11-14 (n = 2)			MO-11-15 (n = 4)			MO-11-21 (n = 4)		
	Average	$2\sigma_{SD}$	$2\sigma_{SE}$	Average	$2\sigma_{SD}$	$2\sigma_{SE}$	Average	$2\sigma_{SD}$	$2\sigma_{SE}$
SiO_2	48.09	1.68	1.19	47.13	0.59	0.30	48.54	2.29	1.15
TiO_2	0.88	0.21	0.15	0.96	0.16	0.08	1.00	0.27	0.13
Cr_2O_3	0.07	0.21	0.15	0.04	0.06	0.03	0.05	0.03	0.02
Al_2O_3	5.83	1.65	1.17	6.37	0.88	0.44	6.71	2.66	1.33
FeO	16.27	0.61	0.43	16.29	0.86	0.43	13.50	1.05	0.52
MnO	0.40	0.01	0.01	0.40	0.07	0.04	0.30	0.03	0.01
MgO	12.45	0.20	0.14	12.48	0.04	0.02	14.25	1.36	0.68
CaO	11.86	0.65	0.46	11.16	0.88	0.44	11.72	0.20	0.10
Na_2O	0.89	0.61	0.43	1.17	0.26	0.13	1.05	0.19	0.09
K_2O	0.49	0.19	0.13	0.60	0.08	0.04	0.55	0.22	0.11
F	0.17	0.02	0.01	0.16	0.20	0.10	0.43	0.68	0.34
Cl	0.04	0.00	0.00	0.04	0.03	0.02	0.05	0.02	0.01
H_2O	1.81	0.01	0.00	1.80	0.08	0.04	1.73	0.31	0.16
Total	99.23			98.60			99.88		
Si	7.09	0.29	0.20	6.97	0.12	0.06	7.01	0.26	0.13
Ti	0.10	0.02	0.02	0.11	0.02	0.01	0.11	0.03	0.02
Cr	0.01	0.02	0.02	0.00	0.01	0.00	0.01	0.00	0.00
Al	1.01	0.28	0.20	1.11	0.14	0.07	1.14	0.44	0.22
Fe3+	0.51	0.29	0.21	0.76	0.41	0.20	0.59	0.11	0.06
Fe2+	1.50	0.23	0.16	1.26	0.31	0.16	1.04	0.21	0.10
Mn	0.05	0.00	0.00	0.05	0.01	0.00	0.04	0.00	0.00
Mg	2.74	0.06	0.04	2.75	0.04	0.02	3.07	0.29	0.15
Ca	1.87	0.11	0.08	1.77	0.13	0.07	1.81	0.04	0.02
Na	0.25	0.17	0.12	0.34	0.08	0.04	0.29	0.06	0.03
K	0.09	0.03	0.02	0.11	0.01	0.01	0.10	0.04	0.02
Mg#	57.71	1.30	0.92	57.72	1.31	0.66	65.26	3.92	1.96

Sample	MO-11-23 (n = 4)			MO-11-26 (n = 2)			MO-10-386 (n = 8)		
	Average	$2\sigma_{SD}$	$2\sigma_{SE}$	Average	$2\sigma_{SD}$	$2\sigma_{SE}$	Average	$2\sigma_{SD}$	$2\sigma_{SE}$
SiO_2	48.83	1.38	0.69	48.06	0.47	0.33	45.58	1.80	0.64
TiO_2	0.79	0.37	0.18	0.87	0.02	0.01	1.46	0.14	0.05
Cr_2O_3	0.04	0.06	0.03	0.05	0.09	0.07	0.04	0.03	0.01
Al_2O_3	6.19	1.84	0.92	5.46	0.40	0.28	7.49	0.46	0.16
FeO	17.61	0.89	0.45	17.47	0.58	0.41	19.06	0.72	0.25
MnO	0.42	0.06	0.03	0.45	0.03	0.02	0.51	0.05	0.02
MgO	11.83	1.10	0.55	11.67	0.13	0.09	10.33	0.62	0.22
CaO	11.78	0.30	0.15	11.61	0.45	0.32	11.00	0.35	0.12
Na_2O	1.04	0.14	0.07	1.15	0.16	0.11	1.63	0.31	0.11
K_2O	0.51	0.12	0.06	0.57	0.05	0.04	0.82	0.08	0.03
F	0.82	1.11	0.56	0.22	0.09	0.06	0.22	0.16	0.06
Cl	0.05	0.03	0.02	0.05	0.01	0.01	0.07	0.03	0.01
H_2O	1.55	0.46	0.23	1.78	0.04	0.03	1.76	0.06	0.02
Total	101.46			99.39			99.97		
Si	7.10	0.13	0.06	7.13	0.13	0.09	6.79	0.17	0.06
Ti	0.09	0.04	0.02	0.10	0.00	0.00	0.16	0.02	0.01
Cr	0.00	0.01	0.00	0.01	0.01	0.01	0.00	0.00	0.00
Al	1.06	0.30	0.15	0.96	0.06	0.04	1.32	0.10	0.03
Fe3+	0.52	0.16	0.08	0.44	0.33	0.23	0.64	0.16	0.06
Fe2+	1.62	0.27	0.14	1.73	0.27	0.19	1.73	0.16	0.06
Mn	0.05	0.01	0.00	0.06	0.00	0.00	0.06	0.01	0.00
Mg	2.56	0.25	0.12	2.58	0.01	0.01	2.29	0.12	0.04
Ca	1.83	0.07	0.04	1.85	0.09	0.06	1.75	0.04	0.01
Na	0.29	0.04	0.02	0.33	0.04	0.03	0.47	0.10	0.03
K	0.09	0.02	0.01	0.11	0.01	0.01	0.15	0.02	0.01
Mg#	54.47	3.49	1.75	54.35	0.55	0.39	49.13	2.38	0.84

Stoichiometric formulas calculated assuming Si + Al + Ti + Mg +Fe + Mn = 13 (i.e., no Mg, Fe, or Mn in the M4 site).

APPENDIX B: *Mineral Chemistry*

Table B-7: Trace element concentrations (ppm) in clinopyroxene

Sample	MO-10-394				MO-10-392				MO-10-323			
	core (n = 4)		*rim (n = 3)*		*core (n = 3)*		*rim (n = 3)*		*core (n = 3)*		*rim (n = 3)*	
	Average	$2\sigma_{SE}$	**Average**	$2\sigma_{SE}$	**Average**	$2\sigma_{SE}$	**Average**	$2\sigma_{SE}$	**Average**	$2\sigma_{SE}$	**Average**	$2\sigma_{SE}$
Li	6.26	1.58	5.97	1.69	5.62		3.62	0.65	3.40		4.51	
Sc	53	4	52	1	72	5	78	3	63	6	65	5
V	98	19	121	5	285	32	307	7	293	230	160	7
Cr	1971	410	1895	111	1102	87	1176	126	1623	615	1781	1397
Co	34.8	0.8	34.5	1.8	31.5	1.9	29.9	0.8	48.1	23.4	36.6	2.9
Ni	152	11	150	5	90	4	90	1	191	76	152	23
Cu	1.35		1.75	0.34								
Zn	29.27	1.81	32.57	1.66	42.72	2.28	41.24	1.67	104.36	145.9 1	35.15	1.58
Ga	2.57	0.55	3.85	0.77	6.39	0.17	6.50	0.01	7.89	4.98	5.12	0.44
Rb	0.153				0.091							
Sr	122.6	9.0	129.7	4.8	90.8	0.6	84.9	0.4	144.4	11.5	152.0	7.1
Y	5.48	1.39	10.51	3.87	14.64	1.21	15.41	1.34	10.76	0.79	10.93	1.83
Zr	7.28	3.01	26.83	16.97	21.99	2.30	25.54	1.39	25.84	7.61	23.07	8.76
Nb	0.088	0.017	0.106	0.017								
Cs												
Ba			0.674	0.809	1.632	0.983	0.824	0.707	4.248	5.004		
La	2.42	0.65	6.02	2.02	3.42	0.26	3.46	0.16	4.59	0.49	4.29	0.65
Ce	8.00	2.14	19.34	7.08	14.68	0.18	15.96	0.73	18.37	2.35	17.49	1.39
Pr	1.254	0.338	2.861	1.012	2.608	0.013	2.760	0.029	3.285	0.510	3.248	0.072
Nd	7.29	1.99	13.96	4.94	14.98	0.71	15.87	0.52	18.98	3.18	18.24	1.52
Hf	0.306	0.164	0.851	0.495	0.971	0.230	1.163	0.208	1.220	0.491	0.998	0.396
Sm	1.91	0.52	3.36	0.71	4.67	0.45	4.87	0.40	5.46	0.71	5.25	0.22
Eu	0.549	0.119	0.793	0.162	1.246	0.126	1.157	0.108	1.486	0.125	1.627	0.015
Gd	1.78	0.49	3.20	0.53	4.36	0.59	4.42	0.34	4.82	0.58	5.09	0.22
Tb	0.222	0.074	0.376	0.132	0.572	0.059	0.569	0.060	0.553	0.066	0.553	0.069
Dy	1.16	0.32	2.13	0.40	3.39	0.34	3.32	0.21	2.64	0.42	2.92	0.20
Ho	0.207	0.055	0.430	0.143	0.583	0.052	0.639	0.062	0.437	0.101	0.425	0.089
Er	0.597	0.160	0.920	0.210	1.553	0.274	1.441	0.185	1.007	0.255	1.034	0.162
Tm	0.070	0.016	0.139	0.034	0.195	0.012	0.208	0.019	0.106	0.024	0.128	0.024
Yb	0.376	0.111	0.932	0.467	1.179	0.065	1.567	0.205	0.755	0.043	0.537	0.109
Lu	0.070	0.030	0.140	0.056	0.180	0.027	0.176	0.025			0.064	0.009
Pb	0.256	0.092	0.557	0.050	0.054				0.341	0.195	0.223	0.087
Th	0.112	0.037	0.354	0.135					0.190	0.061	0.118	0.062
U			0.158	0.072					0.069	0.014		

Sample	MO-11-8		MO-10-325				MO-11-9				MO-11-10	
	core (n = 4)		*core (n = 5)*		*rim (n = 4)*		*core (n = 3)*		*rim (n = 3)*		*core (n = 4)*	
	Average	$2\sigma_{SE}$	**Average**	$2\sigma_{SE}$	**Average**	$2\sigma_{SE}$	**Average**	$2\sigma_{SE}$	**Average**	$2\sigma_{SE}$	**Average**	$2\sigma_{SE}$
Li	9.97	2.53	5.32	1.35	5.46	1.18	17.41	2.34	17.48	2.07	6.09	0.37
Sc	70	3	71	3	68	1	67	3	67	2	74	14
V	332	28	163	18	165	13	209	7	210	21	351	6
Cr	1266	355	694	109	726	80	905	144	904	174	345	126
Co	37.7	0.4	39.3	2.1	36.4	1.5	43.9	1.7	45.5	1.4	41.6	4.9
Ni	159	11	143	8	149	10	172	6	176	7	134	3
Cu							6.23		4.46		1.51	0.46
Zn	54.96	5.57	30.65	2.00	42.53	2.14	75.22	7.22	71.71	2.08	60.94	13.65
Ga	6.57	1.25	4.27	0.11	5.01	0.69	6.71	0.79	6.12	0.86	6.27	1.30
Rb	0.267	0.041	0.114	0.031			1.221	0.463	2.315	1.808	0.355	0.481
Sr	100.1	10.5	143.5	16.9	150.5	9.0	87.1	9.5	70.8	32.4	110.0	7.2
Y	19.48	1.91	7.75	0.99	10.82	1.94	28.49	4.17	29.83	7.20	27.66	12.40
Zr	33.27	19.35	14.84	3.32	21.75	5.40	72.35	17.95	65.22	23.59	38.32	18.69
Nb	0.193	0.088					0.112	0.030			0.207	0.095
Cs	0.095	0.145					0.109	0.045			0.057	0.057
Ba	1.853	2.281	0.690	0.259	1.479	1.504	1.457	0.264	4.230	6.401	4.736	2.964
La	4.82	1.05	3.86	1.13	5.50	0.71	10.40	1.73	10.62	1.36	6.36	2.99
Ce	17.46	1.31	14.62	2.84	21.18	2.25	40.58	5.87	41.28	5.45	27.29	12.87
Pr	3.012	0.422	2.479	0.368	3.498	0.386	6.606	0.847	6.747	0.916	4.850	2.180
Nd	18.66	1.48	13.74	1.64	18.43	2.00	34.41	4.38	35.34	7.61	27.92	13.09
Hf	1.297	0.568	0.666	0.190	0.800	0.343	3.095	0.749	2.557	0.680	1.560	0.907

Sm	5.32	1.12	4.12	0.44	5.38	0.83	8.77	1.17	9.55	2.82	8.23	3.54
Eu	1.474	0.229	1.169	0.113	1.497	0.254	1.495	0.132	1.700	0.198	1.547	0.386
Gd	5.83	0.71	3.71	0.45	4.44	0.81	7.24	0.96	8.31	1.54	7.83	3.18
Tb	0.682	0.177	0.420	0.070	0.589	0.098	1.020	0.116	1.123	0.211	1.013	0.513
Dy	4.17	1.21	1.89	0.28	2.70	0.34	6.04	0.75	6.09	1.11	5.95	3.06
Ho	0.788	0.165	0.336	0.053	0.414	0.075	1.089	0.160	1.119	0.103	1.084	0.553
Er	2.157	0.591	0.634	0.076	0.988	0.065	3.170	0.417	3.382	0.991	2.923	1.358
Tm	0.232	0.159	0.077	0.010	0.135	0.045	0.386	0.063	0.469	0.138	0.384	0.170
Yb	1.663	0.294	0.549	0.123	0.774	0.145	2.776	0.275	2.913	0.901	2.436	1.199
Lu	0.224	0.058	0.069	0.011	0.107	0.012	0.401	0.053	0.391	0.129	0.357	0.182
Pb	0.719	0.156	0.329	0.140	0.285	0.056	1.390	0.252	1.211	0.096	0.556	0.092
Th	0.554	0.352	0.144	0.127	0.153	0.092	0.665	0.210	0.439	0.202	0.121	0.071
U	0.163	0.110	0.066	0.024	0.066	0.010	0.264	0.109	0.172	0.080		

Sample	**MO-11-12**		**MO-11-13**		**MO-11-14**		**MO-11-21**		**MO-11-26**	
	core (n = 4)		*core (n = 3)*		*core (n = 2)*		*core (n = 2)*		*core (n = 5)*	
	Average	$2\sigma_{SE}$	**Average**	$2\sigma_{SE}$	**Average**	$2\sigma_{SE}$	**Average**	$2\sigma_{SE}$	**Average**	$2\sigma_{SE}$
Li	15.14	4.64	14.90	6.15	10.96	3.67	38.41	13.32	40.53	10.38
Sc	71	7	64	6	79	15	61	0	101	22
V	209	25	181	15	409	137	133	10	187	61
Cr	288	49	91	17	587	660	162	68	156	158
Co	33.4	2.5	35.0	1.4	38.8	3.6	32.3	1.1	33.0	7.9
Ni	64	8	51	4	106	35	86	1	94	95
Cu	1.29		1.01		9.98		8.63		1.17	0.49
Zn	90.10	8.10	103.43	7.30	116.89	2.72	93.12	1.91	164.72	42.05
Ga	5.13	0.48	3.60	0.46	9.22	1.40	7.05	0.15	5.44	1.05
Rb	0.274	0.279			0.471	0.078				
Sr	95.0	4.0	58.6	5.3	71.4	7.5	52.0	13.1	43.2	18.1
Y	29.07	2.61	28.49	5.00	38.09	8.11	42.45	15.80	43.34	12.19
Zr	23.31	2.19	13.93	3.47	57.51	6.98	28.40	18.42	12.33	4.15
Nb	0.075	0.048			0.605	0.498	0.483	0.754	0.093	0.019
Cs									0.203	0.223
Ba	0.835	1.056			8.873	5.181				
La	9.53	1.07	7.53	0.74	14.05	0.58	16.10	0.60	12.33	4.50
Ce	36.76	4.31	33.10	3.29	50.07	1.77	67.13	9.32	50.82	15.95
Pr	6.138	0.709	5.728	0.634	7.911	0.375	11.308	2.462	8.931	2.789
Nd	31.41	2.41	29.19	3.50	40.63	5.64	54.37	13.60	45.86	14.23
Hf	1.154	0.157	0.753	0.118	2.478	0.121	1.807	0.230	0.751	0.277
Sm	8.84	0.89	8.00	1.30	11.90	1.88	14.53	4.00	12.84	3.78
Eu	1.360	0.078	1.096	0.153	2.138	0.280	2.234	0.163	0.884	0.276
Gd	7.58	0.69	7.20	0.93	10.23	3.22	11.33	3.22	11.38	3.32
Tb	1.103	0.093	0.938	0.084	1.404	0.413	1.600	0.656	1.685	0.474
Dy	6.43	0.65	5.79	0.59	7.71	2.28	8.56	4.51	10.39	3.14
Ho	1.126	0.137	1.067	0.130	1.425	0.452	1.767	0.597	1.697	0.483
Er	3.201	0.358	3.002	0.850	3.831	0.964	4.661	1.311	4.891	1.481
Tm	0.402	0.047	0.466	0.157	0.512	0.156	0.628	0.222	0.574	0.162
Yb	3.172	0.366	3.141	0.228	3.601	1.458	4.290	1.509	3.979	1.538
Lu	0.434	0.075	0.493	0.055	0.530	0.118	0.760	0.364	0.667	0.258
Pb	0.731	0.119	0.987	0.233	2.179	2.114	1.443	1.117	1.417	0.670
Th	0.108	0.031	0.106	0.012	0.796	0.257	0.782	1.179	0.253	0.276
U			0.054	0.002	0.172	0.038	0.132	0.132	0.133	0.136

Absence of a value indicates that the concentration was below the detection limit.

APPENDIX B: *Mineral Chemistry*

Table B-8: Trace element concentrations (ppm) in biotite

Sample	MO-10-394				MO-10-392		MO-10-323				MO-10-325			
	core (n = 4)		*rim (n = 2)*		*core (n = 3)*		*core (n = 4)*		*rim (n = 2)*		*core (n = 5)*		*rim (n = 5)*	
Info	**Average**	$2\sigma_{SE}$	**Average**	$2\sigma_{SE}$	**Average**	$2\sigma_{SE}$	**Average**	$2\sigma_{SE}$	**Average**	$2\sigma_{SE}$	**Average**	$2\sigma_{SE}$	**Average**	$2\sigma_{SE}$
Li	130.1	5.6	112.9	1.2	10.4	1.1	27.4	4.0	24.4	2.1	75.9	6.6	62.0	4.3
Sc	6.65	0.09	7.73	0.34	13.44	0.31	6.20	1.01	6.50	0.51	8.35	0.49	8.30	0.35
V	283	11	286	0	702	2	301	64	320	12	400	17	393	7
Cr	2520	364	2798	1	2578	82	1497	1150	994	6	812	48	835	33
Co	84.3	1.8	87.2	0.2	67.9	0.6	86.3	4.7	80.4	4.2	94.1	3.4	92.7	1.1
Ni	534	7	532	0	353	4	586	48	562	23	472	8	476	6
Cu	2.83	0.17	2.60	0.42									2.84	0.16
Zn	78.3	3.8	92.1	0.7	74.7	1.5	81.9	5.9	82.5	3.6	117.2	4.8	116.5	3.3
Ga	19.7	0.4	20.2	0.1	17.3	0.1	16.3	0.9	16.0	0.7	20.5	0.9	21.2	0.4
Rb	354	1	366	0	284	4	264	12	244	4	312	10	313	7
Sr	69.2	13.9	32.6	2.8	136.7	2.3	149.1	23.5	156.2	16.3	32.2	2.9	21.4	2.3
Y	0.119	0.022	0.137	0.256	0.226	0.036	0.141	0.020	0.186	0.023	0.189	0.060	0.239	0.076
Zr	11.25	1.73	8.39	1.04	5.81	0.23	2.47	0.73	1.98	0.50	1.48	0.96	1.22	0.79
Nb	39.8	2.5	39.7	0.6	7.0	0.1	4.7	0.6	4.7	0.4	9.1	0.9	7.9	0.5
Cs	4.45	0.36	6.54	0.51	2.56	0.11	3.98	0.41	3.71	0.29	4.77	0.22	4.96	0.16
Ba	2215	461	1414	7	5680	154	3168	150	3224	185	3395	277	3593	244
La	0.061		0.085		0.046		0.144	0.072	0.045		0.128	0.053	0.368	0.186
Ce	0.080		0.358				0.279	0.085	0.066		0.781		0.978	0.584
Pr							0.037				0.095		0.291	
Nd							0.307				0.379		0.575	
Sm													0.234	
Eu	0.079	0.004					0.063		0.084					
Gd			0.199											
Tb					0.026									
Dy													0.141	0.027
Ho											0.046			
Er														
Tm														
Yb							0.369							
Lu														
Hf	0.371	0.040	0.197		0.273	0.004								
Pb	9.11	1.06	6.79	1.13	0.64	0.07	3.35	0.74	3.76	0.72	2.55	0.27	2.30	0.17
Th													0.032	
U			0.036		0.034				0.049				0.066	0.011

Sample	MO-11-8		MO-11-9		MO-11-10		MO-11-12				MO-11-13	
	core (n = 3)		*core (n = 4)*		*core (n = 4)*		*core (n = 4)*		*rim (n = 3)*		*core (n = 6)*	
Info	**Average**	$2\sigma_{SE}$	**Average**	$2\sigma_{SE}$	**Average**	$2\sigma_{SE}$	**Average**	$2\sigma_{SE}$	**Average**	$2\sigma_{SE}$	**Average**	$2\sigma_{SE}$
Li	76.7	8.3	63.6	2.4	67.9	2.8	92.4	7.6	96.0	5.2	122.2	7.4
Sc	10.44	0.43	11.05	0.42	8.41	0.81	6.40	0.34	6.63	0.06	7.68	0.46
V	551	11	609	18	788	24	542	22	533	6	605	26
Cr	2399	77	2644	215	1116	36	814	28	798	26	435	68
Co	74.6	2.7	107.9	1.2	90.4	1.0	75.7	1.8	74.3	2.2	74.4	1.4
Ni	546	15	744	19	505	10	277	12	253	9	196	7
Cu			2.73	0.25			1.64	0.15	1.31	0.03	1.63	0.06
Zn	105.9	7.3	143.3	3.2	118.2	2.4	178.7	10.7	167.9	15.1	196.3	6.6
Ga	20.9	1.4	27.6	0.6	20.9	0.7	28.8	1.3	27.5	1.2	29.4	1.1
Rb	355	55	355	4	339	6	394	12	396	22	324	13
Sr	64.8	11.4	35.2	5.3	61.3	6.2	4.7	0.4	4.6	1.0	4.2	0.3
Y			0.208	0.032	0.195	0.011	0.181	0.018	0.116	0.026	0.126	0.010
Zr	6.01	0.60	14.43	3.84	2.59	0.87	4.63	0.80	4.71	0.84	2.76	0.57
Nb	8.2	1.0	18.1	0.5	8.7	0.5	38.5	1.6	38.4	0.7	38.8	3.2
Cs	9.67	2.96	5.38	0.68	3.88	0.07	7.13	0.87	6.77	0.71	8.83	3.00
Ba	1059	300	3049	232	3962	90	2369	241	1880	277	2042	153
La			0.033								0.061	
Ce			0.131		0.045		0.102	0.047			0.266	0.111
Pr	0.029		0.027				0.047		0.017		0.039	
Nd			0.102		0.121							
Sm											0.222	

Eu	0.097		0.087									
Gd											0.187	
Tb	0.029											
Dy			0.133									
Ho												
Er												
Tm												
Yb											0.259	
Lu												
Hf			0.459	0.120	0.289		0.254	0.032	0.194	0.044	0.220	
Pb	5.95	0.64	8.23	0.46	3.00	0.21	1.49	0.06	1.50	0.18	1.10	0.03
Th	0.052		0.025									
U			0.031									

Sample	**MO-11-14**				**MO-11-21**		**MO-11-26**			
	core (n = 3)		*rim (n = 2)*		*core (n = 5)*		*core (n = 3)*		*rim (n = 3)*	
Info	**Average**	$2\sigma_{SE}$	**Average**	$2\sigma_{SE}$	**Average**	$2\sigma_{SE}$	**Average**	$2\sigma_{SE}$	**Average**	$2\sigma_{SE}$
Li	158.4	9.5	154.3	10.4	199.0	3.5	218.9	10.5	208.7	5.9
Sc	5.86	0.82	5.59	0.82	4.81	0.69	8.95	1.67	8.56	1.49
V	667	57	608	8	445	14	421	14	423	11
Cr	332	47	282	56	654	35	257	17	276	28
Co	70.7	0.7	69.9	0.2	72.5	1.8	58.5	1.4	58.6	0.5
Ni	195	9	179	3	281	10	154	4	155	6
Cu	6.06	4.18	7.67	3.34	19.22	9.39			2.33	0.43
Zn	244.9	4.3	245.7	4.0	198.0	3.7	331.1	7.3	340.7	6.8
Ga	29.0	1.2	28.7	0.2	29.4	0.3	36.5	0.8	36.7	1.5
Rb	354	4	349	4	441	6	528	10	511	5
Sr	3.3	0.2	3.2	0.3	6.5	0.5	2.8	0.2	3.2	0.4
Y	0.109	0.024	0.115	0.038	0.178	0.016	0.125	0.021	0.171	0.073
Zr	1.51	0.47	1.32	0.74	1.65	0.62				
Nb	40.4	5.2	38.3	5.1	46.4	2.4	78.4	4.3	69.7	6.2
Cs	14.91	2.08	13.14	0.06	6.46	0.49	10.73	0.39	11.69	1.61
Ba	1293	72	1268	55	2566	97	907	23	1567	561
La	0.271	0.180	0.371	0.149	0.327	0.078	0.416	0.160	0.719	0.340
Ce	0.108	0.071	0.166	0.069	0.417	0.209	0.831	0.491	1.109	0.592
Pr	0.086		0.085	0.022	0.048		0.085	0.045	0.179	0.038
Nd	0.496				0.234	0.035	0.340	0.103	0.546	
Sm										
Eu										
Gd					0.192		0.270		0.133	
Tb									0.047	
Dy										
Ho										
Er										
Tm							0.020			
Yb					0.131					
Lu										
Hf	0.145				0.412		0.155			
Pb	2.02	0.59	2.80	0.65	2.88	0.46	2.94	0.56	3.21	0.46
Th			0.616		0.362	0.106				
U					0.037					

Absence of a value indicates that the concentration was below the detection limit. For the REE, Pb, Th, and U values are shown without $2\sigma_{SE}$ when only one biotite analysis from a given sample yielded a value above the detection limit.

Table B-9: Trace element concentrations (ppm) in feldspars

Sample	MO-11-12			MO-11-13				MO-11-14			
Mineral	K-feldspar *(n = 3)*		Plagioclase *(n = 1)*	Plagioclase Core *(n = 4)*		Plagioclase Rim *(n = 3)*		K-Feldspar *(n = 3)*		Plagioclase Core *(n = 3)*	
	Average	$2\sigma_{SE}$		**Average**	$2\sigma_{SE}$	**Average**	$2\sigma_{SE}$	**Average**	$2\sigma_{SE}$	**Average**	$2\sigma_{SE}$
Zn	0.97	0.39	1.50	4.09	0.48	2.94	0.32	1.75	0.09	3.65	0.41
Ga	13.1	1.1	9.1	25.4	0.6	23.9	3.1	10.5	0.2	27.0	3.3
Rb	104	17	70					134	3		
Sr	1981	214	1614	2143	146	2370	61	2082	296	1958	31
Y	0.142	0.067	0.183	0.146	0.030	0.173	0.001	0.392	0.070	0.063	
Zr				0.409							
Nb											
Cs	17.0	5.4	5.6					1.0	0.1		
Ba	2846	1311	3048	288	69	199	13	6859	447	169	1
La	1.3	0.3	2.1	11.8	1.0	14.3	0.8	2.2	0.7	16.4	1.8
Ce	0.6	0.2	1.5	16.3	0.9	18.7	0.8	1.2	0.5	19.1	3.0
Pr				1.28	0.12	1.29	0.04	0.13		1.30	0.22
Nd	0.22			3.96	0.24	3.34	0.27	0.22		3.38	0.60
Sm				0.41		0.31				0.35	
Eu	1.34	0.76	1.74	2.36	0.14	3.01	0.20	2.27	0.30	2.24	0.13
Gd								0.288		0.370	
Tb											
Dy				0.335							
Ho										0.042	
Er											
Tm				0.040						0.039	
Yb											
Lu						0.057					
Hf											
Pb	18.2	10.5	25.6	13.8	1.4	15.8	1.7	49.8	6.6	18.5	0.8
Th											
U											

Sample	MO-11-21		MO-11-21		MO-11-26					
Mineral	K-Feldspar (n = 3)		Plagioclase Core (n = 4)		K-Feldspar (n = 3)		Plagioclase Core (n = 4)		Plagioclase Rim (n = 3)	
	Average	$2\sigma_{SE}$	**Average**	$2\sigma_{SE}$	**Average**	$2\sigma_{SE}$	**Average**	$2\sigma_{SE}$	**Average**	$2\sigma_{SE}$
Zn	3.93	0.53	3.82	0.20	2.12		4.37	0.55	4.33	0.54
Ga	25.8	0.8	22.9	1.1	11.9	0.7	28.3	1.2	27.1	0.9
Rb					187	17				
Sr	2381	20	2260	61	1259	100	1257	47	1312	81
Y	0.069		0.136	0.040	0.285	0.046	0.098	0.009		
Zr			0.138		0.107				0.188	
Nb					0.232		0.0743			
Cs					2.4	0.1	0.1		0.6	
Ba	269	78	233	35	5072	604	108	21	155	24
La	13.2	0.4	16.2	1.0	1.8	0.3	16.4	1.9	17.4	4.5
Ce	17.1	1.6	20.5	2.0	1.1	0.3	18.2	2.5	19.4	4.7
Pr	1.28	0.15	1.41	0.22			1.12	0.16	1.37	0.35
Nd	3.09	0.66	4.11	0.69			2.54	0.18	3.34	0.71
Sm	0.30		0.39	0.05					0.38	
Eu	1.91	0.13	1.75	0.13	1.39	0.32	1.59	0.02	1.69	0.06
Gd	0.435						0.382	0.034	0.326	
Tb										
Dy							0.227		0.302	
Ho	0.044				0.053					
Er										
Tm										
Yb										
Lu							0.080		0.089	
Hf										
Pb	22.6	1.1	24.5	0.8	77.3	1.4	26.0	0.4	27.9	0.6
Th										
U										

Absence of a value indicates that the concentration was below the detection limit.

APPENDIX B: *Mineral Chemistry*

Table B-10: Trace element concentrations (ppm) in apatite

Sample	MO-11-10 (n = 4)		MO-11-12 (n = 3)		MO-11-13 (n = 15)		MO-11-14 (n = 3)		MO-11-21 (n = 4)	
	Average	$2\sigma_{SE}$	Average	$2\sigma_{SE}$	Average	$2\sigma_{SE}$	Average	$2\sigma_{SE}$	Average	$2\sigma_{SE}$
Li										
V	22.7	6.1	10.7	0.6	15.2	1.8	22.8	3.9	3.9	3.2
Cr										
Co			0.179	0.028	0.639	0.619			0.164	
Ni										
Cu	1.21	0.43					2.22	0.53		
Zn					2.18	1.74				
Ga	38.5	1.7	69.8	1.5	63.4	5.0	54.9	4.5	87.0	0.5
Rb	0.085	0.048	0.275	0.172	0.211	0.214	0.107	0.007	0.160	0.126
Sr	2580	103	1366	115	1116	36	1073	154	1097	122
Y	343	21	479	44	518	53	365	43	413	30
Zr	5.18	0.57	1.03	0.14	0.62	0.14	2.24	1.10	1.06	0.50
Nb			0.052	0.008	0.049	0.017				
Cs					0.044	0.031				
Ba	1.81	0.69	1.68	0.63	1.47	1.58	0.74	0.08	1.64	0.54
La	630	27	1502	55	953	158	980	141	1643	98
Ce	1594	49	3253	64	2608	261	2258	253	3946	193
Pr	203	7	361	15	324	30	262	24	428	10
Nd	899	37	1388	88	1334	120	1068	95	1581	29
Sm	169	9	234	16	235	19	186	14	232	13
Eu	28.5	1.2	25.3	2.1	21.5	2.2	22.4	4.5	32.1	2.3
Gd	142	9	181	14	185	13	148	13	169	14
Tb	15.3	1.1	19.8	1.8	20.9	1.5	15.8	1.4	17.8	1.4
Dy	74.5	5.1	100.2	8.4	104.3	8.8	78.0	8.1	85.9	6.1
Ho	12.8	0.8	17.3	1.6	18.7	1.7	13.1	1.2	14.8	1.1
Er	31.6	2.0	44.4	3.7	49.9	5.7	33.7	3.7	37.8	3.5
Tm	3.59	0.24	4.92	0.54	5.52	0.75	3.88	0.45	4.21	0.15
Yb	19.6	1.5	28.6	3.0	32.7	4.7	22.3	2.0	26.6	1.5
Lu	2.70	0.19	3.58	0.42	4.25	0.61	3.04	0.31	3.53	0.31
Hf	0.071	0.015								
Pb	3.58	0.26	6.80	0.18	3.98	0.45	5.22	0.33	8.34	0.85
Th	23.0	4.5	46.8	5.1	29.8	1.0	42.0	4.3	61.2	11.2
U	8.3	1.1	33.1	3.4	28.7	3.7	27.6	6.6	63.3	26.7

Absence of a value indicates that the concentration was below the detection limit.

APPENDIX B: *Mineral Chemistry*

Table B-11: Trace element concentrations (ppm) in amphibole

Sample	MO-11-13				MO-11-14		MO-11-21	
	core (n = 3)		*rim (n = 3)*		*core (n = 3)*		*core (n = 3)*	
	Average	$2\sigma_{SE}$	Average	$2\sigma_{SE}$	Average	$2\sigma_{SE}$	Average	$2\sigma_{SE}$
Li	2.98	0.60					6.24	1.14
Sc	75.3	10.1	76.3	11.0	35.7	23.3	56.5	17.6
V	465	23	488	2	367	232	421	129
Cr	233	16	250	25	180	82	517	288
Co	55.1	5.2	57.2	0.8	54.4	2.7	52.6	7.0
Ni	130	9	130	2	115	10	182	24
Cu			1.13	0.11			1.57	0.20
Zn	165	17	172	7	197	4	160	4
Ga	17.4	0.5	17.1	1.5	15.7	5.7	18.8	3.8
Rb	0.77	0.04	0.82	0.25	1.17	0.47	2.01	0.30
Sr	60.8	3.3	59.9	0.6	55.2	27.9	66.1	31.9
Y	110	14	105	12	34	28	66	89
Zr	31.0	11.2	26.7	3.5	26.7	27.0	24.7	26.5
Nb	12.3	1.3	13.3	0.4	10.3	7.1	16.9	19.1
Cs								
Ba	10.6	3.1	9.7	0.1	8.0	8.7	20.0	29.3
La	37.9	8.1	36.2	10.4	22.5	28.8	29.9	47.1
Ce	152	22	152	30	74	90	116	184
Pr	24.9	3.9	24.6	5.6	10.4	12.0	18.3	28.8
Nd	119	17	119	23	48	53	89	133
Sm	29.9	2.2	30.1	5.8	10.9	11.2	22.6	33.7
Eu	3.69	0.22	3.72	0.65	2.70	1.53	3.53	4.16
Gd	25.9	4.3	25.0	2.5	8.8	6.9	19.2	27.0
Tb	3.71	0.51	3.48	0.28	1.05	0.83	2.47	3.52
Dy	21.4	4.2	20.3	2.5	6.7	5.6	13.9	20.0
Ho	4.0	0.6	3.8	0.3	1.2	0.8	2.4	3.2
Er	11.5	1.8	11.0	2.6	3.6	3.1	6.1	8.2
Tm	1.60	0.35	1.47	0.07	0.49	0.42	0.90	1.30
Yb	10.2	1.5	9.7	0.3	3.6	2.9	5.8	7.9
Lu	1.38	0.21	1.40	0.02	0.55	0.52	0.75	0.84
Hf	2.35	0.82	1.85	0.39	1.36	1.20	2.16	2.04
Pb	1.01	0.18	1.04	0.26	1.41	0.63	2.11	0.59
Th	0.220	0.139	0.241	0.139			0.171	0.214
U	0.160	0.042	0.141	0.009	0.121	0.170	0.134	0.101

Absence of a value indicates that the concentration was below the detection limit.

APPENDIX C:
Whole Rock Major and Trace Element Compositions

[1]W = wehrlite, PW = biotite wehrlite, PC = biotite clinopyroxenite, P = phlogopitite, BMG = biotite monzogabbro, BMD = biotite monzodiorite, BM = biotite monzonite, BQM = biotite quartz monzonite, AC = amphibole clinopyroxenite, AMG = amphibole monzogabbro, AG1 = amphibole granitoid (<60 wt.% SiO2), AG2 = amphibole granitoid (>60 wt.% SiO2), GS = other granitoid stocks, PBD = primitive basaltic dike, BD = basaltic dike (<54 wt.% SiO2), ID = intermediate dike (54-63 wt.% SiO2), FD = felsic dike (>63 wt.% SiO2)

[2]Loss on ignition

*Samples beginning with MO-9- were analyzed for FeO^T. For these samples, we only report FeO^T. Samples beginning with MO-10- and MO-11- were analyzed for $Fe_2O_3^T$. For these samples, we report Fe_2O_3 and recalculated $FeO^T = 0.899*Fe_2O_3^T$. Totals reported are for the original analyses and not recalculated FeO^T.

Table C-1: Whole Rock Major and Trace Element Chemistry

Sample #	**MO-10-395**	**MO-10-396**	**MO-12-21**	**MO-10-388**	**MO-10-385**	**MO-10-373**	**MO-9-248**	**MO-10-389**	**MO-10-390**
Longitude	94°13'47.6" E	94°13'14" E	94°14'5.8" E	94°14'18.9" E	94°14'30" E	94°14'29.7" E	94°15'17.6" E	94°14'18.9" E	94°14'18.9" E
Latitude	46°39'16.3" N	46°38'59.1" N	46°38'27.8" N	46°39'19.6" N	46°39'22.4" N	46°39'58.7" N	46°38'57.7" N	46°39'19.6" N	46°39'19.6" N
Rock Type[1]	W	W	W	PW	PW	PW	PW	PW	PW
SiO_2	51.07	51.86	52.67	45.55	46.18	52.02	50.02	45.71	47.61
TiO_2	0.29	0.19	0.15	0.41	0.24	0.06	0.39	0.38	0.41
Al_2O_3	1.50	0.97	0.89	2.93	1.08	1.68	1.98	1.70	2.06
Fe_2O_3*	6.76	4.90	3.87	11.98	10.21	6.36	-	12.23	11.14
FeO^T*	6.09	4.41	0.00	10.78	9.19	5.73	8.20	11.00	10.02
MnO	0.15	0.11	0.09	0.22	0.20	0.14	0.23	0.23	0.25
MgO	18.92	20.17	19.06	24.02	24.36	20.05	20.00	22.61	20.41
CaO	20.01	20.62	21.80	11.67	14.60	17.13	17.86	14.59	16.83
Na_2O	0.15	0.10	0.15	0.19	0.03	0.06	0.26	0.03	0.23
K_2O	0.06	0.05	0.00	0.17	0.06	0.05	0.12	0.04	0.04
P_2O_5	0.01	0.02	0.02	0.03	0.02	0.00	0.02	0.02	0.01
SrO	0.01	0.01	-	0.01	0.01	0.00	0.01	0.01	0.01
BaO	0.00	0.00	-	0.01	0.00	0.00	0.00	0.00	0.00
Cr_2O_3	0.20	0.37	0.53	0.26	0.20	0.22	b.d.	0.17	0.24
NiO	0.03	0.03	0.03	0.08	0.05	0.03	b.d.	0.05	0.05
L.O.I.[2]	1.36	1.12	0.89	2.86	3.07	2.41	b.d.	2.39	0.88
Tot	100.53	100.52	100.17	100.40	100.30	100.20	99.09	100.14	100.17
Mg#	84.71	89.08	90.72	79.89	82.53	86.19	81.29	78.55	78.40
Na_2O+K_2O	0.21	0.15	0.16	0.38	0.09	0.11	0.38	0.07	0.27
K_2O/Na_2O	0.41	0.51	0.03	0.90	2.04	0.74	0.46	1.59	0.20
Sc	51.2	40.3	37.1	35.1	42.4	73.3	61.6	58.3	50.2
V	104	53	46	176	80	192	184	153	194
Cr	1295	2389	3494	1752	1367	1431	993	1133	1599
Co	45.0	39.4	33.3	71.9	73.7	48.2	52.5	77.0	58.4
Ni	200	209	253	604	385	204	234	335	355

Cu	5.4	4.2	6.9	18.6	14.4	2.0	2.7	4.4	1.4
Zn	31.4	17.2	16.3	73.3	42.7	18.0	33.7	51.7	58.5
Ga	2.3	1.7	1.3	4.5	1.4	1.8	3.6	2.8	4.4
Cs	0.22	0.10	0.17	0.34	0.04	0.06	0.21	0.09	0.09
Rb	1.53	1.54	0.29	3.44	1.28	0.70	3.26	1.08	0.80
Ba	5	8	3	82	15	7	19	19	20
Th	0.20	0.22	0.03	0.12	0.07	0.16	0.63	0.05	0.05
U	b.d.	0.07	-	0.05	0.03	0.19	0.20	0.05	b.d.
Nb	b.d.	0.18	0.13	0.54	b.d.	0.05	0.40	b.d.	b.d.
Ta	b.d.	b.d.	-	b.d.	b.d.	b.d.	0.03	b.d.	b.d.
La	3.41	2.12	1.44	4.83	1.68	0.38	3.88	2.09	3.31
Ce	11.20	6.15	4.05	17.32	5.76	0.61	12.42	8.49	13.74
Pb	0.24	0.25	2.05	0.48	0.29	0.69	0.68	0.19	b.d.
Pr	1.84	0.91	0.57	2.85	1.00	0.06	2.12	1.52	2.48
Sr	125	113	119	126	86	14	113	70	75
Nd	9.68	5.74	3.69	14.53	5.70	0.31	13.50	7.93	13.08
Zr	14.7	6.9	5.7	25.2	7.3	3.1	25.5	12.4	21.9
Hf	0.588	0.323	-	1.083	0.302	b.d.	0.897	0.615	0.926
Sm	2.64	1.63	1.15	3.84	1.70	0.24	3.94	2.72	4.29
Eu	0.653	0.422	0.311	1.028	0.503	0.087	0.989	0.787	0.902
Gd	2.33	1.20	1.01	3.90	1.57	0.25	3.98	2.67	4.41
Tb	0.316	0.175	0.100	0.543	0.216	0.045	0.505	0.289	0.561
Dy	1.65	0.76	0.48	2.77	1.09	0.30	2.76	1.81	2.90
Y	7.04	3.97	2.48	14.37	4.49	1.55	13.33	7.82	13.42
Ho	0.351	0.129	-	0.494	0.226	0.075	0.501	0.301	0.542
Er	0.497	0.233	-	1.532	0.508	0.202	1.235	0.908	1.360
Tm	0.082	0.049	-	0.220	0.080	0.034	0.154	0.104	0.145
Yb	0.596	b.d.	-	1.325	0.452	0.290	0.998	0.597	1.378
Lu	0.105	0.048	-	0.165	0.045	0.046	0.138	0.088	0.156

Sample #	**MO-10-394**	**MO-11-8**	**MO-11-9**	**MO-9-247**	**MO-10-391**	**MO-10-323**	**MO-10-322**	**MO-10-392**	**MO-12-12**
Longitude	94°13'50.9" E	94°14'25.2" E	94°14'25.7" E	94°15'17.6" E	94°14'18.9" E	94°12'6" E	94°12'6" E	94°14'18.9" E	94°12'10" E
Latitude	46°39'19.2" N	46°39'10.2" N	46°39'10.8" N	46°38'57.7" N	46°39'19.6" N	46°40'17.9" N	46°40'17.9" N	46°39'19.6" N	46°39'47.2" N
Rock Type[1]	PW	PW	PW	PW	PW	PW	PW	PW	PC
SiO_2	51.02	48.43	51.36	48.36	46.04	45.76	43.94	45.82	46.67
TiO_2	0.28	0.51	0.62	0.41	1.71	0.82	0.89	1.46	1.71
Al_2O_3	1.49	2.83	3.07	1.91	6.66	4.39	5.00	5.35	6.10
Fe_2O_3*	6.73	10.93	10.65	-	8.74	12.05	11.82	10.62	9.53
FeO^T*	6.06	9.83	9.58	10.94	7.86	10.84	10.64	9.56	0.00
MnO	0.15	0.24	0.23	0.28	0.16	0.23	0.21	0.18	0.18
MgO	19.26	17.76	16.99	20.44	18.17	20.48	22.99	19.15	15.06
CaO	19.52	17.33	15.02	16.16	14.31	13.84	10.93	13.83	17.00

APPENDIX C: *Whole Rock Chemistry*

Na_2O	0.19	0.22	0.41	0.22	0.27	0.36	0.33	0.18	0.25
K_2O	0.11	0.23	0.71	0.03	2.74	1.42	1.86	2.15	2.32
P_2O_5	0.02	0.03	0.05	0.02	0.01	0.02	0.14	0.02	0.19
SrO	0.01	b.d.	b.d.	0.01	0.01	0.02	0.02	0.01	-
BaO	0.00	b.d.	b.d.	0.00	0.21	0.07	0.09	0.17	-
Cr_2O_3	0.24	0.17	0.14	b.d.	0.17	0.15	0.20	0.21	0.11
NiO	0.03	0.04	0.03	b.d.	0.04	0.05	0.07	0.03	0.02
L.O.I.[2]	1.14	1.64	1.20	b.d.	1.21	0.62	1.84	1.10	0.82
Tot	100.20	100.36	100.48	98.79	100.45	100.28	100.32	100.29	99.95
Mg#	85.01	76.30	75.96	76.91	80.46	77.10	79.40	78.13	75.81
Na_2O+K_2O	0.30	0.45	1.13	0.25	3.06	1.81	2.24	2.37	2.61
K_2O/Na_2O	0.55	1.07	1.75	0.14	10.32	3.95	5.70	12.23	9.39
Sc	50.1	55.6	52.5	56.8	50.4	41.1	33.1	52.1	58.6
V	98	254	196	260	367	178	173	352	426
Cr	1566	1142	935	848	1051	1031	1345	1397	744
Co	44.6	53.3	50.5	65.6	41.9	82.5	87.4	56.6	41.3
Ni	215	257	209	314	293	378	462	189	148
Cu	4.1	44.4	7.2	3.6	1.0	36.3	101.5	1.6	20.1
Zn	26.5	58.2	68.7	55.0	43.7	55.8	52.5	52.7	37.8
Ga	2.7	5.4	6.2	4.0	7.5	6.3	6.4	6.6	8.5
Cs	0.29	0.34	0.59	0.05	1.10	0.84	1.22	0.60	1.24
Rb	3.09	6.83	22.47	0.63	79.68	39.07	55.26	59.46	75.41
Ba	19	26	251	5	1918	595	826	1530	1122
Th	0.54	0.64	1.39	0.14	0.06	0.25	0.45	0.04	0.17
U	0.14	0.21	0.39	0.03	0.02	0.08	0.15	b.d.	0.11
Nb	0.37	0.57	1.26	0.13	1.79	1.54	1.72	1.41	2.64
Ta	0.03	0.07	b.d.	0.02	0.07	0.09	0.09	0.06	-
La	4.68	4.82	9.78	3.58	2.62	5.12	6.82	2.37	10.80
Ce	14.00	14.27	31.27	13.01	10.20	17.48	20.41	9.53	36.97
Pb	0.49	1.00	1.34	0.36	0.18	0.84	1.29	b.d.	0.44
Pr	1.97	2.62	5.14	2.41	1.85	3.00	3.14	1.80	6.46
Sr	123	109	108	90	120	171	164	95	100
Nd	10.84	15.78	25.67	14.60	10.39	16.17	15.50	10.24	33.87
Zr	21.4	37.1	67.0	25.0	21.7	29.3	25.8	19.1	86.4
Hf	0.759	1.449	2.212	1.184	0.790	1.141	0.988	0.861	3.683
Sm	2.53	4.99	6.84	4.62	3.13	4.95	4.01	2.97	8.93
Eu	0.667	1.229	1.408	1.158	0.905	1.316	1.120	0.813	2.166
Gd	2.09	4.93	6.33	4.83	3.53	4.06	3.61	2.87	8.67
Tb	0.302	0.663	0.835	0.603	0.423	0.533	0.439	0.389	1.039
Dy	1.86	3.65	5.06	3.84	2.57	2.57	2.10	2.43	5.35
Y	7.84	18.15	24.73	17.64	11.20	10.14	8.67	10.04	22.23
Ho	0.308	0.694	0.901	0.661	0.411	0.371	0.352	0.380	0.969
Er	0.850	1.731	2.537	1.650	1.249	0.912	0.811	1.016	1.873

Tm	0.120	0.252	0.375	0.228	0.131	0.125	0.103	0.098	0.244
Yb	0.589	1.501	2.465	1.448	1.039	0.685	0.612	0.949	1.510
Lu	0.099	0.170	0.269	0.253	0.133	0.094	0.092	0.128	0.265

Sample #	**MO-10-301**	**MO-10-324**	**MO-10-325**	**MO-11-10**	**MO-11-51**	**MO-11-114**	**MO-11-12**	**MO-11-13**	**MO-11-72**
Longitude	94°9'57.1" E	94°12'6" E	94°12'6" E	94°14'25.9" E	94°36'29.2" E	94°34'24.5" E	94°14'25.2" E	94°14'26.9" E	94°13'56.9" E
Latitude	46°41'5.4" N	46°40'17.9" N	46°40'17.9" N	46°39'10.8" N	46°25'56.6" N	46°22'41.2" N	46°39'10.2" N	46°39'11" N	46°38'29.7" N
Rock Type[1]	PC	PC	PC	P	BMG	BMG	BMG	BMG	BMG
SiO_2	47.76	50.31	50.36	42.71	51.60	52.37	49.25	50.14	50.41
TiO_2	0.94	0.63	0.65	2.73	1.63	1.32	1.24	1.02	0.96
Al_2O_3	10.49	4.60	3.83	8.25	17.37	15.40	6.29	15.95	12.71
Fe_2O_3*	9.21	8.65	7.22	11.37	9.54	9.25	11.87	9.47	8.45
FeO^T*	8.29	7.78	6.50	10.23	8.58	8.32	10.68	8.52	7.61
MnO	0.18	0.25	0.17	0.18	0.17	0.17	0.27	0.17	0.16
MgO	11.35	12.71	14.65	15.57	3.67	5.73	12.13	6.45	9.49
CaO	13.78	19.75	20.66	11.55	7.80	8.26	13.26	8.99	9.48
Na_2O	1.61	0.75	0.36	0.39	4.09	3.12	0.69	3.40	2.79
K_2O	2.98	1.21	0.94	4.40	2.12	1.77	3.33	2.65	2.96
P_2O_5	0.34	0.34	0.12	1.38	0.76	0.47	0.33	0.61	0.65
SrO	0.08	0.05	0.03	b.d.	b.d.	b.d.	b.d.	b.d.	b.d.
BaO	0.09	0.11	0.10	b.d.	b.d.	b.d.	b.d.	b.d.	b.d.
Cr_2O_3	0.10	0.09	0.08	0.11	0.00	0.02	0.07	0.03	0.08
NiO	0.02	0.02	0.02	0.04	0.00	0.00	0.02	0.01	0.02
L.O.I.[2]	1.39	0.87	1.17	1.15	1.19	2.14	1.29	1.00	1.31
Tot	100.32	100.35	100.34	99.84	99.94	100.03	100.02	99.88	99.48
Mg#	70.93	74.44	80.07	73.08	43.26	55.11	66.93	57.44	68.99
Na_2O+K_2O	4.69	1.99	1.32	4.86	6.28	4.99	4.07	6.11	5.85
K_2O/Na_2O	1.85	1.61	2.64	11.25	0.52	0.57	4.84	0.78	1.06
Sc	41.8	47.0	62.2	40.6	14.3	22.6	43.7	23.5	21.4
V	218	196	195	558	183	226	292	236	175
Cr	651	613	518	739	35	162	426	192	530
Co	36.5	34.6	36.9	60.7	19.0	24.3	39.2	28.3	33.7
Ni	142	134	139	289	11	29	115	68	150
Cu	7.3	2.0	5.4	11.0	33.9	19.9	3.3	5.5	65.1
Zn	59.5	49.5	29.1	64.0	71.8	60.4	78.0	65.1	65.2
Ga	10.8	9.5	6.1	12.4	22.1	16.6	11.2	17.9	15.6
Cs	14.65	0.90	0.54	1.80	3.02	1.53	2.23	1.73	4.79
Rb	126.02	41.90	29.76	152.47	69.74	57.58	105.06	73.05	129.25
Ba	843	1024	900	2287	497	424	962	674	988
Th	6.31	3.35	1.01	0.97	18.39	7.32	3.02	2.25	6.65
U	1.47	0.92	0.26	0.32	2.98	1.88	0.95	0.85	2.08
Nb	6.31	3.56	1.46	5.34	21.23	10.92	12.53	10.27	12.02

Ta	0.35	0.22	0.11	0.31	0.90	0.71	0.82	0.60	0.74
La	31.23	33.00	11.92	28.21	101.40	33.79	24.31	38.56	56.91
Ce	68.34	84.45	35.48	70.81	185.17	70.18	60.17	88.56	129.29
Pb	3.84	1.41	1.11	0.99	8.41	6.95	4.17	5.21	4.58
Pr	8.27	11.04	5.37	10.29	19.87	8.17	7.88	11.37	16.69
Sr	687	409	256	197	960	786	200	1388	1541
Nd	34.96	49.88	27.50	51.28	80.64	33.58	36.19	48.94	70.30
Zr	116.9	130.9	57.2	28.2	115.0	176.2	71.0	153.5	140.1
Hf	3.070	3.789	1.916	0.969	3.049	4.321	2.132	3.609	3.263
Sm	7.83	10.76	6.46	11.84	15.05	6.64	8.12	9.74	11.61
Eu	1.885	2.710	1.823	1.833	3.288	1.744	1.273	2.750	2.907
Gd	6.90	8.40	6.31	9.49	11.60	5.85	7.08	8.53	8.03
Tb	0.924	1.126	0.791	1.085	1.290	0.732	0.959	0.958	0.920
Dy	5.21	5.45	3.95	6.25	7.29	4.01	5.28	5.83	4.85
Y	23.84	24.94	15.45	30.38	34.87	21.54	25.94	30.62	22.71
Ho	0.848	0.953	0.608	1.139	1.132	0.801	0.939	1.108	0.734
Er	2.346	2.312	1.741	2.920	3.612	2.072	2.438	3.029	2.035
Tm	0.337	0.341	0.160	0.337	0.449	0.259	0.320	0.362	0.263
Yb	2.023	1.935	0.874	2.019	2.661	2.120	2.390	2.771	1.657
Lu	0.306	0.310	0.163	0.313	0.424	0.313	0.409	0.398	0.300

Sample #	**MO-9-244**	**MO-9-243**	**MO-10-337**	**MO-10-400**	**MO-11-52**	**MO-10-380**	**MO-10-336**	**MO-12-13**	**MO-12-16**
Longitude	94°15'23.0" E	94°15'23.0" E	94°12'9"E	94°11'54.5"E	94°36'29.2" E	94°14'48.4"E	94°12'9"E	94°17'50.8" E	94°17'14.6" E
Latitude	46°38'55.6" N	46°38'55.6" N	46°40'17.5"N	46°39'3.4"N	46°25'56.6" N	46°39'23.8"N	46°40'17.5"N	46°38'3.8"N	46°38'1.3"N
Rock Type[1]	BMG	BMG	BMG	BMG	BMG	BMG	BMG	BMG	BMG
SiO_2	51.60	51.50	47.41	47.65	50.28	50.41	46.68	51.98	52.34
TiO_2	1.29	1.39	1.29	0.96	1.50	0.82	1.31	0.79	0.79
Al_2O_3	18.02	17.35	16.98	13.98	14.66	14.23	17.23	11.88	13.61
Fe_2O_3*	-	-	8.39	9.40	9.78	8.41	8.68	9.61	9.24
FeO^T*	7.20	7.54	7.55	8.46	8.80	7.57	7.81	0.00	0.00
MnO	0.15	0.15	0.17	0.16	0.22	0.15	0.18	0.19	0.17
MgO	5.09	5.32	8.37	10.18	7.08	9.49	8.20	8.16	7.28
CaO	7.86	7.93	8.44	8.83	9.36	7.32	8.67	10.90	9.23
Na_2O	3.91	3.73	2.36	2.56	2.69	2.81	2.42	2.50	2.67
K_2O	3.07	3.27	4.05	2.08	2.77	2.85	3.76	2.48	2.52
P_2O_5	0.67	0.73	0.63	0.45	0.49	0.34	0.62	0.50	0.52
SrO	0.20	0.16	0.21	0.10	b.d.	0.08	0.25	-	-
BaO	0.15	0.11	0.23	0.11	b.d.	0.11	0.20	-	-
Cr_2O_3	b.d.	b.d.	0.02	0.10	0.05	0.07	0.02	0.04	0.04
NiO	b.d.	b.d.	0.01	0.02	0.01	0.03	0.01	0.01	0.01
L.O.I.[2]	b.d.	b.d.	1.70	3.73	1.20	3.31	2.18	0.87	1.48
Tot	99.20	99.16	100.27	100.32	100.10	100.43	100.41	99.90	99.90

APPENDIX C: *Whole Rock Chemistry*

Mg#	55.77	55.72	66.38	68.21	58.93	69.09	65.18	62.75	60.97
Na_2O+K_2O	7.04	7.05	6.56	4.85	5.52	5.88	6.35	5.08	5.32
K_2O/Na_2O	0.79	0.88	1.72	0.81	1.03	1.02	1.56	0.99	0.94
Sc	17.7	18.6	21.9	24.8	20.7	23.1	23.2	32.1	25.5
V	156	165	208	166	163	160	234	240	220
Cr	108	115	145	647	347	467	163	288	270
Co	21.8	22.8	30.2	37.8	27.0	35.2	31.8	34.7	32.2
Ni	56	55	58	153	42	181	58	78	91
Cu	24.3	6.2	3.8	33.4	61.7	5.0	5.6	66.4	40.3
Zn	60.7	70.6	67.7	63.3	77.5	51.0	68.3	64.4	63.5
Ga	19.1	18.2	18.2	13.8	18.0	13.4	21.7	12.4	14.1
Cs	1.46	1.45	3.01	0.73	2.09	0.14	0.74	1.47	0.87
Rb	82.11	84.83	154.98	55.95	121.23	68.29	115.10	39.42	39.81
Ba	1325	926	2104	997	637	1025	1796	920	932
Th	2.24	2.86	1.41	4.27	6.47	2.58	1.58	1.84	3.71
U	0.76	0.89	0.43	1.31	2.02	0.87	0.42	0.48	1.18
Nb	13.20	15.87	11.07	4.75	16.61	4.84	13.62	2.05	4.85
Ta	0.59	0.70	0.39	0.23	0.85	0.24	0.53	-	0.14
La	42.55	43.10	44.68	38.09	34.50	26.18	53.19	25.48	29.96
Ce	83.89	88.85	109.44	82.69	71.19	59.30	128.94	57.51	63.52
Pb	8.26	8.69	6.29	10.39	8.13	1.88	5.01	8.87	9.18
Pr	10.35	11.07	13.56	9.97	8.59	7.41	16.38	7.77	8.20
Sr	1589	1314	1798	873	692	686	2086	1208	1202
Nd	44.29	48.77	56.67	43.68	35.67	32.04	71.21	34.62	34.47
Zr	306.8	376.3	74.0	103.3	227.2	93.0	100.9	65.8	94.3
Hf	6.350	7.694	2.228	2.447	5.445	2.310	3.138	2.661	2.732
Sm	8.68	9.97	11.35	8.22	6.78	6.05	13.61	7.54	7.30
Eu	2.628	2.496	3.176	2.267	1.766	1.607	3.636	2.188	2.022
Gd	6.89	7.95	8.61	6.03	5.38	4.90	11.34	6.55	5.92
Tb	0.815	0.886	1.081	0.804	0.661	0.622	1.318	0.900	0.764
Dy	4.50	4.84	5.47	4.10	3.57	3.54	6.86	4.54	4.13
Y	21.30	24.77	23.91	19.98	19.37	17.40	32.61	21.34	20.90
Ho	0.832	0.909	0.838	0.778	0.667	0.629	1.258	0.865	0.898
Er	2.175	2.581	2.122	1.928	1.995	1.977	3.101	1.706	1.914
Tm	0.278	0.303	0.287	0.239	0.232	0.239	0.330	0.268	0.271
Yb	1.640	1.852	1.680	1.661	1.537	1.648	2.469	1.937	1.673
Lu	0.281	0.324	0.213	0.236	0.240	0.262	0.317	0.326	0.299

Sample #	**MO-12-18**	**MO-12-26**	**MO-12-36**	**MO-9-257**	**MO-9-266**	**MO-11-14**	**MO-11-15**	**MO-11-18**	**MO-11-21**
Longitude	94°16'38.4" E	94°33'54" E	94°42'43" E	94°14'56.2"E	94°16'27.3"E	94°14'28.1" E	94°14'28.7" E	94°14'29.7" E	94°14'30.7" E
Latitude	46°38'8.9"N	46°23'19.9"N	46°24'11.8"N	46°38'29.6"N	46°37'32.1"N	46°39'11.2" N	46°39'11.2" N	46°39'10.8" N	46°39'12.1" N
Rock Type[1]	BMG	BMG	BMG	BMD	BMD	BMD	BMD	BMD	BMD

APPENDIX C: *Whole Rock Chemistry*

SiO_2	53.54	50.31	50.64	51.58	53.25	53.24	51.59	51.69	52.47
TiO_2	0.84	1.38	1.37	1.92	0.44	1.07	1.10	1.13	1.14
Al_2O_3	14.43	12.96	21.95	11.83	4.48	15.80	16.15	15.85	14.05
Fe_2O_3*	8.58	11.58	6.57	-	-	8.19	8.85	8.88	8.38
FeO^T*	0.00	0.00	0.00	12.97	10.32	7.37	7.96	7.99	7.54
MnO	0.16	0.21	0.10	0.33	0.34	0.16	0.16	0.17	0.15
MgO	6.48	7.80	2.16	6.76	14.15	5.27	5.83	5.92	7.51
CaO	8.27	8.93	7.73	7.80	13.64	7.09	7.94	7.66	9.02
Na_2O	3.16	2.36	4.29	1.75	0.68	3.57	3.77	3.53	2.96
K_2O	2.96	1.66	2.46	2.62	0.59	3.53	2.71	3.20	2.51
P_2O_5	0.52	0.43	0.62	0.86	0.92	0.57	0.62	0.62	0.59
SrO	-	-	-	0.04	0.02	b.d.	b.d.	b.d.	b.d.
BaO	-	-	-	0.10	0.03	b.d.	b.d.	b.d.	b.d.
Cr_2O_3	0.03	0.04	0.00	b.d.	b.d.	0.02	0.02	0.02	0.05
NiO	0.01	0.00	0.00	b.d.	b.d.	0.01	0.01	0.01	0.02
L.O.I.[2]	0.92	2.27	2.01	b.d.	b.d.	1.20	1.42	1.11	1.24
Tot	99.89	99.92	99.91	98.56	98.85	99.73	100.18	99.80	100.07
Mg#	59.97	57.19	39.50	48.16	70.97	56.04	56.64	56.91	63.96
Na_2O+K_2O	6.23	4.17	6.94	4.44	1.28	7.21	6.57	6.82	5.54
K_2O/Na_2O	0.94	0.70	0.57	1.49	0.86	0.99	0.72	0.91	0.85
Sc	22.8	31.9	10.9	31.5	50.2	18.1	21.0	22.2	20.9
V	212	264	118	239	189	210	230	224	175
Cr	194	224	17	53	597	152	160	163	321
Co	28.1	34.4	14.1	26.8	43.6	23.5	24.7	25.3	27.6
Ni	72	48	-	11	143	54	55	58	104
Cu	5.0	24.0	20.8	6.7	8.8	13.0	14.4	13.3	31.6
Zn	72.1	94.9	122.8	105.7	101.4	69.5	73.9	62.5	64.4
Ga	15.2	18.6	22.7	17.6	9.9	17.6	19.4	18.2	18.0
Cs	0.87	1.25	3.21	0.21	0.29	2.02	1.34	1.47	2.33
Rb	52.52	54.77	79.45	36.12	8.08	72.63	70.06	76.41	96.46
Ba	1163	492	861	905	231	1302	755	1305	810
Th	1.15	4.98	1.79	7.36	6.45	4.19	2.66	2.65	4.75
U	0.33	1.16	0.90	2.06	1.50	1.18	0.80	0.75	1.76
Nb	2.56	10.69	16.94	30.79	3.84	11.95	13.38	11.62	15.42
Ta	0.06	0.56	0.96	1.42	0.30	0.72	0.83	0.91	0.72
La	26.85	39.79	39.04	82.40	72.96	35.44	37.16	40.29	45.66
Ce	57.56	88.69	85.28	185.64	162.66	75.46	80.23	80.53	101.86
Pb	12.96	6.04	17.09	4.21	4.15	11.05	8.54	8.69	10.77
Pr	7.22	11.03	10.16	23.99	21.19	8.96	9.42	9.87	12.03
Sr	1084	540	1195	324	206	1252	1407	1423	1128
Nd	31.08	46.34	41.12	99.40	91.20	37.63	39.65	42.99	50.33
Zr	52.0	126.4	243.0	574.5	151.8	150.1	168.2	192.0	132.8
Hf	1.201	3.315	5.083	13.723	4.526	3.873	3.709	4.694	3.227

Sm	6.89	9.63	8.14	19.29	18.64	8.05	7.92	9.37	9.84
Eu	2.223	1.953	2.404	2.787	1.917	2.449	2.170	2.177	2.099
Gd	5.76	8.43	6.50	15.10	15.67	6.39	7.07	7.52	7.12
Tb	0.626	1.089	0.738	1.870	2.039	0.732	0.838	0.852	0.844
Dy	3.88	6.72	4.39	10.43	11.47	4.31	4.17	5.01	4.98
Y	19.71	31.44	20.36	54.23	58.97	21.25	22.04	26.68	24.53
Ho	0.709	1.198	0.834	1.892	2.152	0.762	0.749	0.944	0.932
Er	1.813	3.370	2.326	5.331	5.826	1.892	2.094	2.570	2.603
Tm	0.301	0.457	0.301	0.742	0.798	0.336	0.313	0.346	0.274
Yb	1.656	2.904	1.885	4.552	5.041	2.009	2.248	2.436	1.822
Lu	0.183	0.363	0.210	0.636	0.795	0.284	0.234	0.333	0.338

Sample #	**MO-11-22**	**MO-10-377**	**MO-10-383**	**MO-12-27**	**MO-10-320**	**MO-11-23**	**MO-12-37**	**MO-12-30**	**MO-12-32**
Longitude	94°14'31.6" E	94°14'33"E	94°14'43.9"E	94°33'59.3" E	94°11'16.6"E	94°14'32.9" E	94°42'13.1" E	94°37'16" E	94°35'26.4" E
Latitude	46°39'12.1" N	46°39'53.8"N	46°39'25.1"N	46°23'57.8"N	46°41'4"N	46°39'12.4" N	46°24'25.7"N	46°22'56.8"N	46°24'4.9"N
Rock Type[1]	BMD	BMD	BMD	BMD	BM	BM	BM	BQM	BQM
SiO_2	54.70	54.60	53.30	55.47	53.94	57.80	56.64	60.86	60.15
TiO_2	0.98	1.33	0.73	1.01	0.98	0.77	0.72	0.79	0.82
Al_2O_3	17.13	15.17	14.16	17.06	16.36	17.40	15.13	16.42	15.62
Fe_2O_3*	7.33	9.03	8.63	7.36	9.51	5.42	6.74	5.48	6.34
FeO^T*	6.59	8.12	7.77	0.00	8.56	4.87	0.00	0.00	0.00
MnO	0.13	0.15	0.18	0.14	0.18	0.09	0.14	0.10	0.13
MgO	4.06	5.39	6.64	3.99	4.91	2.87	5.84	2.42	3.38
CaO	5.74	5.66	8.21	6.33	7.18	4.64	7.26	4.51	5.53
Na_2O	4.02	3.22	2.89	3.81	2.71	4.24	3.71	3.96	2.98
K_2O	4.43	3.23	3.27	3.26	2.73	4.69	2.27	3.79	3.03
P_2O_5	0.47	0.36	0.29	0.38	0.25	0.40	0.25	0.28	0.26
SrO	b.d.	0.09	0.09	-	0.07	b.d.	-	-	-
BaO	b.d.	0.11	0.11	-	0.08	b.d.	-	-	-
Cr_2O_3	0.02	0.00	0.04	0.01	0.01	0.01	0.05	0.01	0.01
NiO	0.01	0.00	0.01	0.00	0.00	0.01	0.01	0.00	0.00
L.O.I.[2]	1.12	1.92	1.77	1.46	1.41	1.49	1.20	1.31	1.36
Tot	100.13	100.26	100.33	100.28	100.34	99.83	99.97	99.92	99.64
Mg#	52.35	54.20	60.40	51.82	50.56	51.24	63.20	46.65	51.38
Na_2O+K_2O	8.54	6.62	6.30	7.21	5.55	9.08	6.10	7.90	6.16
K_2O/Na_2O	1.10	1.00	1.13	0.85	1.01	1.11	0.61	0.96	1.02
Sc	13.3	25.5	19.5	14.4	25.0	10.2	16.5	10.2	13.5
V	137	215	162	154	174	89	131	95	104
Cr	128	28	283	74	62	78	358	40	100
Co	18.2	23.3	22.2	19.4	20.7	12.2	21.9	13.4	15.1
Ni	45	16	49	30	8	26	42	-	-
Cu	16.3	1.5	4.0	17.9	b.d.	5.8	15.0	-	4.2

APPENDIX C: *Whole Rock Chemistry*

Zn	66.5	72.2	66.6	61.3	81.2	51.7	58.2	44.8	64.1
Ga	19.2	16.9	14.3	17.8	18.7	20.4	16.3	19.3	17.3
Cs	2.48	1.69	0.21	1.23	1.81	2.69	2.46	1.82	2.74
Rb	114.10	94.94	61.19	65.21	89.15	117.77	56.51	99.42	93.27
Ba	1329	1029	948	1186	748	1558	778	737	814
Th	4.15	4.35	3.89	2.54	4.81	4.59	4.54	23.33	12.55
U	1.14	1.14	1.48	0.83	1.43	1.42	1.46	1.77	1.97
Nb	15.16	10.37	7.71	12.65	10.35	16.23	8.97	18.16	12.79
Ta	0.73	0.60	0.45	0.61	0.57	0.66	0.56	1.07	0.84
La	45.78	27.63	21.26	39.26	27.60	40.14	34.40	59.20	45.11
Ce	91.34	64.38	47.09	78.41	59.93	76.37	66.96	116.40	89.10
Pb	15.75	7.88	6.91	13.64	10.94	19.40	13.00	15.18	14.14
Pr	10.15	7.88	5.80	9.26	6.81	8.85	7.57	12.62	10.00
Sr	1118	736	782		604	1202	709	629	586
Nd	40.91	31.95	24.24	37.38	27.42	36.42	27.98	44.33	36.49
Zr	304.8	93.4	130.4	244.9	153.7	331.9	158.5	399.3	209.6
Hf	6.560	2.661	3.268	5.507	3.883	7.888	3.574	9.673	5.664
Sm	7.13	6.41	4.86	7.24	5.54	6.52	5.72	8.13	6.97
Eu	1.903	1.726	1.297	2.154	1.346	2.050	1.588	1.713	1.572
Gd	5.76	6.02	4.49	5.90	5.17	4.51	4.47	5.96	5.31
Tb	0.687	0.844	0.598	0.656	0.685	0.622	0.529	0.694	0.654
Dy	3.96	4.59	3.29	3.94	3.98	3.17	3.59	4.04	4.30
Y	18.78	22.00	18.17	19.94	22.46	16.49	17.25	20.94	20.93
Ho	0.686	0.791	0.683	0.765	0.857	0.525	0.670	0.771	0.850
Er	1.765	2.180	1.836	1.934	2.399	1.475	2.102	2.445	2.580
Tm	0.170	0.283	0.294	0.255	0.353	0.218	0.302	0.311	0.346
Yb	1.530	1.808	2.076	1.535	2.375	1.369	1.714	1.733	1.952
Lu	0.312	0.252	0.275	0.121	0.345	0.162	0.219	0.239	0.328

Sample #	**MO-9-256**	**MO-11-26**	**MO-10-359**	**MO-10-386**	**MO-10-401**	**MO-10-333**	**MO-10-340**	**MO-11-106**	**MO-11-53**
Longitude	94°15'1.3"E	94°14'34.6" E	94°11'57.3"E	94°14'27"E	94°11'20.3"E	94°12'1.7"E	94°11'23.1"E	94°18'14.6" E	94°36'18.7" E
Latitude	46°38'38.2"N	46°39'13.1" N	46°41'23.7"N	46°39'18.9"N	46°39'12.6"N	46°40'17.3"N	46°41'7.2"N	46°30'13.3" N	46°25'38.9" N
Rock Type[1]	BQM	BQM	BQM	BQM	BQM	BQM	BQM	BQM	BQM
SiO_2	60.48	59.75	60.71	62.37	63.39	63.20	63.07	59.58	65.26
TiO_2	0.65	0.81	0.58	0.59	0.52	0.50	0.55	0.92	0.53
Al_2O_3	17.12	16.72	17.84	16.04	17.97	18.09	15.87	16.04	15.62
Fe_2O_3*	-	5.61	4.46	4.55	3.41	3.35	4.49	6.14	3.80
FeO^T*	4.86	5.04	4.01	4.09	3.07	3.02	4.04	5.52	3.42
MnO	0.11	0.10	0.11	0.09	0.06	0.07	0.09	0.12	0.08
MgO	4.15	2.92	1.49	2.23	1.14	1.12	1.98	3.14	1.41
CaO	3.60	4.48	3.02	3.67	3.40	2.61	3.46	5.41	3.11
Na_2O	4.16	4.14	5.51	3.91	4.61	4.82	4.14	3.99	3.76

K_2O	3.85	4.19	5.10	4.81	4.51	4.82	4.69	3.36	4.49
P_2O_5	0.28	0.40	0.39	0.31	0.20	0.20	0.23	0.52	0.19
SrO	0.09	b.d.	0.18	0.11	0.11	0.15	0.11	b.d.	b.d.
BaO	0.10	b.d.	0.18	0.12	0.18	0.18	0.16	b.d.	b.d.
Cr_2O_3	b.d.	0.01	0.00	0.01	0.00	0.00	0.00	0.01	0.00
NiO	b.d.	0.01	0.00	0.00	0.00	0.00	0.00	0.00	0.00
L.O.I.[2]	b.d.	0.86	0.50	1.11	0.52	1.17	1.43	0.87	0.88
Tot	99.46	99.99	100.08	99.90	100.01	100.29	100.28	100.09	99.14
Mg#	60.38	50.78	39.85	49.28	39.85	39.85	46.58	50.34	42.29
Na_2O+K_2O	8.06	8.40	10.71	8.87	9.19	9.75	8.97	7.41	8.40
K_2O/Na_2O	0.93	1.01	0.92	1.23	0.98	1.00	1.13	0.84	1.20
Sc	12.5	10.7	2.6	7.9	4.3	3.9	7.7	9.2	5.3
V	102	99	43	72	33	30	67	85	54
Cr	59	70	39	54	22	19	32	56	35
Co	12.9	13.2	8.7	11.7	6.7	7.0	11.8	12.6	6.6
Ni	27	33	12	25	b.d.	b.d.	b.d.	16	7
Cu	2.3	10.6	5.5	6.5	2.4	2.1	2.1	13.0	74.4
Zn	30.5	63.1	65.6	49.5	29.4	39.1	48.8	62.7	37.7
Ga	15.5	21.0	20.8	17.4	20.4	19.7	19.0	19.1	17.6
Cs	0.33	3.71	1.67	2.42	1.64	1.20	2.25	2.37	2.07
Rb	91.09	126.28	118.68	118.43	111.79	112.84	130.98	87.89	113.93
Ba	905	1203	1639	1084	1570	1621	1414	1081	772
Th	9.35	11.28	29.30	8.43	14.68	13.67	17.00	17.22	31.45
U	2.76	2.23	4.75	2.60	2.92	2.05	2.57	2.65	4.47
Nb	7.86	16.74	24.74	13.75	15.97	14.69	18.20	20.48	14.48
Ta	0.55	0.79	1.65	0.94	1.11	0.79	1.19	1.39	1.03
La	41.11	44.43	113.60	33.79	103.57	67.45	61.82	68.44	51.59
Ce	84.85	88.06	200.98	69.12	165.01	123.25	116.22	134.85	91.64
Pb	8.40	19.38	27.83	23.48	17.16	19.89	20.05	17.56	16.43
Pr	9.97	9.68	20.79	7.89	16.97	12.35	11.95	14.92	9.83
Sr	709	972	1545	905	970	1310	966	1004	599
Nd	38.60	39.11	73.16	30.06	58.08	42.86	44.30	56.78	36.93
Zr	151.0	317.5	372.0	247.3	284.4	299.2	250.0	291.8	234.6
Hf	3.540	7.685	8.943	6.088	7.047	6.475	5.901	7.039	6.309
Sm	6.24	7.00	9.76	5.81	7.89	6.34	6.92	9.55	5.51
Eu	1.796	1.624	2.566	1.594	2.082	1.840	1.820	2.051	1.312
Gd	5.34	5.38	7.00	4.21	4.49	4.43	5.58	6.91	4.69
Tb	0.635	0.568	0.906	0.612	0.582	0.538	0.637	0.802	0.539
Dy	3.76	3.84	4.00	3.06	3.02	2.77	3.22	4.79	2.99
Y	18.25	18.54	21.72	14.98	15.24	13.29	17.96	24.63	16.54
Ho	0.637	0.535	0.752	0.523	0.503	0.451	0.641	0.800	0.544
Er	1.849	1.844	1.732	1.592	0.968	1.263	1.653	2.467	1.613
Tm	0.254	0.213	0.299	0.230	0.208	0.161	0.240	0.305	0.242

APPENDIX C: *Whole Rock Chemistry*

Yb	1.969	1.677	2.348	1.639	1.370	1.145	1.740	1.993	1.422
Lu	0.237	0.235	0.381	0.177	0.205	0.122	0.219	0.314	0.224

Sample #	**MO-10-319**	**MO-10-335**	**MO-10-328**	**MO-10-334**	**MO-10-327**	**MO-10-329**	**MO-10-330**	**MO-10-338**	**MO-9-258**
Longitude	94°10'47.3"E	94°12'9"E	94°12'6"E	94°12'9.7"E	94°12'6"E	94°12'6"E	94°12'6"E	94°12'9"E	94°14'56.2"E
Latitude	46°41'12.3"N	46°40'17.5"N	46°40'17.9"N	46°40'18.2"N	46°40'17.9"N	46°40'17.9"N	46°40'17.9"N	46°40'17.5"N	46°38'29.6"N
Rock Type[1]	BQM	AC	AC	AC	AC	AC	AC	AC	AC
SiO_2	61.71	42.98	37.06	39.23	40.02	41.10	41.78	43.51	46.37
TiO_2	0.49	1.55	2.83	2.20	2.15	2.14	1.89	2.04	1.72
Al_2O_3	16.88	10.93	9.71	12.09	9.81	10.38	9.39	10.45	7.76
Fe_2O_3*	3.87	14.57	19.79	16.44	16.18	15.23	13.75	12.30	-
FeO^T*	3.48	13.11	17.81	14.80	14.56	13.70	12.38	11.07	17.03
MnO	0.07	0.31	0.26	0.31	0.24	0.23	0.25	0.19	0.48
MgO	3.15	10.46	10.34	8.88	11.58	12.00	13.41	12.79	9.33
CaO	5.10	14.01	14.29	14.31	15.56	14.79	14.69	14.33	12.60
Na_2O	5.62	1.19	1.58	1.40	1.34	1.53	0.93	1.42	0.96
K_2O	1.89	1.88	1.23	1.92	1.12	1.16	1.64	1.24	0.87
P_2O_5	0.20	0.46	2.04	1.48	0.91	0.59	0.60	0.62	0.97
SrO	0.12	0.08	0.10	0.12	0.08	0.08	0.05	0.07	0.02
BaO	0.16	0.11	0.05	0.15	0.04	0.04	0.11	0.05	0.00
Cr_2O_3	0.02	0.05	0.01	0.01	0.01	0.01	0.02	0.05	b.d.
NiO	0.01	0.02	0.01	0.01	0.01	0.01	0.01	0.02	b.d.
L.O.I.[2]	1.03	1.66	0.84	1.58	0.90	1.07	1.80	1.25	b.d.
Tot	100.31	100.27	100.14	100.11	99.93	100.37	100.33	100.36	98.11
Mg#	61.75	58.72	50.87	51.67	58.63	60.96	65.89	67.30	49.40
Na_2O+K_2O	7.60	3.17	2.89	3.43	2.52	2.75	2.65	2.72	1.86
K_2O/Na_2O	0.34	1.58	0.78	1.37	0.84	0.76	1.76	0.88	0.91
Sc	9.0	39.8	43.0	30.6	48.1	46.0	53.3	45.9	54.4
V	66	307	579	392	452	404	362	405	270
Cr	126	352	44	49	68	74	110	358	196
Co	13.7	42.6	64.2	52.2	62.0	61.2	61.3	49.4	38.2
Ni	30	94	73	26	66	90	97	146	32
Cu	11.0	89.9	74.5	136.1	58.6	35.9	71.5	14.2	10.9
Zn	24.4	108.6	116.8	112.5	80.8	76.5	78.1	63.1	153.0
Ga	16.7	15.7	22.8	22.0	16.9	17.2	14.8	16.6	19.3
Cs	0.86	0.26	0.46	0.14	0.05	0.08	0.79	0.10	0.06
Rb	50.36	35.85	11.90	23.80	5.94	6.42	41.69	17.74	3.17
Ba	1451	962	462	1364	366	395	988	463	54
Th	8.31	2.25	4.38	4.66	1.40	1.43	1.20	1.66	4.71
U	2.15	0.60	0.91	0.73	0.24	0.30	0.31	0.48	1.29
Nb	13.16	10.04	17.80	17.58	7.98	10.41	7.40	11.66	36.38
Ta	0.56	0.45	0.68	0.75	0.42	0.52	0.36	0.47	1.45

La	45.48	37.45	102.77	107.41	43.36	35.47	31.48	36.70	94.95
Ce	78.53	102.82	253.91	259.08	120.99	103.76	89.66	102.57	244.20
Pb	9.14	25.16	4.93	5.97	1.47	2.98	4.93	7.34	3.54
Pr	7.42	13.99	32.79	32.66	17.15	14.93	12.60	14.59	34.66
Sr	1030	653	811	983	656	657	444	558	177
Nd	27.25	64.85	149.81	141.25	81.73	71.91	60.47	69.96	156.35
Zr	207.4	178.7	163.5	284.5	130.1	144.2	109.5	132.3	125.0
Hf	4.571	5.615	5.836	8.290	4.662	5.296	3.736	4.509	4.708
Sm	4.44	14.52	31.21	28.40	18.48	16.60	14.32	16.33	33.88
Eu	1.075	3.580	7.338	7.168	4.734	4.424	3.495	4.163	4.198
Gd	2.99	12.25	24.44	22.34	15.97	14.07	11.60	13.84	27.38
Tb	0.512	1.487	2.648	2.420	1.771	1.629	1.390	1.795	3.534
Dy	2.96	7.46	12.93	12.43	9.17	8.57	6.88	8.99	19.82
Y	14.70	33.32	54.78	55.21	38.41	36.08	28.53	39.07	96.39
Ho	0.563	1.237	2.086	1.989	1.446	1.365	1.110	1.403	3.621
Er	1.444	3.186	5.121	5.011	3.578	3.438	2.683	3.761	9.797
Tm	0.196	0.355	0.562	0.588	0.388	0.442	0.338	0.482	1.237
Yb	1.590	2.423	3.362	3.419	2.287	2.373	1.963	2.567	7.019
Lu	0.237	0.303	0.439	0.480	0.309	0.313	0.251	0.404	1.111

Sample #	**MO-9-254**	**MO-9-251**	**MO-9-255**	**MO-10-384**	**MO-10-398**	**MO-11-7**	**MO-10-309a**	**MO-10-382**	**MO-10-430**
Longitude	94°15'9.1"E	94°15'16.4"E	94°15'9.1"E	94°14'42.7"E	94°12'42.8"E	94°14'29.7" E	94°10'31.3"E	94°14'43.9"E	94°14'27.4"E
Latitude	46°38'42.3"N	46°38'46.7"N	46°38'42.3"N	46°39'24.6"N	46°39'2.7"N	46°39'22.3" N	46°40'49"N	46°39'25.1"N	46°40'7.4"N
Rock Type[1]	AC	AC	AC	AC	AC	AMG	AMG	AMG	AMG
SiO_2	47.93	52.13	51.30	50.57	52.67	45.86	47.46	48.64	48.25
TiO_2	1.66	0.60	1.19	0.99	0.34	1.94	2.16	1.63	1.69
Al_2O_3	9.78	4.78	9.00	9.32	3.34	17.08	13.25	14.16	13.55
Fe_2O_3*	-	-	-	8.75	5.61	11.16	13.72	11.59	11.16
FeO^T*	10.32	11.45	8.50	7.87	5.05	10.04	12.35	10.43	10.04
MnO	0.21	0.36	0.21	0.17	0.13	0.17	0.24	0.20	0.18
MgO	12.01	14.10	11.02	12.19	15.75	4.78	7.48	8.03	8.87
CaO	11.78	13.46	13.54	13.55	18.98	8.67	8.87	9.18	9.20
Na_2O	1.64	0.72	1.82	1.72	0.57	3.60	3.26	2.61	2.35
K_2O	1.96	0.44	1.27	0.85	1.02	3.20	1.41	1.65	1.95
P_2O_5	1.45	0.64	1.10	0.09	0.15	1.30	0.75	0.48	0.13
SrO	0.06	0.02	0.07	0.05	0.03	b.d.	0.07	0.09	0.06
BaO	0.06	0.01	0.05	0.03	0.02	b.d.	0.05	0.06	0.06
Cr_2O_3	b.d.	b.d.	b.d.	0.12	0.28	0.00	0.01	0.00	0.01
NiO	b.d.	b.d.	b.d.	0.02	0.02	0.00	0.00	0.01	0.00
L.O.I.[2]	b.d.	b.d.	b.d.	1.93	1.34	2.08	1.55	1.86	2.73
Tot	98.85	98.73	99.06	100.33	100.26	99.83	100.29	100.17	100.20
Mg#	67.48	68.72	69.82	73.41	84.76	45.90	51.91	57.86	61.17

APPENDIX C: *Whole Rock Chemistry*

Na_2O+K_2O	3.64	1.18	3.11	2.63	1.62	6.95	4.80	4.38	4.46
K_2O/Na_2O	1.20	0.62	0.70	0.50	1.81	0.89	0.43	0.63	0.83
Sc	47.5	44.4	41.7	47.0	43.2	12.9	27.1	32.4	51.0
V	348	172	276	215	98	189	240	303	380
Cr	185	500	207	783	1790	23	70	8	90
Co	43.4	39.8	38.4	40.8	30.9	26.4	32.3	43.7	37.9
Ni	131	208	112	128	104	21	5	40	29
Cu	34.6	112.4	25.9	42.8	6.9	23.9	3.2	26.7	9.9
Zn	64.9	111.7	59.7	48.4	25.2	88.6	89.3	91.5	62.2
Ga	14.2	7.8	13.0	10.4	4.5	20.6	19.6	17.1	14.9
Cs	2.07	0.33	0.47	0.30	0.51	1.58	0.20	0.52	2.04
Rb	38.66	5.04	19.09	16.64	31.25	56.87	20.84	39.37	46.36
Ba	501	54	391	243	184	2052	444	498	548
Th	5.75	5.08	5.60	2.87	2.10	7.44	3.97	3.43	2.06
U	1.46	1.58	1.34	0.69	0.66	1.59	1.11	0.99	1.10
Nb	14.46	3.54	10.11	5.25	1.51	26.64	15.75	15.22	10.42
Ta	1.03	0.38	0.74	0.29	0.12	1.30	0.91	1.02	0.69
La	50.54	28.38	39.91	16.64	10.52	80.08	36.21	39.80	19.21
Ce	115.18	59.05	97.45	41.43	25.14	175.53	86.03	100.19	48.83
Pb	4.63	5.18	4.13	6.13	2.27	9.27	8.06	5.16	6.10
Pr	16.36	7.98	13.33	5.47	3.41	19.26	11.23	12.52	6.69
Sr	467	148	561	453	220	1834	556	785	466
Nd	76.28	39.08	61.87	26.05	15.63	73.42	50.73	53.13	31.60
Zr	75.5	54.1	54.3	112.2	39.3	238.8	100.1	100.1	82.1
Hf	3.079	2.293	2.481	3.171	1.441	4.988	3.542	3.118	2.793
Sm	17.82	9.13	13.98	6.00	3.82	12.62	10.75	10.50	8.21
Eu	3.462	1.403	3.164	1.610	0.993	2.988	2.607	2.495	1.864
Gd	15.11	8.52	11.78	5.26	3.14	8.62	9.86	8.87	7.35
Tb	1.921	1.139	1.500	0.673	0.429	1.006	1.339	1.186	1.103
Dy	10.41	6.38	7.88	4.10	2.17	5.77	7.36	6.23	6.32
Y	52.68	31.99	39.67	17.24	10.26	27.67	39.23	32.59	31.08
Ho	1.795	1.179	1.460	0.678	0.338	0.927	1.513	1.190	1.229
Er	4.995	3.422	4.072	1.850	0.995	2.532	4.404	3.358	3.304
Tm	0.603	0.400	0.480	0.232	0.131	0.329	0.473	0.397	0.467
Yb	4.050	2.921	3.125	1.414	0.692	2.329	3.026	2.510	2.760
Lu	0.574	0.424	0.448	0.202	0.116	0.314	0.473	0.351	0.383

Sample #	**MO-9-235**	**MO-9-252**	**MO-10-308**	**MO-10-309b**	**MO-10-381**	**MO-10-313**	**MO-10-312**	**MO-12-41**	**MO-9-236**
Longitude	94°16'48.0"E	94°15'16.4"E	94°10'31.3"E	94°10'31.3"E	94°14'43.9"E	94°10'50.1"E	94°10'50.1"E	94°42'2.3"E	94°16'48.0"E
Latitude	46°36'52.3"N	46°38'46.7"N	46°40'49"N	46°40'49"N	46°39'25.1"N	46°40'46.5"N	46°40'46.5"N	46°24'51.2"N	46°36'52.3"N
Rock Type[1]	AMG	AMG	AMG	AMG	AMG	AMG	AMG	AMG	AG1
SiO_2	49.57	51.60	51.01	51.48	51.53	51.84	52.59	50.41	53.76

TiO_2	1.36	1.13	1.72	1.55	0.94	1.43	0.99	1.73	1.03
Al_2O_3	18.87	17.31	15.27	15.51	15.32	15.95	19.06	17.69	18.98
Fe_2O_3*	-	-	10.61	10.85	8.92	10.08	8.29	9.46	-
FeO^T*	9.27	6.97	9.55	9.76	8.03	9.07	7.46	0.00	6.96
MnO	0.20	0.12	0.18	0.20	0.18	0.18	0.15	0.16	0.16
MgO	4.35	6.66	6.15	5.60	6.54	5.20	3.27	4.92	3.44
CaO	8.70	8.65	7.57	7.66	9.00	7.11	5.02	8.91	6.98
Na_2O	3.74	3.21	2.72	2.99	3.42	3.49	4.53	2.60	4.15
K_2O	1.87	2.58	2.64	2.27	1.81	2.39	3.80	1.87	2.85
P_2O_5	0.71	0.72	0.35	0.48	0.32	0.45	0.39	0.65	0.51
SrO	0.23	0.17	0.09	0.10	0.12	0.10	0.14	-	0.19
BaO	0.09	0.10	0.10	0.08	0.05	0.08	0.18	-	0.22
Cr_2O_3	b.d.	b.d.	0.01	0.01	0.06	0.01	0.00	0.00	b.d.
NiO	b.d.	b.d.	0.00	0.00	0.01	0.00	0.00	0.00	b.d.
L.O.I.[2]	b.d.	b.d.	1.67	1.61	2.06	1.79	2.03	1.47	b.d.
Tot	98.97	99.23	100.10	100.39	100.30	100.10	100.45	99.86	99.23
Mg#	45.56	63.00	53.44	50.55	59.21	50.54	43.88	50.76	46.85
Na_2O+K_2O	5.67	5.84	5.51	5.39	5.37	6.04	8.54	4.59	7.05
K_2O/Na_2O	0.50	0.81	0.97	0.76	0.53	0.68	0.84	0.72	0.69
Sc	20.8	20.5	24.9	22.9	23.9	20.9	10.6	25.8	13.3
V	146	202	215	192	180	167	77	140	103
Cr	14	137	71	65	400	60	36	32	19
Co	23.3	29.6	26.7	25.8	27.5	24.1	14.6	22.7	15.5
Ni	14	59	7	b.d.	62	b.d.	b.d.	14	10
Cu	26.7	21.0	2.7	10.0	7.4	10.5	48.8	2.7	4.0
Zn	79.1	48.9	69.2	91.1	71.1	74.4	45.6	71.2	64.5
Ga	19.6	17.0	18.5	20.0	18.1	18.8	19.4	18.8	19.5
Cs	0.56	1.90	0.43	0.84	0.95	0.74	0.52	2.93	0.84
Rb	47.13	56.74	51.06	57.95	46.40	47.06	71.29	57.25	53.85
Ba	704	865	861	675	478	691	1572	641	1754
Th	2.39	5.94	4.42	4.93	4.26	5.03	5.82	5.05	5.59
U	0.60	1.63	1.16	1.55	1.29	1.32	1.35	1.47	1.09
Nb	17.32	9.90	12.97	13.55	11.20	13.30	12.16	14.54	12.67
Ta	0.65	0.87	0.68	0.79	0.71	0.77	0.70	0.82	0.47
La	54.59	36.06	28.32	32.85	32.42	33.30	35.12	40.16	57.25
Ce	116.23	77.06	64.74	73.73	79.12	73.07	69.91	82.18	107.74
Pb	7.10	10.07	8.24	8.68	7.25	12.97	9.68	5.27	10.09
Pr	14.84	10.04	8.20	9.21	9.74	9.07	8.08	10.77	12.72
Sr	1715	1426	775	821	1004	820	1215	773	1458
Nd	61.36	45.06	37.83	39.30	40.33	38.45	31.98	45.10	53.03
Zr	215.8	65.7	100.7	129.6	207.5	153.4	245.5	118.5	300.6
Hf	5.515	2.592	3.227	3.869	4.764	4.465	5.402	3.595	7.534
Sm	11.66	9.77	7.42	8.54	8.06	7.98	6.08	9.32	9.19

Eu	2.621	2.594	2.191	2.318	2.068	2.306	1.919	2.414	2.579
Gd	9.05	7.77	7.30	7.93	7.05	7.37	5.26	8.75	7.77
Tb	1.199	0.971	1.062	1.025	0.907	0.990	0.669	1.242	0.913
Dy	6.24	5.50	5.66	5.60	5.04	5.41	4.00	6.80	4.65
Y	32.92	27.48	29.91	29.44	23.75	29.00	20.86	32.29	24.27
Ho	1.164	0.983	1.056	1.051	0.884	1.026	0.755	1.315	0.903
Er	3.028	2.627	2.950	3.174	2.382	2.856	2.398	3.587	2.516
Tm	0.431	0.379	0.397	0.428	0.340	0.395	0.323	0.426	0.307
Yb	2.639	2.154	2.604	2.797	2.615	2.691	1.885	2.687	1.668
Lu	0.523	0.316	0.392	0.369	0.348	0.383	0.326	0.395	0.333

Sample #	**MO-9-233**	**MO-9-237**	**MO-9-232**	**MO-9-229**	**MO-9-221**	**MO-12-20**	**MO-12-85**	**MO-9-241**	**MO-10-318**
Longitude	94°16'54.1"E	94°16'46.2"E	94°16'54.8"E	94°16'54.1"E	94°16'53.0"E	94°15'48.6"E	94°39'21.7" E	94°16'47.5"E	94°10'36.7"E
Latitude	46°36'53.7"N	46°36'50.4"N	46°36'52.9"N	46°36'51.4"N	46°36'52.1"N	46°37'54.2"N	46°26'56.7"N	46°36'50.9"N	46°41'14.8"N
Rock Type[1]	AG1	AG1	AG1	AG1	AG1	AG1	AG1	AG2	AG2
SiO_2	56.16	51.59	56.84	58.28	59.50	58.18	57.70	67.71	68.34
TiO_2	0.98	1.27	0.95	0.88	0.89	0.81	1.02	0.47	0.27
Al_2O_3	17.98	18.45	17.70	16.45	16.28	16.99	16.07	16.43	17.01
Fe_2O_3*	-	-	-	-	-	6.51	7.43	-	2.00
FeO^T*	6.34	8.55	6.23	4.43	4.30	0.00	0.00	2.46	1.80
MnO	0.14	0.19	0.15	0.11	0.10	0.12	0.14	0.05	0.03
MgO	3.30	4.66	3.20	3.39	3.49	2.59	3.87	1.09	0.69
CaO	6.60	7.26	6.38	5.42	5.26	5.40	5.98	2.75	1.42
Na_2O	4.14	3.87	4.08	4.13	4.35	3.71	3.51	3.95	5.94
K_2O	2.95	2.38	3.08	5.29	4.27	3.40	3.38	4.27	3.29
P_2O_5	0.41	0.58	0.41	0.58	0.58	0.34	0.36	0.18	0.08
SrO	0.13	0.15	0.13	0.27	0.26	-	-	0.14	0.10
BaO	0.16	0.10	0.15	0.27	0.26	-	-	0.22	0.20
Cr_2O_3	b.d.	b.d.	b.d.	b.d.	b.d.	0.00	0.02	b.d.	0.00
NiO	b.d.	b.d.	b.d.	b.d.	b.d.	0.00	0.00	b.d.	0.00
L.O.I.[2]	b.d.	b.d.	b.d.	b.d.	b.d.	0.86	0.82	b.d.	0.79
Tot	99.30	99.05	99.31	99.51	99.52	98.91	100.30	99.73	100.15
Mg#	48.17	49.27	47.80	57.75	59.11	44.10	50.84	44.25	40.54
Na_2O+K_2O	7.14	6.31	7.21	9.47	8.65	7.30	6.97	8.24	9.31
K_2O/Na_2O	0.71	0.62	0.76	1.28	0.98	0.92	0.96	1.08	0.55
Sc	13.9	21.3	14.1	8.9	8.7	10.5	19.7	3.4	2.1
V	103	153	111	82	81	105	125	24	22
Cr	21	36	29	65	61	-	241	16	12
Co	14.8	19.2	15.2	15.1	14.3	13.8	21.5	6.4	4.5
Ni	13	13	11	44	47	13	72	9	b.d.
Cu	9.4	13.2	8.1	22.0	18.4	7.7	45.4	2.0	10.7
Zn	56.9	80.4	58.8	46.1	45.2	71.4	75.7	31.6	27.1

Ga	17.7	21.4	19.0	18.4	17.8	19.4	16.7	16.9	20.6
Cs	0.84	0.97	0.99	0.74	0.59	2.23	2.30	0.63	0.78
Rb	58.15	67.19	65.93	78.38	59.82	88.20	118.73	69.81	69.72
Ba	1279	897	1342	2461	2329	1243	812	1962	1795
Th	3.16	3.47	5.12	4.68	6.71	10.83	11.63	14.86	7.68
U	0.44	0.58	0.50	1.76	1.60	2.63	2.10	0.96	2.27
Nb	13.68	20.07	15.13	12.43	12.61	14.04	14.71	12.25	13.04
Ta	0.57	0.91	0.69	0.55	0.57	0.61	0.98	0.73	0.76
La	43.43	55.48	52.09	76.08	80.82	48.63	41.06	65.34	32.69
Ce	82.14	119.56	97.87	144.20	151.43	100.22	81.80	102.43	60.20
Pb	10.29	8.47	10.81	12.20	7.31	16.73	15.04	13.90	22.26
Pr	10.18	14.99	11.53	16.94	17.83	11.60	9.59	10.56	5.89
Sr	1020	1213	1067	2228	2159	998	577	1194	833
Nd	43.64	67.46	47.77	67.64	70.18	44.37	35.83	37.20	20.46
Zr	304.9	420.7	342.2	279.2	279.6	239.8	299.6	278.0	163.8
Hf	7.113	10.269	8.417	6.227	6.312	5.440	7.493	5.997	4.261
Sm	8.31	12.81	8.83	9.96	10.15	7.38	6.77	5.30	3.52
Eu	2.129	2.646	2.349	2.586	2.611	2.324	1.670	1.390	0.833
Gd	6.87	10.87	6.92	6.88	6.34	5.86	6.27	3.86	2.36
Tb	0.767	1.369	0.925	0.767	0.729	0.681	0.709	0.405	0.329
Dy	4.67	7.78	5.01	3.48	3.46	4.02	4.16	1.91	1.64
Y	22.50	38.88	25.57	17.87	16.06	20.44	24.63	10.33	8.57
Ho	0.789	1.367	0.958	0.648	0.535	0.719	0.819	0.353	0.248
Er	2.279	3.824	2.557	1.678	1.452	2.315	2.225	1.101	0.881
Tm	0.277	0.487	0.343	0.206	0.198	0.346	0.265	0.118	0.122
Yb	1.653	2.950	2.344	1.123	1.240	1.973	1.777	1.039	0.646
Lu	0.304	0.501	0.342	0.192	0.162	0.168	0.257	0.121	0.152

Sample #	**MO-10-314**	**MO-10-315**	**MO-10-431**	**MO-9-220**	**MO-9-219**	**MO-10-365**	**MO-10-317**	**MO-9-242**	**MO-10-362**
Longitude	94°10'2.2"E	94°10'0.5"E	94°14'28.5"E	94°16'50.3"E	94°16'52.6"E	94°17'18.7"E	94°10'36.7"E	94°16'48.0"E	94°20'2.4"E
Latitude	46°40'59.8"N	46°41'13.6"N	46°40'4.4"N	46°36'51.5"N	46°36'53.4"N	46°35'15.5"N	46°41'14.8"N	46°36'52.3"N	46°36'20.2"N
Rock Type[1]	AG2	AG2	AG2	AG2	AG2	AG2	AG2	AG2	BD
SiO_2	70.40	72.49	72.16	60.15	62.29	63.55	64.68	60.92	44.92
TiO_2	0.21	0.13	0.21	0.68	0.25	0.48	0.39	0.28	2.46
Al_2O_3	15.52	15.57	14.53	20.97	21.68	16.20	17.61	21.61	15.44
Fe_2O_3*	1.45	0.99	1.64	-	-	4.54	3.21	-	14.63
FeO^T*	1.30	0.89	1.47	2.45	1.50	4.09	2.89	1.72	13.17
MnO	0.04	0.02	0.04	0.05	0.03	0.10	0.06	0.04	0.21
MgO	0.50	0.49	0.75	1.12	0.64	2.33	1.40	0.84	5.43
CaO	1.51	0.57	0.76	4.46	5.11	4.94	2.76	5.56	8.46
Na_2O	5.65	5.98	3.39	5.26	5.17	3.97	5.86	5.90	2.84
K_2O	3.97	2.98	4.96	3.95	2.76	2.35	3.26	2.55	1.15

APPENDIX C: *Whole Rock Chemistry*

P_2O_5	0.06	0.04	0.05	0.16	0.11	0.18	0.15	0.12	0.41
SrO	0.09	0.05	0.06	0.21	0.19	0.08	0.10	0.16	0.09
BaO	0.18	0.14	0.15	0.27	0.09	0.13	0.16	0.11	0.06
Cr_2O_3	0.00	0.00	0.00	b.d.	b.d.	0.01	0.00	b.d.	0.00
NiO	0.00	0.00	0.00	b.d.	b.d.	0.00	0.00	b.d.	0.00
L.O.I.[2]	0.80	0.78	0.85	b.d.	b.d.	1.24	0.60	b.d.	4.09
Tot	100.38	100.25	99.55	99.73	99.83	100.08	100.26	99.81	100.21
Mg#	40.63	49.58	47.46	44.81	43.07	50.36	46.37	46.68	42.37
Na_2O+K_2O	9.67	9.02	8.47	9.23	7.95	6.42	9.18	8.46	4.21
K_2O/Na_2O	0.70	0.50	1.46	0.75	0.53	0.59	0.56	0.43	0.40
Sc	2.2	1.4	1.9	2.1	2.9	10.3	3.9	3.4	19.6
V	15	10	7	29	24	75	47	21	236
Cr	10	17	9	7	7	35	15	7	40
Co	3.4	2.7	3.4	6.3	5.9	12.1	6.6	4.9	40.2
Ni	b.d.	b.d.	4	6	4	23	4	5	37
Cu	1.9	3.3	3.6	1.1	8.0	1.1	6.6	1.7	35.7
Zn	30.5	8.5	13.2	26.0	10.9	53.3	33.1	19.4	100.6
Ga	19.6	14.3	11.8	18.6	17.9	16.7	19.8	18.5	20.1
Cs	0.42	0.52	1.38	1.29	1.38	0.89	2.50	1.19	0.45
Rb	78.66	47.14	88.17	63.39	77.47	37.64	83.36	44.17	24.67
Ba	1574	1216	1329	2437	988	1170	1419	961	541
Th	10.01	2.36	7.18	5.22	5.88	6.80	8.27	7.24	2.15
U	3.71	1.01	0.97	0.79	0.43	1.16	2.34	1.14	0.55
Nb	11.66	4.62	7.07	13.48	3.49	7.42	11.52	7.86	19.84
Ta	0.62	0.39	0.51	0.73	0.16	0.24	0.68	0.45	1.37
La	29.80	9.74	20.43	41.13	48.98	30.40	35.78	35.45	21.70
Ce	55.42	16.16	33.18	63.58	66.33	58.57	64.80	54.23	45.69
Pb	21.53	13.75	17.62	14.92	11.54	16.54	18.20	14.73	2.61
Pr	5.75	1.59	3.14	6.91	5.72	6.39	6.40	5.33	5.92
Sr	765	433	482	1772	1519	682	862	1321	730
Nd	21.13	5.85	11.10	25.37	18.23	23.73	22.01	19.36	26.53
Zr	141.7	79.2	111.8	267.7	91.7	129.7	173.6	111.9	152.3
Hf	3.694	1.980	3.219	5.775	2.197	3.236	4.141	3.023	4.236
Sm	3.97	0.94	1.61	2.92	2.37	3.27	3.56	3.02	6.57
Eu	0.864	0.289	0.579	1.882	1.607	1.258	0.957	1.849	2.015
Gd	2.89	0.81	1.15	1.99	1.37	3.71	3.03	1.88	6.67
Tb	0.346	0.117	0.166	0.257	0.128	0.425	0.367	0.239	0.783
Dy	1.78	0.68	1.03	1.02	0.92	2.06	2.07	1.27	4.55
Y	8.47	3.64	5.27	5.66	4.68	12.20	11.30	7.85	23.53
Ho	0.282	0.117	0.158	0.177	0.118	0.570	0.363	0.270	0.995
Er	0.731	0.315	0.429	0.459	0.413	1.666	1.075	0.832	2.818
Tm	0.098	0.081	0.054	0.068	0.060	0.253	0.156	0.098	0.332
Yb	0.576	0.382	0.301	0.379	0.486	b.d.	1.394	0.697	1.994

Lu	0.092	0.055	0.048	0.080	0.096	0.137	0.195	0.132	0.326

Sample #	**MO-9-238**	**MO-11-74**	**MO-10-397**	**MO-11-50**	**MO-11-75**	**MO-9-245**	**MO-11-99**	**MO-10-326**	**MO-10-360**
Longitude	94°16'48.1"E	94°13'42"E	94°14'13.77"E	94°36'26.9"E	94°13'42"E	94°15'21.9"E	94°12'7.3"E	94°12'6"E	94°11'52.2"E
Latitude	46°36'49.8"N	46°38'52.2"N	46°38'58"N	46°25'55.2"N	46°38'52.2"N	46°38'55.5"N	46°39'32.6"N	46°40'17.9"N	46°41'9.8"N
Rock Type[1]	BD	BD	BD	BD	BD	BD	PBD	BD	BD
SiO_2	47.39	46.53	45.05	48.17	48.24	49.73	50.01	51.41	48.90
TiO_2	1.96	1.60	0.61	2.29	1.58	1.37	0.97	0.44	1.25
Al_2O_3	16.53	15.78	17.65	14.75	17.25	13.53	14.67	4.35	15.16
Fe_2O_3*	-	10.23	6.25	12.51	9.62	-	8.00	7.29	8.53
FeO^T*	10.43	9.21	5.62	11.26	8.65	9.62	7.20	6.56	7.67
MnO	0.19	0.18	0.41	0.20	0.17	0.25	0.14	0.21	0.16
MgO	6.73	6.10	15.09	5.63	4.63	7.63	8.83	13.20	6.47
CaO	9.98	8.16	1.18	8.37	7.05	10.12	7.57	20.10	6.56
Na_2O	3.84	3.97	0.67	3.90	4.00	2.58	3.46	0.88	4.11
K_2O	1.03	2.86	5.98	1.39	3.48	2.98	2.28	0.81	2.33
P_2O_5	0.58	1.01	0.44	0.75	1.06	0.88	0.44	0.15	0.54
SrO	0.13	b.d.	0.12	b.d.	b.d.	0.12	b.d.	0.06	0.10
BaO	0.06	b.d.	0.53	b.d.	b.d.	0.10	b.d.	0.12	0.07
Cr_2O_3	b.d.	0.01	0.00	0.00	0.01	b.d.	0.07	0.09	0.04
NiO	b.d.	0.01	0.00	0.00	0.01	b.d.	0.03	0.02	0.02
L.O.I.[2]	b.d.	3.30	6.34	2.00	2.88	b.d.	3.54	1.02	6.16
Tot	98.84	99.74	100.31	99.99	99.96	98.93	100.00	100.15	100.41
Mg#	53.51	54.17	82.71	47.15	48.82	58.58	68.62	78.20	60.05
Na_2O+K_2O	4.93	7.07	7.13	5.39	7.71	5.63	5.95	1.72	6.90
K_2O/Na_2O	0.27	0.72	8.92	0.36	0.87	1.15	0.66	0.92	0.57
Sc	28.2	16.9	5.4	30.1	12.2	27.2	19.5	52.5	16.2
V	219	172	22	276	165	209	145	168	119
Cr	24	100	14	47	54	245	470	595	266
Co	33.2	27.9	10.3	32.4	22.4	34.3	33.1	31.8	28.6
Ni	50	65	b.d.	26	35	108	182	125	137
Cu	33.9	21.8	13.9	32.5	20.2	552.2	37.2	2.6	18.7
Zn	60.5	82.1	90.0	80.7	83.8	80.2	61.2	39.5	76.8
Ga	14.7	17.9	19.7	17.9	19.4	17.1	16.1	7.2	17.4
Cs	0.59	0.44	3.53	0.75	0.43	1.59	0.21	0.47	2.82
Rb	36.88	45.87	143.52	49.03	56.57	91.54	57.98	26.28	103.59
Ba	452	1547	4756	348	1868	914	860	1063	646
Th	0.77	5.28	12.18	1.36	6.29	3.71	4.44	4.07	13.14
U	0.28	1.38	2.90	0.52	1.47	1.30	1.04	1.14	5.16
Nb	6.52	19.95	12.44	9.60	22.96	15.85	8.31	1.45	12.71
Ta	0.40	1.06	0.87	0.35	1.03	0.79	0.52	0.13	0.83
La	18.21	73.18	60.96	23.26	78.58	56.29	35.84	20.67	46.06

Ce	44.30	154.30	121.79	57.63	170.50	122.05	75.22	56.65	88.45
Pb	2.84	9.03	36.29	3.62	13.12	6.56	11.08	1.23	16.96
Pr	6.47	18.02	12.83	7.90	18.79	15.29	8.64	7.91	10.56
Sr	949	1574	995	765	1870	962	930	467	834
Nd	31.19	71.94	47.45	36.84	72.60	67.34	33.84	36.51	46.22
Zr	142.8	222.6	222.9	177.1	241.6	220.3	119.2	88.8	203.5
Hf	3.715	4.795	5.667	4.137	5.200	5.363	2.876	2.555	5.675
Sm	6.77	12.46	8.58	7.97	11.85	13.22	5.40	9.33	8.69
Eu	1.950	3.041	1.861	2.478	3.022	2.224	1.566	2.205	2.135
Gd	6.56	8.70	5.01	8.53	8.85	10.96	4.71	7.41	7.58
Tb	0.817	1.023	0.669	1.115	0.910	1.391	0.514	0.948	0.885
Dy	5.78	5.50	3.80	7.18	5.22	6.97	3.21	4.58	5.05
Y	31.07	27.55	19.46	40.33	26.15	35.37	14.59	19.66	23.38
Ho	1.085	1.044	0.689	1.493	0.888	1.400	0.494	0.805	0.890
Er	3.668	2.742	1.827	4.441	3.030	3.511	1.516	1.942	2.492
Tm	0.509	0.387	0.306	0.597	0.357	0.428	0.168	0.219	0.288
Yb	3.119	2.248	1.991	4.311	2.231	2.628	1.255	1.380	1.686
Lu	0.484	0.360	0.316	0.593	0.336	0.460	0.236	0.225	0.372

Sample #	**MO-11-24**	**MO-9-217**	**MO-10-376**	**MO-9-218**	**MO-10-332**	**MO-10-331**	**MO-12-10**	**MO-12-14**	**MO-9-222**
Longitude	94°14'34.4"E	94°16'52.3"E	94°14'30"E	94°16'52.3"E	94°12'6"E	94°12'6"E	94°12'36"E	94°17'50.8"E	94°16'51.3"E
Latitude	46°39'13.1"N	46°36'52.7"N	46°39'56.6"N	46°36'52.7"N	46°40'17.9"N	46°40'17.9"N	46°39'47"N	46°38'3.8"N	46°36'52.3"N
Rock Type[1]	BD	BD	BD	BD	BD	BD	BD	BD	ID
SiO_2	51.61	52.18	50.70	53.24	52.86	45.05	45.71	46.25	54.53
TiO_2	1.18	0.96	0.87	0.80	1.00	1.72	1.43	1.98	0.97
Al_2O_3	14.16	18.95	16.73	19.59	16.14	13.98	14.18	16.51	17.65
Fe_2O_3*	8.14	-	8.45	-	7.90	13.40	9.87	11.97	-
FeO^T*	7.32	8.61	7.60	8.18	7.11	12.06	0.00	0.00	7.16
MnO	0.19	0.29	0.14	0.25	0.14	0.26	0.19	0.18	0.17
MgO	6.99	1.75	5.63	1.42	5.59	6.47	8.05	5.46	3.77
CaO	8.11	7.14	5.39	6.21	6.29	11.79	12.27	9.16	6.50
Na_2O	2.98	3.40	3.74	4.20	3.78	2.48	3.00	3.46	4.50
K_2O	4.16	4.31	3.35	4.04	4.33	2.54	1.69	2.50	3.06
P_2O_5	0.82	0.38	0.44	0.34	0.40	1.02	1.07	1.20	0.59
SrO	b.d.	0.49	0.09	0.39	0.18	0.31	-	-	0.15
BaO	b.d.	0.59	0.12	0.45	0.19	0.74	-	-	0.14
Cr_2O_3	0.04	b.d.	0.01	b.d.	0.02	0.01	0.04	0.01	b.d.
NiO	0.02	b.d.	0.00	b.d.	0.00	0.00	0.01	0.01	b.d.
L.O.I.[2]	1.20	b.d.	4.39	b.d.	1.40	1.23	2.41	0.97	b.d.
Tot	99.59	99.04	100.04	99.09	100.22	101.00	99.92	99.66	99.21
Mg#	62.98	26.66	56.88	23.61	58.36	48.87	61.80	47.50	48.42
Na_2O+K_2O	7.26	7.79	7.48	8.31	8.27	5.10	4.86	6.12	7.62

APPENDIX C: *Whole Rock Chemistry*

K_2O/Na_2O	1.40	1.27	0.90	0.96	1.14	1.02	0.56	0.72	0.68
Sc	14.9	3.0	20.2	2.1	18.8	11.7	22.4	16.2	17.0
V	141	61	179	45	148	81	197	186	179
Cr	267	6	41	10	132	b.d.	271	74	7
Co	24.8	13.4	25.8	12.6	24.3	18.2	38.1	33.7	18.2
Ni	124	5	15	7	28	b.d.	120	45	6
Cu	257.8	16.1	16.0	4.5	19.5	28.2	79.5	36.1	43.6
Zn	74.5	106.2	76.5	104.1	41.8	24.5	55.6	93.6	53.3
Ga	18.9	18.2	17.2	18.4	17.3	20.1	17.2	19.4	16.7
Cs	1.90	1.20	0.21	0.84	2.42	0.61	2.04	1.05	0.66
Rb	126.43	78.55	63.31	68.35	130.27	93.24	56.29	48.60	59.70
Ba	1361	5298	1076	4002	1736	6674	507	1161	1283
Th	6.22	8.62	4.45	10.12	13.88	18.75	5.57	6.29	4.56
U	1.66	1.08	1.83	1.38	3.94	4.63	1.29	1.54	1.38
Nb	20.14	27.75	6.30	24.11	14.70	2.46	17.69	24.87	10.48
Ta	0.79	1.14	0.27	1.33	0.90	0.09	0.81	1.10	0.52
La	72.35	105.53	39.03	88.00	49.33	56.41	78.36	72.48	45.93
Ce	153.10	217.70	94.66	181.75	104.01	110.00	166.80	161.39	89.37
Pb	12.34	12.01	4.00	12.63	6.47	17.14	3.76	9.73	11.00
Pr	17.57	25.37	12.21	21.35	11.55	12.31	19.79	19.31	10.94
Sr	953	3857	782	3112	1540	2584	2242	1452	1260
Nd	68.99	97.89	51.74	85.45	46.99	48.17	75.27	74.09	46.81
Zr	283.1	209.3	128.8	169.3	208.4	219.9	192.0	230.7	211.5
Hf	6.825	4.626	2.969	4.295	4.992	5.241	3.977	5.594	5.250
Sm	11.66	15.15	9.09	13.63	8.65	8.94	11.34	12.33	8.97
Eu	2.246	3.796	2.664	3.557	2.204	3.816	3.346	3.075	2.427
Gd	8.60	10.78	7.25	9.14	7.51	6.82	8.41	9.84	7.67
Tb	1.034	1.303	0.829	1.141	0.953	0.853	1.014	1.197	1.025
Dy	5.23	6.45	4.28	5.97	4.87	3.64	5.31	6.07	5.23
Y	27.85	34.00	21.27	28.95	23.30	19.60	24.78	28.02	26.49
Ho	0.923	1.175	0.769	0.927	0.848	0.680	0.992	1.134	0.915
Er	2.620	3.115	2.274	2.813	2.407	1.958	2.540	2.333	2.660
Tm	0.323	0.402	0.285	0.320	0.299	0.205	0.316	0.327	0.327
Yb	2.045	2.840	2.051	2.389	1.933	1.813	2.203	2.340	2.466
Lu	0.382	0.408	0.351	0.367	0.254	0.239	0.302	0.355	0.377

Sample #	**MO-9-246**	**MO-9-249**	**MO-11-17**	**MO-10-393**	**MO-9-216**	**MO-10-300a**	**MO-10-300b**	**MO-9-264**	**MO-11-20**
Longitude	94°15'23.0"E	94°15'16.1"E	94°14'28.9"E	94°14'16.8"E	94°16'52.3"E	94°9'57.1"E	94°9'57.1"E	94°16'12.0"E	94°14'30.5"E
Latitude	46°38'55.6"N	46°38'50.1"N	46°39'11.1"N	46°39'23"N	46°36'52.7"N	46°41'5.4"N	46°41'5.4"N	46°37'44.5"N	46°39'11.7"N
Rock Type[1]	ID	ID	ID	ID	ID	ID	ID	ID	ID
SiO_2	54.86	56.27	53.82	53.75	57.22	57.14	56.86	57.33	54.68
TiO_2	0.99	1.33	0.80	0.81	0.63	0.62	0.64	1.14	0.68

APPENDIX C: *Whole Rock Chemistry*

Al_2O_3	13.94	17.45	16.41	16.41	19.06	14.28	14.00	14.73	17.11
Fe_2O_3*	-	-	6.87	6.81	-	6.27	6.65	-	6.31
FeO^T*	7.02	6.46	6.18	6.13	5.68	5.65	5.98	7.21	5.68
MnO	0.17	0.13	0.14	0.14	0.19	0.12	0.14	0.13	0.13
MgO	5.63	3.22	3.54	3.69	1.02	6.25	6.91	5.66	2.54
CaO	9.74	5.83	5.84	5.58	4.39	5.04	5.36	6.90	5.50
Na_2O	3.10	5.16	3.32	3.20	3.94	4.32	4.14	3.66	3.47
K_2O	3.12	2.28	2.98	3.21	6.24	4.32	3.95	1.91	3.04
P_2O_5	0.35	0.84	0.41	0.41	0.25	0.18	0.18	0.34	0.44
SrO	0.12	0.17	b.d.	0.09	0.32	0.05	0.07	0.10	b.d.
BaO	0.17	0.13	b.d.	0.14	0.42	0.09	0.09	0.09	b.d.
Cr_2O_3	b.d.	b.d.	0.01	0.01	b.d.	0.06	0.07	b.d.	0.00
NiO	b.d.	b.d.	0.00	0.00	b.d.	0.01	0.01	b.d.	0.00
L.O.I.[2]	b.d.	b.d.	5.70	5.71	b.d.	1.46	1.39	b.d.	5.68
Tot	99.22	99.28	99.84	99.98	99.37	100.22	100.47	99.20	99.60
Mg#	58.85	47.02	50.51	51.76	24.22	66.39	67.32	58.34	44.33
Na_2O+K_2O	6.27	7.50	6.68	6.86	10.24	8.80	8.23	5.61	6.94
K_2O/Na_2O	1.01	0.44	0.90	1.00	1.58	1.00	0.95	0.52	0.87
Sc	23.0	61.7	11.3	11.4	2.2	17.0	19.7	16.5	8.0
V	154	195	79	76	34	117	127	130	37
Cr	268	1081	64	53	6	357	438	203	35
Co	21.6	59.2	15.5	15.9	10.4	22.1	24.9	29.1	11.8
Ni	41	253	25	9	7	72	78	109	9
Cu	8.6	3.9	21.6	10.0	9.6	22.6	2.9	27.4	21.3
Zn	54.3	45.6	78.0	75.8	71.0	36.3	38.4	55.6	65.1
Ga	14.7	4.1	18.9	17.4	16.8	13.2	13.2	16.8	19.3
Cs	0.82	0.21	1.72	1.16	3.58	0.44	0.54	0.87	1.33
Rb	60.63	1.63	82.11	79.12	123.69	83.89	71.53	40.51	84.60
Ba	1465	24	1140	1218	3799	811	837	805	1122
Th	4.74	0.32	8.75	8.69	10.33	5.66	5.23	6.15	10.93
U	1.09	1.15	1.90	2.10	1.96	1.46	1.30	1.25	1.77
Nb	8.24	0.20	10.79	10.23	29.27	9.37	9.96	7.58	11.04
Ta	0.58	0.03	0.54	0.61	1.29	0.72	0.65	0.48	0.75
La	30.22	3.09	45.85	47.61	78.41	22.87	21.78	36.35	54.74
Ce	58.60	17.06	99.84	97.90	165.18	44.90	42.92	68.53	101.01
Pb	28.43	0.34	14.24	16.74	17.01	7.39	5.63	5.63	9.36
Pr	7.24	2.12	10.44	10.70	18.52	4.77	4.64	7.90	11.39
Sr	1029	113	765	756	2665	423	604	861	873
Nd	30.38	12.70	41.67	40.84	68.97	18.28	18.13	33.00	44.20
Zr	152.1	29.1	174.5	172.7	141.0	126.4	120.2	123.0	213.7
Hf	3.952	1.648	4.306	4.480	3.351	3.541	3.231	3.587	5.173
Sm	6.40	3.94	6.72	6.98	10.48	3.57	3.33	5.64	7.80
Eu	1.745	0.989	1.647	1.751	3.069	0.950	0.957	1.609	1.830

Gd	5.66	3.98	4.35	4.97	7.37	3.49	3.12	5.01	5.50
Tb	0.761	0.505	0.606	0.607	0.833	0.466	0.463	0.644	0.728
Dy	4.62	2.76	3.25	4.09	4.38	3.00	3.11	3.91	3.96
Y	22.48	17.02	18.60	18.40	24.45	17.08	17.10	20.36	21.20
Ho	0.812	0.501	0.614	0.656	0.785	0.609	0.657	0.738	0.694
Er	2.286	1.235	1.981	1.901	2.055	1.763	1.787	2.043	2.274
Tm	0.316	0.154	0.217	0.232	0.290	0.219	0.248	0.227	0.250
Yb	2.217	0.998	1.758	1.685	1.890	2.096	1.659	1.413	1.890
Lu	0.325	0.138	0.269	0.207	0.282	0.315	0.289	0.239	0.306

Sample #	**MO-10-331**	**MO-9-240a**	**MO-9-212**	**MO-11-94**	**MO-11-95**	**MO-11-96**	**MO-11-71**	**MO-9-240b**	**MO-9-215**
Longitude	94°12'6"E	94°16'52.4"E	94°16'52.1"E	94°11'37.1"E	94°11'33.8"E	94°11'42.4"E	94°13'56.9"E	94°16'52.4"E	94°16'52.4"E
Latitude	46°40'17.9"N	46°36'52.3"N	46°36'52.2"N	46°39'49.1"N	46°39'7.7"N	46°39'7.1"N	46°38'29.7"N	46°36'52.3"N	46°36'52.3"N
Rock Type[1]	ID	ID	ID	ID	ID	ID	FD	FD	FD
SiO_2	61.23	62.95	58.88	54.10	57.63	57.49	69.75	69.96	73.76
TiO_2	0.15	0.25	0.58	1.01	0.55	0.97	0.31	0.20	0.22
Al_2O_3	16.59	19.43	19.07	17.75	14.53	15.55	15.69	16.35	14.22
Fe_2O_3*	2.45	-	-	8.37	5.20	6.35	1.44	-	-
FeO^T*	2.20	2.37	4.23	0.00	0.00	0.00	1.30	0.79	1.48
MnO	0.07	0.07	0.13	0.16	0.12	0.10	0.02	0.03	0.05
MgO	2.17	1.16	1.00	4.86	5.13	5.28	0.64	0.34	0.46
CaO	4.98	1.13	4.25	6.38	4.47	5.54	1.56	0.64	1.97
Na_2O	4.50	6.04	4.23	4.36	4.20	3.63	4.45	4.91	3.81
K_2O	6.55	6.02	6.22	2.27	3.23	2.64	4.88	6.42	3.68
P_2O_5	0.26	0.07	0.25	0.55	0.21	0.28	0.17	0.07	0.07
SrO	0.17	0.04	0.30	-	-	-	b.d.	0.03	0.05
BaO	0.17	0.20	0.40	-	-	-	b.d.	0.18	0.05
Cr_2O_3	0.00	b.d.	b.d.	0.01	0.03	0.03	0.00	b.d.	b.d.
NiO	0.00	b.d.	b.d.	0.01	0.01	0.01	0.00	b.d.	b.d.
L.O.I.[2]	1.04	b.d.	b.d.	0.23	4.26	1.92	0.87	b.d.	b.d.
Tot	100.32	99.74	99.53	100.05	99.58	99.79	99.78	99.91	99.84
Mg#	63.73	46.62	29.56	53.52	66.19	62.24	46.98	43.13	35.60
Na_2O+K_2O	11.15	12.09	10.50	6.70	7.84	6.45	9.44	11.35	7.51
K_2O/Na_2O	1.46	1.00	1.47	0.52	0.77	0.73	1.10	1.31	0.97
Sc	21.2	1.8	2.4	15.2	15.2	18.2	2.3	1.4	3.0
V	299	32	30	143	127	115	18	13	11
Cr	37	11	7	49	191	188	33	10	8
Co	40.1	7.4	8.0	23.3	19.7	23.6	4.8	4.7	3.6
Ni	37	10	4	40	74	101	14	8	5
Cu	40.1	0.6	6.3	8.9	33.4	35.9	5.3	1.2	2.5
Zn	79.4	26.3	44.0	419.0	39.6	49.7	10.9	7.1	16.8
Ga	21.7	16.6	14.3	17.5	12.5	15.7	15.7	10.9	13.5

APPENDIX C: *Whole Rock Chemistry*

Cs	0.66	0.71	1.04	0.47	0.79	1.01	1.65	0.94	0.85
Rb	57.84	172.37	101.05	45.56	73.88	87.31	111.63	216.11	101.80
Ba	1518	1928	3498	1198	1042	908	1289	1811	479
Th	8.48	19.28	5.63	3.81	9.87	9.92	16.80	21.56	17.15
U	2.11	3.96	1.26	1.08	3.87	3.05	3.96	3.54	3.03
Nb	17.14	8.74	17.87	8.41	5.20	11.99	14.45	7.62	12.67
Ta	0.77	1.44	1.11	0.36	0.35	0.73	1.88	1.06	1.27
La	94.24	23.98	66.15	45.38	28.18	36.75	61.13	31.57	25.70
Ce	224.27	55.19	121.02	95.75	56.79	74.57	107.77	62.36	50.73
Pb	5.01	5.02	17.24	263.46	38.66	14.92	12.26	5.86	12.95
Pr	26.72	5.35	13.71	11.54	6.52	8.84	10.92	6.41	5.42
Sr	1415	384	2431	1225	511	809	828	268	383
Nd	112.89	19.08	54.37	45.84	23.93	32.79	35.83	21.47	19.49
Zr	298.4	131.8	83.8	164.2	123.5	219.8	222.9	152.7	125.1
Hf	7.823	4.328	2.208	3.268	2.536	5.730	5.088	4.269	4.029
Sm	23.27	3.38	8.92	7.75	4.78	6.44	5.71	3.64	3.51
Eu	5.662	1.039	3.032	2.390	1.331	1.460	0.936	0.568	0.735
Gd	17.98	2.80	5.95	6.86	3.88	4.88	4.17	2.96	2.57
Tb	2.106	0.426	0.746	0.754	0.525	0.680	0.525	0.396	0.471
Dy	10.89	2.25	3.83	4.10	2.88	4.08	2.49	2.20	2.47
Y	45.65	12.68	21.49	22.03	17.10	22.72	14.63	11.71	15.34
Ho	1.624	0.469	0.791	0.780	0.635	0.907	0.502	0.418	0.471
Er	4.506	1.197	1.840	2.318	2.120	2.392	1.915	1.098	1.556
Tm	0.464	0.208	0.284	0.318	0.271	0.409	0.134	0.149	0.196
Yb	3.234	1.333	1.841	1.705	1.576	2.570	1.082	1.330	1.817
Lu	0.416	0.246	0.291	0.320	0.251	0.362	0.071	0.224	0.262

Sample #	**MO-9-211**	**MO-11-16**	**MO-9-214**	**MO-9-231**	**MO-11-25**	**MO-11-54**	**MO-11-11**	**MO-11-55**	**MO-10-337**
Longitude	94°16'51.0"E	94°14'28.9"E	94°16'52.4"E	94°16'54.1"E	94°14'34.4"E	94°36'18.7"E	94°14'26.7"E	94°35'58.6"E	94°12'9"E
Latitude	46°36'52"N	46°39'11.1"N	46°36'52.3"N	46°36'53.7"N	46°39'13.1"N	46°25'38.9"N	46°39'10.7"N	46°24'29.9"N	46°40'17.5"N
Rock Type[1]	FD	FD	FD	FD	FD	FD	FD	FD	FD
SiO_2	75.15	74.58	62.86	76.55	67.07	68.25	71.84	75.43	72.38
TiO_2	0.08	0.11	0.18	0.06	0.24	0.11	0.12	0.17	0.15
Al_2O_3	13.90	13.72	19.65	13.17	16.43	17.44	14.75	13.07	14.50
Fe_2O_3*	-	1.05	-	-	2.08	0.67	0.71	1.19	0.97
FeO^T*	0.66	0.95	2.30	0.45	1.87	0.61	0.64	1.07	0.87
MnO	0.04	0.01	0.04	0.02	0.03	0.01	0.01	0.02	0.03
MgO	0.07	0.25	0.18	0.05	0.82	0.23	0.28	0.26	0.84
CaO	0.80	0.69	1.53	0.67	2.02	1.86	1.04	0.67	2.33
Na_2O	4.04	3.64	4.44	3.61	4.25	4.46	3.99	3.55	5.91
K_2O	5.09	5.34	8.30	5.28	5.13	5.97	5.53	4.99	1.68
P_2O_5	0.01	0.03	0.05	0.01	0.11	0.04	0.03	0.04	0.06

SrO	0.02	b.d.	0.07	0.03	b.d.	b.d.	b.d.	b.d.	0.07
BaO	0.06	b.d.	0.14	0.06	b.d.	b.d.	b.d.	b.d.	0.04
Cr_2O_3	b.d.	0.00	b.d.	b.d.	0.00	0.00	0.00	0.00	0.00
NiO	b.d.	0.00	b.d.	b.d.	0.00	0.00	0.00	0.00	0.00
L.O.I.[2]	b.d.	0.72	b.d.	b.d.	0.79	0.47	0.86	0.55	1.09
Tot	99.93	100.15	99.74	99.95	98.97	99.52	99.16	99.94	100.04
Mg#	15.30	32.21	11.94	16.87	43.89	40.47	43.97	29.99	63.23
Na_2O+K_2O	9.13	9.03	12.77	8.89	9.55	10.53	9.69	8.59	7.67
K_2O/Na_2O	1.26	1.47	1.87	1.46	1.21	1.34	1.39	1.40	0.28
Sc	1.3	1.3	1.2	1.1	3.6	1.6	1.9	1.2	2.8
V	1	9	10	2	27	9	7	8	10
Cr	7	25	b.d.	8	38	31	27	19	14
Co	5.2	1.1	4.0	2.6	3.4	1.1	1.8	1.2	3.8
Ni	11	16	6	8	11	16	11	10	6
Cu	2.3	43.5	8.8	1.0	41.1	26.3	7.2	31.4	4.8
Zn	11.9	5.3	19.6	8.1	19.7	6.1	4.1	10.2	12.0
Ga	15.8	12.0	17.9	15.7	16.2	13.9	15.2	11.7	15.9
Cs	1.32	1.27	0.68	3.22	1.39	1.33	0.83	2.28	1.46
Rb	173.14	99.88	98.04	200.19	97.62	130.05	100.04	153.05	45.66
Ba	576	678	1284	577	2016	3560	1795	411	385
Th	26.09	16.37	36.05	13.96	13.80	11.40	16.30	28.15	9.85
U	3.40	2.81	2.65	1.80	2.56	1.48	1.96	4.88	2.51
Nb	23.49	6.94	2.15	8.91	8.22	2.15	6.47	12.92	9.66
Ta	1.71	1.30	0.11	0.62	0.82	0.35	0.87	1.88	0.81
La	15.72	29.72	76.51	12.84	57.06	34.60	38.33	21.15	9.53
Ce	31.73	49.03	117.79	22.47	88.06	54.14	55.08	35.84	26.24
Pb	32.95	19.77	29.71	29.55	21.90	18.34	14.53	16.51	16.12
Pr	3.00	4.19	10.73	2.14	8.33	4.69	4.47	3.41	3.37
Sr	215	314	619	243	1022	868	631	192	558
Nd	10.80	15.26	33.11	7.22	27.43	14.16	14.77	9.93	13.20
Zr	119.2	100.9	605.0	52.4	174.6	59.4	95.7	85.6	84.8
Hf	4.390	3.377	10.348	1.720	4.686	1.659	3.310	2.905	2.494
Sm	1.86	2.49	3.54	1.17	4.18	2.16	1.85	1.45	2.57
Eu	0.459	0.527	1.793	0.381	1.415	0.842	0.718	0.460	0.727
Gd	1.49	1.41	2.00	0.67	2.89	1.37	1.29	1.35	1.83
Tb	0.211	0.185	0.248	0.129	0.322	0.169	0.158	0.215	0.244
Dy	1.21	1.20	1.29	0.67	2.05	b.d.	1.00	1.14	1.27
Y	7.88	8.09	8.34	3.88	9.99	2.29	4.68	6.89	6.85
Ho	0.311	0.246	0.323	0.081	0.324	0.143	0.161	0.184	0.231
Er	0.712	0.961	0.959	0.360	0.848	0.342	0.623	0.892	0.633
Tm	0.140	0.122	0.159	0.045	0.153	b.d.	0.152	0.078	0.075
Yb	0.971	0.970	1.059	0.459	0.801	b.d.	1.084	0.523	0.631
Lu	0.186	0.178	0.219	0.097	0.140	b.d.	0.145	0.227	0.085

APPENDIX C: *Whole Rock Chemistry*

Sample #	**MO-12-15**	**MO-11-19**	**MO-9-263**	**MO-9-230**	**MO-9-224**	**MO-9-225**	**MO-9-226**	**MO-9-228**	**MO-12-38**
Longitude	94°17'50.8"E	94°14'29.8"E	94°16'10.3"E	94°16'53.7"E	94°16'51.0"E	94°16'47.9"E	94°16'47.9"E	94°16'49.6"E	94°41'45"E
Latitude	46°38'3.8"N	46°39'11.7"N	46°37'46.1"N	46°36'51.6"N	46°36'53.6"N	46°36'51.7"N	46°36'51.7"N	46°36'50.4"N	46°24'40.7"N
Rock Type[1]	FD	PBD	PBD	PBD	PBD	PBD	PBD	PBD	GS
SiO_2	71.70	48.69	50.10	50.29	51.54	52.27	52.77	52.92	71.60
TiO_2	0.30	1.25	1.23	0.61	0.87	0.90	0.90	0.79	0.23
Al_2O_3	14.54	14.09	12.68	14.17	12.19	13.19	12.59	13.96	15.06
Fe_2O_3*	1.93	9.27	-	-	-	-	-	-	1.81
FeO^T*	0.00	8.34	8.38	7.48	8.29	8.66	8.41	6.83	0.00
MnO	0.04	0.17	0.18	0.19	0.21	0.20	0.22	0.18	0.06
MgO	0.64	9.60	12.01	11.92	10.63	8.86	8.52	10.51	0.49
CaO	2.13	9.45	10.48	10.63	10.55	10.00	9.76	9.39	1.78
Na_2O	3.90	2.60	1.89	1.82	2.33	2.84	2.44	2.13	4.14
K_2O	4.03	2.76	1.41	1.63	1.85	1.47	2.80	2.13	4.22
P_2O_5	0.10	0.66	0.53	0.25	0.44	0.43	0.41	0.26	0.08
SrO	-	b.d.	0.10	0.09	0.07	0.12	0.11	0.08	-
BaO	-	b.d.	0.07	0.08	0.10	0.10	0.13	0.06	-
Cr_2O_3	0.00	0.08	b.d.	b.d.	b.d.	b.d.	b.d.	b.d.	0.00
NiO	0.00	0.02	b.d.	b.d.	b.d.	b.d.	b.d.	b.d.	0.00
L.O.I.[2]	0.61	1.49	b.d.	b.d.	b.d.	b.d.	b.d.	b.d.	0.89
Tot	99.91	100.12	99.07	99.17	99.08	99.04	99.07	99.24	100.36
Mg#	39.68	67.24	71.87	73.96	69.57	64.57	64.36	73.28	35.04
Na_2O+K_2O	8.00	5.43	3.34	3.48	4.22	4.35	5.28	4.29	8.42
K_2O/Na_2O	1.03	1.06	0.74	0.90	0.79	0.52	1.15	1.00	1.02
Sc	4.1	22.8	25.6	29.3	33.7	28.0	27.0	23.9	2.6
V	21	197	152	188	191	198	183	132	12
Cr	24	520	643	642	661	405	390	643	-
Co	5.0	32.0	42.1	37.8	31.8	28.3	28.0	31.8	3.4
Ni	-	144	277	171	60	37	35	166	-
Cu	2.8	16.9	39.9	13.7	40.6	33.9	22.2	3.2	5.1
Zn	18.2	66.9	62.1	64.1	58.0	64.9	70.2	57.5	26.9
Ga	14.1	17.3	13.4	12.5	12.6	13.7	13.2	12.9	15.5
Cs	1.59	1.39	0.75	2.34	0.38	0.49	0.66	1.76	1.65
Rb	105.12	75.55	30.57	61.85	38.41	21.79	49.84	76.48	137.27
Ba	817	1007	684	729	890	870	1127	561	969
Th	24.47	7.48	6.75	7.93	5.00	2.17	2.34	7.44	15.49
U	4.00	1.89	1.26	1.75	1.50	0.98	1.84	1.82	1.90
Nb	11.23	16.30	15.16	3.25	6.93	6.09	9.75	8.32	16.11
Ta	0.72	0.99	0.93	0.19	0.48	0.28	0.44	0.53	2.07
La	44.45	59.00	45.79	38.28	30.42	26.83	30.17	29.79	33.38
Ce	81.84	123.97	90.68	76.98	63.08	54.89	67.27	62.00	56.30

Pb	14.59	7.86	6.52	2.39	5.98	6.82	7.14	4.86	19.05
Pr	8.57	14.80	11.09	9.06	8.31	7.20	8.73	7.14	5.69
Sr	533	1181	785	772	598	995	857	614	444
Nd	26.60	59.94	45.64	38.95	37.57	32.24	40.04	28.28	18.42
Zr	152.8	263.9	188.0	89.9	128.6	147.2	132.7	124.7	153.9
Hf	4.703	6.039	4.555	2.134	3.521	3.493	3.169	3.266	4.292
Sm	3.55	10.54	8.59	7.18	8.07	6.77	8.53	5.25	3.55
Eu	0.711	2.643	1.975	1.756	1.854	1.763	2.116	1.405	0.799
Gd	2.32	7.74	6.93	5.68	7.65	5.88	6.86	4.68	2.08
Tb	0.351	1.029	0.865	0.717	0.906	0.793	0.907	0.626	0.269
Dy	1.79	5.11	4.77	3.84	5.25	4.45	5.44	3.59	1.61
Y	10.90	26.06	24.83	19.63	27.06	23.61	27.45	19.65	10.25
Ho	0.404	0.928	0.902	0.761	0.995	0.851	0.935	0.739	0.353
Er	0.683	2.223	2.740	2.029	2.714	2.432	2.939	2.190	1.156
Tm	0.190	0.298	0.330	0.312	0.338	0.339	0.447	0.237	0.155
Yb	1.346	2.008	2.259	1.869	2.664	2.126	2.430	1.519	-
Lu	0.173	0.312	0.307	0.274	0.345	0.317	0.408	0.256	0.167

Sample #	**MO-10-318**	**MO-10-314**	**MO-10-315**	**MO-10-431**	**MO-10-365**	**MO-10-317**
Longitude	94°10'36.7"E	94°10'2.2"E	94°10'0.5"E	94°14'28.5"E	94°17'18.7"E	94°10'36.7"E
Latitude	46°41'14.8"	46°40'59.8"N	46°41'13.6"N	46°40'4.4"N	46°35'15.5"N	46°41'14.8"N
Rock Type[1]	GS	GS	GS	GS	GS	GS
SiO_2	68.34	70.40	72.49	72.16	63.55	64.68
TiO_2	0.27	0.21	0.13	0.21	0.48	0.39
Al_2O_3	17.01	15.52	15.57	14.53	16.20	17.61
Fe_2O_3*	2.00	1.45	0.99	1.64	4.54	3.21
FeO^T*	1.80	1.30	0.89	1.47	4.09	2.89
MnO	0.03	0.04	0.02	0.04	0.10	0.06
MgO	0.69	0.50	0.49	0.75	2.33	1.40
CaO	1.42	1.51	0.57	0.76	4.94	2.76
Na_2O	5.94	5.65	5.98	3.39	3.97	5.86
K_2O	3.29	3.97	2.98	4.96	2.35	3.26
P_2O_5	0.08	0.06	0.04	0.05	0.18	0.15
SrO	0.10	0.09	0.05	0.06	0.08	0.10
BaO	0.20	0.18	0.14	0.15	0.13	0.16
Cr_2O_3	0.00	0.00	0.00	0.00	0.01	0.00
NiO	0.00	0.00	0.00	0.00	0.00	0.00
L.O.I.[2]	0.79	0.80	0.78	0.85	1.24	0.60
Tot	99.95	100.24	100.15	99.39	99.62	99.94
Mg#	40.54	40.63	49.58	47.46	50.36	46.37
Na_2O+K_2O	9.31	9.67	9.02	8.47	6.42	9.18
K_2O/Na_2O	0.55	0.70	0.50	1.46	0.59	0.56

Sc	2.1	2.2	1.4	1.9	10.3	3.9
V	22	15	10	7	75	47
Cr	12	10	17	9	35	15
Co	4.5	3.4	2.7	3.4	12.1	6.6
Ni	0	0	0	4	23	4
Cu	10.7	1.9	3.3	3.6	1.1	6.6
Zn	27.1	30.5	8.5	13.2	53.3	33.1
Ga	20.6	19.6	14.3	11.8	16.7	19.8
Cs	0.78	0.42	0.52	1.38	0.89	2.50
Rb	69.72	78.66	47.14	88.17	37.64	83.36
Ba	1795	1574	1216	1329	1170	1419
Th	7.68	10.01	2.36	7.18	6.80	8.27
U	2.27	3.71	1.01	0.97	1.16	2.34
Nb	13.04	11.66	4.62	7.07	7.42	11.52
Ta	0.76	0.62	0.39	0.51	0.24	0.68
La	32.69	29.80	9.74	20.43	30.40	35.78
Ce	60.20	55.42	16.16	33.18	58.57	64.80
Pb	22.26	21.53	13.75	17.62	16.54	18.20
Pr	5.89	5.75	1.59	3.14	6.39	6.40
Sr	833	765	433	482	682	862
Nd	20.46	21.13	5.85	11.10	23.73	22.01
Zr	163.8	141.7	79.2	111.8	129.7	173.6
Hf	4.261	3.694	1.980	3.219	3.236	4.141
Sm	3.52	3.97	0.94	1.61	3.27	3.56
Eu	0.833	0.864	0.289	0.579	1.258	0.957
Gd	2.36	2.89	0.81	1.15	3.71	3.03
Tb	0.329	0.346	0.117	0.166	0.425	0.367
Dy	1.64	1.78	0.68	1.03	2.06	2.07
Y	8.57	8.47	3.64	5.27	12.20	11.30
Ho	0.248	0.282	0.117	0.158	0.570	0.363
Er	0.881	0.731	0.315	0.429	1.666	1.075
Tm	0.122	0.098	0.081	0.054	0.253	0.156
Yb	0.646	0.576	0.382	0.301	0.000	1.394
Lu	0.152	0.092	0.055	0.048	0.137	0.195

APPENDIX D: Oxygen Isotope Data and Modeling

Table D.1a: UWG-2 Gore Mountain Garnet Standard Measurements for ILFT Analyses

Date	*Mass (mg)*	*Time (min:sec)*	*Pressure (torr)*	$\delta^{18}O$ (‰)	1σ
10/15/13	1.725	2:15	25.9	5.867	0.026
10/15/13	1.963	2:02	29.5	5.863	0.008
10/15/13	1.908	2:18	28.1	5.88	0.018
10/15/13	1.961	2:22	29.5	5.826	0.015
4/27/14	1.732	2:52	25.7	5.823	0.009
4/27/14	2.023	2:31	30.0	5.743	0.008
4/27/14	1.840	2:20	27.3	5.685	0.012
4/27/14	1.603	2:15	23.6	5.655	0.015
4/27/14	1.868	2:17	27.7	5.655	0.017
4/29/14	1.797	2:32	26.5	5.797	0.025
4/29/14	2.027	2:39	30.1	5.724	0.019
4/29/14	2.050	2:21	30.5	5.679	0.012
4/29/14	1.814	2:30	27.0	5.620	0.009
4/29/14	1.653	2:12	24.5	5.612	0.016
6/20/14	1.717	2:29	25.3	5.851	0.009
6/20/14	1.810	2:39	25.9	5.994	0.010
6/20/14	1.972	2:25	29.4	5.886	0.008
6/20/14	1.825	2:24	27.0	5.839	0.006
6/20/14	1.724	2:12	25.8	5.793	0.007
6/24/14	1.898	1:46	28.1	5.870	0.010
6/24/14	1.704	1:36	25.4	5.905	0.020
6/24/14	1.521	2:18	22.7	5.783	0.006
6/24/14	1.606	2:18	24.0	5.825	0.017
6/25/14	1.547	2:36	23.0	5.935	0.010
6/25/14	1.690	2:38	25.3	5.913	0.008
6/25/14	1.513	1:46	22.7	5.83	0.011
6/25/14	1.700	2:01	25.4	5.864	0.014
6/26/14	1.927	1:48	28.9	5.887	0.018
6/26/14	1.956	1:38	29.3	5.924	0.013
6/26/14	1.797	2:30	26.9	5.827	0.012
6/28/14	1.900	3:27	28.2	5.863	0.012
6/28/14	1.591	1:53	25.7	5.984	0.011
6/28/14	1.857	2:48	27.9	5.823	0.014
6/28/14	1.834	1:40	27.2	5.845	0.007
6/28/14	1.575	1:36	23.6	5.810	0.027
6/29/14	1.649	1:42	24.6	5.842	0.025
6/29/14	1.500	1:37	22.4	5.858	0.011
7/1/14	1.644	1:58	24.3	6.042	0.003
7/1/14	1.520	1:47	22.9	6.006	0.006
7/1/14	1.498	-	22.4	5.949	0.006
7/1/14	1.926	-	28.7	5.834	0.017
7/1/14	1.645	1:30	24.6	5.863	0.018
7/2/14	1.712	2:01	25.7	5.967	0.018
7/2/14	1.834	1:51	27.5	5.937	0.024
7/2/14	1.910	1:40	28.5	5.883	0.006

Average: 5.841 ± 0.100 (1σ)

Table D.1b: KHX-1 Olivine Standard Measurements for ILFT Analyses

Date	*Mass (mg)*	*Time (min:sec)*	*Pressure (torr)*	$\delta^{18}O$ (‰)	1σ
10/15/13	2.108	2:43	32.6	5.288	0.023
10/15/13	2.088	2:32	32.1	5.282	0.019
10/15/13	2.108	2:36	32.4	5.303	0.025
10/15/13	2.042	2:30	31.3	5.281	0.026
4/27/14	1.750	2:22	26.2	5.203	0.017
4/27/14	1.633	2:09	24.8	5.189	0.013
4/27/14	1.867	2:26	28.3	5.083	0.012
4/27/14	1.773	2:23	26.7	5.118	0.009
4/29/14	2.074	2:48	31.5	5.160	0.010
4/29/14	2.028	2:33	30.7	5.078	0.016
4/29/14	1.652	2:27	25.1	5.107	0.014
4/29/14	1.556	~2:15	23.8	5.180	0.012
6/20/14	1.998	2:38	30.6	5.335	0.009
6/20/14	1.692	2:23	25.8	5.331	0.012
6/20/14	1.784	2:04	27.2	5.236	0.011
6/24/14	1.839	2:13	27.0	5.334	0.009
6/24/14	1.938	2:27	29.6	5.249	0.009
6/24/14	1.761	2:21	26.9	5.312	0.014
6/25/14	1.630	2:11	24.9	5.363	0.006
6/25/14	1.950	2:27	29.8	5.256	0.013
6/25/14	1.866	2:12	28.8	5.234	0.015
6/25/14	1.944	2:17	30.0	5.368	0.007
6/26/14*	1.962	1:33	23.7	5.376	0.009
6/26/14*	1.689	2:23	21.2	5.317	0.018
6/28/14	1.820	3:16	28.1	5.301	0.007
6/28/14	1.554	1:44	24.0	5.373	0.010
6/28/14	1.780	1:45	27.5	5.316	0.014
6/28/14	1.980	1:35	30.4	5.244	0.013
6/29/14	1.825	1:54	28.5	5.254	0.008
6/29/14	1.556	1:38	24.2	5.292	0.013
6/29/14	1.949	1:33	30.0	5.206	0.022
6/29/14	1.675	1:37	25.6	5.254	0.016
7/1/14	1.988	1:54	30.5	5.325	0.018
7/1/14	1.723	1:48	26.6	5.362	0.013
7/1/14	1.814	1:47	28.0	5.239	0.014
7/2/14	1.823	2:11	28.0	5.349	0.013
7/2/14	1.953	1:46	29.8	5.239	0.006
7/2/14	1.574	1:35	24.2	5.413	0.009

*Std. yields on this run are low because the shield became foggy.

Average: 5.267 ± 0.083 (1σ)

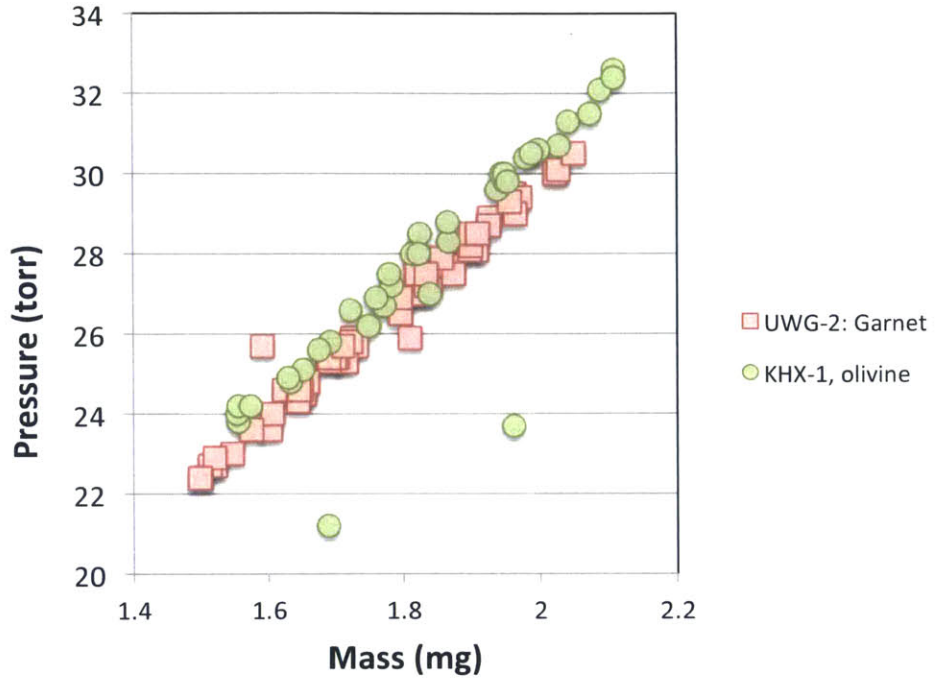

Figure D-1: Pressure of O_2 (torr) versus mass of analyzed ILFT standards. Two low KHX-1 olivine standards are due to incomplete lazing due to foggy shield. These standard analyses were not included in data reduction.

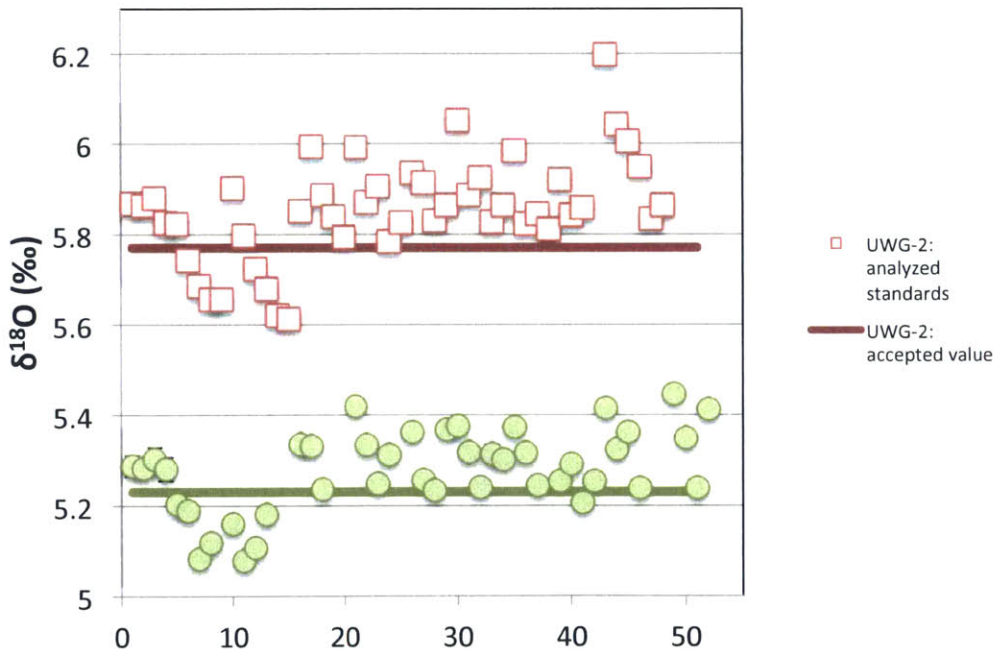

Figure D-2: Analyzed ILFT standard values versus accepted values. Horizontal axis indicates order of analysis.

Table D.2: SIMS Zircon Oxygen Isotope Analyses – Standards and Samples

Comment	$\delta^{18}O$ ‰ VSMOW	2SD (ext.)	Mass Bias (‰)	$\delta^{18}O$ ‰ measured	2SE (int.)	^{16}O (Gcps)	IP (nA)	Yield (Gcps/nA)	$^{16}OH/^{16}O$	Analysis Notes*
WI-STD-12 KIM-5 SW				6.072	0.260	2.520	**1.944**	1.296	2.658E-04	
WI-STD-12 KIM-5 SW beam#8				6.455	0.212	2.508	**1.936**	1.295	2.654E-04	
WI-STD-12 KIM-5 SW egun-HV=9999				6.337	0.218	2.509	**1.925**	1.304	2.780E-04	
WI-STD-12 KIM-5 SW				6.503	0.233	2.489	**1.914**	1.301	2.444E-04	
WI-STD-12 KIM-5 SW				6.439	0.239	2.477	**1.901**	1.303	2.460E-04	
average and 2SD				**6.434**	**0.140**					
Mount1 KIM-5 g1 A				6.641	0.131	2.420	**1.871**	1.293	5.671E-04	
Mount1 KIM-5 g1 B				6.616	0.205	2.414	**1.867**	1.293	5.637E-04	
Mount1 KIM-5 g1 C				6.433	0.273	2.406	**1.863**	1.291	6.153E-04	
Mount1 KIM-5 g1 D				6.298	0.296	2.384	**1.852**	1.287	5.921E-04	
average and 2SD				**6.497**	**0.324**					
Mount1 MO-11-12 z1-A	**9.06**	**0.29**		10.463	0.205	2.393	**1.839**	1.301	6.136E-04	Low ^{16}O cps Analysis near crack
Mount1 MO-11-12 z1-B	**9.33**	**0.29**		10.730	0.229	2.380	**1.838**	1.295	6.172E-04	Low ^{16}O cps
Mount1 MO-11-12 z2-A Cs-Res=177	**9.35**	**0.29**		10.751	0.206	2.597	**1.991**	1.304	5.828E-04	Analysis on crack Overlap with dark core (in CL)
Mount1 MO-11-12 z2-B	**9.06**	**0.29**		10.454	0.172	2.618	**2.009**	1.303	6.037E-04	
Mount1 MO-11-12 z6	**8.57**	**0.29**		9.973	0.221	2.600	**2.018**	1.288	5.290E-04	Analysis on crack
Mount1 MO-11-12 z9	**9.32**	**0.29**		10.717	0.216	2.646	**2.026**	1.306	5.781E-04	
Mount1 MO-11-12 z10	**9.19**	**0.29**		10.591	0.307	2.640	**2.032**	1.299	5.993E-04	
Mount1 MO-11-12 z11-A	**9.27**	**0.29**		10.670	0.134	2.645	**2.033**	1.301	5.536E-04	
Mount1 MO-11-12 z11-B	**9.12**	**0.29**		10.517	0.222	2.630	**2.030**	1.295	5.627E-04	
Mount1 MO-11-12 z14	**9.45**	**0.29**		10.849	0.213	2.637	**2.026**	1.302	5.392E-04	
Mount1 KIM-5 g2 A				6.451	0.189	2.607	**2.022**	1.289	5.906E-04	
Mount1 KIM-5 g2 B				6.296	0.192	2.619	**2.021**	1.296	5.812E-04	
Mount1 KIM-5 g2 C				6.666	0.251	2.400	**1.887**	1.272	7.607E-04	
Mount1 KIM-5 g2 D				6.467	0.269	2.476	**1.907**	1.299	6.247E-04	
average and 2SD				**6.470**	**0.303**					
bracket average and 2SD	**5.09**		**1.39**	**6.484**	**0.292**					
Mount1 MO-11-12 z17	**9.38**	**0.37**		10.652	0.239	2.520	**1.945**	1.296	5.917E-04	
Mount1 MO-11-12 z23	**9.67**	**0.37**		10.948	0.191	2.555	**1.960**	1.304	5.949E-04	
Mount1 MO-11-12 z35	**9.93**	**0.37**		11.209	0.178	2.570	**1.970**	1.304	6.081E-04	High $^{16}OH/^{16}O$
Mount1 MO-11-12 z34	**9.43**	**0.37**		10.707	0.219	2.576	**1.973**	1.306	6.066E-04	
Mount1 MO-11-12 z33	**9.36**	**0.37**		10.633	0.204	2.563	**1.974**	1.298	1.696E-03	High $^{16}OH/^{16}O$
Mount1 MO-11-12 z32	**9.66**	**0.37**		10.938	0.175	2.549	**1.973**	1.292	5.975E-04	
Mount1 MO-11-12 z27	**9.11**	**0.37**		10.388	0.254	2.560	**1.977**	1.295	6.011E-04	
Mount1 MO-11-12 z29-A	**9.65**	**0.37**		10.930	0.156	2.560	**1.979**	1.294	5.917E-04	
Mount1 MO-11-12 z29-B	**9.58**	**0.37**		10.862	0.247	2.568	**1.979**	1.298	5.504E-04	
Mount1 MO-11-16 z4-A	**9.31**	**0.37**		10.588	0.162	2.573	**1.982**	1.298	6.324E-04	
Mount1 MO-11-16 z4-B	**9.29**	**0.37**		10.566	0.231	2.569	**1.983**	1.295	5.848E-04	
Mount1 MO-11-16 z4-C	**9.34**	**0.37**		10.619	0.201	2.566	**1.983**	1.294	5.646E-04	
Mount1 KIM-5 g2 E				6.291	0.232	2.551	**1.987**	1.283	8.953E-04	
Mount1 KIM-5 g3 A				6.162	0.163	2.557	**1.981**	1.291	6.515E-04	
Mount1 KIM-5 g3 B				6.457	0.182	2.552	**1.977**	1.291	6.495E-04	
Mount1 KIM-5 g3 C				6.102	0.256	2.555	**1.981**	1.290	6.096E-04	
average and 2SD				**6.253**	**0.314**					
bracket average and 2SD	**5.09**		**1.27**	**6.362**	**0.368**					
Mount1 MO-11-16 z12	**8.37**	**0.35**		9.661	0.201	2.554	**1.967**	1.299	5.738E-04	
Mount1 MO-11-16 z14	**10.02**	**0.35**		11.319	0.159	2.565	**1.967**	1.304	9.201E-04	High $^{16}OH/^{16}O$
Mount1 MO-11-16 z16	**8.57**	**0.35**		9.861	0.262	2.553	**1.966**	1.299	5.648E-04	
Mount1 MO-11-16 z31	**8.35**	**0.35**		9.647	0.195	2.558	**1.965**	1.302	6.182E-04	
Mount1 MO-11-16 z29	**8.52**	**0.35**		9.815	0.196	2.542	**1.962**	1.296	5.600E-04	
Mount1 MO-11-16 z18	**11.47**	**0.35**		12.767	0.256	2.539	**1.958**	1.296	5.875E-04	
Mount1 MO-11-16 z27	**9.24**	**0.35**		10.540	0.271	2.533	**1.955**	1.296	5.498E-04	
Mount1 MO-11-16 z26	**9.32**	**0.35**		10.616	0.258	2.533	**1.953**	1.297	5.561E-04	

Mount1 MO-11-16 z36	**8.51**	**0.35**		9.810	0.240	2.528	**1.950**	1.296	6.247E-04	
Mount1 MO-11-16 z38-A	**8.55**	**0.35**		9.850	0.192	2.520	**1.948**	1.294	5.927E-04	
Mount1 MO-11-16 z38-B	**8.38**	**0.35**		9.673	0.196	2.522	**1.947**	1.296	5.483E-04	
Mount1 MO-11-16 z24	**8.95**	**0.35**		10.242	0.238	2.529	**1.945**	1.300	5.518E-04	
Mount1 MO-11-16 z22	**8.82**	**0.35**		10.118	0.174	2.516	**1.942**	1.295	6.030E-04	
Mount1 KIM-5 g3 D				6.584	0.225	2.516	**1.942**	1.295	6.572E-04	
Mount1 KIM-5 g3 E				6.493	0.194	2.517	**1.939**	1.298	6.276E-04	
Mount1 KIM-5 g3 F				6.417	0.244	2.518	**1.941**	1.297	6.556E-04	
Mount1 KIM-5 g4 A				6.541	0.190	2.485	**1.941**	1.280	6.107E-04	
average and 2SD				**6.509**	**0.143**					
bracket average and 2SD	**5.09**		**1.28**	**6.381**	**0.355**					
Mount1 MO-11-16 z13	**8.99**	**0.27**		10.359	0.165	2.511	**1.938**	1.295	6.067E-04	
Mount1 MO-11-16 z15	**8.77**	**0.27**		10.137	0.151	2.503	**1.930**	1.297	5.838E-04	
Mount1 MO-11-23 z3	**9.42**	**0.27**		10.784	0.173	2.497	**1.922**	1.300	7.214E-04	High $^{18}OH/^{16}O$
Mount1 MO-11-23 z14	**9.10**	**0.27**		10.461	0.258	2.507	**1.926**	1.302	5.711E-04	
Mount1 MO-11-23 z17-A	**9.10**	**0.27**		10.465	0.173	2.502	**1.930**	1.296	5.973E-04	
Mount1 MO-11-23 z17-B	**9.18**	**0.27**		10.549	0.238	2.509	**1.934**	1.298	5.651E-04	
Mount1 MO-11-23 z18-A	**9.18**	**0.27**		10.548	0.200	2.514	**1.936**	1.299	5.640E-04	
Mount1 MO-11-23 z18-B	**9.39**	**0.27**		10.757	0.253	2.517	**1.938**	1.299	5.759E-04	On crack
Mount1 MO-11-23 z26	**8.96**	**0.27**		10.323	0.264	2.522	**1.933**	1.305	5.680E-04	
Mount1 MO-11-23 z27	**9.28**	**0.27**		10.645	0.216	2.509	**1.940**	1.293	5.655E-04	
Mount1 MO-11-23 z31-A	**9.00**	**0.27**		10.362	0.195	2.520	**1.939**	1.300	5.563E-04	
Mount1 MO-11-23 z31-B	**9.11**	**0.27**		10.477	0.246	2.511	**1.936**	1.298	5.649E-04	
Mount1 MO-11-23 z32	**9.00**	**0.27**		10.364	0.203	2.520	**1.933**	1.303	5.625E-04	
Mount1 KIM-5 g4 B				6.380	0.236	2.505	**1.933**	1.296	6.023E-04	
Mount1 KIM-5 g4 C				6.542	0.268	2.500	**1.939**	1.289	6.475E-04	
Mount1 KIM-5 g4 D				6.157	0.153	2.519	**1.945**	1.295	6.317E-04	
Mount1 KIM-5 g5 A				6.487	0.208	2.523	**1.945**	1.297	5.894E-04	
average and 2SD				**6.392**	**0.340**					
bracket average and 2SD	**5.09**		**1.35**	**6.450**	**0.272**					
Mount1 MO-11-23 z34	**9.18**	**0.35**		10.477	0.208	2.534	**1.951**	1.299	5.545E-04	
Mount1 MO-11-23 z36	**8.86**	**0.35**		10.157	0.245	2.547	**1.953**	1.304	5.695E-04	
Mount1 MO-11-23 z23	**9.05**	**0.35**		10.349	0.206	2.537	**1.952**	1.300	5.593E-04	
Mount1 MO-11-23 z20	**9.01**	**0.35**		10.305	0.221	2.539	**1.952**	1.301	5.576E-04	
Mount1 MO-11-23 z21-A	**8.75**	**0.35**		10.040	0.259	2.543	**1.956**	1.300	5.605E-04	
Mount1 MO-11-23 z21-B	**9.25**	**0.35**		10.543	0.229	2.544	**1.959**	1.299	5.543E-04	
Mount1 MO-11-23 z9	**8.96**	**0.35**		10.252	0.199	2.552	**1.959**	1.303	5.678E-04	
Mount1 MO-11-23 z11-A	**9.21**	**0.35**		10.507	0.203	2.551	**1.964**	1.299	5.542E-04	
Mount1 MO-11-23 z11-B	**9.12**	**0.35**		10.418	0.161	2.556	**1.966**	1.300	5.656E-04	
Mount1 MO-11-14 z24	**8.26**	**0.35**		9.558	0.265	2.557	**1.963**	1.303	5.429E-04	
Mount1 MO-11-14 z22	**8.38**	**0.35**		9.677	0.164	2.541	**1.958**	1.298	6.357E-04	High $^{18}OH/^{16}O$
Mount1 MO-11-14 z25-A	**8.36**	**0.35**		9.649	0.210	2.547	**1.955**	1.303	5.425E-04	
Mount1 MO-11-14 z25-B	**8.43**	**0.35**		9.726	0.186	2.550	**1.953**	1.306	5.329E-04	
Mount1 KIM-5 g5 B				6.396	0.262	2.530	**1.947**	1.299	5.901E-04	
Mount1 KIM-5 g5 C				6.613	0.231	2.509	**1.943**	1.292	6.070E-04	
Mount1 KIM-5 g5 D				6.116	0.198	2.515	**1.937**	1.299	5.932E-04	
Mount1 KIM-5 g6 A				6.343	0.207	2.515	**1.929**	1.304	6.045E-04	
average and 2SD				**6.367**	**0.408**					
bracket average and 2SD	**5.09**		**1.28**	**6.379**	**0.349**					
Mount1 MO-11-14 z26	**8.39**	**0.38**		9.598	0.167	2.529	**1.928**	1.312	5.514E-04	
Mount1 MO-11-14 z20	**8.23**	**0.38**		9.437	0.219	2.511	**1.925**	1.304	5.442E-04	
Mount1 MO-11-14 z4	**8.46**	**0.38**		9.670	0.210	2.505	**1.925**	1.301	5.619E-04	
Mount1 MO-11-14 z17-A	**8.37**	**0.38**		9.576	0.231	2.518	**1.927**	1.306	5.415E-04	
Mount1 MO-11-14 z17-B	**8.18**	**0.38**		9.389	0.253	2.530	**1.934**	1.308	5.420E-04	
Mount1 MO-11-14 z12	**8.39**	**0.38**		9.599	0.293	2.519	**1.933**	1.303	5.456E-04	
Mount1 MO-11-14 z2-A	**8.60**	**0.38**		9.805	0.152	2.504	**1.924**	1.302	5.496E-04	
Mount1 MO-11-14 z2-B	**8.30**	**0.38**		9.514	0.216	2.501	**1.915**	1.306	5.449E-04	

Mount1 MO-11-14 z13-A	8.36	0.38		9.569	0.175	2.490	1.909	1.304	6.359E-04	High $^{16}OH/^{16}O$
Mount1 MO-11-14 z13-B	8.01	0.38		9.215	0.237	2.473	1.911	1.294	7.522E-04	High $^{16}OH/^{16}O$
Mount1 MO-11-14 z15	8.32	0.38		9.526	0.216	2.489	1.910	1.303	5.496E-04	
Mount1 MO-11-14 z30-A	8.30	0.38		9.507	0.197	2.482	1.906	1.303	5.392E-04	
Mount1 MO-11-14 z30-B	8.22	0.38		9.425	0.215	2.471	1.904	1.298	5.341E-04	
Mount1 MO-11-14 z16	8.49	0.38		9.702	0.295	2.480	1.907	1.301	5.908E-04	
Mount1 KIM-5 g6 B				6.221	0.209	2.486	1.912	1.300	5.962E-04	
Mount1 KIM-5 g6 C				6.080	0.160	2.489	1.914	1.300	6.151E-04	
Mount1 KIM-5 g6 D				6.125	0.172	2.487	1.915	1.299	5.826E-04	
Mount1 KIM-5 g6 E				6.470	0.207	2.480	1.915	1.295	5.899E-04	
average and 2SD				**6.224**	**0.348**					
bracket average and 2SD	5.09		1.20	6.296	0.383					
Mount1 MO-11-19 z36-A	7.87	0.37		9.125	0.177	2.485	1.910	1.301	5.645E-04	
Mount1 MO-11-19 z36-B	7.83	0.37		9.079	0.246	2.480	1.909	1.299	5.549E-04	
Mount1 MO-11-19 z23-A	7.58	0.37		8.832	0.190	2.479	1.911	1.297	6.263E-04	High $^{16}OH/^{16}O$
Mount1 MO-11-19 z23-B	7.74	0.37		8.991	0.172	2.497	1.917	1.303	5.503E-04	
Mount1 MO-11-19 z24	7.83	0.37		9.077	0.235	2.505	1.923	1.303	5.378E-04	
Mount1 MO-11-19 z25	7.87	0.37		9.119	0.205	2.504	1.923	1.303	5.542E-04	
Mount1 MO-11-19 z26-A	7.74	0.37		8.996	0.242	2.511	1.919	1.308	5.682E-04	
Mount1 MO-11-19 z26-B	7.76	0.37		9.013	0.178	2.495	1.917	1.301	5.364E-04	
Mount1 MO-11-19 z33	7.54	0.37		8.790	0.246	2.482	1.912	1.298	5.472E-04	Analysis on crack
Mount1 MO-11-19 z31	8.03	0.37		9.278	0.229	2.472	1.906	1.297	5.377E-04	
Mount1 MO-11-19 z29	7.77	0.37		9.026	0.215	2.473	1.907	1.297	5.467E-04	
Mount1 MO-11-19 z10	8.00	0.37		9.256	0.153	2.475	1.899	1.304	5.223E-04	
Mount1 MO-11-19 z11	8.24	0.37		9.489	0.191	2.468	1.897	1.301	5.430E-04	Analysis on dark area of zircon in CL (radiation damage?)
Mount1 KIM-5 g6 F				6.583	0.221	2.450	1.895	1.293	6.274E-04	
Mount1 KIM-5 g7 A				6.505	0.233	2.444	1.889	1.293	5.833E-04	
Mount1 KIM-5 g7 B				6.408	0.214	2.443	1.886	1.295	5.918E-04	
Mount1 KIM-5 g8 A				6.312	0.176	2.443	1.875	1.303	5.547E-04	
average and 2SD				**6.452**	**0.235**					
bracket average and 2SD	5.09		1.24	6.338	0.368					
Mount1 MO-11-19 z12	8.00	0.21		9.346	0.178	2.425	1.863	1.302	5.425E-04	
Mount1 MO-11-19 z13	7.82	0.21		9.167	0.213	2.421	1.861	1.301	5.360E-04	
Mount1 MO-11-19 z6	7.94	0.21		9.279	0.178	2.410	1.857	1.298	5.320E-04	
Mount1 MO-11-19 z1	8.91	0.21		10.253	0.209	2.409	1.855	1.299	5.541E-04	Low ^{16}O cps
Mount1 MO-11-19 z20	8.12	0.21		9.460	0.198	2.399	1.852	1.296	5.564E-04	Low ^{16}O cps
Mount1 MO-11-19 z37	7.91	0.21		9.252	0.185	2.420	1.852	1.307	5.519E-04	
Mount1 MO-11-26 z7-A	8.67	0.21		10.017	0.238	2.405	1.849	1.301	5.565E-04	Low ^{16}O cps, high $^{16}OH/^{16}O$
Mount1 MO-11-26 z7-B	9.40	0.21		10.749	0.257	2.393	1.846	1.297	5.587E-04	Low ^{16}O cps, high $^{16}OH/^{16}O$
Mount1 MO-11-26 z6 Cs-Res=178	9.48	0.21		10.822	0.213	2.629	2.015	1.305	5.091E-04	Analysis on dark area of zircon in CL (radiation damage?)
Mount1 MO-11-26 z5	8.75	0.21		10.089	0.181	2.658	2.032	1.308	4.986E-04	Analysis on crack
Mount1 MO-11-26 z12	9.01	0.21		10.350	0.248	2.650	2.041	1.299	5.095E-04	
Mount1 MO-11-26 z3-A	9.11	0.21		10.453	0.178	2.666	2.046	1.303	4.996E-04	
Mount1 MO-11-26 z3-B	8.88	0.21		10.221	0.163	2.670	2.064	1.294	4.953E-04	
Mount1 KIM-5 g8 B				6.268	0.245	2.702	2.070	1.305	5.310E-04	
Mount1 KIM-5 g8 C				6.458	0.186	2.706	2.074	1.305	5.239E-04	
Mount1 KIM-5 g8 D				5.484	0.163	2.555	2.054	1.244	5.568E-04	Low ^{16}O cps
Mount1 KIM-5 g8 E				6.507	0.181	2.654	2.041	1.300	5.243E-04	
Mount1 KIM-5 g8 F				6.390	0.251	2.655	2.044	1.299	5.332E-04	
average and 2SD				**6.406**	**0.207**					
bracket average and 2SD	5.09		1.33	6.429	0.211					
Mount1 MO-11-26 z1	9.03	0.15		10.335	0.243	2.637	2.039	1.293	4.991E-04	
Mount1 MO-11-26 z17	9.01	0.15		10.310	0.226	2.633	2.037	1.293	4.982E-04	
Mount1 MO-11-26 z19-A	9.16	0.15		10.458	0.213	2.639	2.026	1.302	5.437E-04	High $^{16}OH/^{16}O$
Mount1 MO-11-26 z19-B	9.27	0.15		10.578	0.241	2.602	2.018	1.289	4.919E-04	
Mount1 MO-11-26 z30-A	9.22	0.15		10.518	0.279	2.610	2.010	1.299	5.085E-04	
Mount1 MO-11-26 z30-B	9.21	0.15		10.515	0.182	2.594	2.006	1.293	5.035E-04	

Mount1 MO-11-26 z31	**9.02**	**0.15**		10.325	0.252	2.596	**2.001**	1.297	4.901E-04	
Mount1 MO-11-26 z35	**9.42**	**0.15**		10.722	0.203	2.581	**1.999**	1.291	4.986E-04	
Mount1 MO-11-26 z36	**9.15**	**0.15**		10.456	0.228	2.593	**1.997**	1.299	4.980E-04	
Mount1 MO-11-26 z37	**9.00**	**0.15**		10.299	0.265	2.592	**1.992**	1.301	5.051E-04	
Mount1 MO-11-26 z23	**9.42**	**0.15**		10.725	0.279	2.596	**1.993**	1.303	5.338E-04	High $^{16}OH/^{16}O$
Mount1 MO-11-26 z24	**9.27**	**0.15**		10.575	0.174	2.605	**1.998**	1.304	5.175E-04	
Mount1 MO-11-26 z25	**9.30**	**0.15**		10.601	0.210	2.606	**2.002**	1.302	5.079E-04	
Mount1 KIM-5 g9 A				6.366	0.208	2.611	**2.006**	1.302	5.052E-04	
Mount1 KIM-5 g9 B				6.325	0.149	2.615	**2.007**	1.303	5.104E-04	
Mount1 KIM-5 g9 C				6.370	0.237	2.631	**2.016**	1.305	5.337E-04	
Mount1 KIM-5 g9 D				6.417	0.161	2.628	**2.017**	1.303	5.286E-04	
average and 2SD				**6.370**	**0.075**					
bracket average and 2SD	**5.09**		**1.29**	**6.388**	**0.149**					
Mount1 MO-11-16 z1-A	**8.45**	**0.18**		9.805	0.123	2.621	**2.008**	1.305	5.571E-04	
Mount1 MO-11-16 z1-B	**8.61**	**0.18**		9.966	0.195	2.604	**2.002**	1.300	5.290E-04	Analysis partially on dark zoned rim and core
Mount1 MO-11-16 z35	**9.02**	**0.18**		10.381	0.221	2.587	**1.986**	1.303	5.439E-04	
Mount1 MO-11-16 z37	**8.58**	**0.18**		9.938	0.265	2.574	**1.987**	1.296	5.254E-04	
Mount1 MO-11-16 z6	**9.49**	**0.18**		10.843	0.176	2.561	**1.976**	1.296	5.133E-04	
Mount1 MO-11-16 z10	**10.95**	**0.18**		12.304	0.264	2.585	**1.980**	1.306	5.421E-04	Dark oscillatory rim. Analysis on crack
Mount1 MO-11-12 z8	**9.50**	**0.18**		10.859	0.281	2.575	**1.980**	1.301	5.119E-04	
Mount1 MO-11-12 z24	**9.72**	**0.18**		11.075	0.232	2.446	**1.977**	1.237	5.311E-04	Low ^{16}O cps
Mount1 MO-11-12 z18	**9.18**	**0.18**		10.539	0.198	2.588	**1.980**	1.307	5.247E-04	
Mount1 MO-11-12 z20	**9.46**	**0.18**		10.822	0.191	2.573	**1.982**	1.299	5.177E-04	
Mount1 MO-11-26 z22	**9.16**	**0.18**		10.515	0.221	2.563	**1.977**	1.296	5.009E-04	
Mount1 MO-11-26 z27	**9.09**	**0.18**		10.442	0.219	2.566	**1.974**	1.299	5.066E-04	
Mount1 MO-11-26 z29	**8.90**	**0.18**		10.256	0.185	2.574	**1.979**	1.300	4.968E-04	
Mount1 KIM-5 g9 E				6.427	0.223	2.573	**1.982**	1.298	6.070E-04	
Mount1 KIM-5 g9 F				6.572	0.182	2.572	**1.983**	1.297	5.364E-04	
Mount1 KIM-5 g9 G				6.540	0.211	2.563	**1.977**	1.296	5.464E-04	
Mount1 KIM-5 g9 H				6.512	0.234	2.552	**1.977**	1.291	5.759E-04	
average and 2SD				**6.513**	**0.124**					
bracket average and 2SD	**5.09**		**1.34**	**6.441**	**0.180**					

*Analyses in red were not considered robust. See notes.

Table D.3: Quartz-Mineral Fractionation Factors Used in Calculations

MINERAL B*	A	B	C	Reference	Temperature Range (°C)	Method
Albite	0.94	-	-	Clayton et al., (1989)	600-800	Experimental
Anorthite	1.99	-	-	Clayton et al., (1989)	600-800	Experimental
K-Feldspar	0.16	1.50	-0.62	Zheng (1993a)	-	Theoretical - Modified Increment Method
Nepheline	0.37	2.77	-1.15	Zheng (1993a)	-	Theoretical - Modified Increment Method
Hornblende	0.59	3.80	-1.59	Zheng (1993b)	-	Theoretical - Modified Increment Method
Pargasite	0.71	4.22	-1.77	Zheng (1993b)	-	Theoretical - Modified Increment Method
Phlogopite	2.16	-	-	Summarized by Chacko et al., (2001). Based on data by Chacko et al., (1996).	650-800	Direct exchange experiments.
Apatite	2.51	-	-	Fortier & Lüttge (1995)	350-800	Direct exchange experiments.
Zircon	2.64	-	-	Valley et al., (2003)	-	Empirical. Based on Natural Samples.
Almandine	2.71	-	-	Valley et al., (2003)	-	Empirical. Based on Natural Samples.
Grossular	3.03	-	-	Valley et al., (2003)	-	Empirical. Based on Natural Samples.
Diopside	2.75	-	-	Summarized by Chacko et al., (2001). Based on data of Chiba et al., (1989).	600-1200	Direct exchange experiments.
Enstatite	0.51	3.45	-1.44	Zheng (1993a)	-	Theoretical - Modified Increment Method
Forsterite	3.67	-	-	Summarized by Chacko et al., (2001). Based on data of Chiba et al., (1989).	700-1300	Direct exchange experiments.
Spinel	2.06	10.04	-5.38	Zheng (1991)	0-1200	Theoretical - Modified Increment Method
Rutile	4.69	-	-	Summarized by Chacko et al., (2001). Based on data of Chacko et al., (1996).	800-1000	Direct exchange experiments.
Ilmenite	1.36	8.61	-4.57	Zheng (1991)	0-1200	Theoretical - Modified Increment Method
Magnetite	6.29	-	-	Summarized by Chacko et al., (2001). Based on data of Chiba et al., (1989).	800-1200	Direct exchange experiments.

* $\Delta_{Qtz\text{-}B} \approx 1000*\ln(\alpha_{Qtz\text{-}B})) = 10^6(A/T^2) + 10^3(B/T)+C$

REFERENCES:

Chacko T, Hu X, Mayeda TK, Clayton RN (1996) Oxygen isotope fractionations in muscovite, phlogopite, and rutile. Geochimica et Cosmochimica Acta. v. 60, n. 14, pp. 2595-2608.

Chacko T, Cole DR, Horita J (2001) Equilibrium oxygen, hydrogen and carbon isotope fractionation factors applicable to geologic systems. Reviews in mineralogy and geochemsitry.

Chiba H, Chacko T, Clayton RN (1989) Oxygen isotope fractionations involving diopside, forsterite, magnetite, and calcite: Application to geothermometry. Geochmicia et Cosmochimica Acta, v. 53, pp. 2985-2995.

Clayton RN, Goldsmith JR, Mayeda TK (1989) Oxygen isotope fractionation in quartz, albite, anorthite and calcite. Geochimica et Cosmochimica Acta. V. 53, pp. 725-733.

Fortier SM, Lüttge A (1995) An experimental calibration of the temperature dependence of oxygen isotope fractionation between apatite and calcite at high temperatures (350–800°C). Chemical Geology 125:281–290.

Valley, J. W., Bindeman, I. N., and Peck, W. H. (2003). *Empirical calibration of oxygen isotope fractionation in zircon.* Geochimica et Cosmochimica Acta, v. 67, n. 17, pp. 3257-3266.

Zheng YF (1991) Calculation of oxygen isotope fractionation in metal oxides. Geochimica et Cosmochimica Acta, v. 55, pp. 2299-2307.

Zheng YF (1993a) Calculation of oxygen isotope fractionation in anhydrous silicate minerals. Geochimica et Cosmochimica Acta, v. 57, pp. 1079-1091.

Zheng YF (1993) Calculation of oxygen isotope fractionation in hydroxyl-bearing silicates. Earth and Planetary Science Letters 120:247–263.

Modeling $\delta^{18}O_{melt}$ during Closed System Fractional Crystallization

In this supplement, we describe our model for calculating the changes in $\delta^{18}O_{melt}$ during fractional crystallization. This model is applicable to any LLD for which the following parameters are known:

1) Melt fractions
2) Melt composition at each remaining melt fraction
3) Mass percent of crystallizing cumulate for each crystallizing mineral
4) Temperature during crystallization

A: Mass Balance Equations

We present a small increment, forward step mass balance model to account for the effect of fractional crystallization on the oxygen isotopic composition of a melt.

We assume an initial $\delta^{18}O_{melt}$ at fractionation step $i = 1$. In subsequent equations, superscripts indicate the fractionation step. The total melt fraction (F) at $i = 1$ is $F^1 = 1$, corresponding to a parental melt that has not experienced crystallization. Using mass balance constraints (see Fig. D.3):

$$C_{melt}^{i+1}(\delta^{18}O_{melt}^{i+1})(X^{i+1}) + C_{cumulate}^{i+1}(\delta^{18}O_{cumulate}^{i+1})(1 - X^{i+1}) = C_{melt}^{i}\delta^{18}O_{melt}^{i} \quad (1)$$

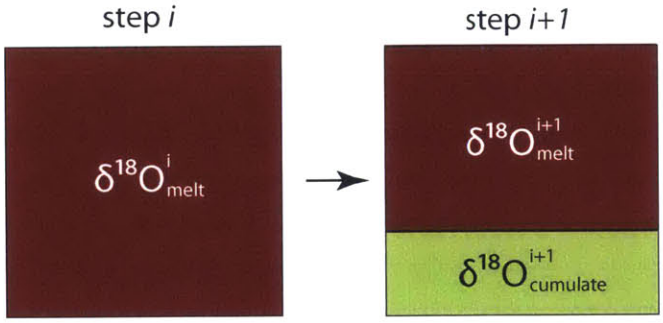

Figure D-3: Schematic of mass balance calculations involving cumulates and melt.

where $X^{i+1} = F^{i+1}/F^{i}$, which accounts for the decreasing melt mass during fractionation, and C is the mass fraction of oxygen in the melt or bulk cumulate. For most silicate minerals and melts, C = 0.4-0.5, and therefore the C terms can be ignored. However, for cumulates dominated by oxides or Fe-end members of Fe-Mg silicates, C could be significantly different from the melt and must be considered. If C is ignored for simplicity, Eq. 1 may be rearranged to solve for $\delta^{18}O_{melt}^{i+1}$:

$$\delta^{18}O_{melt}^{i+1} = \frac{\delta^{18}O_{melt}^{i} - (\delta^{18}O_{cumulate}^{i+1})(1-X^{i+1})}{X^{i+1}} \quad (2)$$

We let Δ^{i+1} denote the bulk cumulate-melt per mil fractionation:

$$\Delta^{i+1} = \delta^{18}O_{cumulate}^{i+1} - \delta^{18}O_{melt}^{i+1} = \sum(M_n^{i+1} \times \Delta_n^{i+1}(T)) \quad (3)$$

where M_n^{i+1} is the mass fraction of the bulk cumulate oxygen contained in crystallizing mineral n and $\Delta_n^{i+1}(T)$ is the temperature and melt composition-dependent mineral-melt fractionation for

mineral *n*. We describe the method used to calculate $\Delta_n^{i+1}(T)$ for each crystallizing mineral in section B. We can then rewrite Eq. 3 to solve for $\delta^{18}O_{cumulate}^{i+1}$:

$$\delta^{18}O_{cumulate}^{i+1} = \delta^{18}O_{melt}^{i+1} + \Delta^{i+1} \quad (4)$$

Substituting Eq. 4, into Eq. 2 yields:

$$\delta^{18}O_{melt}^{i+1} = \frac{\delta^{18}O_{melt}^{i} - (\delta^{18}O_{melt}^{i+1} + \Delta^{i+1})(1 - X^{i+1})}{X^{i+1}} \quad (5)$$

which then simplifies to the primary equation for the melt at the next fractionation step ($\delta^{18}O_{melt}^{i+1}$) underlying the mass balance model:

$$\delta^{18}O_{melt}^{i+1} = \delta^{18}O_{melt}^{i} - \Delta^{i+1}(1 - X^{i+1}) \quad (6)$$

If C is included in Eq. 1, a similar equation can be derived if mass fractions of the melt versus cumulates are considered:

$$\delta^{18}O_{melt}^{i+1} = \frac{C_{melt}^{i}\delta^{18}O_{melt}^{i} - C_{cumulate}^{i+1}(\Delta^{i+1})(1 - X^{i+1})}{C_{melt}^{i+1}X^{i+1} + C_{cumulate}^{i+1}(1 - X^{i+1})} \quad (7)$$

B: Calculation of Mineral-Melt Fractionations

We calculate mineral-melt fractionation factors following the CIPW normative method described in Eiler (2001). At each fractionation step *i*, the CIPW norm of the melt composition is calculated. Next, treating the melt as a mixture of CIPW normative minerals, using estimated melt temperatures, and implementing experimentally-determined temperature-dependent relationships for mineral-mineral oxygen isotope fractionations, we calculate the temperature and melt composition-dependent mineral-melt fractionations ($\Delta_n^i(T)$) for each crystallizing mineral *n*.

To illustrate this method, we present an example calculation. Consider the normalized basaltic melt composition (in wt.%) from experiment SV44 of Villiger et al., (2004):

SiO_2	TiO_2	Al_2O_3	FeO	MnO	MgO	CaO	Na_2O	K_2O	Total
50.28	0.59	14.47	6.86	0.16	14.16	11.81	1.60	0.08	100.00

with a mass percent CIPW normative composition (considering all Fe and FeO):

Anorthite	Albite	Orthoclase	Diopside	Hypersthene	Olivine	Ilmenite	Total
31.51	14.09	0.47	21.26	17.62	13.93	1.12	100

and the mass percent of total oxygen contained in the CIPW normative minerals:

Anorthite	Albite	Orthoclase	Diopside	Hypersthene	Olivine	Ilmenite	Total
32.11	15.23	0.48	20.87	18.66	11.86	0.78	100

To calculate $\Delta_{olivine-melt}$ for the SV44 glass composition at 1300°C (the temperature of olivine saturation), the fractionations of the melt CIPW normative minerals with olivine must be calculated. For example, equilibrium forsterite-anorthite (Fo-An) fractionations are calculated:

$$\delta^{18}O_{Fo} - \delta^{18}O_{An} = \Delta_{Fo-An} \approx 1000\ln(\alpha_{Fo-An}) = A_{Fo-An}(\frac{10^6}{T^2}) \quad (7)$$

where T is temperature in Kelvin, $\alpha_{Fo-An} = \frac{(^{18}O/^{16}O)_{Fo}}{(^{18}O/^{16}O)_{An}}$, and A_{Fo-An}= -1.68 (Chacko et al., 2001). At 1300°C = 1573 K, Δ_{Fo-An}= -0.679 ‰. Effects of Fe-Mg substitution in mafic minerals on mineral-mineral fractionations are generally small (Hoefs, 2008) and were ignored in this study. Olivine fractionations with other normative minerals (e.g., albite, orthoclase, diopside, hypersthene, olivine, and ilmenite) must also be calculated at 1300°C following the same equations, but using A values appropriate for each mineral (see Valley (2003) for summary and Table D.4 for values used in this study). Total olivine-melt fractionations can then be calculated as:

$$\Delta_{olivine-melt} = N_{An}^{melt} * \Delta_{Fo-An} + N_{Ab}^{melt} * \Delta_{Fo-Ab} + N_{Or}^{melt} * \Delta_{Fo-Or} + N_{Hy}^{melt} * \Delta_{Fo-Hy} + N_{Ilm}^{melt} * \Delta_{Fo-Ilm}$$
$$= 0.3211 * \Delta_{Fo-An} + 0.1523 * \Delta_{Fo-Ab} + 0.0048 * \Delta_{Fo-Or} + 0.1866 * \Delta_{Fo-Hy} + 0.0078 * \Delta_{Fo-Ilm} \quad (8)$$

where N_{min}^{melt} is the mass fraction of total oxygen in bulk CIPW composition contained in a specified mineral. Mineral-melt fractionation calculations must be done at every fractionation step (with a new temperature and melt composition) for every crystallizing mineral phase. These mineral-fractionations are equivalent to $\Delta_n^{i+1}(T)$ in Eq. 3, which are summed in proportion to the mass % of each crystallizing mineral to yield a bulk cumulate-melt fractionation.

C: Comparison to Bindeman et al., (2004) Model

Notably, the calculated increases in $\delta^{18}O$ produced by our model are higher than the maximum of 0.4‰ increase predicted by the modeled "normal $\delta^{18}O$ array" of Bindeman et al., (2004) (Fig. 1 in manuscript). This stems from a critical difference in our modeling setup. As written, the right hand side of Bindeman et al.'s Equation 1 is actually equal to the bulk cumulate $\delta^{18}O$ value and not that of the crystallizing melt, as reported. The "normal $\delta^{18}O$ array" of Bindeman therefore, should be considered the bulk cumulate value and not that of the melt $\delta^{18}O$. In our model, we use a similar formulation for calculating bulk cumulate-melt fractionation (Δ^{i+1}, Eq. 3) and bulk cumulate $\delta^{18}O$ (Eq. 4), but then include another step to account for the effect of this fractionation on the crystallizing melt oxygen isotopic composition (Eq. 5-6).

References

Chacko, T., Cole, D.R., Horita, J., 2001. Equilibrium oxygen, hydrogen and carbon isotope fractionation factors applicable to geologic systems. Reviews in Mineralogy and Geochemistry 43, 1–81.

Hoefs, J., 2008. Stable isotope geochemistry, 6 ed. Springer Berlin Heidelberg.

Valley, J.W., 2003. Oxygen isotopes in zircon. Reviews in Mineralogy and Geochemistry 53, 343–385.

APPENDIX E:
Cathodoluminescence Images of Zircons Analyzed for CA-IDTIMS U-Pb Geochronology

MO-11-12
Monzogabbro

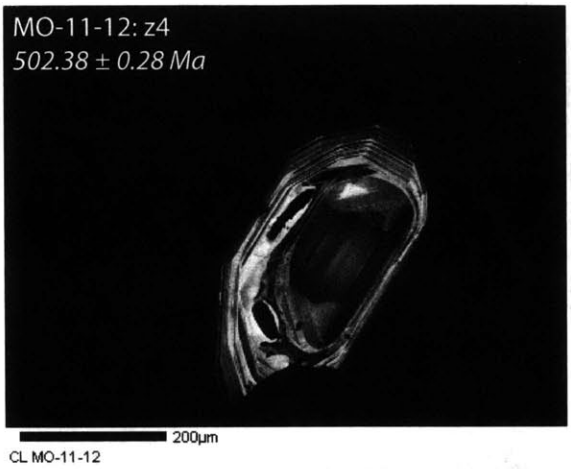

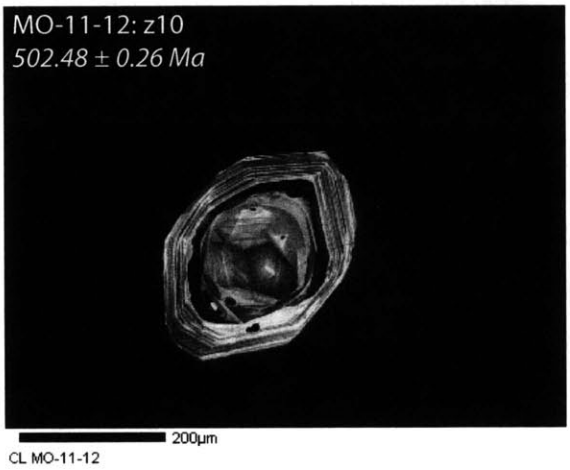

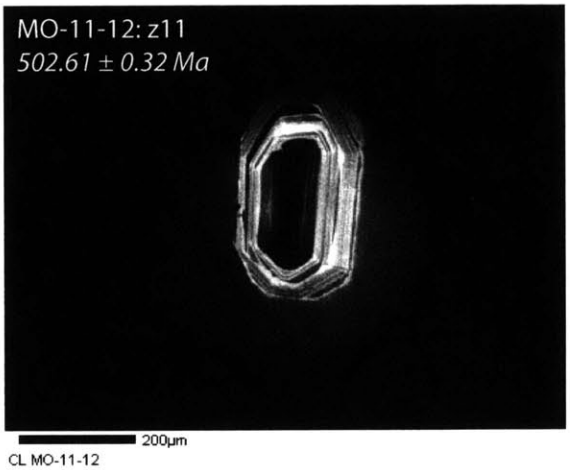

MO-11-14
Monzodiorite

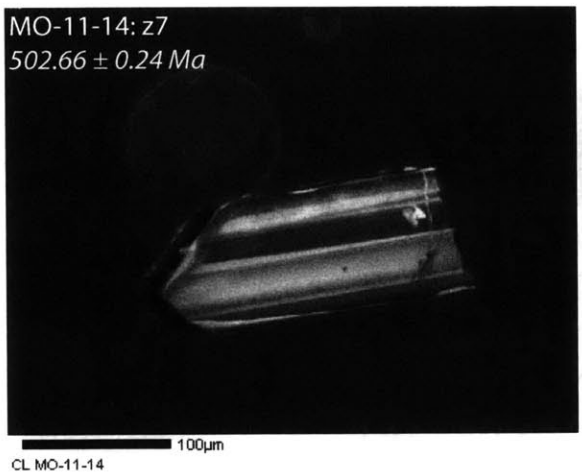

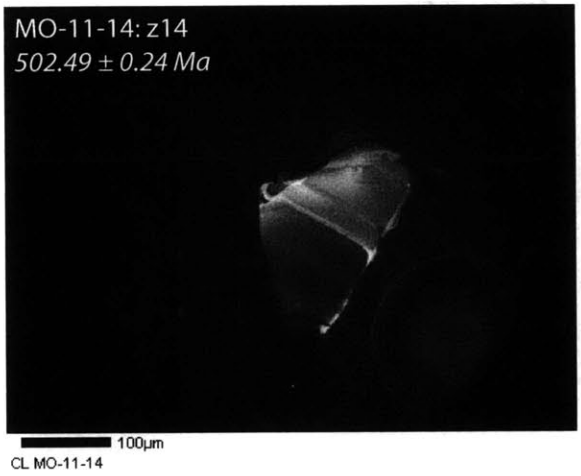

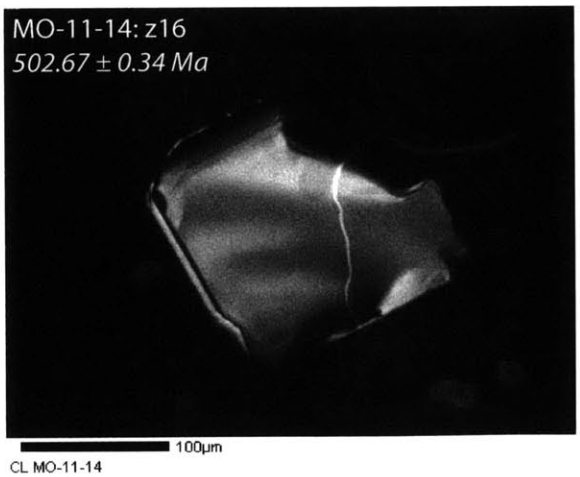

MO-11-19
Primitive Lamprophyre

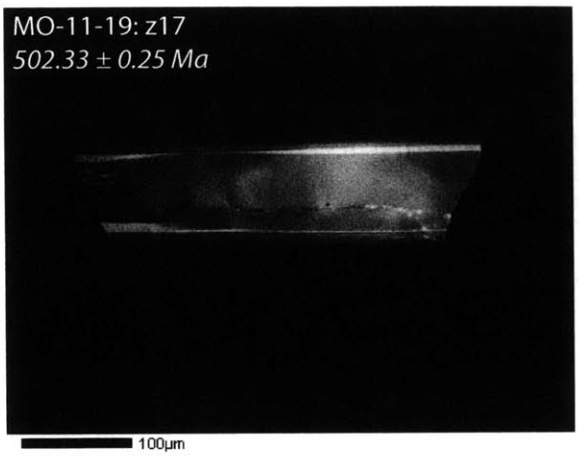

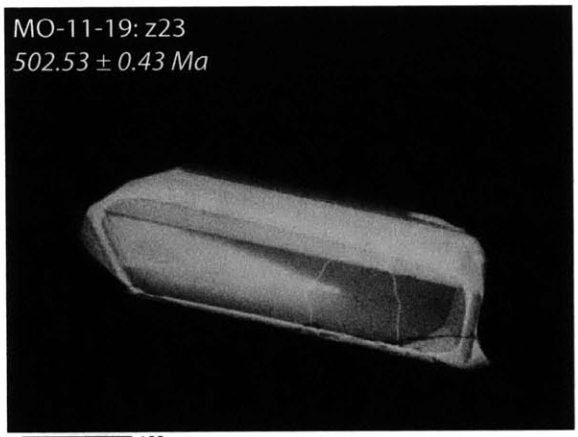

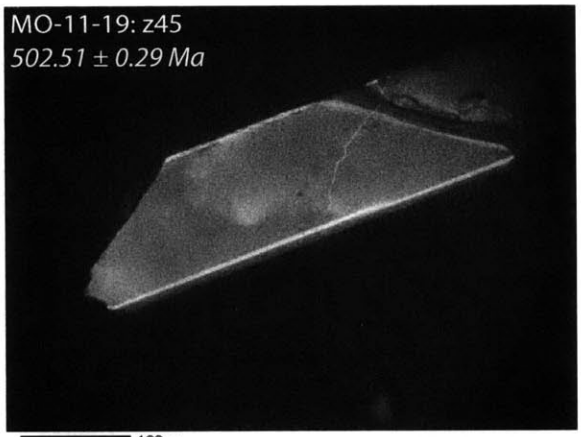

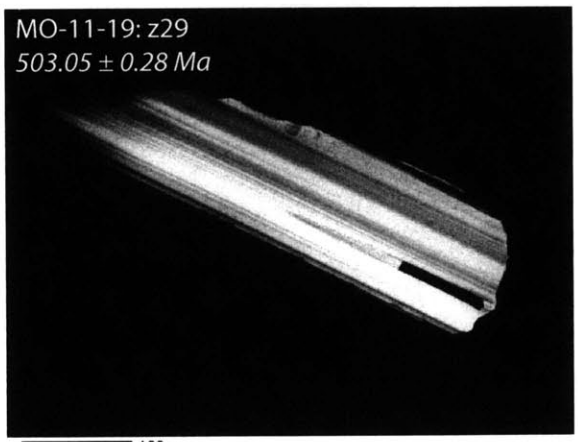

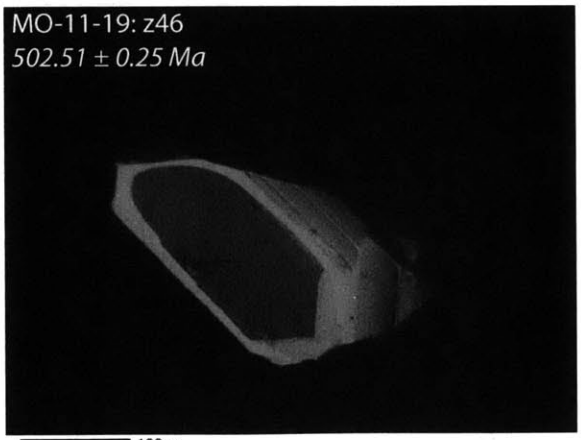

MO-11-26:
Quartz Monzonite